+

Super Wide Band Antennas for Medical Imaging Applications

Wasan Althubitat Alamro

2023

School of Engineering, Computer and Mathematical Sciences, Department of Electrical and Electronic Engineering

A thesis submitted to

Auckland University of Technology

in (partial) fulfilment of the requirements for the degree of

Doctor of Philosophy (PhD)

Abstract

Microwave imaging for cancer detection has gained traction due to the urgent need for safe, affordable, and comfortable imaging methods. Spatial resolution is crucial for effective imaging. Super Wide Band (SWB) antennas is a technology of particular interest within the field of microstrip antennas, and it has garnered significant attention in recent years. These antennas are known for their ability to cover a wide bandwidth, typically achieving a bandwidth ratio of 10 to 1. Several key performance parameters, such as compactness, return loss, peak gain, radiation pattern, and radiation efficiency, play a critical role in determining the effectiveness of SWB antennas, especially when they are deployed for specific applications like medical imaging. It is crucial to understand the designed antenna through an appropriate equivalent circuit model (ECM), especially in the case of integrating the antenna with other systems and when tuning and optimising various parameters.

A comprehensive literature review revealed research gaps in implementing SWB technology in microwave imaging applications. Therefore, this thesis investigates SWB antenna designs for medical imaging, with a particular emphasis on detecting lung and skin tumours.

The thesis presents an optimized ECM of a fractal slot loaded SWB antenna. The SWB antenna has an overall compact dimension of 40×35×1.57 mm^3 and is fabricated on Rogers RT Duroid 5870 substrate (ε_r = 2.33; tanδ = 0.0012). The antenna's bandwidth and gain are enhanced to achieve the desired performance for medical imaging. The achieved measured bandwidth is 36.9 GHz over the frequency range of 3.1 to 40 GHz with a bandwidth ratio of 13:1. A peak realized gain of 9.7 dBi, average radiation efficiency of 94%, and stable radiation pattern are achieved over the covered bandwidth. The presented ECM is derived based on transmission line theory and the individual behaviour of each antenna element. The thesis further presents a dual sequential optimization approach to determine the optimal value of each lumped element. The modeled results are found to be in good agreement with both full-wave simulated and measured results. The presented ECM can accurately capture the antenna's behaviour in terms of its magnitude of reflection coefficient $|S_{11}|$, and both

real and imaginary impedances with low mean absolute percentage error of 4.9%, 7.5%, and 7.7%, respectively, over the super-wide operating bandwidth.

Then a SWB radio frequency imaging approach is developed and evaluated for detecting early stages of deep-seated lung and in-situ skin tumors. A life-sized human torso phantom is constructed of tissue mimicking materials and their dielectric properties are thoroughly investigated over the covered frequency range of 3.1–40 GHz. An array of SWB antenna elements is employed in an imaging setup to assess the detection capabilities of the SWB imaging approach for both lung and skin tumors. Images reconstructed using the acquired backscattering information and confocal beamforming algorithms demonstrate successful detection with accurate tumor size and location estimation. This Thesis establishes the foundation for further exploration of SWB imaging in clinical trials, potentially revolutionizing early cancer detection and treatment monitoring.

Contents

List of Figures

List of Tables

List of Appendices

Attestation of Authorship

I hereby declare that this submission is my own work and that, to the best of my knowledge and belief, it contains no material previously published or written by another person (except where explicitly defined in the acknowledgements), nor material which to a substantial extent has been submitted for the award of any other degree or diploma of a university or other institution of higher learning.

_____ _____

Signature Date

Acknowledgements

First and foremost, I extend my heartfelt gratitude to my primary supervisor, Professor Boon-Chong Seet. Professor Seet's valuable guidance and support throughout my PhD journey have been completely significant. His belief in my abilities, coupled with his encouragement in navigating the challenges we encountered over the past few years, has been invaluable. Professor Seet's firm advice and continued motivation have played an extremely influential role. It has been an absolute privilege collaborating with him. His expertise in problem-solving and academic analysis will undoubtedly continue to shape not only my academic and professional life but also the broader field of research. Without his tireless contributions, completing this thesis within three years would have indeed been a possible task.

Next, I wish to express my deep appreciation to my secondary supervisor, Professor Lulu Wang, whose expertise lies in the field of medical imaging—an area that falls outside my core competence as an electrical engineering student. Professor Wang's guidance has proven to be an invaluable asset to my research journey. I also extend my heartfelt gratitude for her helpful role in securing funding for one of our conference publications, which significantly enhanced the visibility and impact of our work.

Additionally, I want to acknowledge my co-supervisor, Dr. Prabakar Parthiban, for his valuable guidance and profound professional insights that enriched my research experience and contributed to the depth and quality of my work.

I am deeply grateful to the AUT EEE technician team for their valuable assistance and expertise. Mr. Brett Holden, who skillfully assembled the rotating platform and performed complex antenna soldering; Mr. Stephen Hartley, who was responsible for sourcing essential components and materials; and Mr. Ramon Lewis, whose contributions were integral to the fabrication of the antenna shafts. Their dedication and technical proficiency were pivotal to the success of my experiments and the overall completion of my research.

Furthermore, I would like to recognise the substantial financial support I received from AUT, including the tuition fee scholarship from the school. This financial support not only

eased the financial burden of pursuing my doctoral studies but also allowed me to fully immerse myself in my research and academic endeavors.

I extend my heartfelt thanks to the friends I have made in New Zealand for their warm companionship throughout my time here. Their support added an enriching dimension to my life and made my academic journey more memorable.

Lastly, I want to convey my love, respect, and boundless gratitude to my husband and child, who accompanied me on this challenging yet rewarding journey, and to my parents for their endless understanding and support. Without their endless love, this thesis would never have been completed.

List of Acronyms

2D	Two Dimensional
3D	Three Dimensional
AMC	Artificial Magnetic Conductor
AUT	Antenna Under Test
BDR	Bandwidth Dimension Ratio
CF-DAS	Coherence Factor Based Das
CMI	Confocal Medical Imaging
CPW	Co-Planar Waveguide
CR-DAS	Channel Ranked Delay and Sum
CSF	Cerebrospinal Fluid
CT	Computed Tomography
DA	Data Adaptive
DAS	Delay And Sum
DI	Data Independent
DGS	Defected Ground Structure
EIRP	Effective Isotropic Radiated Power
DMAS	Delay Multiply and Sum
EBG	Electromagnetic Band Gap
ECM	Equivalent Circuit Model
EM	Electromagnetic

FEM	Finite Element Method
FSPL	Free Space Path Loss
GPR	Ground Penetrating Radar
HFSS	High Frequency Structural Simulator
HMI	Holographic Microwave Imaging
IDAS	Iterative Delay And Sum
MIMO	Multi Input Multi Output
mmW	Millimetre-Wave
MAPE	Mean Absolute Percentage Error
MRI	Magnetic Resonance Imaging
MTA	Microwave Thermal Ablation
MTM	Metamaterial
MUT	Material Under Test
NSCLC	Non-Small Cell Lung Cancer
PCA	Principal Component Analysis
RCB	Robust Capon Beamformer
RF	Radio Frequency
RFMI	Radio Frequency Medical Imaging
RLC	Resistor-Inductor-Capacitor
RMSE	Root Mean Squar Error
SAR	Specific Absorption Rate

SCLC	Small Cell Lung Cancer
SNR	Signal To Noise Ratio
SOLT	Short-Open-Load-Thru
SWB	Super Wide Band
TSA	Tapered Slot Antenna
UWB	Ultra Wide Band
VNA	Vector Network Analyser
WHO	World Health Organization

List of Symbols

α	Attenuation constant
α_n	Distribution parameter
β	Phase constant; wave number
γ	Complex propagation constant
ε_i	Imaginary part of relative permittivity
ε_o	Vacuum permittivity
$\Delta\varepsilon_n$	Dispersion magnitude
ε_r	Relative permittivity
ε_s	Static permittivity
θ	Elevation angle of radiation pattern
λ	Wavelength
λ_c	Cut-off wavelength
λ_o	Free space wavelength
λ_{og}	Sample wavelength
μ	Complex Permeability
σ	Conductivity
φ	Azimuth angle of radiation pattern
$\varphi(\omega)$	Phase variation as a function of frequency
ω	Angular frequency
Γ	Reflection coefficient

η	Antenna radiation efficiency
η_T	Antenna overall efficiency
τ_g	Group delay
τ_n	Relaxation time
C_{eq}	Equivalent capacitor
cm	Centimetres
dB	Decibels
dBd	Decibels relative to a dipole antenna
dBi	Decibels relative to an isotropic antenna
f_r	Resonant frequency
G_{eq}	Equivalent conductance
G_r	Receiving antenna gain
G_{re}	Realised gain
G_t	Transmitting antenna gain
Hz	Hertz
L_{eq}	Equivalent inductor
mm	Millimetres
µm	Micrometres
P_a	Total power accepted by an antenna
P_r	Received power of an antenna
P_s	Total power supplied to antenna

P_t	Transmitted power of an antenna
R_{eq}	Equivalent resistance
$\boldsymbol{r}_m$	Antenna position
s_m	Resultant reflected signal
T	Transmission coefficient
tanδ	Loss tangent
t_m	Time-of-flight of s_m
x_m^U	Recorded signals from the unhealthy phantom
x_m^H	Recorded signals from the healthy phantom
Z_o	Characteristic impedance

Ethics Approval

Not required.

Chapter 1 Introduction

1.1 Overview

Microwave imaging has seen focused attention in the past few years. It is considered the promising diagnostic and monitoring tool for different cancerous and severe diseases over the conventional means owing to various characteristics such as non-ionising radiation, low cost, less painful, and non-invasive technique[1, 2]. The dielectric contrast between healthy and unhealthy tissues represents the basis of microwave imaging for cancer detection [3]. Lung cancer is considered one of the leading causes of death in the world. Different previous works have been reported in the literature, which presented various designs of patch antennas to detect lung cancer and fluid accumulation.

Super wideband (SWB) antennas have garnered significant attention due to their potential applications in modern communication systems. This technology is seen as an expansion of Ultra Wide Band (UWB) technology, which operates within the unlicensed frequency range of (3.1 – 10.6) GHz, as designated by the Federal Communication Commission (FCC)[4]. A significant challenge in realising super-wide bandwidth lies in the ability to maintain a compact antenna size. Equivalent lumped element circuit models have found extensive application in the design of wideband and UWB antennas [5]. They prove highly effective in the examination of antenna behaviour and the enhancement of their operational capabilities. Recent years have witnessed the investigation of various setups of SWB antennas equipped with equivalent circuit models (ECMs) [4, 6, 7]. Limited research has been conducted on the feasibility of employing SWB antennas in microwave imaging. In this specific application, several key parameters are essential for successful detection.

Melanoma is a serious and malignant type of skin cancer, and New Zealand has one of the highest rates of cutaneous melanoma in the world in terms of both occurrence and fatality [8]. Human trunk, i.e. chest and back, is the site of the body with the highest occurrence of melanoma especially in men [9]. Melanoma has different stages: from stage 0 or in-situ stage where the tumour is on the skin's outermost layer (epidermis) to stage 4 where the tumour has spread beyond lymph nodes to other organs.

During in-situ melanoma stage, the tumour has not spread to lymph nodes and has no more than 1 mm thickness. In recent years, microwave imaging has attracted much interest as a noninvasive detection technique for different cancer types and for frequent monitoring after a curative procedure, due to its capability in detecting the presence of cancer lesions, high safety, and low cost [10].

In this context, this thesis focuses on investigating SWB antenna with enhanced parameters over the operating frequency 3.1 to 40 GHz and modelling a simplified and accurate ECM. In addition to testing the capability of the proposed antenna in medical imaging applications. Specifically, the objectives of this thesis are to deliver:

- A novel SWB antenna design with enhanced parameters to fulfil the requirements of microwave imaging applications.
- An accurate and simplified ECM of the SWB antenna using dual sequential optimisation approach to find the optimal values of the lumped elements.
- Studying the dielectric properties of different mixtures mimicking the behaviour of human torso phantom over the SWB frequency range.
- Detecting the early stage of both deep-seated lung and in-situ skin tumours in human torso phantoms.

1.2 Research Gaps, Motivations and Scope

From the literature review, it has been found that there is still exist a number of research gaps in enhancing the performance of SWB antenna especially in terms of the operation factors required for microwave imaging and circuit modelling:

- No study has been conducted previously on the possibility of implementing SWB antenna with efficient detection parameters; including the high $|S_{11}|$ level at the resonant frequencies [7, 11, 12], high gain [13], low mutual coupling with high isolation and good radiation efficiency for different cancer types like lung and skin.
- Lack of the precision level of the equivalent circuit model [4, 6, 7] existed in literature in modelling the exact SWB antenna performance. In addition to the complexity of the existed models. Notably, there remains a significant gap in the existing research as mathematical connections between the ECM and transmission line theory have yet to be explored.

- Primary limitations and challenges that revolve around the lung cancer detection by microwave imaging [3, 14-17]; which include the low resolution detection and the study of only the superficial lung tumours.
- Lack of studies on the dielectric properties of different human tissues mimicking phantoms especially the tissues included in the human torso phantoms at high frequency range [14, 15, 18]. In addition to the lack of studies on detecting lung tumour using a cylindrical human sized torso phantom with anatomical representation of the several torso layers that made of different mimicking material [14-16].
- None of the reported studies discussed the possibility of using one SWB antenna structure in different cancer types of detection [10].
- Lack of studies on skin cancer detection [19-23], all previous works detect skin tumour located at some depth of the skin layer or even lower in the adipose layer [19, 21, 22], while the existence of this particular type of tumours is usually in the external skin layer.

In terms of motivation, first of all, designing an enhanced performance antenna with large bandwidth and compact size is challenging in designing SWB antenna. Several techniques [24] need to be incorporated in the design along with different parametric studies of several physical parameters. Therefore, achieving optimum parameters like improved $|S_{11}|$ level ($\leq$-20 dB), high realised peak gain with 9.7 dBi maximum value and good radiation efficiency above 90% can significantly improve the efficiency of different applications in which this SWB antenna can be deployed, specifically in medical imaging applications [10, 25] .

ECM based on the lumped elements of SWB antenna has been studied in literature using different optimisation techniques [6, 26]. However, the accuracy of the presented models was not high besides the complexity of them. Accordingly investigating a new approach which involve the implementation of dual sequential optimisers enhances the precision and simplified the proposed model which considered beneficial in understanding the antenna performance in different applications.

Besides, for the best of our knowledge, none of the reported literature studied the capability of deploying SWB antenna in medical imaging applications like lung and skin tumours [3, 14, 16, 19, 20] especially in the early stages and with small radius size. Hence, incorporating SWB antenna in medical imaging application can be a promising approach of replacing the current imaging techniques, especially with the concluded capabilities that evolved the high obtained resolution, accurate localisation and prediction of the tumour size.

1.3 Contributions and Publications

This thesis makes the following four key contributions:

- **Novel SWB antenna design with enhanced parameters for microwave reflectometry to detect early-stage tumours.** A fractal slot loaded SWB antenna with dimensions of 40×35×1.57 mm^3 is designed with different bandwidth and gain enhancement techniques; like using tapered feedline, semi-elliptical slotted shape ground plane and modified elliptical shape patch embedded with two fractal slots at the upper corners. An operating bandwidth 3.1 to 40 GHz (12.9:1) is achieved with -20.7 dB, -19.4 dB and -34.2 dB $|S_{11}|$ level obtained at the first three resonant frequencies 3.8, 6.7 and 9.6 GHz, respectively. The proposed design offers a peak gain of 3.4 to 9.7 dBi over the covered bandwidth with 94% radiation efficiency. All the above enhanced parameters make the proposed antenna a good candidate in microwave imaging applications.
- **A precise and simple ECM that represents the SWB behaviour over the covered bandwidth.** An approach employing dual sequential optimisation is suggested for determining the optimal values of each lumped element. When comparing the modelled outcomes with both full-wave simulated and measured results, it becomes evident that the proposed model accurately match the antenna's performance, exhibiting a notably low mean absolute percentage error of 4.9%, 7.5%, and 7.7% for $|S_{11}|$, real impedance, and imaginary impedance, respectively.
- **Successful implementation of SWB microwave reflectometry technique for improved detection of lung tumours**, particularly in their early stages in deep-seated and superficial locations, to increase the chance of a successful

treatment. To the best of our knowledge, no previous study has investigated the detection of lung tumours in both deep and superficial positions based on the variance of their backscattered signals from all antenna elements as demonstrated in this thesis. Detection of deep-seated lung tumour with 15 mm radius is achieved with high resolution using a human sized five layers torso phantom, showing the potential of SWB microwave reflectometry in precisely determining the size of early-stage tumours even in deep locations. The dielectric properties of the phantom layers are measured over the covered bandwidth.

- **Investigating the capability of a super wideband (SWB) antenna based imaging system for in-situ skin cancer detection.** The imaging system consists of eight antenna elements in a circular array positioned around a human trunk phantom modelled as five concentric layers of skin, fat, muscle, rib bone and lung tissues. The dielectric properties of the phantom tissues are measured over the operating bandwidth (3.1 to 40) GHz. The skin tumour is modelled as cylindrical shape on the outer skin layer with 1mm thickness and 7.5mm radius. The reconstructed 2D images of the trunk area reveal better image resolution and consequently more accurate estimation in terms of the tumour's radius and thickness.

This research has resulted in the following publications:

1. W. Alamro, B. -C. Seet, L. Wang and P. Parthiban, "Experimental Detection of Early-Stage Lung and Skin Tumors Based on Super Wideband Imaging," in *IEEE Journal of Electromagnetics, RF and Microwaves in Medicine and Biology*, vol. 8, no. 2, pp. 182-189, June 2024, doi: 10.1109/JERM.2024.3395923.
2. W. Alamro, B.C. Seet, L. Wang, P. Parthiban, "Equivalent Circuit Modeling and Optimization for Fractal Slot Loaded Super Wideband Antenna for Medical Imaging Applications", (under submission to a journal)
3. W. Alamro, B.C. Seet, L. Wang, P. Parthiban, "Early-Stage Lung Tumor Detection Based on Super-Wideband Microwave Reflectometry", *Electronics*, vol. *12*, no. 36, 2023. https://doi.org/10.3390/electronics12010036
4. W. A. Alamro and B. C. Seet, ''Review of practical antennas for microwave and millimetre-wave medical imaging'' (Healthcare Technologies, 2021), Chapter 6 in *Electromagnetic Waves and Antennas for Biomedical Applications,* IET, UK, 2021, pp. 185-207, DOI: 10.1049/PBHE033E_ch6
5. W. A. Alamro, B. C. Seet, L. Wang and P. Parthiban, "Compact Super-Wideband Antenna for Medical Imaging Applications*",* 2021 IEEE Conference on Antenna Measurements & Applications (CAMA)*, 2021, pp. 505-508.* DOI: 10.1109/CAMA49227.2021.9703550.
6. W. Alamro, B. C. Seet, L. Wang and P. Parthiban, "High Resolution In-Situ Skin Cancer Microwave Imaging Using Super Wideband Antenna, " *2023 16th*

International Congress on Image and Signal Processing, BioMedical Engineering and Informatics (CISP-BMEI), Taizhou, China, 2023, pp. 1-5, doi: 10.1109/CISP-BMEI60920.2023.10373355.

7. W. Alamro, B.C. Seet, L. Wang, P. Parthiban, "Early-Stage Lung and Skin Tumour Detection with Super Wideband Antenna Array Imaging", oral abstract presentation, *Workshop on Sensing, Measurement and Instrumentation for Healthcare, Food, Agriculture, Environment and Security,* IEEE Instrumentation and Measurement Society New Zealand Chapter, 2023.

1.4 Thesis Organisation

The thesis is organised as follows:

Chapter 2 provides overview of three main areas: fundamental concepts of microstrip circular antennas, transmission line theory, and microwave imaging concept along with a discussion of different detection techniques. Which form a background of this research. In addition, the simulation environment and measurement facilities used for this work are presented in this chapter.

Chapter 3 reviews relevant research literature, including the state-of-the-art design of SWB antenna. Next, different ECM approaches are introduced. Besides, several medical imaging systems in different applications are discussed.

Chapter 4 investigates the design of SWB antenna structure, the contribution of each technique implemented in the design into the final antenna performance. Besides, performing measurements of the key behaviour parameters in frequency and time domain. Finally, this chapter presented the ECM of the proposed antenna and discusses the accuracy of the proposed model.

Chapter 5 presents the application of the proposed SWB in lung tumour detection, including presenting the imaging setup including the torso phantom dielectric properties measurement. Then, different detection states are studied in both deep-seated and superficial locations. Finally, the reconstructed images that reveals the lung tumour detection are displayed.

Chapter 6 first proposes the SWB array imaging system for in-situ skin cancer detection considering small radius of the tumour lesion. Next, the reflection and the transmission coefficients of the backscattered signals are discussed. Finally, the imaging results are

introduced with analysis of the capability of high resolution, localisation, and prediction of the tumour size in simulation and measurement environments.

Chapter 7 concludes this thesis with a summary of the contributions and some discussion on future research directions.

Chapter 2 Background

2.1 Introduction

Super wideband antennas (SWB) have garnered focused attention in the last few years due to their large bandwidth, compactness, high data rates and the coverage of both short- and long-range transmission [12, 24].

Microstrip patch antennas can be analysed using different methods, transmission line and cavity approaches. Transmission line (TL) model is one of the popular techniques used to understand the antenna behaviour while giving physical insight through the lumped elements equivalent circuit model (ECM). It is important to introduce some concepts and techniques used to model the performance of SWB antenna over large, covered bandwidth in order to enhance the comprehension of how the antenna behaves.

Over the past two decades, extensive research has been conducted on Microwave Imaging (MI) methods, which offer a promising alternative to conventional imaging modalities. During this period, various types of antennas have been incorporated into microwave imaging systems for detecting different diseases [10].

This chapter aims to establish a foundational understanding of three key areas. Firstly, it will introduce the fundamental concepts of microstrip circular antennas, including their essential parameters and the theory of transmission line modelling. Secondly, it will provide an overview of the microwave imaging concept, along with a discussion of different detection techniques. Lastly, a brief introduction will be given regarding the simulation software and measurement facilities employed in this study.

2.2 Microstrip Antennas

In this section microstrip antennas are discussed along with the design procedures of circular microstrip antenna. Later, the general equivalent circuit model of the microstrip antenna is presented.

2.2.1 Key Features

Microstrip antennas have garnered significant attention since the 1970s [27], these antennas, comprise an extremely thin metallic strip, also known as a patch, positioned a small fraction of a wavelength above a ground plane. The patch and the ground plane are separated by a dielectric sheet, referred to as the substrate, as depicted in Figure 2-1(a) where L and W are the length and width of the patch, respectively, h is the substrate height and ε_r is the dielectric constant of the substrate. However, the equivalent circuit model of the microstrip antenna is a simple resonant RLC (resistor-inductor-capacitor) circuit in series with inductor which contribute to the patch inductive nature as illustrated in Figure 2-1 (b).

Various substrates are available for microstrip antenna design, with their dielectric constants typically ranging from 2.2 to $\varepsilon_r \leq 12$. Optimal antenna performance is often associated with thick substrates at the lower end of the dielectric constant range. As the dielectric constant ε_r of the substrate decreases, the fringing field (radiating fields) becomes more pronounced, causing the field to extend further away from the patch in a "bowing" fashion. These substrates offer improved efficiency, larger bandwidths, loosely bound fields for radiation into space, and may result in larger element sizes [27, 28]. However, with increased substrate height, surface waves become a factor, typically considered undesirable because they tend to absorb power from the overall available for direct radiation which are space waves. These surface waves propagate within the substrate and are subject to scattering at bends and surface irregularities, including instances such as dielectric and ground plane truncation. This scattering process has a detrimental effect on the antenna's pattern and polarization characteristics. However, the presence of surface waves can be mitigated, while still preserving large bandwidth, through the utilization of cavities, stacking and other methods, to expand the antenna's bandwidth.

Microstrip antennas are often interchangeably referred to as patch antennas. The radiating elements and feed lines are typically photoetched onto the dielectric substrate. Radiating patches can take various shapes, square, rectangular, dipole (strip), and circular shapes are the most common due to their ease of analysis and fabrication, as well as their favorable radiation characteristics, particularly low cross-polarization radiation.

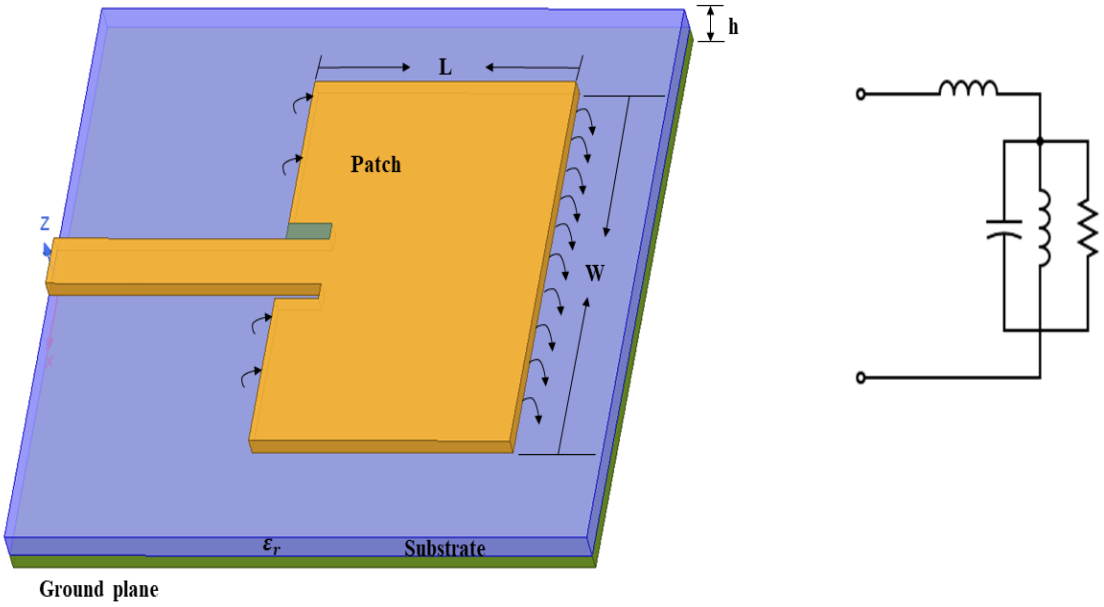

(a) *(b)*

Figure 2- 1 Microstrip antenna, (a) structure; (b) equivalent circuit.

2.2.2 Circular Microstrip Antenna

Circular shaped patch microstrip antenna can be designed based on the cavity model approach, the procedures include prior assumption of the dielectric constant of the substrate (ε_r), the resonant frequency f_r in Hz and the thickness of the substrate h in cm. The radius of the circular patch (a) can be calculated as shown:

$$a = \frac{F}{\left\{1 + \frac{2h}{\pi\,\varepsilon_r\,F}\left[\ln\left(\frac{\pi F}{2h}\right) + 1.7726\right]\right\}^{1/2}} \tag{2.1a}$$

$$F = \frac{8.791 \times 10^9}{f_r\sqrt{\varepsilon_r}} \tag{2.1b}$$

Due to the typically small thickness of the microstrip, the waves generated within the dielectric substrate (between the patch and the ground plane) undergo significant reflections upon reaching the patch's edge. Consequently, only a minor portion of the incident energy is emitted, rendering the antenna highly inefficient. Beneath the patch, the fields take on the form of standing waves, which can be represented using cosine wave functions. Given the minimal height of the substrate ($h \ll \lambda$, where λ is the wavelength within the dielectric), variations in the field along the height are considered negligible. Furthermore, owing to the substrate's extremely small height, the field fringing along the patch's edges is also minimal, resulting in an electric field that is nearly perpendicular to the patch's surface. Consequently, only transverse magnetic TM_x field configurations within the cavity will be taken into account, where x is the field mode which can be controlled by the patch radius.

2.3 Fundamentals Parameters of Antennas

Several key parameters are discussed under this section, which are considered the antenna figure-of-merit, and different optimisation and enhancement techniques are implemented to improve them.

2.3.1 Radiation Pattern

It is typically defined as the antenna pattern, which serves as a mathematical function or graphical representation detailing the antenna's radiation characteristics concerning spatial coordinates. Around the antenna, both near-field and far-field are the encountered regions, but in most cases, only far-field radiation is considered. This preference arises because the angular distribution of an antenna remains independent of the measuring distance from the antenna [29]. If the antenna under examination has a maximum physical dimension denoted as D, its far-field region starts from $\frac{2D^2}{\lambda}$ of the antenna, where λ represents the wavelength of the operating frequency.

Antenna radiation patterns can be described using either 3D or 2D coordinates. Specifically, for a linearly polarized antenna, its radiation patterns can be graphically represented in the E-plane and H-plane. The E-plane is defined as the plane encompassing the electric field vector and the direction of maximum radiation, while the H-plane is orthogonal to the E-plane, encompassing the magnetic field vector and the direction of maximum radiation. Figure 2-2 provides illustrations of the antenna patterns of a dipole antenna in both 3D and 2D formats, highlighting the E-plane (xz and yz-plane) and H-plane (xy-plane).

An isotropic radiator, defined as a theoretical, lossless antenna that radiates equally in all directions, while not physically achievable, often serves as a reference for expressing the directive characteristics of actual antennas. In contrast, a directional antenna is one that effectively radiates or receives electromagnetic waves more efficiently in certain directions than in others.

This term is typically applied to antennas whose maximum directivity significantly surpasses that of a half-wave dipole. In Figure 2-3, the pattern is non-directional in the azimuth plane (H-plane) [$\theta = \pi/2$] and directional in the elevation plane (E-plane) [ϕ = constant]. This specific pattern is referred to as omnidirectional, defined as one that exhibits an essentially non-directional pattern in a given plane (in this case, azimuth) and a directional pattern in any orthogonal plane (in this case, elevation).

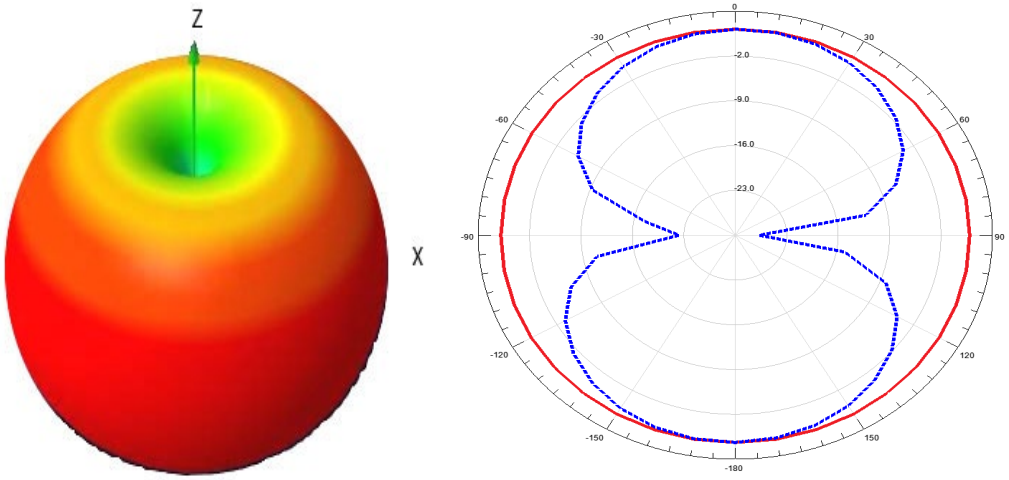

Figure 2- 2 Radiation pattern of dipole antenna: (a)3D pattern; (b)2D radiation pattern (Solid line is the H-plane and the dashed line is the E-plane).

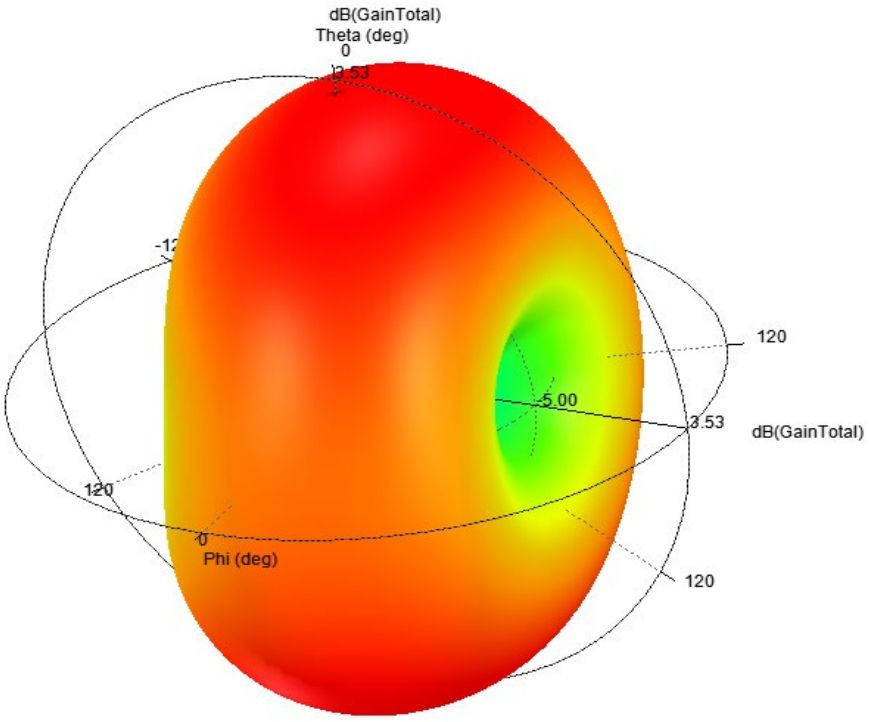

Figure 2- 3 Omnidirectional antenna pattern.

2.3.2 Gain

The antenna's gain in a specific direction is defined as the ratio of the intensity in that particular direction over the radiation intensity that would result if the power received by the antenna were radiated uniformly in all directions. The radiation intensity corresponding to the isotropic radiation power equals the power received (input) by the antenna divided by 4π. It is usually measured in dBi (reference to isotropic antenna) or in dBd (reference to dipole antenna).

In the majority of instances, the relative gain, a concept defined as the proportion of power gain in a specific direction to the power gain of a reference antenna in its specified direction. It's important to note that the power input must remain consistent for both antennas under consideration. Typically, the reference antenna is chosen to be a dipole, horn, or any other antenna for which the gain can be computed or is already known. Nevertheless, in many scenarios, the reference antenna is a lossless isotropic source.

There are two gains definitions: gain (G) and realised gain (G_{re}), where the latter takes into account the reflection and the mismatch losses.

$$G_{re}(\theta, \varphi) = (1 - |\Gamma|^2 \, G(\theta, \varphi) \quad (2.2)$$

where Γ is the reflection coefficient, θ and φ are the elevation and azimuth angles, respectively.

Antenna pattern and gain are typically assessed in an open environment or within an RF anechoic chamber designed to replicate open-space conditions. During measurements within the chamber, the antenna under examination (AUT) is mounted to a rotatable antenna positioner. This positioner may be positioned beyond the far-field boundary of the source antenna and is located within the chamber's quiet zone [27]. As the AUT is rotated, the data includes the power received by the AUT from the source antenna is recorded at different θ and φ, which are then mapped on either a 3D or 2D system to obtain radiation patterns.

2.3.3 Bandwidth

The impedance Bandwidth of the antenna is defined as the frequency range confined under the condition of preserving reflection coefficient $|S_{11}| \leq$-10 dB. For broadband antennas the bandwidth can be defined in terms of the ration bandwidth (R_{BW}:1) where R_{BW} is the upper to lower frequency ratio. In the case of SWB antenna the ratio bandwidth should be maintained with at least 10:1. In the case of narrow band antennas, the bandwidth is usually expressed in terms of the fractional bandwidth (FBW) which is the percentage of the frequency difference $(f_H - f_L)$ over the centre frequency of the covered bandwidth ($f_c = \frac{f_H + f_L}{2}$). Usually the FBW varies between (0% to 200%) where antennas with FBW $<$ 20% are referred to narrowband while having FBW $\geq$ 20% contributed to wideband antennas. Ultra-wideband antennas are usually with 50% or more FBW.

2.3.4 Friis Transmission Equation

The Friis Transmission Equation establishes a connection between the received power and the transmitted power when dealing with two antennas positioned at a distance $R > \frac{2D^2}{\lambda}$ apart, where D signifies the largest dimension of either antenna.

The two identical antenna method is employed for measuring the realised gain in this thesis. Briefly there are two steps for the measurement that performed in the RF anechoic chamber. In the first step, the difference between the received and the transmitted power is measured at each frequency point within the covered bandwidth. In the second step, the gain is calculated using equation (2.4).

If the input power at the transmitting antenna's terminals is P_t, then at a distance R from the antenna, then the ratio of the received to the input power can be expressed as:

$$\frac{P_r}{P_t} = \frac{G_t G_r \lambda^2}{(4\pi R)^2} \tag{2.3}$$

where P_r is the received power, G_t and G_r are the transmitting and the receiving antenna gain, respectively. The Free Space Path Loss (FSPL) is defined as $\left(\frac{4\pi R}{\lambda}\right)^2$, while the Effective Isotropic Radiated Power (EIRP) is defined as $P_t \times G_t$ (Watt). Since the antennas are identical then the gain can be found using:

$$G^2 = \left(\frac{4\pi R}{\lambda}\right)^2 \frac{P_r}{P_t} \tag{2.4}$$

2.4 Transmission Line Theory

A transmission line is commonly represented schematically as a two-wire configuration since transmission lines, for the propagation of transverse electromagnetic (TEM) waves, always comprise a minimum of two conductors. The infinitesimal length segment Δz shown in Figure 2-4(a) can be conceptualized as a lumped-element circuit [28], as depicted in Figure 2-4(b). In this representation, the per-unit-length quantities R, L, G, and C are defined as follows:

R represents the series resistance per unit length for both conductors, measured in ohms per meter (Ω/m), L corresponds to the series inductance per unit length for both conductors, expressed in henrys per meter (H/m). G signifies the shunt conductance per unit length, denoted in siemens per meter (S/m), and C represents the shunt capacitance per unit length, measured in farads per meter (F/m).

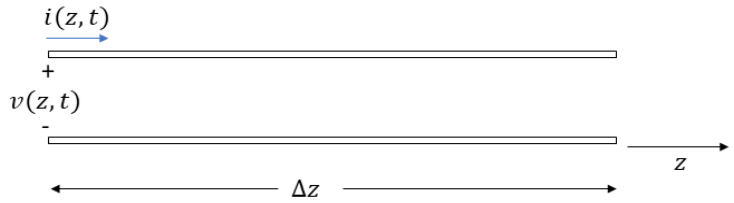

(a)

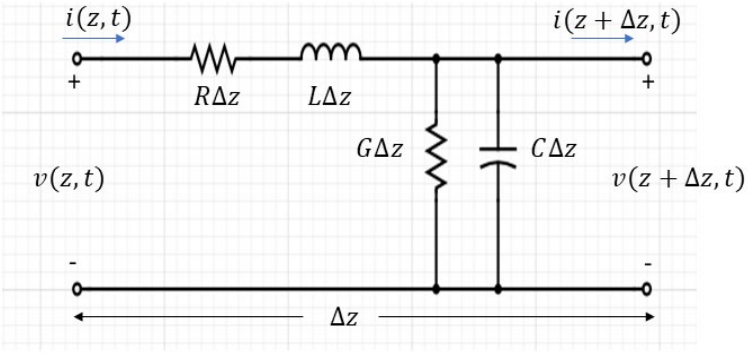

(b)

Figure 2- 4 (a)Voltage and current definitions for incremental length of transmission line; (b)lumped element equivalent circuit.

The series inductance L accounts for the combined self-inductance of both conductors, while the shunt capacitance C is attributed to the close proximity of these conductors. In contrast, the series resistance R reflects the resistance due to finite conductivity of each individual conductor, and the shunt conductance G arises due to dielectric loss within the material situated between the conductors. Essentially, R and G represent loss in the system.

When examining a finite length of transmission line, it can be viewed as a sequence of sections relative to the one depicted in Figure 2-4(b). In reference to this circuit, applying Kirchhoff's voltage and current laws yields:

$$v(z,t) - R\Delta z i(z,t) - L\Delta z \frac{\partial i(z,t)}{\partial t} - v(z+\Delta z,t) = 0 \tag{2.5a}$$

$$i(z,t) - G\Delta z v(z+\Delta z,t) - C\Delta z \frac{\partial v(z+\Delta z,t)}{\partial t} - i(z+\Delta z,t) = 0 \tag{2.5b}$$

Dividing equations (2.5a) and (2.5b) by Δz and then taking the limit as Δz approaches zero, the following set of differential equations can be obtained:

$$\frac{\partial v(z,t)}{\partial z} = -Ri(z,t) - L\frac{\partial i(z,t)}{\partial t} \quad (2.6a)$$

$$\frac{\partial i(z,t)}{\partial z} = -Gv(z,t) - C\frac{\partial v(z,t)}{\partial t} \quad (2.6b)$$

These equations represent the time-domain formulation of the transmission line equations, commonly referred to as the telegrapher equations [30]. Under the conditions of sinusoidal steady-state with cosine-based phasors, equations (2.6a) and (2.6b) can be further simplified to:

$$\frac{dV(z)}{dz} = -(R + j\omega L)\, I(z) \quad (2.7a)$$

$$\frac{dI(z)}{dz} = -(G + j\omega C)\, V(z) \quad (2.7b)$$

Both equations (2.7a) and (2.7b) can be simultaneously solved, resulting in wave equations for $V(z)$ and $I(z)$:

$$\frac{d^2V(z)}{dZ^2} - \gamma^2 V(z) = 0 \quad (2.8a)$$

$$\frac{d^2I(z)}{dZ^2} - \gamma^2 I(z) = 0 \quad (2.8b)$$

where γ is the complex propagation constant, frequency dependant parameter, α is the attenuation constant and β is the phase constant. γ can be defined as:

$$\gamma = \alpha + j\beta = \sqrt{(R + j\omega L)(G + j\omega C)} \quad (2.8c)$$

The travelling wave solution can be written as:

$$V(z) = V_\circ^+ e^{-\gamma z} + V_\circ^- e^{\gamma z} \quad (2.9a)$$

$$I(z) = I_\circ^+ e^{-\gamma z} + I_\circ^- e^{\gamma z} \quad (2.9b)$$

where $e^{-\gamma z}$ term signifies the transmission of waves in the positive z-direction, while the $e^{\gamma z}$ term signifies wave propagation in the negative z-direction. When we apply equation (2.7a) to the voltage described in equation (2.9a), we obtain the current along the transmission line:

$$I(z) = \frac{\gamma}{R + j\omega L}(V_\circ^+ e^{-\gamma z} + V_\circ^- e^{\gamma z}) \quad (2.9c)$$

By comparing the above equation (2.9c) with (2.9b), the characteristics impedance, Z_o, can be defined as:

$$Z_o = \frac{R + j\omega L}{\gamma} = \sqrt{\frac{R + j\omega L}{G + j\omega C}} \quad (2.9d)$$

2.5 Radio Frequency Medical Imaging (RFMI) Profile

According to the World Health Organization (WHO), breast cancer and lung cancer are the most common cancer in women, and men, respectively [31]. Skin cancer is another prominent type of cancer that affects both genders, with New Zealand having one of the highest incidence rates in the world [32]. Breast cancer occurs when an abnormal overgrowth of breast cells leads to the formation of malignant (cancerous) tumour. The symptoms include a lump or swelling in the breast, abnormal nipple discharge, and changes to the nipple or breast shape and texture. Lung fluid accumulation is an acute respiratory system complication, which can occur inside the lung (pulmonary edema) or around the lung (pleural effusion). The latter is commonly caused by lung cancer [18], [33]. Skin cancer can be melanoma or non-melanoma. The former is more deadly as it can spread rapidly but less common than the latter [22]. Brain tumour, even if benign (non-cancerous), can be life-threatening when located in deep and delicate part of the brain [34]. Brain stroke is generally caused by the lack of blood flow in the brain due to blood bleed or blood clot [35]. Both brain tumour and brain stroke can cause severe brain injuries [36].

Early-stage detection of the aforementioned disease types plays an important role in controlling their prevalence [37, 38]. A reliable diagnosis at an early stage could greatly enhance the prognosis and the treatment outcomes. The first step of breast, brain, lung and skin cancer detection is the physical examination or the conventional imaging techniques such as X-ray mammography, computed tomography (CT), ultrasound, and magnetic resonance imaging (MRI) [39].

X-ray mammography is the most popular detection method for early-stage breast cancer [40], while CT is most appropriate for lung cancer and fluid accumulation detection [41]. Using these methods, however, can be painful and difficult to pin-point the precise location of the tumour. X-ray mammogram is usually followed by ultrasound scanning to detect tumour sizes down to a few millimetres (mm), but it is still difficult to differentiate between benign and malignant tumours. MRI and CT are the common methods to identify pathological changes and structural variations of biological tissues such as brain, lung and skin tissues [42], but they are not suitable for continuous monitoring of tumours due to high cost and high time consumption.

Medical imaging techniques using radio frequency (RF) waves in the microwave and millimetre-wave (mmW) regimes, which it referred to as radio frequency medical imaging (RFMI), have been developed in the past two decades as a promising complementary technology for early-stage detection and the treatment of cancer and other serious diseases. Recently, different studies are conducted on the feasibility of RFMI in bone fracture detection [43] and osteoporosis monitoring [44]. Microwave Thermal Ablation (MTA) is one of the clinical treatment adopted in liver cancer treatment, RFMI system is proposed in [45] to monitor the changes undergoing in the thermally treated liver tissue. The reconstructed image quality of the tumours and other abnormalities in the body by the RFMI system depends heavily on the characteristics of the used antennas such as the radiation pattern, gain, and operational bandwidth. For instance, using an antenna with high gain or directionality minimises the environmental noise effects and increases the signal penetration into the human target area, resulting in improved signal-to-noise ratio (SNR) and consequently higher quality images.

It is also desirable for the antenna to have an operational bandwidth of several GHz to achieve high- resolution imaging down to millimetre scale. A wider operating bandwidth correlates directly with higher image resolution. There are several advantages of RFMI over conventional imaging tools. Firstly, it is less intrusive than X-ray mammography with no need for breast compression. Secondly, the produced radiation is non-ionised, and thus is safer for pregnant women unlike CT and X-ray mammography [33], [46]. Thirdly, the amount of energy absorption by the human body from its radiation field is less and usually within a safe level of specific absorption rate (SAR) [47]. Lastly, it is comparatively less expensive. These advantages of RFMI make it a prospective mechanism to overcome the limitations of traditional imaging methods.

In RFMI, the radio waves are scattered differently by the cancerous tissues because of their higher dielectric properties than the adjacent healthy tissues. Such dielectric discrepancy between different tissue types is the basic principle utilised by RFMI for cancer detection [48]. The scattered signals from human target area are acquired, pre-processed to reduce clutter produced by skin reflection and environmental background noise, and then used for reconstructing images of the target area through the application of signal processing.

2.6 RFMI Techniques and Signal Processing Algorithms

RFMI techniques can be classified as active, passive or hybrid [49]. Active RFMI is the most common technique, where human tissues are illuminated using low-power RF signals to reconstruct the images of the area under test, based on a contrast of the dielectric properties between cancerous and healthy tissues due to differences in their water, sodium and protein content. Cancerous tissues can be malignant with higher sodium content than normal tissues that lead to high water retention and thus high permittivity and conductivity values; or benign with mainly fatty or adipose tissues that have lower dielectric properties than normal tissues [22, 50]. On the other hand, the passive RFMI relies on the temperature contrast between cancerous and healthy tissues to reconstruct images. Distinctively, the lower thermo-regulatory potential of the cancerous tissues causes them to dissipate more heat than typical host tissues. This technique is referred to as radiometry performed with a radiometer. The hybrid RFMI also use thermo-heating RF signals to illuminate the human tissue. However, the detection is based on using an ultrasound transducer to detect the pressure waves generated due to heated tissue expansion, which are more significant for cancerous tissues. This difference in the level of generated pressure waves between cancerous and healthy tissues is used for reconstructing an image of the area. Examples of hybrid RFMI techniques include RF induced ultrasound imaging, RF elastography and thermo-acoustic tomography.

Active RFMI can be further classified into: tomography (transmission-reflection imaging); and UWB radar. Tomography is a non-linear scattering approach for reconstructing the dielectric profile of the target area using the incident and received fields, shape of the target area, and spatial distribution of electrical permittivity.

Tomography imaging is based on the scattered RF field of a single frequency or multiple frequencies by transmitting a narrowband signal by a single antenna at a distinct location from the object and the reflected signals are received by receiver antennas placed at opposite location. If the target area tissue is cancerous and malignant, it would increase the strength of the scattered signals, resulting in high permittivity and conductivity values [51]. However, image reconstruction by tomography is an ill-posed inverse problem that is very prone to noise in the signal data [52].

On the other hand, UWB radar-based imaging is a linear scattering approach that transmits a short pulse towards a target area and measures the scattered pulse to create an image [17]. Several radar-based imaging approaches including confocal medical imaging (CMI) [16] and holographic microwave imaging (HMI) have been proposed for different diseases [53]. A cancerous malignant tissue will produce a spot with high intensity of energy due to high reflection. The antennas are used to transmit short pulses or modulated RF signal, and the scattered signals are received by either the same transmitting antennas or different receiver antennas located at different positions. Despite the differences between these two active approaches, they share the same general architecture for imaging systems as shown in Fig. 2-5.

In CMI, the target images can be reconstructed using radar-based beamforming algorithms. An effective reconstruction algorithm provides a precise localisation of tumours, while suppressing clutter and any residual artefacts from pre-processing stage. The algorithms implement coherent addition of the backscattered signals received after illuminating the target area with short UWB pulses. The algorithms can be classified as data independent (DI) or data adaptive (DA). To compensate path attenuation and dispersion, DI algorithms perform coherent addition using an assumed propagation model while DA algorithms estimate the propagation model from received signals and then utilise this model (applied with certain compensation factors) to perform coherent addition [54].

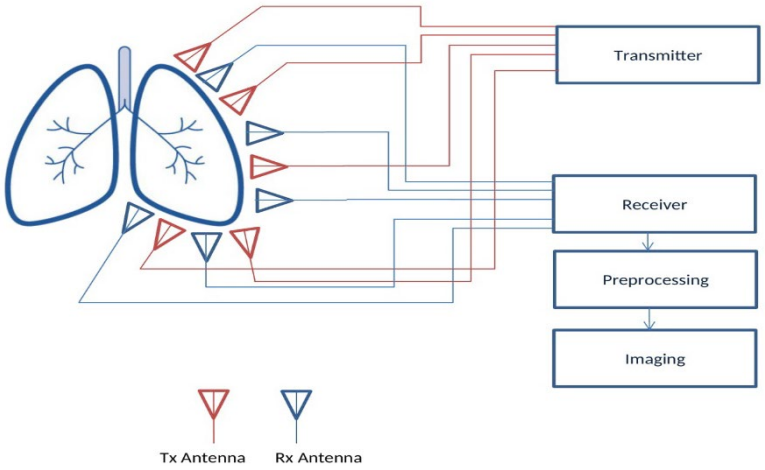

Figure 2- 5 RFMI system architecture in example application for lung imaging

Different radar-based image reconstruction algorithms such as Delay-and-Sum (DAS), Improved Delay-And-Sum (IDAS), Delay-Multiply-and-Sum (DMAS), Coherence Factor Based DAS (CF-DAS), Channel Ranked DAS (CR-DAS) and Robust Capon Beamformer (RCB) have been proposed in literature, which can be used with both monostatic and multistatic UWB radar systems [54]. DAS, IDAS, DMAS, CF-DAS and CR-DAS are DI algorithms, whereas RCB is a DA algorithm. Among these algorithms, DMAS exhibits the best overall performance in clutter reduction and tumour localisation. Different algorithms can detect the depth of tumour like DAS beamforming algorithm and Ground Penetrating Radar (GPR) algorithm[55]. All algorithms above can be used to reconstruct two-dimensional (2D) or three-dimensional (3D) images. In most cases, 2D images can provide sufficient information, such as the existence of tumours, number of tumours, location, shape, and size of detected tumours. However, if tumour depth is an important parameter, or there exist multiple tumours at the same location, then a 3D image is required. In dense fibro-glandular tissues, a 3D image can also provide more accurate detection and localisation of cancerous tissues than 2D images.

2.7 Lung and Skin Tumours

Lung tumour encompasses several distinct types, each with its own characteristics and behaviours. The primary types of lung cancer are non-small cell lung cancer (NSCLC) and small cell lung cancer (SCLC). Non-small cell lung cancer further subdivides into adenocarcinoma, squamous cell carcinoma, and large cell carcinoma [56]. These subtypes differ in terms of their histological appearance, treatment approach, and prognosis. The stage of lung tumour depends on factors such as size, location, and spread. For instance, in stage I of lung tumour, the tumour measures 3 cm or less and is confined to the lung without spreading to other organs [57].

Regarding dielectric properties, lung cancer tissues typically exhibit different electromagnetic properties compared to non-neoplastic (normal) lung tissues. Specifically, cancerous tissues tend to have altered dielectric properties due to changes in cellular structure, composition, and density, affecting their electrical conductivity and permittivity.

In comparison to non-neoplastic tissues, lung cancer tissues often have higher electrical properties. The denser structure and higher water content of tumours result in dielectric properties approximately two-fold higher than those observed in non-neoplastic lung tissue [58]. In lung tissue, cancerous tissue demonstrates a relative permittivity 2-3 times greater than that of normal tissue, alongside a conductivity 1.6-2 times higher [59]. These differences stem from factors such as increased cell density, altered water content, and changes in cellular architecture. Such variations in dielectric properties hold potential for diagnostic applications, including the development of electromagnetic imaging techniques for detecting and characterizing lung tumours.

However, it is crucial to consider potential confounding factors that may affect the interpretation of dielectric measurements in lung tissues. For example, dense fibrosis can significantly impact the electromagnetic properties of lung parenchyma, exhibiting conductivity and permittivity similar to tumour tissue. This dense fibrosis reduces air spaces, forming dense connective tissue areas, resulting in higher conductivity akin to tumour growth.

Skin cancer encompasses various malignant growths that develop in the skin, with the primary types being basal cell carcinoma (BCC), squamous cell carcinoma (SCC), and melanoma [60].

Melanoma, the most aggressive form, originates from pigment-producing cells (melanocytes) in the skin. Unlike other skin cancers, melanoma can develop in any part of the body, even areas not exposed to the sun. Its appearance varies, often presenting as a dark, irregularly shaped mole or lesion, though it can also be pink, red, or flesh-colored. Early detection and treatment are crucial since melanoma can metastasize to other organs, posing a life-threatening risk [61].

Concerning dielectric properties, skin cancer tissues typically demonstrate different electromagnetic characteristics compared to non-neoplastic skin tissues. Cancerous skin tissues tend to have altered dielectric properties due to changes in cellular structure, composition, and density. In comparison to healthy skin tissues, cancerous skin tissues may exhibit higher electrical conductivity and altered permittivity. These changes stem from factors such as increased cell density, altered water content, and changes in cellular architecture associated with malignancy. Notably, there's a significant contrast between healthy and unhealthy skin, with the latter often showing permittivity levels 2 to 10 times higher than the former [19].

2.8 Simulation Environment and Measurement System

In order to support the design and evaluation of the SWB antenna and the imaging setup presented in this thesis, a simulation software and RF measurement equipment are employed. Therefore, it is crucial to provide an introduction to the software environment utilized throughout various design stages and simulations, as well as the facilities employed to gauge the performance of the constructed structure.

2.8.1 Finite Element Method and ANSYS Electronic Desktop

The finite element method (FEM), also known as finite element analysis, is a numerical approach used to solve a wide range of problems, including structural analysis, fluid dynamics, and electromagnetic field analysis. FEM is typically employed to derive solutions for boundary value problems by utilizing a series of partial differential equations. This method initially divides the problem domain into multiple subdomains or meshes. Subsequently, it formulates a set of element equations to represent each of these subdomains.

These element equations are then systematically combined to create a global system of equations, which serves as the basis for the final calculations. This global system of equations employs established solution techniques and is computed based on the initial values of the original problem, resulting in a numerical solution [62].

Ansys' High Frequency Structural Simulator (HFSS) stands as a renowned platform for simulating electromagnetic (EM) circuits and systems. The HFSS workflow begins with the creation of a 3D model representing the RF device, which is subsequently subdivided into smaller subsections. HFSS employs a tetrahedral finite element method, and these tetrahedra collectively constitute what is known as a mesh. Afterward, boundary conditions are applied to the model.

The software proceeds to derive solutions for the electromagnetic fields within these finite elements. These solutions are interconnected in such a way that they satisfy Maxwell's Equations across the boundaries between these elements. This process ultimately yields a comprehensive field solution for the original structure. Finally, the generalized S-matrix solution is computed to complete the analysis as illustrated in Figure 2-6.

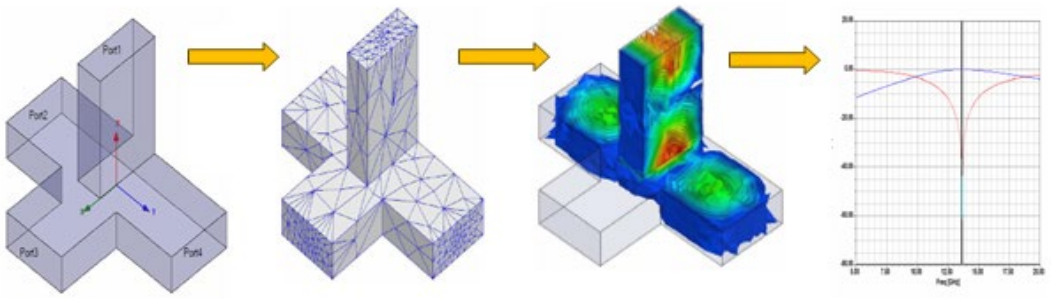

(a) *(b)* *(c)* *(d)*

Figure 2- 6 FEM process in HFSS: (a)3D model; (b)meshed structure; (c)field solution; (d)S-matrix solution.

2.8.2 Measurement Facilities

To evaluate the performance of the constructed prototype of the SWB antenna and to draw comparisons with the simulated results, three primary measurement facilities are utilized in this study: a vector network analyser (VNA) for S-parameter measurements, an anechoic chamber for acquiring radiation patterns, and a 3D rotatable mechanical antenna positioner for radiation pattern measurements.

The S-parameter measurements are conducted using a portable Anritsu Site Master S820E, equipped with built-in VNA modules. The S820E boasts an expansive operating frequency range spanning from 1 MHz to 40 GHz, which aligns perfectly with the designed SWB antenna's specifications. Additionally, for antenna measurements, the VNA serves dual purposes: as a transmitting source for the standard reference antenna and as the receiving terminal for the antenna under test (AUT).

Furthermore, an indoor RF anechoic chamber, supplied by Holland Shielding Systems, is employed to replicate conditions relative to an open space environment while maintaining control over the field conditions (refer to Figure 2-7(a)). This chamber incorporates a Faraday cage and RF absorbers lining the inner walls, floor, and ceiling. This comprehensive setup effectively minimizes both external and internal RF interference.

The testing configuration for the antenna mechanical positioning system within the chamber, designed to assess the far-field radiation of the AUT, is depicted in Figure 2-7(b). It includes three linear polarised horns, each covering a specific portion of the operating bandwidth (2.45 to 35.4) GHz. These antennas include the (JH-H-18G-18-SMAJ-AL) operating in the (800 MHz-18 GHz) range with a gain of (3-18) dBi, Mi-Wave's K-Band Horn Antenna 261K-15/595 (WR-42) functioning in the (18 – 26.5) GHz range with a gain of (15) dBi, and U233A1 Maury Microwave (WR-28) operating within the (26.5 to 40) GHz range with a 15 dBi gain. These antennas serve as the source antennas, while the mechanically rotatable antenna positioner facilitates full 360˚ scanning in both θ and φ directions for the AUT. The AUT is positioned within the quiet zone of the chamber, and the measured transmission coefficients are recorded using the S820E for the subsequent plotting of radiation patterns in MATLAB.

Additionally, various other antenna measurement parameters are determined within the anechoic chamber under far-field conditions. These parameters encompass radiation efficiency, the reflection coefficient, gain, group delay, and measurements of dielectric properties for different mixtures that mimic the layers of the human torso, including skin, fat, muscle, bone, and lung.

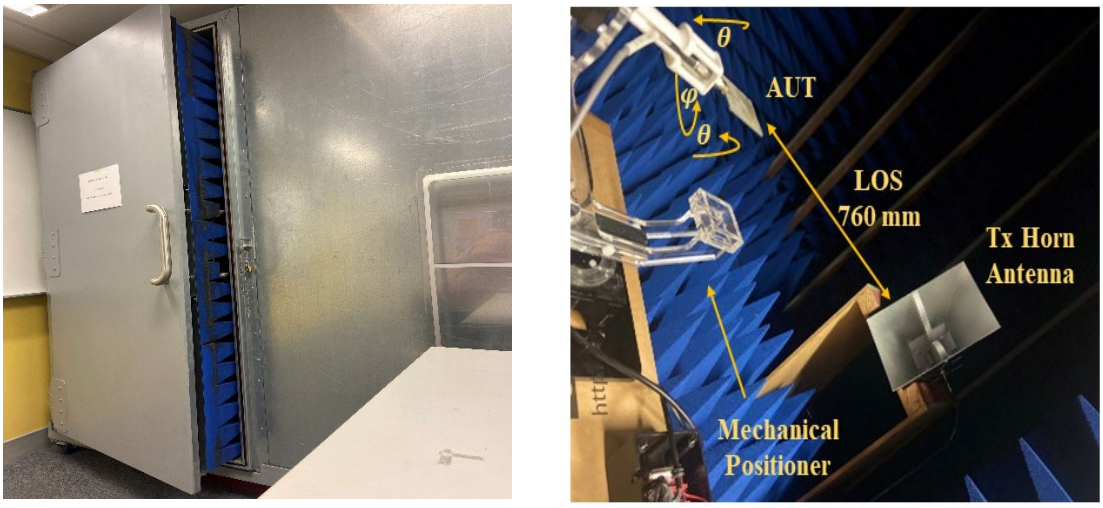

(a) *(b)*

Figure 2- 7 (a)RF anechoic chamber; (b)antenna positioning system.

Chapter 3 Literature Review

3.1 Introduction

RFMI, or Radio Frequency Microwave Imaging, presents an attractive domain of medical imaging with two distinct approaches: radar-based imaging and tomography-based imaging. The former involves the acquisition of a scattering map, revealing the dielectric contrast within human tissues. Meanwhile, the latter depends on the complex reconstruction of the electrical profile for specific human tissue. This complex process involves solving non-linear and ill-posed scattering problems. In the domain of radar-based imaging, two cutting-edge methodologies are implemented: confocal imaging and holographic imaging [63-65]. Both approaches share the common feature of transmitting an UWB pulse into the target tissue. However, their divergence lies in the signal processing algorithms they employ.

SWB technology becomes popular in various applications as it provides a very wide bandwidth with ratio (10:1) which covers different frequency bands. Several techniques have been reported in the literature to present SWB antennas. In [66] a SWB antenna designed on Rogers RO3003 laminate ($\varepsilon_r = 3$, $\tan\delta = 0.0013$) and operates from 1.39 – 160 GHz is achieved through enhancing the copper patch with additional layer of 28.5 mm thickness. A novel circular disc SWB antenna is built on flexible substrate ULTRALAM 3850 ($\varepsilon_r = 2.9$, $\tan\delta = 0.0025$) in [67], it covers the frequency range 1.74 – 100 GHz by inserting a square slot into the patch and thin rectangular slit in the ground plane. A modified bow-tie shaped vertical patch and two asymmetrical ground planes fabricated on FR4 ($\varepsilon_r = 4.4$, $\tan\delta = 0.02$) are presented in [68]. The anticipated antenna has vertical radiator coupled well with the two coplanar ground planes which enabled the proposed antenna to achieve an operating band of 3.035–17.39 GHz (140.56%). Several techniques were incorporated into antenna design to achieve the super-wide bandwidth in [69, 70]. In [69] a steering-shaped circular ring radiator is designed on FR4 ($\varepsilon_r = 4.4$, $\tan\delta = 0.02$). A modified slotted U-shaped monopole antenna is designed on FR4 ($\varepsilon_r = 4.4$, $\tan\delta = 0.02$) to operate within 3 to 20 GHz is presented in [70]. A co-planar waveguide (CPW) feeding is one of the approaches implemented for super wideband (SWB) characteristics; a CPW fed planar elliptical antenna designed on Rogers RT/Duroid 5880 ($\varepsilon_r = 2.2$, $\tan\delta = 0.0009$) and a clown-shaped patch antenna designed on Rogers

RT/Duroid 5880 (ε_r = 2.2, tanδ = 0.0009) with 33.78:1 ration bandwidth have been investigated and presented in [71, 72], respectively. By using a semi ring-shaped structure with a tapered feed line, an impedance bandwidth of 180.66% has been observed from 1.27 to 25 GHz with a ratio bandwidth of 19.68:1 [71]. Fractal loaded slot is another technique that has been implemented in several SWB structures [73-75] with different shapes. A Koch fractal slot [76] is a special type of fractal slots that has been incorporated in different SWB antennas. A good enhancement in the lower end of bandwidth is observed in [77] when inserting fractal slots to the edge of the antipodal Vivaldi antenna. In [73] a staircase fractal curve is applied on a microstrip line fed truncated corner square patch antenna mounted on designed on FR4 substrate (ε_r = 4.4, tanδ = 0.02) to achieve Super Wide Band (SWB) operation. The proposed antenna covers an impedance bandwidth from 0.1 GHz to 30 GHz with a ratio impedance bandwidth of 300:1 for $S_{11} \leq$ -10 dB. Frequency Selective Surfaces (FSS) is one of the methods that has been implemented in different SWB antenna geometries [78, 79] to enhance the surface current distribution which results in improved gain and covered bandwidth. A compact SWB antenna is presented in [7], the proposed antenna is fabricated on Rogers RT/Duroid 5880 (ε_r = 2.2, tanδ = 0.0009). Different slots were embedded into the patch and the ground plane to cover the frequency range from 1.22 to 47.5 GHz. Metamaterial, an electromagnetic technology, that has been involved with SWB antenna design by including metamaterial unit cells which resulted in improving the antenna performance and efficiency [13]. Meander lines structure is another technique that has been included in different SWB antenna geometries [80, 81]. A z-shaped SWB antenna designed on Rogers RT/Duroid 5880 (ε_r = 2.2, tanδ = 0.0009) with 156% fractional bandwidth is presented in [80] which consists of stepped meander lines to achieve the SWB bandwidth and high efficiency. In [81] an s-shaped SWB with stepped meander lines and Defected Ground Structure (DGS) is proposed to cover 3.09 to 40.2 GHz, the antenna is fabricated on Rogers RT/Duroid 5880 (ε_r = 2.2, tanδ = 0.0009). Moreover, a modified diamond shape SWB antenna with customized three layers substrate to reduce the dielectric loss is presented in [82] which operated in the frequency band 2.3 to 23 GHz, the reported antenna is fabricated on Rogers RO3003 laminate (ε_r = 3, tanδ = 0.0013).

Different SWB antennas were reported with band rejection capabilities [4, 6, 11, 83]. A 20.4 GHz SWB antenna was proposed with triple rejection bands by inserting different

slots in the patch and the feedline [6]. In [83] a 3D SWB antenna with the addition of three dielectric cuboids in the radiator is presented, the rejection feature is achieved by means of upside-down T-shaped resonator placed in the patch. U-shaped and L-shaped stubs were inserted in [11] to allow dual band rejection. In [4] two inserted parallel PIN diodes are used to control the band rejection feature of frequency diversity hexagonal shaped SWB antenna over frequency range 3.37 to 27.71 GHz. A compact triple elliptical antenna covering a SWB ratio bandwidth of 22.77:1 for 5G applications is presented in [84].

Equivalent lumped element circuit models have been widely used in designing wideband and ultra-wideband (UWB) antennas [5], efficiently analysing their behaviour and improving their performance. Different configurations of SWB antennas with equivalent circuit model (ECM) have been studied in recent years [4, 6, 7, 83]. In [7], a concentric-shaped SWB antenna operating in the frequency range 1.25–40 GHz with ECM is presented. The results showed that the presented ECM cannot accurately model the antenna performance particularly at frequencies from 15 to 40 GHz. Moreover, its efficacy is not discussed in terms of transmission line theory or error validation. Rectangular and hexagonal SWB antennas with ECM optimised based on Quasi-Newton method, are presented in [6], and [4], respectively.

Similarly, the ECM is not found to be sufficiently accurate at high-frequency bands due to complexity of high-order modes. A three-dimensional (3D) SWB antenna that operates over 2.45–20 GHz with ECM is proposed in [83]. While the ECM has been discussed based on the antenna's geometry; it has been devised using an iterative method that offers weak accuracy. Several researchers have proposed equivalent lumped elements circuit models for SWB antennas loaded with fractal slots [85, 86]. However, their ECMs are either too complex or not sufficiently accurate. Other researchers have investigated methods to optimise the ECM [26, 87]. In [26], a multi-objective particle swarm optimisation is performed to obtain optimal extracted values of an ECM for a frequency selective surface (FSS), which are found to provide an approximate prediction of the real response. In [87], an ECM for an UWB multi-input multi-output (MIMO) antenna is proposed and optimised using advanced design system (ADS), but neither the optimisation type nor the accuracy of the model are discussed. Furthermore, mathematical relationships between the ECM and transmission line

theory have not been discussed.

With the proliferation of different cancerous diseases in the world and the limitations of the conventional methods for their early detection, radio frequency medical imaging (RFMI) has emerged as a promising technique with attractive properties to overcome the detection challenges. Antennas play an essential role in RFMI as they directly impact the system detection efficiency. The parameters that need to be considered while designing the antenna for RFMI include operating bandwidth, directionality, gain, design complexity and the cost of fabrication. This chapter reviews different practical antennas proposed in the literature for RFMI in microwave and millimetre-wave (mmW) regimes for the detection of breast cancer, lung cancer, lung fluid accumulation, skin cancer, brain tumour and brain stroke.

The rest of the chapter is organised as follows. Section 3.3–3.5 reviews current state-of-the-art antenna designs for detection of: (i) breast cancer; (ii) brain cancer and stroke; (iii) lung cancer and fluid accumulation; and (iv) skin cancer, respectively. The antennas are discussed in terms of their performance, compactness, and the quality of reconstructed images. Section 3.6 concludes the chapter with some directions for future research.

3.2 Antennas for Breast Cancer Detection

Due to increasing prevalence of breast cancer in women, antenna design for RFMI based detection of breast tumours has attracted much attention [88]. Usually, in medical imaging applications the MI system is tested on phantoms that mimics the frequency response of certain tissue type at a specific frequency [89]. Typically, a breast phantom is used as a hemi-spherical model of breast tissue to evaluate the effectiveness of a proposed imaging system. Table 3-1 shows the parameters of the model, including thickness, relative dielectric permittivity and conductivity for different layers of skin, fat, and glandular tissues that constitute the breast tissue [90, 91]. The key types of antennas proposed in literature for breast cancer detection include Vivaldi, fractal, and planar monopole antennas of semicircular, circular, rectangular, spiral, and triangular configurations. Their performance in terms of bandwidth, gain, radiation pattern, and compactness are discussed.

Table 3- 1 *Hemi-spherical breast model parameters for 2-4 GHz band*

Layer	Thickness (mm)	Relative dielectric constant ε_r	Conductivity σ (S/m)
Skin	2	34.95	3.89
Fat	8	4.94	0.31
Glandular tissue	40	11-15	0.4-0.5

3.2.1 Vivaldi Antennas

Vivaldi antennas are end-fire type antennas that have been widely used in RFMI because of their wide operating bandwidth, high directional capability and ease of fabrication. In general, a Vivaldi antenna is made up of a uniform slot with λ/4 length attached directly to an exponentially tapered slot. Hence, the Vivaldi antenna is also known as a tapered slot antenna (TSA). Recently, different methods have been used to enhance their directivity through better impedance matching, and extend their operating frequency into lower bands by embedding slots in radiators to lengthen the path of the surface electric currents. In [92], the authors designed a Vivaldi antenna with three metal patches applied on the end-fire, which served as directors to increase the antenna gain by approximately 4 dBi. The proposed antenna is fabricated on 1 mm thick F4B substrate (ε_r = 2.55) with overall dimensions of 70×79×1 mm^3, an operating frequency range of 2.4−13 GHz, peak gain of ~ 9.5 dBi at 12 GHz, and a consistent directional radiation pattern over the operating frequency range. A 29×26.6×1.575 mm^3 tapered slot antenna loaded with star shaped parasitic elements is proposed in [93]. The proposed antenna operates over UWB range 3.8 to 10.1 GHz with 6 dBi realised gain, an array of the two TSA elements was placed over heterogeneous fabricated breast phantom for 10 mm diameter tumour detection. The reconstructed images reveal successful detection with quite low resolution. In [94] a side slotted tapered slot antenna with modified fins by etching nine rectangular side slots to enhance the electrical length and improve the gain is presented. The proposed antenna has an overall dimension of 51×42×1.57 mm^3 and covers the frequency range 2.8 to 7 GHz. Authors tested the antenna for breast tumour detection using nine antenna elements array placed around a heterogeneous breast

phantom, with one and two tumour inclusions. The detection was successful. However, the tumour sizes were not reported, and their placement was relatively superficial.

3.2.2 Fractal Antennas

A fern shaped fractal leaf configuration of antipodal Vivaldi antenna was presented in [95]. A good enhancement in the lower impedance bandwidth is offered, in which the lower frequency band is decreased in the second iteration of the leaf structure by 19% as compared with the first leaf structure. This reduction is accomplished by the reorientation of modes induced by current distribution. The antenna was fabricated on FR4 substrate (ε_r = 4.4) with a total size of 50.8×62×0.8 mm^3 and operates at the frequency range of 1.3–20 GHz. There is a high directive gain of ~ 10 dBi and stable radiation pattern. A good agreement between simulated and measured results of the proposed antenna is reported.

3.2.3 Planar Monopole Antennas

Several monopole antennas with different patch shapes have been widely used for RFMI because of their distinctive properties. The antenna classifications adopted in literature for RFMI are described as follow:

Circular and Semicircular Patch Antennas

A four circular radiating elements that operate as multi-input multi-output (MIMO) antenna is proposed in [31]. The design approach to increase operational bandwidth is that of inserting slots into the ground plane, etching an elliptical slot into the patch, and laying out the ground plane in a staircase style. The designed antenna is printed on 40×30×1.5 mm^3 FR4 substrate (ε_r = 4.4) and covers a bandwidth that spans the frequency range of 2.8–20 GHz. The results show a stable omnidirectional radiation pattern over the operational bandwidth.

In [39], the authors presented a semicircular shaped patch antenna element and 16-element antenna array. The proposed structure improves impedance matching and operating bandwidth by the use of trapezoidal shaped ground plane and inclusion of semicircular slot in the patch. Fabricated on Rogers RT5880 substrate (ε_r = 2.2) with dimensions of 41×42×1.575 mm^3, the proposed antenna exhibits a total bandwidth of 8.7 GHz over the frequency range of 2.3–11 GHz, peak gain of 5.8 dBi and stable directional radiation pattern. An elliptical UWB antenna with stub loading to shift the

frequency to lower bands is presented in [19, 96] with operating bandwidth 3.9 to 30 GHz. It is fabricated on Rogers 5880 with a low profile of 15×15×1.575 mm^3 and peak gain of 6.48 dBi. Authors placed a semi-spherical array arrangements of nine antenna elements around fabricated breast phantom of skin and fat layers for tumour detection in breast skin. A 4 mm diameter tumour placed at the boundary of skin and fat layers is successfully detected. However, the used phantom is simplified one without representation of the glandular breast tissue and the detection was a superficial location.

Rectangular, Spiral and Triangular Patch Antennas

Two flexible 4×4 arrays: one of rectangular patch and another of spiral antenna are designed and fabricated on flexible Kapton polyimide with a thickness of 50 µm and overall size of 20×20 mm^2 in [48] as shown in Figure 3-1. The rectangular patch antenna improves the impedance matching and bandwidth by cutting multiple steps at the lower patch corners and using a coplanar waveguide (CPW) network feeder. The single-arm spiral antenna is used to induce currents in both x and y directions equally, with the antenna being made of several rectangular components of equal length, positioned horizontally and vertically. The proposed rectangular and spiral antenna arrays can provide a wideband impedance bandwidth over the frequency range of 2–4 GHz. Figure 3-2 (a) and (b) show the S-parameters measurement setup using spiral antenna array on a breast mimicking phantom, and top view of the antenna array, respectively.

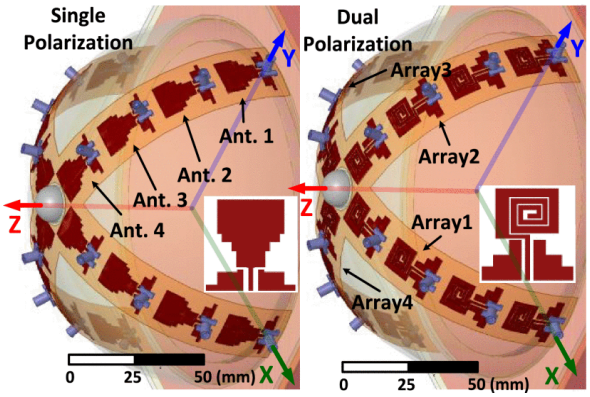

Figure 3- 1 Overview of single arm spiral and monopole antenna arrays for breast cancer detection [48].

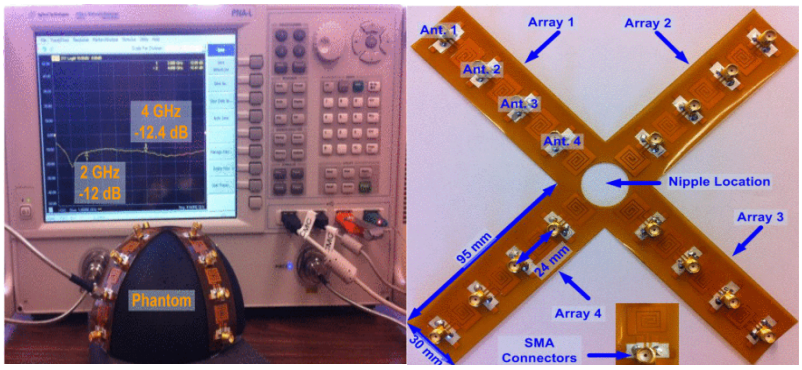

(a) *(b)*

Figure 3- 2 (a) Antenna array on breast mimicking phantom; (b) Top view of spiral antenna array [48].

Several other rectangular patch antennas for breast imaging have been proposed in [40], [46], [97]. A rectangular patch antenna with cut slots at lower edges is reported in [97]. Fabricated on FR4 substrate with a size 36×34×1.6 mm^3, the proposed structure achieves a wideband bandwidth over the frequency range of 2.4–4.7 GHz and is shown to be a good candidate for breast cancer detection at different depths. In [46], a structure consisting of a rectangular patch with stair case configuration at the lower ends and extended distance between the patch and ground plane that significantly improve the performance is proposed. In [40], the authors introduced a planar rectangular monopole antenna backed by a reflector to reduce the unwanted backward radiation towards the human body. Both proposed antenna and reflector have the same dimensions of 50×33×1.635 mm^3 implemented over a FR4 substrate. A unidirectional gain of 3.6 dBi is achieved over the operating frequency range of 2.5–6 GHz. Similarly, a triangular shaped patch monopole antenna on FR4 substrate operating in the frequency range of 0.5–3 GHz is proposed in [52]. A metamaterial -based CPW fed textile antenna which operates over two frequency ranges; one reconfigurable between 2.42 to 3.2 GHz and another static range 4 to 15 GHz with 7.56 dBi peak gain is presented in [98]. The overall dimension of the proposed antenna is 80×61 mm^2, and it is tested using two elements to successfully detect 10 mm diameter tumour in heterogeneous breast phantom over the frequency range 2 to 4 GHz. However, the localisation of the detected

tumour was slightly shifted from the real position. A summary of the aforementioned antenna designs for breast cancer detection is given in Table 3-2.

Table 3- 2 *Summary of antenna designs for breast cancer detection*

Ref.	Antenna type	Frequency (GHz)	Size (mm^3)	Gain (dBi)	Key features/Remarks/Drawbacks
[31]	circular patch	2.8–20	40×30×1.5	n/a	• MIMO antenna fabricated and tested on realistic phantom • Ultra-wide bandwidth for enhancing image resolution, but no reconstructed image produced • Principal Component Analysis (PCA) method used in tumour detection
[39]	semicircular patch	2.3–11	41×42×1.575	5.6	• 16-element array to scan 240 locations and detect tumour of diameter ≥ 5 mm • Ultra-wide bandwidth and directional radiation to enhance image resolution, and signal penetration, respectively • Antenna is not tested on realistic phantom
[40]	rectangular patch	2.5–6	50×33×1.635	3.8	• Proposed antenna backed by a reflector • Can detect tumour size of 15×15×10 mm^3 in dense fibro glandular tissue • The used bandwidth is quite narrow • Tested on simulated not fabricated realistic phantom
[46]	rectangular patch	2–4	n/a	n/a	• 16-element array on wearable device to construct 2D tumour images • Proposed antenna size, gain, and radiation pattern not specified

[48]	rectangular/ spiral patch	2–4	20×20×0.05	n/a	• 4×4 array tested on realistic phantom • Reported proposed antenna's reflection coefficient and efficiency, but not its gain and radiation pattern • The used bandwidth is quite small • No evaluation on image reconstruction
[52]	triangular patch	0.5–3	n/a	n/a	• Tested on realistic phantom to detect tumour size ≥ 16 mm • Proposed antenna size, gain, and radiation pattern not specified
[92]	Vivaldi	2.4–13	70×79×1	9.5	• Use metallic directors to increase gain at lower frequency range • Offers ultra-wideband bandwidth and high directive gain • Antenna size is quite large • Not tested on realistic phantom
[93]	Tapered slot	3.8-10.1	29×26.6×1.575	6 dBi	• Four star shaped parasitic elements were used for better gain and impedance matching • Offers ultra-wideband bandwidth and high directive gain • Two antenna elements placed around the phantom, which is relatively small and resulted in lower resolution • Successful detection of 10 mm diameter tumour with low resolution

[94]	Side slotted Vivaldi	2.8-7	51×42×1.57	7.5	• Nine irregular side slots were inserted to enhance the gain and radiation • Antenna size is quite large • Nine antenna elements array were used for two tumour inclusion detection around breast phantom • Tumour sizes were not reported, and their placement was quite superficial
[95]	fractal	1.3–20	50.8×62×0.8	10	• Offers super-wideband bandwidth and high directive gain • Not tested on simulated or fabricated realistic phantom
[19, 96]	elliptical	3.9-30	15×15×1.575	6.48	• Low profile antenna, Offers ultra-wideband bandwidth and high directive gain • Successful detection of 4 mm diameter tumour • Tested on simple two layers breast phantom without glandular tissue • The detected tumour placed at superficial location
[97]	rectangular patch	2.4–4.7	36×34×1.6	n/a	• Tested on realistic phantom to detect tumour size ≥ 16 mm at depths ≤ 30 mm in breast tissue • The covered bandwidth is narrow • Proposed antenna gain and radiation pattern not specified

[98]Metamaterial CPW-fed	2.42-3.2, 4-15	80×61	7.56	• Antenna size is quite large • The imaging measurement performed over narrow bandwidth with small antenna numbers • Localization of detected tumour was slightly shifted from the original one.

3.3 Antennas for Brain Cancer and Stroke Detection

Brain injury can be caused by traumatic and non-traumatic disorders such as brain cancer, and brain stroke, respectively [99, 100]. Generally, strokes occurred due to blood flow deficiency as a result of either blood bleeding (haemorrhagic stroke) or blood clot (ischemic stroke) [101]. The incidence of brain cancer and stroke are growing rapidly and posing a severe threat to human life. This motivates many researchers to develop different antennas for RFMI to detect brain tumour and stroke by contrasting the brain tissue dielectric properties. Table 3-3 shows the model parameters of a healthy human head phantom that consists of six layers: skin, fat, skull, dura, cerebrospinal fluid (CSF) and brain (mixture of gray and white matter). The relative dielectric constant and conductivity values are given for 1.6 GHz [102],[103] , which is the optimal imaging frequency for brain injury. In contrast, the dielectric properties of brain tumour and stroke are (ε_r = 59.7, σ = 1.91 S/m), and (ε_r = 55, σ = 7 S/m), respectively. The main types antennas discussed here are planar monopole antennas of various configurations including rectangular, modified-shaped circular, circular, triangular, trapezoidal-shaped and Bowtie. Their performance, such as in terms of antenna bandwidth, gain, radiation pattern, and compactness are also discussed.

Table 3- 3 *Human head model parameters*

Layer	Thickness (mm)	Relative dielectric constant ε_r	Conductivity σ (S/m)
Skin	1	39.2	1.11
Fat	1.4	5.37	0.07
Skull	4.1	12	0.24
Dura	0.5	43.2	1.23
CSF	2	67.5	2.79
Brain	81	44	1.01

3.3.1 Antennas for Brain Cancer Detection

Rectangular Patch Antennas

A rectangular microstrip patch antenna with symmetrical defected ground structure (DGS) is presented in [104]. This antenna is fabricated on a 0.812 mm thick Rogers's 4004 lossy substrate (ε_r = 3.55). A 30×22 mm DGS is incorporated to reduce the antenna loss at resonant frequency of 5.8 GHz and extend its operating bandwidth to 1.9 GHz from 89 MHz obtained with simple rectangular antenna. However, the antenna gain is reduced from 6.97 dB (simple rectangular antenna) to 3.496 dB (with DGS). Another rectangular patch antenna with dimensions 25.92×31.017×1.03 mm^3 is proposed in [34] to detect brain tumour. A circular electromagnetic band gap (EBG) structure is incorporated on antenna's ground plane in order to enhance the reflection coefficient and imaging quality. Rogers R03003 with ε_r = 3 is chosen as the substrate. The antenna operates in the frequency range of 7.5-7.79 GHz with a flat gain of 6.7 dBi. A tumour of 5 mm radius can be detected in a simulated head phantom. In [105] a W-shaped slot-loaded U-shaped rectangular patch antenna with overall dimension of 56×37×1.6 mm^3 is presented for head imaging. It operates within 1.4 to 2.52 GHz with 3.5 dBi maximum gain, slots have been used to enhance efficiency and gain. An array of nine antenna elements were placed around simulated model of head phantom with brain tumour inclusion. The reconstructed images show successful tumour detection. While the tumour size was not reported in addition of being simulated-based study without fabrication and any measurements.

Circular and Modified-Circular Patch Antennas

A modified circular patch antenna fabricated on 1.575 mm thick Rogers Duroid RT5880 substrate (ε_r = 2.2) is presented in [106]. A 34.5×20 mm^2 antenna structure is analysed, which operates in the frequency range of 3.1-10.6 GHz, providing an ultra-wide bandwidth with 7.573 dBi peak gain. A unidirectional radiation pattern is obtained by utilisation of aluminum plate reflector (ε_r = 3.4) with total dimensions 50×40×2 mm^3. The reflector is placed at the back side of the antenna to suppress undesired radiation lobes. Another UWB antenna array is made up of four identical circular patches of 15 mm diameter is proposed in [107]. It is fabricated on a 45×80×1.5748 mm^3 Taconic (TLY-

5) substrate with ε_r = 2.2. The antenna has a frequency range of 2.6-13.1 GHz and relative peak gain of 12.12 dB when measured on a phantom at different positions.

3.3.2 Antennas for Brain Stroke Detection

Rectangular, Trapezoidal, Triangular and Metamaterial Patch Antennas

A trapezoidal shaped patch antenna with CPW feeding network is reported in [108]. The antenna element is fabricated on 70×30×0.2 mm^3 FR4 substrate. The operating frequency range of the antenna is between 1-4 GHz to ensure good penetration inside human head tissues. Since the radiation of monopole antennas is bidirectional, the back lobe radiation is suppressed by incorporating a lossy dielectric absorber EN-74 with thickness of 19 mm where the antenna gain is doubled (5 dBi). Eight antenna elements are arranged in a hat shaped structure that can be worn for head imaging. The simulated power distribution on modelled head phantom is presented for two resonant frequencies of 1.5 GHz and 3.5 GHz, which provides better penetration, and better reconstructed image resolution, respectively. In [35], the authors presented an isosceles triangular patch antenna with fractal ground plane as shown in Figure 3-3. It is fabricated on 68.28×79×1.5 mm^3 FR4 substrate (ε_r = 4.7) and operates in the frequency range of 1.55-1.65 GHz. It is designed to detect haemorrhagic stroke which is modelled using a small tube containing blood mimicking material with circular cross-sectional radius of 5 mm and length of 35 mm. It is shown to be a good candidate for stroke detection through reconstructed images in both simulation and measurements. Figure 3-4 shows the measurement setup for brain stroke detection using triangular patch antennas and brain mimicking phantom. Another triangular shaped antenna similarly fabricated on FR4 has dimensions of 70×50×1.55 mm^3 and operating frequency range of 0.8–1.2 GHz is proposed in [109]. A triangular shaped radiator, defected ground plane and feedline with two stubs are the components of this antenna, which exhibits an omnidirectional radiation pattern. Both simulated and measured results indicate that it can identify the presence of a spherical stroke with radius of 12.5 mm. A metamaterial loaded 3D antenna is presented for portable head imaging in [110]. The proposed antenna has two slotted dipole elements with arrays of MTM unit cell and folded parasitic patch, it operates over 1.95 to 4.5 GHz with overall dimension of 70×30×15 mm^3 and 7.22 dBi gain. Authors tested the proposed antenna in nine antenna elements circular array around the fabricated head phantom with haemorrhage inclusion. The reconstructed

images show the feasibility of the proposed antenna to be implemented in portable head imaging system. However, antenna size is quite large. In [111] a modified rectangular patch antenna is proposed for stroke detection. The presented antenna operates over 1.3 to 3.7 GHz with an overall dimension of 70×60×1.6 mm^3 and peak gain of 6 dBi. The inset-fed geometry along with ground slot allowed for better impedance matching and wider bandwidth. Authors discussed the simulated study of the proposed antenna in stroke detection using simulated head model based on the electric field distribution. However, no reconstructed images were presented for the successful detection.

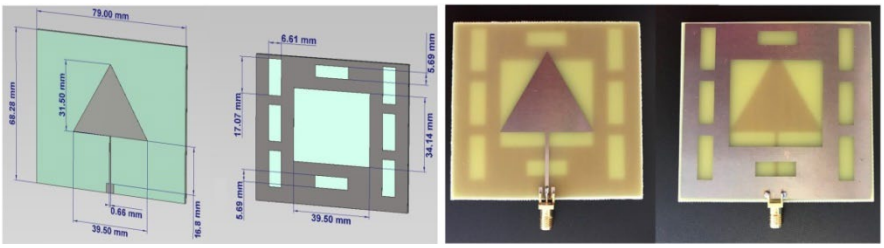

Figure 3- 3 The front and back view of the designed (left) and fabricated (right) isosceles triangular patch antenna [35].

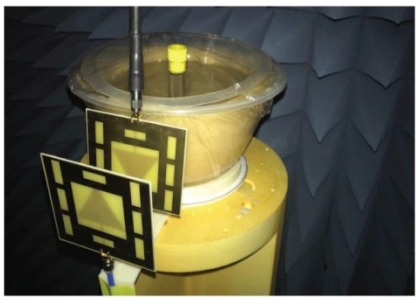

Figure 3- 4 Measurement setup for brain stroke detection [35].

Bowtie Patch Antennas

An inset fed meandered bowtie antenna with dimensions 18×18×0.5 mm^3 is proposed in [102]. It is fabricated on FR4 substrate (ε_r = 4.3) and has an operating frequency range of 0.75–4 GHz. It is fed by a discrete port placed between two central vertices. To reduce the antenna size, a meandering technique is implemented on the exterior region of the bowtie antenna. The bowtie elements are connected to each other using the meandered lines to create a long loop. The antenna element is tested on head of real human subject

and the results indicate that the proposed antenna provides a good radiation efficiency and target penetration.

Vivaldi Antennas

Tapered slots antennas in eight circular antenna array were studied for brain stroke detection [112]. The study was based on the difference in the S-parameters with and without the inclusion of 10 mm diameter clot inclusion in the head model. Results show a significant difference across the frequency range 2 to 3.5 GHz where the reflection coefficient with blood stroke is higher than the normal tissue. An antipodal Vivaldi antenna with Sierpinski fractal slots is presented in [113] for brain clot imaging. The main purpose of including the fractal slots in the antenna design is to enhance the bandwidth, gain and directivity. The proposed antenna has an overall dimension of $65\times65\times1.6$ mm^3 and it covers the frequency range 2.35 to 3.79 GHz with 7.35 dBi maximum gain. Authors tested the proposed antenna using simulated head model for a blood clot and the presented S-parameters show different responses with healthy and unhealthy head models. In [114] an antipodal Vivaldi antenna operated over 2.06 to 2.61 GHz is proposed for brain stroke detection. The antenna has size of 50×60 mm^2 and it is placed in nine elements circular array around the fabricated head phantom. The colour plot results show the capability of stroke detection. However, the reconstructed images were not provided. A summary of aforementioned antenna designs for brain tumour and stroke detection is presented in Table 3-4.

Table 3- 4 *Summary of antenna designs for brain tumour and stroke detection*

Ref.	Antenna type	Frequency (GHz)	Size (mm^3)	Gain (dBi)	Key features/Remarks/Drawbacks
[35]	triangular patch	1.55–1.65	68.28×79×1.5	n/a	• For brain stroke detection • Narrow bandwidth of 0.1 GHz • No detailed characterisation of antenna features, e.g. gain

[34]	rectangular patch	7.5–7.79	25.92×31.017×1.03	6.7	• For brain tumour detection • Circular EBG enhances reflection coefficient and image quality • Narrow bandwidth of 0.29 GHz • Not fabricated or tested on realistic phantom
[104]	rectangular patch	4.85–6.75	n/a	3.497	• For brain tumour detection • DGS enhances antenna bandwidth and impedance matching, but reduces antenna gain • Not fabricated or tested on realistic phantom
[105]	U-shaped rectangular patch	1.4-2.52	56×37×1.6	3.5	• Antenna size is quite large • Narrow bandwidth of 1.12 GHz • Simulated tumour size is not mentioned • Not fabricated or tested on realistic phantom
[106]	modified circular patch	3.1–10.6	34.5×20×1.575	7.573	• For brain tumour detection • Uses reflector to suppress backlobes and enhance antenna gain • Not tested on realistic phantom
[107]	circular patch	2.6–13.1	45×80×1.5748	12.12	• For brain tumour detection • Relatively low backlobe radiation • Tested only on simulated, not realistic phantom

[108]	trapezoidal patch	1–4	70×30×0.2	5	• For brain stroke detection • 8-element array in a hat-shaped wearable structure • Antenna gain doubled by the use of dielectric absorber • Not tested on realistic phantom
[109]	triangular patch	0.8–1.2	70×50×1.55	n/a	• For brain stroke detection • Radiation pattern is omnidirectional • No detailed characterisation of antenna features, e.g. gain
[110]	MTM folded parasitic patch	1.95-4.5	70×30×15	7.22	• For brain stroke detection • Antenna size is quite large • Antenna is proposed for portable imaging system • MTM optimisation enhanced the covered bandwidth • Narrow covered bandwidth of 2.55 GHz • Successful detection of brain stroke over fabricated head phantom, however stroke size was not reported
[111]	Modified rectangular patch	1.3-3.7	70×60×1.6	6	• For brain stroke detection • Antenna size is quite large • Narrow covered bandwidth of 2.4 GHz • Not tested on realistic phantom

[113]	Antipodal Vivaldi	2.35-3.79	65×65×1.6	7.35	• For brain stroke detection • Antenna size is quite large • Fractal slots included to enhance the gain • Not tested on realistic phantom
[114]	Antipodal Vivaldi	2.06-2.61	50×60	NA	• For brain stroke detection • Antenna size is quite large • Narrow bandwidth of 0.55 GHz • Detection was based on colour plot results with no reconstructed images
[102]	bowtie patch	0.75–4	18×18×0.5	n/a	• For brain stroke detection • Tested on real human subject • No medical images generated

3.4 Antennas for Lung Cancer and Fluid Accumulation Detection

Lung cancer is another leading cause of cancer death. Different stages of this disease are medically identified based on the tumour size and spread of abnormal cell growth in the human body. In the first stage of lung cancer, the tumour size is small and has not spread to any lymph nodes. Early-stage detection of lung cancer enables higher success rates of treatment and prevents the cancerous tissues from further spreading [37, 38]. Meanwhile, screening modalities such as computed tomography (CT) scans and X-ray devices are one of the diagnostic methods used in revealing lung cancer and for periodic monitoring during the treatment journey. However, the cumulative exposure of patients to such ionising radiation may result in cancer cells growth and spread. On the other hand, CT image-guided lung biopsy surgery is an invasive detection method that may also pose some risks of complications during or after the surgery [115]. Therefore, there

is a critical need to develop a safer, and yet affordable diagnostic tool for lung cancer detection [10].

Recently, medical imaging based on microwave reflectometry has attracted significant interest as a non-invasive technique for detection of different serious diseases such as breast cancer [46, 53, 116], brain stroke and tumour [34, 35, 42, 99], chest fluid accumulation [18, 33, 41], and skin cancer [22, 23]; and for frequent post-surgery monitoring due to its being low cost and safe from harmful radiation [109]. Comparatively, fewer works have explored microwave reflectometry for lung cancer detection [3, 14, 15, 17, 49, 117], in particular for lung tumour in deep-seated locations. In [3], the authors investigated the use of microwave reflectometry in the frequency range of 1.5–3 GHz for lung cancer detection based on the distribution of scattered fields in the imaging domain. However, the detection was done using a low-gain slot-rotated antenna for detecting tumours in superficial locations with no capability to determine their sizes. In [14], another similar study was conducted but using a small lung phantom, which does not mimic the normal size of a human chest. The authors discussed the effects of lung exhalation/inhalation and selected 10 GHz as the resonant frequency for tumour detection. However, the images of the two superficially placed tumour inclusions were barely distinguishable due to low resolution of the reconstructed images caused by weak signal penetration inside the phantom. On the other hand, a life-size phantom of a human chest was introduced in [15] and tested using off-the-shelf antennas. However, the phantom was utilised based on tissue equivalent liquids, which does not mimic the anatomical structure and real dielectric properties of human torso tissues. The authors in [49] studied lung tumour detection over 3-4 GHz frequency range using spherical tumour placed at depth of 60 mm inside small square-shaped lung phantom. The results showed that tumours of radius 4 mm and 10 mm can be detected. However, simulations were performed using a single antenna in front of non-realistic rectangular lung phantom shape with very small size ($60 \times 60 \times 101$ mm^3) and at superficial location. In [17], lung tumour detection is investigated using directional elliptical patch antenna operating in a frequency range of 3–10.7 GHz. Simulations were performed using a rectangle-shaped lung phantom with a dimension of $300 \times 133 \times 130$ mm^3 and square shape lung tumour inclusion. However, this study included lung phantom without rib bone layer and the reflection coefficient results were not clear in terms of detecting tumour at superficial depth. Another study in [117] proposed a

cupcake shaped antenna operating in the frequency range of 2.9–12 GHz for lung tumour detection. It was found that the antenna can detect lung cancer from stage II onwards. However, the simulation was again done using rectangular shaped lung phantom without rib bone layer. Moreover, the size of proposed lung phantom (60 × 40 × 26.66 mm^3) does not mimic the life-sized human torso.

The accumulation of lung fluid is one end stage of lung cancer complication typically from stage III to IV, as well as the result of some other diseases like COVID19 [118, 119]. It is further classified into two types: pulmonary edema where fluid accumulates inside the lung; and pleural effusion where the fluid accumulation occurs around the lung. Different antenna designs for lung cancer and fluid accumulation detection have been studied in literature through simulation and realistic phantoms of thoracic tissues that consist of multiple layers: skin, fat, muscle, rib bone, pleura and lung. Their average dielectric properties are given in Table 3-5 for 2–14 GHz frequency range [117]. Materials mimicking a lung tumour (ε_r = 54, σ = 2.5 S/m) and fluid (ε_r = 73, σ = 0.005 S/m) are inserted within the thoracic phantom.

Table 3- 5 *Thoracic model parameters*

Layer	Thickness (mm)	Relative dielectric constant ε_r	Conductivity σ (S/m)
Skin	3	33.036	6.273
Fat	2	9.35	1.317
Muscle	20	45.46	8.235
Rib Bone	6	18.85	0.754
Lung	70	17.32	3.28

Various antenna designs for lung cancer and fluid accumulation detection have been proposed for RFMI systems. The main types are planar monopole antennas of different configurations such as circular, elliptical, cupcake-shaped, slot rotated, loop-dipole, folded and metasurface antenna, which are discussed in the following sub-sections.

3.4.1 Antennas for Lung Cancer Detection

A slot rotated antenna designed for the frequency range of 1.5–3 GHz is utilised to circularly scan the artificial human torso phantom to detect lung tumour [3]. It has dimensions of 22×46×10 mm^3 and 2.6 dBi peak gain. The antenna scans the phantom at 12 different positions, and the produced images indicate its ability to accurately detect and localise the inserted tumour in the torso. In [49], a circular shaped microstrip

antenna is proposed and constructed on 60×40×1.513 mm^3 FR4 substrate (εr = 4.4). The detection of lung tumour is studied for the frequency range of 3–4 GHz. The antenna performance is evaluated in terms of optimum distance between the antenna and phantom, the size of spherical tumour model, and tumour location. Results show that the antenna can detect tumour sizes of 4 mm radius or larger at a 10 mm optimum distance from phantom where the lowest reflection coefficient is achieved. It is also shown to detect similarly sized tumours at different positions at a depth of 60 mm in the phantom where the upper and middle regions are more detectable than those at the lower region particularly at the model's lower edge corners.

An elliptical patch antenna with dimensions of 44×44×1.6 mm^3 fabricated on FR4 substrate to operate in a frequency range of 3–10.7 GHz is presented in [17]. The antenna is loaded with a box shaped cavity to make it a directional antenna which is then tested using a thoracic model with an inserted tumour. Results show that the antenna can detect tumour particularly when placed in close proximity to the model. The authors in [117] proposed a cupcake shaped antenna operating in the frequency range of 2.9–12GHz. The antenna is fabricated on 40×30×1.524 mm^3 Roger RO4350 substrate (ε_r = 3.66) and evaluated on a thoracic model. It is found to exhibit an omnidirectional radiation pattern, and can detect lung cancer from stage II onwards. A holographic microwave imaging system is proposed in [14] to detect 5mm lung tumour at different superficial positions. Unlike the previous imaging systems that relies on VNA in collecting the S-parameters data; this holographic system uses a microwave source and a miniaturized circuit board. However, the imaging setup seemed more complicated than the radar-based imaging system because they used a translation stage to perform the raster scan over 2D plane. The recorded hologram is used to reconstruct the complex information of lung phantom based on the interference of the backscattered object signals. Authors implement 45.19×17.53×0.8 mm^3 metametrial Vivaldi antenna that operates over 3.3 to 21.6 GHz; to image the tumour circular shaped inside gelatine layered phantom with 12 cm diameter. Results show weak detection with low resolution of lung tumour because they performed the measurement using a single frequency of 10 GHz during the imaging measurement. However, the tumour was placed at superficial

positions in relatively small phantom size that doesn't mimic the size of real human chest.

3.4.2 Antennas for Lung Fluid Accumulation Detection

In [18], a 7×5 unit cell metasuface antenna with three rectangular microstrip fed slot radiator is proposed as shown in Figure 3-5. The unit cell has dimensions of 46.875×46.875 mm^2, while that of the entire antenna are 337.5×262.5×22.5 mm^3. It operates in the frequency range of 0.8–1.05 GHz and provides a gain of 8 dBi. Six PIN diodes are utilised to create three distinct beams by switching three radiating slots. The microstrip lines and slots are located on opposite sides of a 1.6 mm thick FR4 substrate (ε_r = 4.3), while the metasurface unit cells are configured into square shapes. The metasurface is printed on another 0.8 mm thick FR4 substrate and is designed to increase the directivity and bandwidth of the antenna. This directional antenna is successfully tested to detect 20 mL of fluid (water) inside a realistic torso using generated images that differentiate between healthy and unhealthy cases. Figure 3-6 shows the measurement setup for lung fluid accumulation detection using mimicking torso phantom.

A pattern reconfigurable loop dipole antenna for pleural effusion detection is proposed in [33]. It consists of one wavelength loop, a modified half wavelength bowtie shaped dipole and two parasitic directors to achieve an operating frequency range of 0.8–1.4 GHz and high front-to-back ratio. The antenna has dimensions of 78×130×1.6 mm^3 and shows high directional radiation pattern with a peak gain of 5 dBi. It is fabricated on FR4 substrate (ε_r = 4.3). Two PIN diodes are embedded across the parasitic directors to electronically control the current distribution, hence steering the radiation pattern.

Two linear arrays consisting of wideband antennas inserted into a foam-based bed and operating in the frequency range of 0.7–1 GHz for pulmonary edema detection are presented in [41]. The array element comprises a meandered loop, an L-shaped monopole antenna and a parasitic patch. They are printed and bonded to form a 3-dimensional structure using soldering and copper taping. The structure is fabricated on 1.6 mm thick FR4 substrate (ε_r = 4.4), and offers a directional radiation pattern, moderate gain of 1.9 dBi, and compact size of 20×80×48 mm^3. Each 8×2 antenna array is tested with different water volumes inserted into the torso phantom. The generated images show the capability of the system to detect water contents as small as 1 mL. Two

different commercial UWB horn antennas were utilised for lung tumour detection, imaging setup was performed using two concentric elliptically shaped layers filled with liquids dielectrically mimicking the torso tissues. The external layer mimics the combined muscle, fat and rib bone tissues while the internal one mimics the inflated lung tissue. A 15mL cylindrical shape tube filled with tap water is positioned inside the internal layer to mimic the lung lesion. The size of phantom structure has 82 cm circumference, the imaging procedures were performed based on Huygens' principle and the reconstructed images show a successful detection of lung lesions in superficial position [15]. A summary of the aforementioned antenna designs is given in Table 3-6.

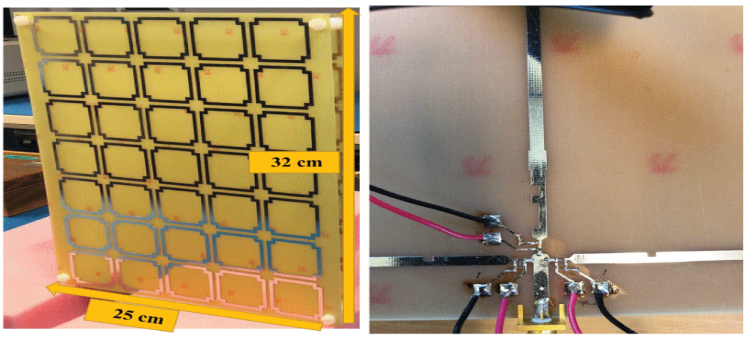

Figure 3- 5 The antenna unit cells (left) and biasing circuit (right) of the fabricated metasurface antenna for lung fluid accumulation [18].

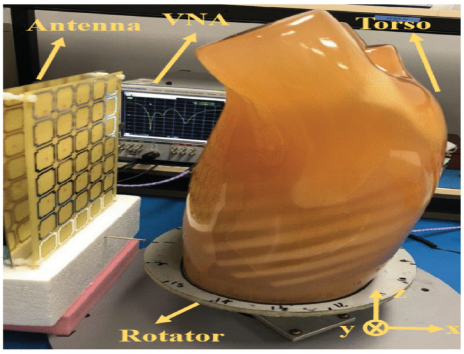

Figure 3- 6 Measurement setup for lung fluid accumulation detection [18].

Table 3- 6 *Summary of antenna designs for lung tumour and fluid accumulation detection*

Ref.	Antenna type	Frequency (GHz)	Size (mm^3)	Gain (dBi)	Key features/Remarks/Drawbacks
[18]	metasurface	0.8–1.05	337.5×262.5×22.5	8	• For fluid accumulation detection • Offer stable high gain and electronic beam scanning • Large antenna size and narrow operating bandwidth
[33]	loop-dipole	0.8–1.4	78×130×1.6	5	• For pleural effusion detection • Electronically steerable tri-state radiation pattern • Not tested on realistic phantom • Detection efficacy not evaluated
[41]	3D loop, monopole & parasitic patch	0.7–1.0	20×80×48	1.9	• For pulmonary edema detection • Tested on realistic torso phantom inserted with real lamb lung and injected with water • Can detect different levels of fluid accumulation • Antenna gain can be improved
[49]	circular shaped microstrip	3–4	60×40×1.513	n/a	• For lung tumour detection • Not fabricated or tested on realistic phantom • Can detect tumours of 4 mm radius at depth of 60 mm in, and distance of 10 mm from simulated phantom

[17]	elliptical patch	3–10.7	44×44×1.6	n/a	• For lung tumour detection • Ultra-wide bandwidth, directional • Not fabricated or tested on realistic phantom • Tested on simulated thoracic model
[117]	cupcake shaped	2.9–12	40×30×1.524	n/a	• For lung tumour detection • Ultra-wide bandwidth • Can detect lung cancer from stage II • Not tested on realistic phantom
[3]	slot rotated	1.5–3	22×46×10	2.6	• For lung tumour detection • Tested on human torso phantom • Can detect and localise tumour of dimensions 10×10×20 mm^3
[14]	Vivaldi metamaterial	3.3-21.6	45.19×17.53×0.8	4.2	• For lung tumour detection • Imaging at single frequency (10 GHz) • Tested on circular layered phantom with 12 cm diameter. • Weak detection of 5mm tumour diameter at superficial position
[15]	UWB horn antennas	1-5	NA	NA	• For lung lesion detection • Utilised antennas are commercial ones • Phantom size mimic a real small human chest size • Phantom was built using tissue mimicking liquids, and they combined (fat, muscle and rib bone) into one layer while the skin layer wasn't represented.

3.5 Antennas for Skin Cancer Detection

Skin cancer detection using RFMI technique similarly relies on contrasting between the dielectric properties of cancerous skin tissues (ε_r = 54, σ = 2.5 S/m) and healthy ones (ε_r = 39.2, σ = 1.11 S/m). Unlike the detection of aforementioned diseases that require deep penetration of the RF signal into human tissues, skin cancer detection requires only marginal signal penetration to detect the pathological changes in the skin layers. Hence, higher signal frequencies in millimeter wave (mm-wave) regime, i.e. between 30-300 GHz, which has a penetration depth of only 600 µm – 1.2 mm, have been explored recently for high-resolution imaging for skin cancer detection.

In [22], four substrate integrated waveguide (SIW) based antipodal Vivaldi antennas as shown in Figure 3-7, each operating in a different frequency range that extends into the mm-wave regime are proposed. They are fabricated on RT Duroid 6002 substrate of either 10 or 20 mm thicknesses, each having different dimensions as follows. Antenna 1 (12–37 GHz): 27.1×27.34×20 mm^3; Antenna 2 (37–55 GHz): 18.86×13.56×20 mm^3; Antenna 3 (55–75 GHz): 16.15×8.36×10 mm^3; and Antenna 4 (75–110 GHz): 14.44×4.46×20 mm^3. Collectively, the antennas provide an ultra-wide bandwidth of 98 GHz, stable high gain 10–12 dBi over the covered sub-bands and directional radiation pattern. Antennas 1 and 2 are fabricated on 20 mm thick substrates, while Antennas 3 and 4 used 10 mm thick substrates. All antennas are evaluated on artificial skin phantom embedded with two spherical droplet tumours of 400 µm diameter at 1mm depth inside the phantom. Imaging results show high resolution in detecting both tumours, but the performed measurements had considered only the effect of skin layer in the imaging setup. Moreover, unlike other types of tumours, the skin tumour starts on the outer skin layer, not below it. Figure 3-8 shows the measurement setup for skin cancer detection using the sub-bands Vivaldi antennas.

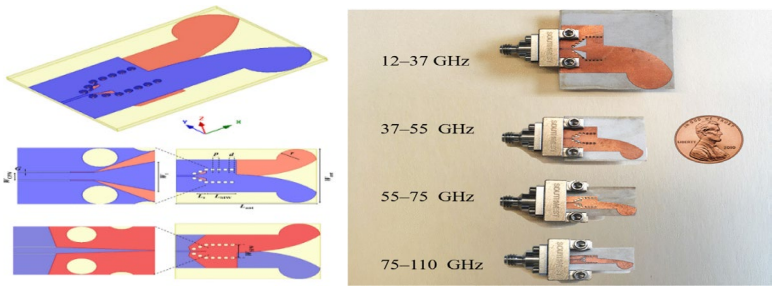

Figure 3- 7 The designed (left) and fabricated (right) sub-band Vivaldi antennas [22].

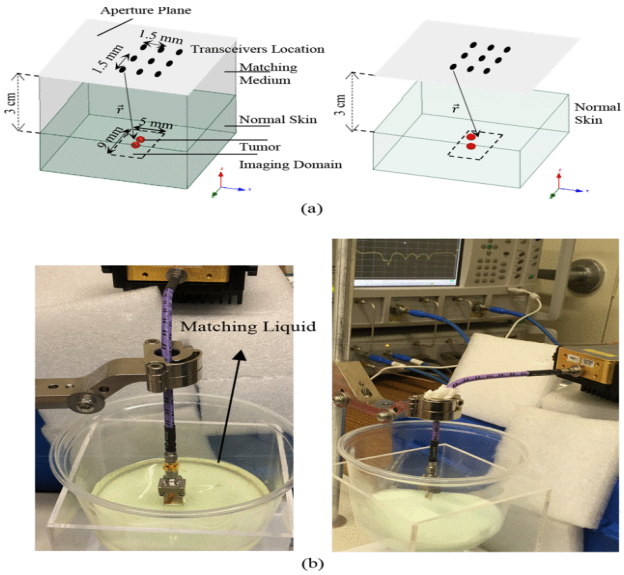

Figure 3- 8 Measurement setup for skin cancer detection: (a) schematic setup; (b) experimental setup [22].

The authors in [23] presented an artificial magnetic conductor (AMC) based hexagonal shaped patch antenna with CPW fabricated on 2.2 mm thick felt fabric substrate (ε_r = 1.22). It consists of a hexagonal patch of dimensions 32×38 mm^2, which is separated from the AMC by a 2 mm thick foam layer. The AMC is fabricated on zelt conductive fabric with dimensions of 44×48 mm^2 that consists of 4×4 unit cells with periodic hexagonal and rhombic shapes. Without AMC, the CPW-fed hexagonal patch antenna achieves a peak gain of 3.2 dB in the frequency range of 8–12 GHz. The addition of AMC increases the antenna's peak gain to 6.5 dBi due to the absorption of its back radiation. The proposed antenna is tested on a three-layer phantom consisting of skin, fat and muscle. The simulated S-parameters result show discrepancy between healthy and cancerous tissues. However, the tumour size, thickness and the imaging results are not discussed. In [20] authors proposed 36×30×4.85 mm^3 UWB stacked aperture coupled microstrip patch antenna (SAMPA) which has three layered stacked aperture coupled geometry with a DGS, it operates over 5.72 to 12.37 GHz and 6.4 dB gain for in-vitro skin cancer detection. The reported antenna is tested on 100 mm diameter forearm phantom with four layers (skin, fat, muscle, and bone). Imaging results show a successful detection of 20 mm diameter tumour placed on the outer skin layer with 2 mm thickness. However, only one antenna is used during measurement with manual placements at different positions around the phantom. An UWB imaging method

applied to a forearm phantom of three layers: cortical bone, adipose-muscle and skin tumour, is presented in [21]. Although successful in detecting the skin tumour, the skin layer presented is using an external plastic cylinder with tumour contained inside the adipose layer. Table 3-7 summarises the above antenna designs for skin cancer detection.

Table 3- 7 *Summary of antenna designs for skin cancer detection*

Ref.	Antenna type	Frequency (GHz)	Size (mm^3)	Gain (dBi)	Key features/Remarks/Drawbacks
[22]	antipodal Vivaldi	12–110	various	10–12	• 4 antennas with distinct sub-bands to cover desired frequency range • Ultra-wide bandwidth, high stable gain, and 200 μm resolution
[23]	hexagonal patch	6–12	44×48×6.2	6.5	• AMC improves antenna gain • Complex multi-layer structure • Not tested on realistic phantom • No medical images generated
[20]	Three layered SAMPA	5.72-11	36×30×4.85	6.4	• Antenna is tested on forearm phantom • Detection of 19 mm skin tumour diameter • Tumour size is quite large • Antenna is not tested for smaller tumour sizes

3.6 Summary

The past decade has seen rapid advancement of RFMI for biomedical applications such as for detection of different cancer types and other critical diseases. It is one of the most promising biomedical imaging techniques owing to its non-invasiveness, non-ionising radiation with low illumination power level, relatively low-cost, and sustained reliability. This chapter focuses on the antenna element of the RFMI system, which is a key factor controlling the RFMI performance.

Different antennas have been proposed in literature for different cancer and disease detection in different parts of the human body such as breast, brain, lung and skin. Typically, imaging deep tissue requires an antenna with lower operating frequency than

those for shallow ones. Furthermore, compact antennas are more desirable as more antennas can be employed to cover a given target area, thereby increasing the number of measurement points and consequently precision of detection. Moreover, increasing the bandwidth of antenna will improve the resolution of reconstructed images. However, higher frequencies can result in lower penetration levels and are more susceptible to attenuation. Thus, to obtain good resolution and penetration with minimized attenuation, the designed antenna should have ultra-wide bandwidth and high gain. The latter can concentrate the radiated power on the area under test and increase the penetration depth. In addition, radiation sidelobes should be minimized to reduce interference with the main lobes of other antenna elements and the possibility of clutter generation. Also, to avoid false mapping while reconstruction in the imaging system.

Chapter 4 Fractal Slot Loaded Super Wide Band Antenna: Design, Measurements and ECM

In this chapter, the design stages of the SWB antenna to cover simulated operating bandwidth over the frequency range (2.45 – 35.4) GHz is presented. Several parameters are discussed to verify the efficiency of the proposed antenna to be a good candidate in medical imaging applications. Different parametric studies are conducted over the covered frequency range to choose the optimum values of different physical dimensions. The fabrication process of the final design is discussed accompanied with several measurement setups of the main performance parameters. Moreover, the lumped element equivalent circuit model (ECM) is presented and optimised to accurately mimic the performance of the proposed antenna. Then, an optimised ECM is presented for the proposed fractal slot loaded super wideband (SWB) antenna that designed to operate over a frequency range of 2.45–35.4 GHz with a simulated bandwidth ratio of 14.4:1. The proposed model is based on the transmission line theory and relates the antenna performance to its physical geometry.

4.1 Introduction

The potential of SWB antennas in applications like lung and cancer detection relies heavily on various aspects of antenna performance. Firstly, a wide bandwidth is imperative to achieve high-resolution image generation. Secondly, a high gain is necessary to enable deeper signal penetration into the target object. Additionally, a high radiation efficiency, coupled with a stable radiation pattern, plays a crucial role in enhancing the accuracy of detection. Lastly, a compact size is desirable to facilitate the placement of multiple antennas around the object under examination [7]. The proposed antenna fulfils the key parameters for cancer detection by microwave imaging based on the background obtained from previous designs.

The main contributions of this chapter are designing an efficient SWB for microwave imaging applications with large, measured bandwidth 171.23% over the frequency range 3.1 to 40 GHz; to improve the resolution of the reconstructed images and the detection accuracy. This is the first time that a SWB antenna is designed for the detection of different cancer types, implementing a high covered bandwidth of 36.9 GHz and

enhanced gain within the range of 3.4 to 9.7 dBi. Also, it contributes to investigate an accurate ECM for our SWB antenna whose original design is reported in [25], but has been modified to achieve a super wide bandwidth of 32.9 GHz. A secondary contribution is to examine an effective and efficient approach to optimising the ECM's accuracy based on the antenna's geometry. This chapter addresses the knowledge gaps in utilising enhanced-performance SWB antenna in the detection of several cancer types and locations, the equivalent circuit modelling of SWB antennas based on transmission line theory, including the limited consideration of the antenna's geometry, and the lack of exploration of different optimisation techniques. To the best of our knowledge, this is also the first time that a dual sequential optimisation approach based on Gradient and Quasi-Newton methods is investigated for optimising the performance of a SWB antenna. The results are fast convergence and high modelling accuracy over a super wide bandwidth from 2.5 to 40 GHz.

4.2 SWB Antenna Design Stages

This section presents various design stages undertaken to achieve the desired performance of the proposed SWB antenna, all simulations are conducted using full wave simulator Ansys HFSS simulation software. Figure 4-1 illustrates the different design phases, progressing from the initial "Antenna 0" configuration to the final antenna structure. The initial antenna configuration begin with a simple circular patch paired with a semi-elliptical ground plane. Subsequently, several modifications and techniques are applied in the development of the SWB antenna structure, as depicted in Figure 4-1 (b-i), to enhance its overall performance.

Figure 4-2 displays the simulated results of the reflection coefficient $|S_{11}|$ (dB) for different stages of the antenna's evolution. In the initial stage, the antenna exhibits a relatively narrow bandwidth. In Figure 4-1 (b), a tapered feedline is introduced to improve impedance matching between the 50 Ω coaxial cable, connected to the 2.92mm K-type connector, and the high impedance at the patch's edge. Following that, intersecting ellipses are incorporated into the circular patch, as shown in Figure 4-1 (c). This addition increased the electrical length of the antenna, resulting in a broader bandwidth and raising the $|S_{11}|$ level to -14.7 dB at the first resonant frequency.

Furthermore, a polygon is introduced, as depicted in Figure 4-1 (d), to smooth the

transition of surface current at the bottom of the patch's radius. This enhancement led to improved $|S_{11}|$ levels at the first two resonant frequencies, reaching -16.3 dB and -42.6 dB at 4.1 and 9.3 GHz, respectively. The introduction of slots in the main radiator with various shapes, lengths, and positions has a notable impact on antenna performance, particularly in terms of shifting resonance frequencies [6, 7]. In this context, a circular slot is incorporated in the centre of the patch, as shown in Figure 4-1 (e). This modification shifts the second resonant frequency to 8.3 GHz while enhancing impedance matching between (18.7-19.2) GHz.

Moreover, two circles are added to the circular radiator to increase the electrical length and enhance the patch's inductive nature as shown in Figure 4-1 (f). This resulted in improved impedance matching, a broader bandwidth spanning from 2.5 GHz to 37 GHz, and a shift in the first resonant frequency to 3.8 GHz, with an improved $|S_{11}|$ level of -26.7 dB. Subsequently, two fractal slots with duplicated rectangular shapes are introduced on both sides of the radiator as displayed in Figure 4-1 (g), further increasing the electrical length and enhancing the first resonant frequency with a $|S_{11}|$ level of -32.2 dB at 3.9 GHz.

Nevertheless, two notches are observed around 18 GHz and in the (30-31) GHz range. To address this, two elliptical slots are embedded in the ground plane, and a rectangular slot is incorporated at the edge of the feedline, as shown in Figure 4-1 (h). These adjustments helped fine-tune the capacitive coupling between the patch plane and the ground plane [120], resulting in enhanced impedance matching and a bandwidth covering the frequency range of (2.5-35.3) GHz, along with improved $|S_{11}|$ levels of -36 dB and -40.3 dB at the first resonant frequencies of 3.8 and 7.7 GHz, respectively.

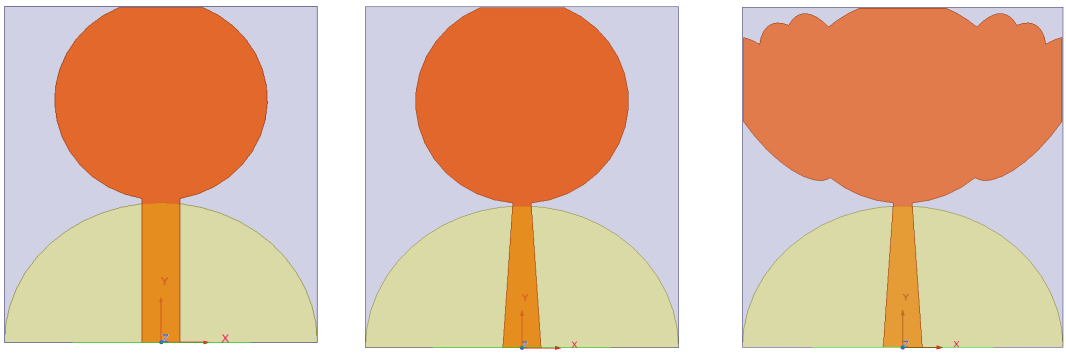

(a) *(b)* *(c)*

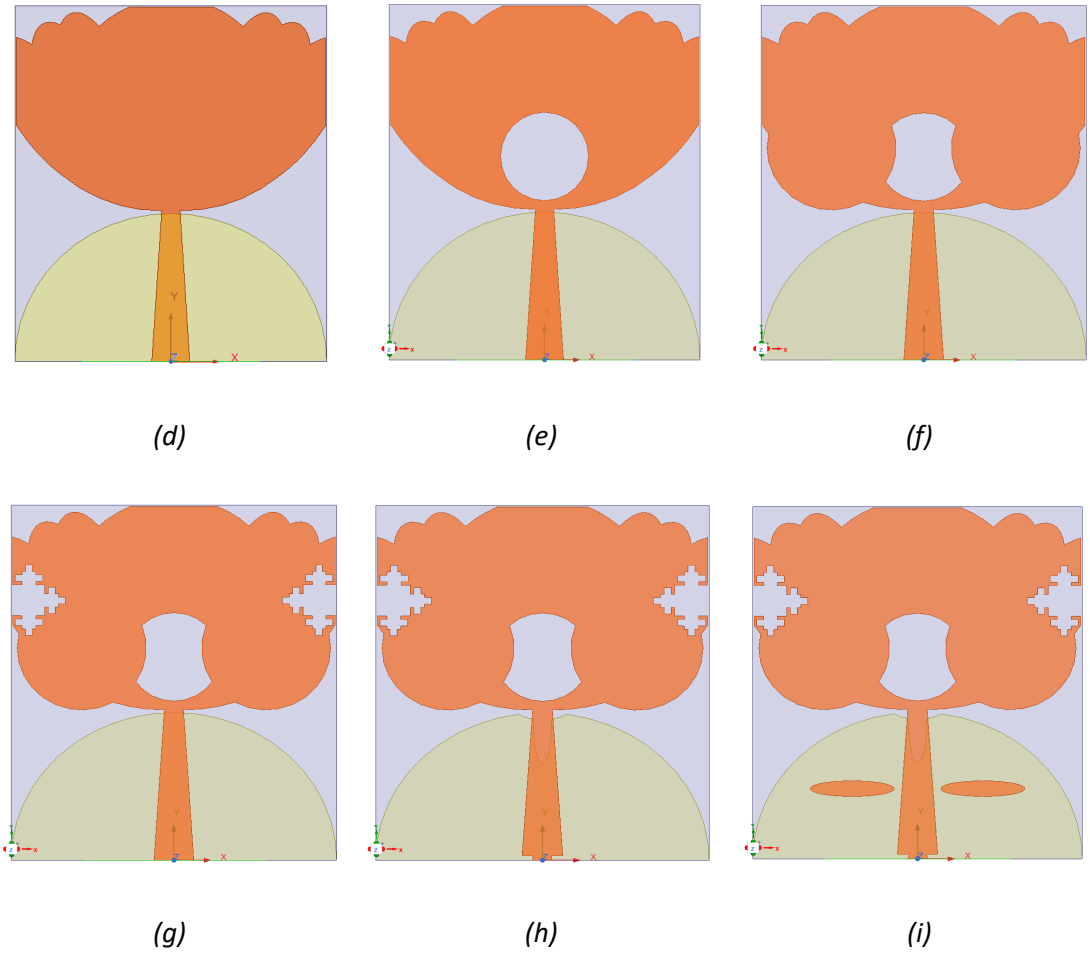

Figure 4- 1 SWB antenna design phases (a) antenna 0; (b) antenna 1; (c) antenna 2; (d) antenna 3; (e) antenna 4; (f) antenna 5; (g) antenna 6; (h) antenna 7; (i) final antenna.

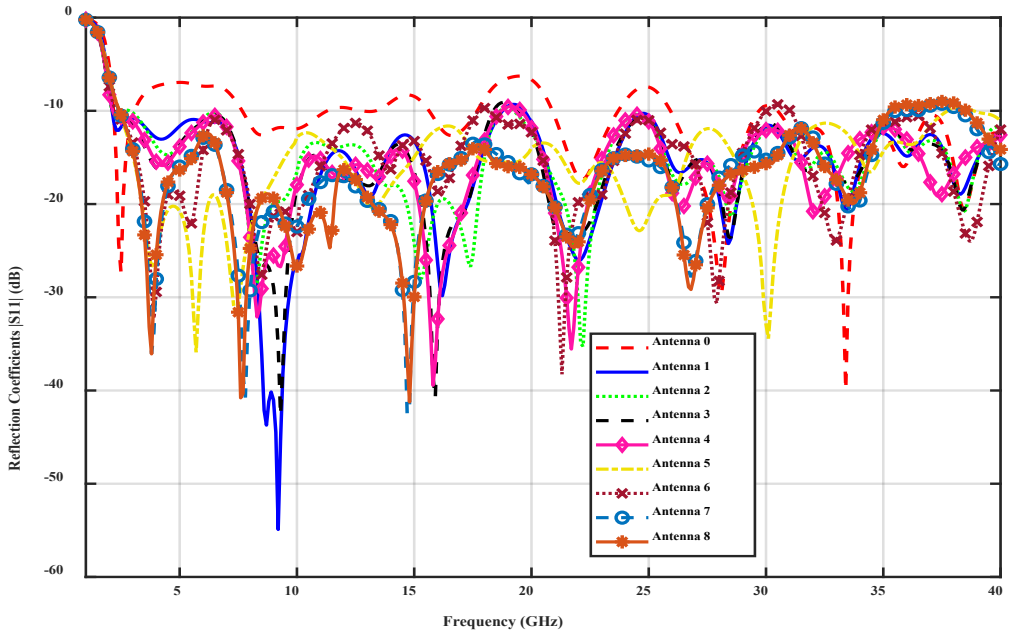

Figure 4- 2 Reflection coefficients simulated results of different antenna stages.

In addition, two elliptically shaped parasitic elements are introduced on either side of the tapered feedline as illustrated in Figure 4-1 (i). These elements are not directly connected electrically to the patch; instead, they resonate in response to the radiator's influence. With the incorporation of these parasitic elements, impedance matching was notably improved, particularly within the (9.3-12) GHz range. As a result, the antenna's overall simulated bandwidth expanded to cover the frequency range of (2.45-35.4) GHz, achieving a bandwidth ratio of 14.4:1 as illustrated in Figure 4-2.

4.3 SWB Antenna Parametric Studies

In this section, each parameter of the proposed antenna is optimised by varying one parameter while keeping the other parameters fixed to study the effect of different parameters dimensions on the antenna performance over the covered bandwidth (2.5-40) GHz; using Quasi-Newton optimizer supported in HFSS simulator.

4.3.1 Patch Radius

Starting with the initial antenna structure (Antenna 0), different parameters are optimised to achieve good performance; One of them is the radius of the circular patch. Simulations were conducted with various radius values (10mm, 11mm, 12mm and 13mm), as presented in Figure 4-3. It is clear that the optimal radius for the circular slot is 12mm, as it provides the best impedance matching.

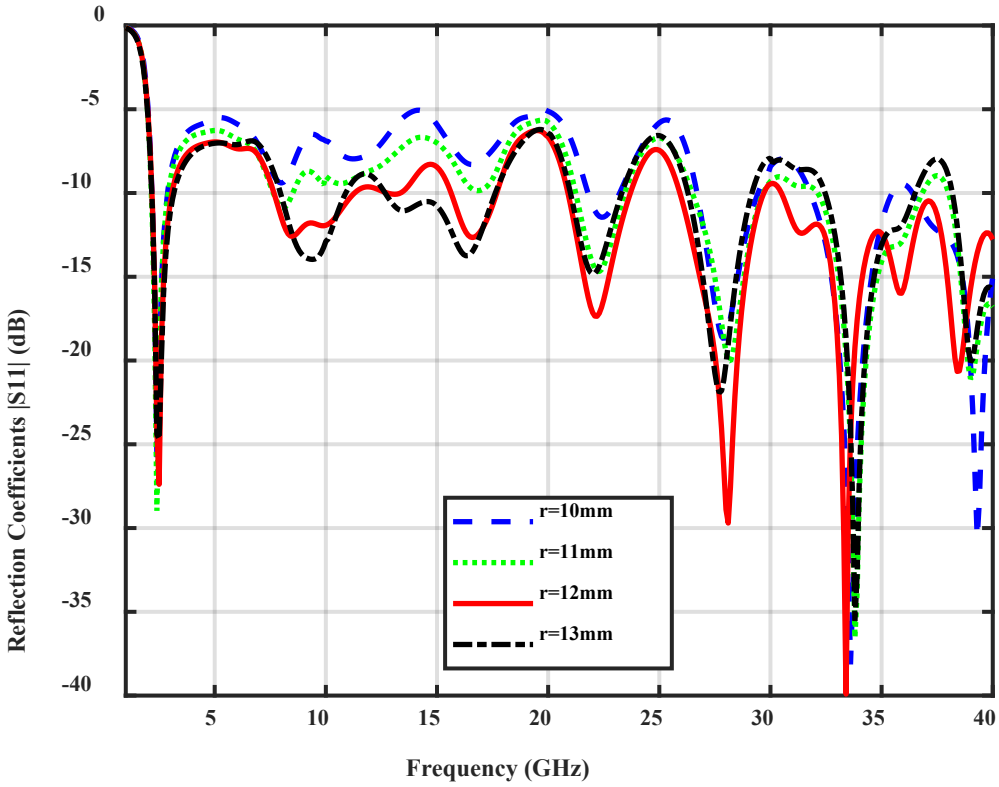

Figure 4- 3 Patch radius parametric study.

4.3.2 Gap Distance Between Patch and Ground Plane (G)

The gap distance between the patch plane and the ground plane which is displayed in Figure 4-4(a) has been optimised across the entire bandwidth. Simulations were performed using different gap spacing values (0.29mm, 0.49mm, and 0.69mm), as illustrated in Figure 4-4(b). It becomes evident that the optimal gap size is 0.49mm, as it yields improved impedance matching across the entire bandwidth, notably within the (13.2 to 16.7) GHz range.

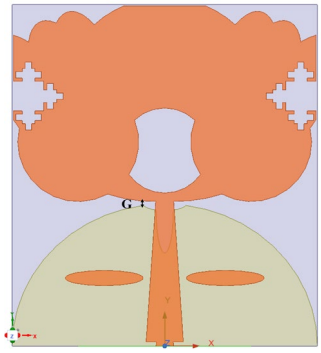

(a)

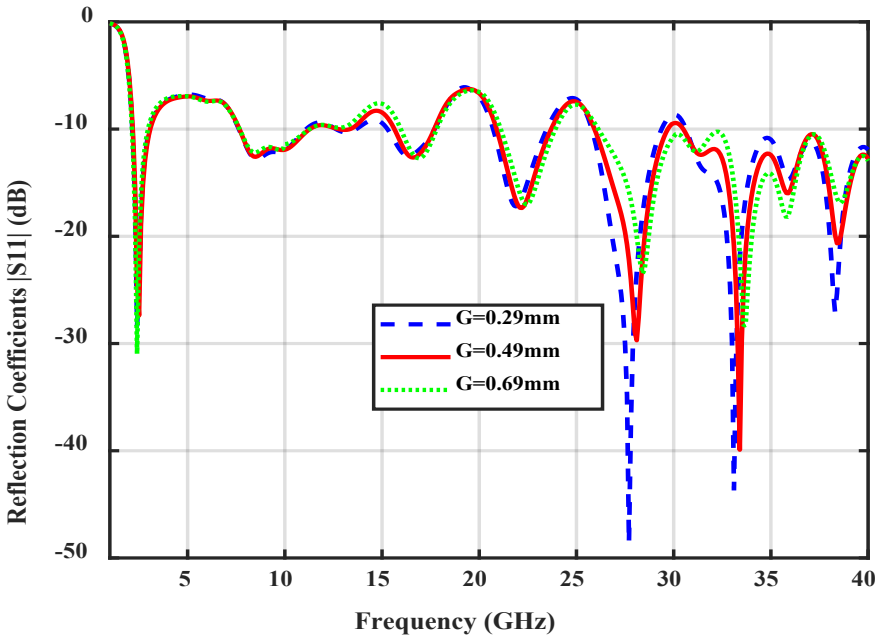

(b)

Figure 4- 4 Gap parametric study: (a) gap parameter display; (b)reflection coefficient result.

4.3.3 Feedline Width

The feedline bottom and top widths have been optimised across the entire bandwidth. Simulations were performed for the bottom width using different width values (2.3mm, 3.3mm, 4.3 mm and 5.3mm), as illustrated in Figure 4-5(a). It becomes evident that the optimal feedline width size is 4.3mm, as it results in the best $|S_{11}|$ level at the first resonant frequency (-27 dB). Furthermore, the top feedline width is simulated using different width values (1.5mm, 2mm, and 2.5mm), as illustrated in Figure 4-5(b). It can be noted that the optimal feedline top width size is 2mm, as it results in the best $|S_{11}|$ level at the third resonant frequency (-54 dB). Also, it shows the best impedance matching especially at higher frequency range.

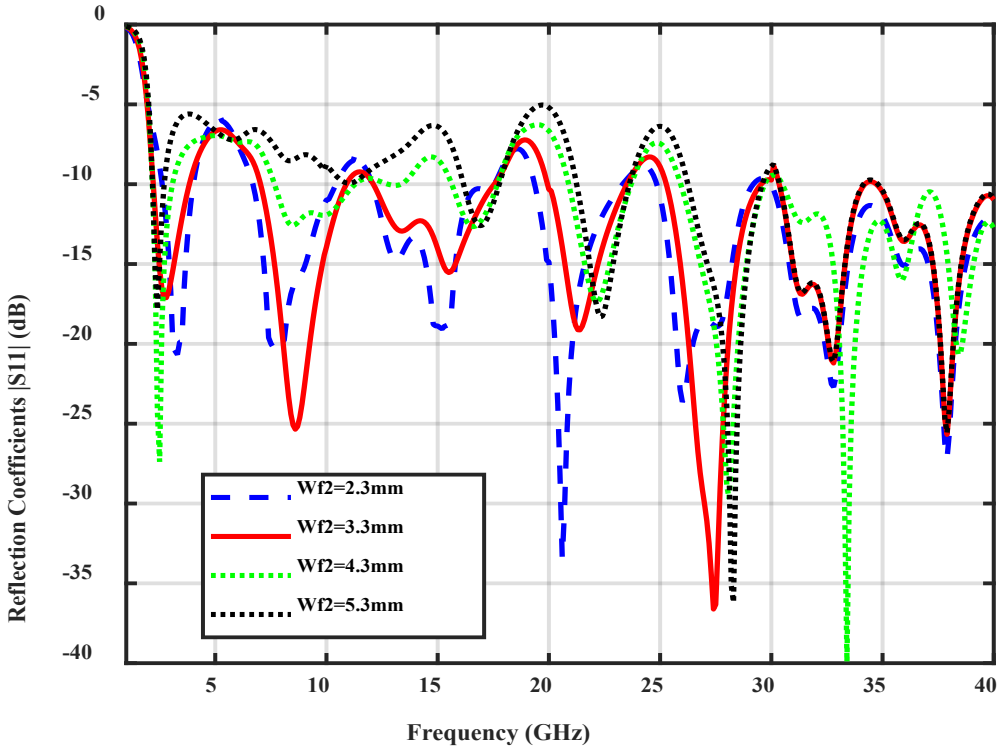

(a)

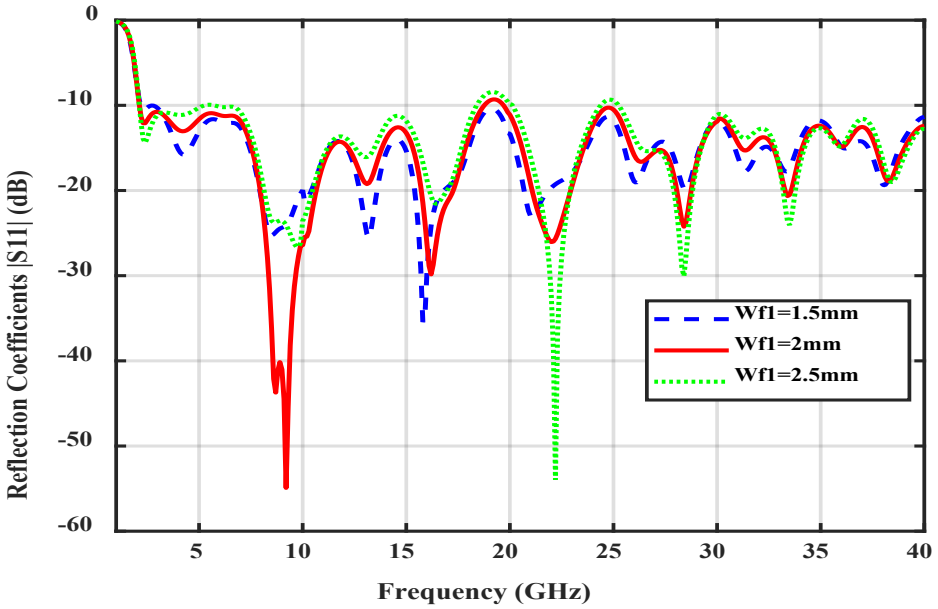

(b)

Figure 4- 5 Feedline width parametric study: (a) bottom width; (b)top width.

4.3.4 Patch Slot Radius

Following the introduction of a circular slot in the centre of the patch element, simulations were conducted with various radius values (4.5mm, 5mm, and 5.5mm), as displayed in Figure 4-6. The results indicate that the optimal radius for the circular slot is 5mm, as it provides the most favourable impedance matching, particularly at higher frequency bands.

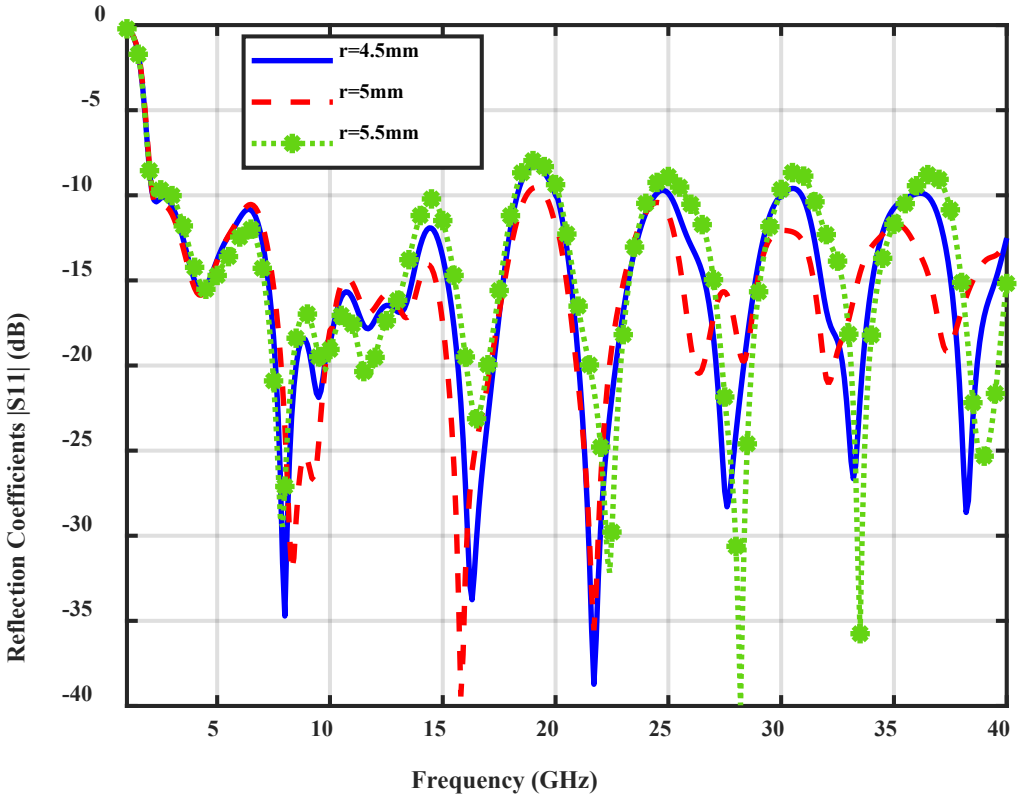

Figure 4- 6 Patch slot radius parametric study.

4.3.5 Radius of the Added Circles

Two circles were incorporated at the lower corners of the radiator and a parametric study is conducted on several radius values (6.4mm, 6.7mm 7mm and 7.3 mm). The simulated results are presented in Figure 4-7. The figure illustrates that the optimal radius for the circles is 7mm, as it yields the highest $|S_{11}|$ levels, particularly at the first two resonant frequencies.

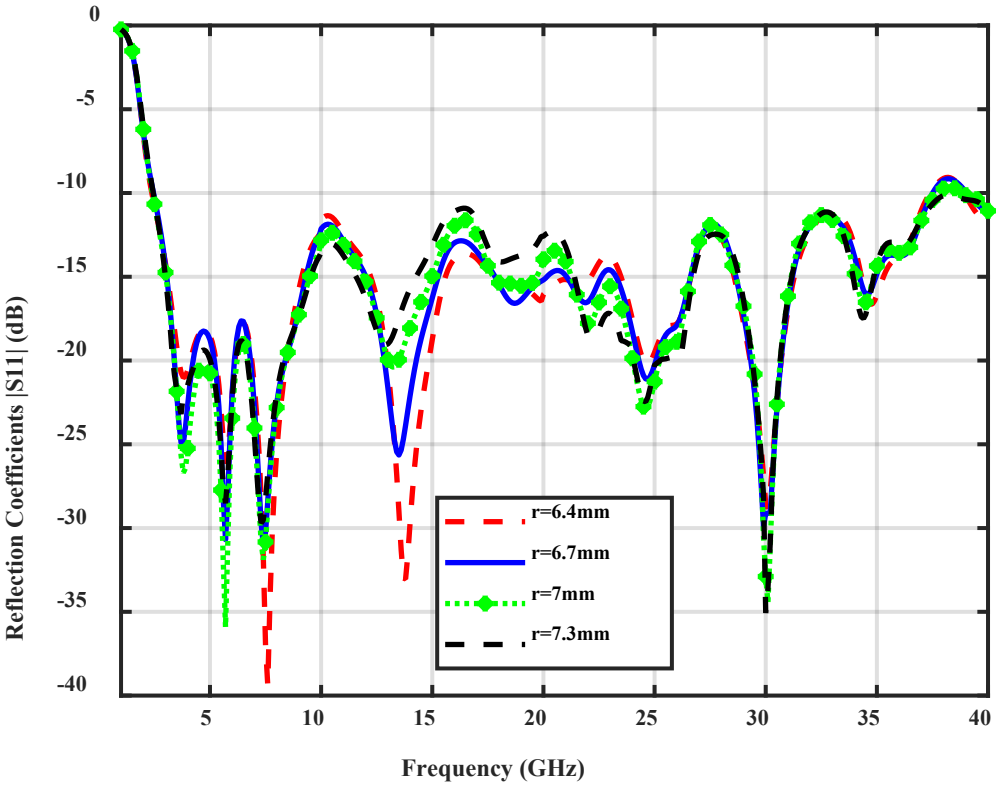

Figure 4- 7 Patch circles radius parametric study.

4.3.6 Position of Elliptical Parasitic Elements

Two elliptical shaped parasitic elements were added around the tapered feedline, a parametric study is conducted on several height values (7.5mm, 8mm and 8.5 mm). The results are shown in Figure 4-8 (a). It can be observed from above results that the optimum value for the parasitic elements height is 8mm which offers the highest $|S_{11}|$ level at the first resonant frequency (3.8 GHz) and maintains better impedance matching at higher frequency range. Also, another parametric study is performed on the major radius of the parasitic elements for different values (4mm, 4.5mm and 5mm). From the results that are displayed in Figure 4-8 (b), it can be noted that the optimum value for the parasitic elements major radius is 4.5mm which offers the highest $|S_{11}|$ level at the first resonant frequency (3.8 GHz) and maintains better impedance matching at the X-band (7.5 to 12.5) GHz and at higher frequency range.

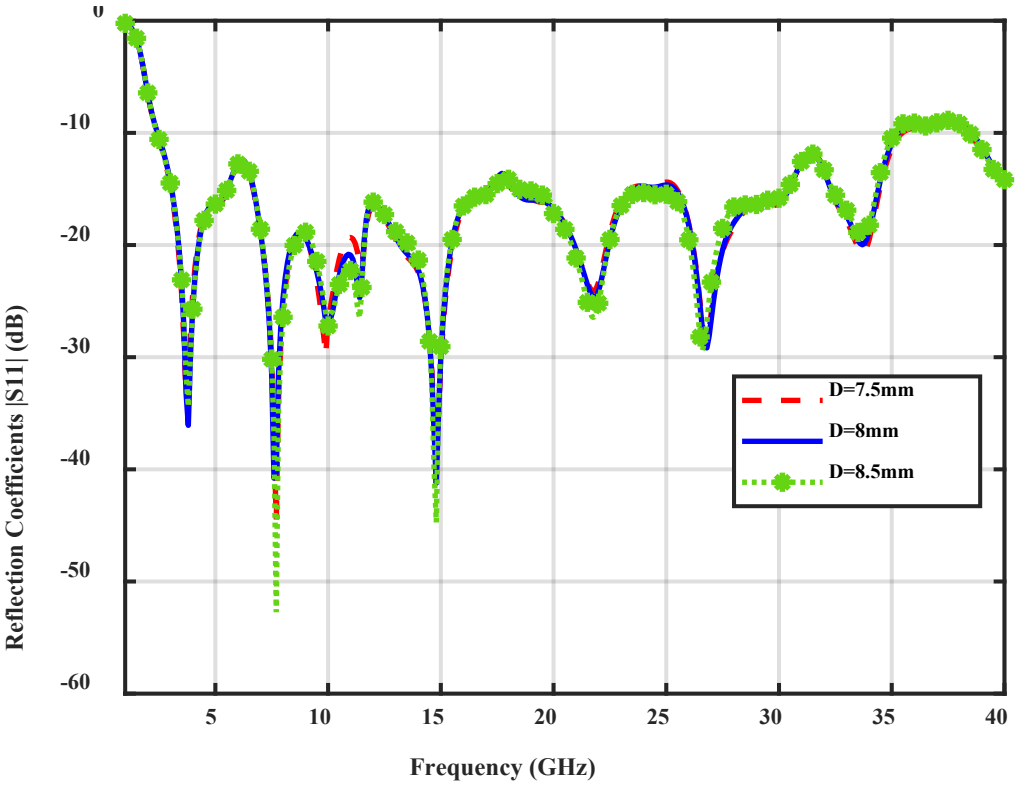

(a)

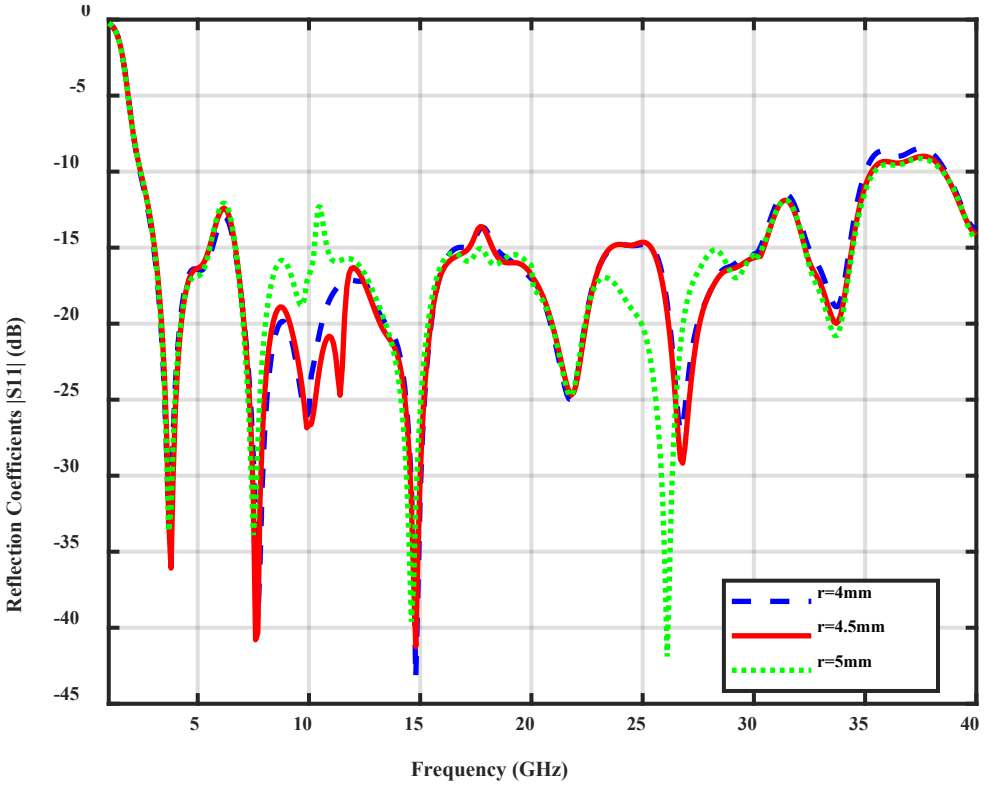

(b)

Figure 4- 8 Parasitic elements parametric study: (a) position; (b)major radius.

4.4 SWB Antenna Final structure

In this section, the Final structure and the fabricated prototype of the proposed SWB antenna is shown in Figure 4-9 with related dimensions. It has overall compact dimensions of 40×35×1.57 mm^3 and electrical dimensions of 0.32λ × 0.28λ (where λ corresponds to the lower operating frequency (2.45 GHz)). Hence, the designed antenna offers a good bandwidth dimension ratio (BDR), which is defined as the ratio of the percentage bandwidth to the electrical area of the antenna as in equation (4.1), with value of 1943.2. The antenna is built on Rogers RT Duroid 5870 substrate (ε_r= 2.33; tanδ = 0.0012) and evaluated on Ansys HFSS simulation software. The proposed antenna is fabricated using PCB manufacturing process, on high frequency Rogers sample sheets, specifically RT Duroid 5870 with a thickness of 0.062'' (1.575 mm) and 1 oz. (0.35µm) H1/H1 copper cladding, provided by Rogers Corporation. An immersion silver is used as a surface finish to provide smooth flat surface, protection against any oxidation and improve the signal quality at high frequency. It has a good conductivity which minimises the signal loss and enhances the overall antenna performance. The detailed dimension of the proposed antenna is listed in Table 4-1.

$$BDR = \frac{\%BW}{\lambda_w \times \lambda_L} \tag{4.1}$$

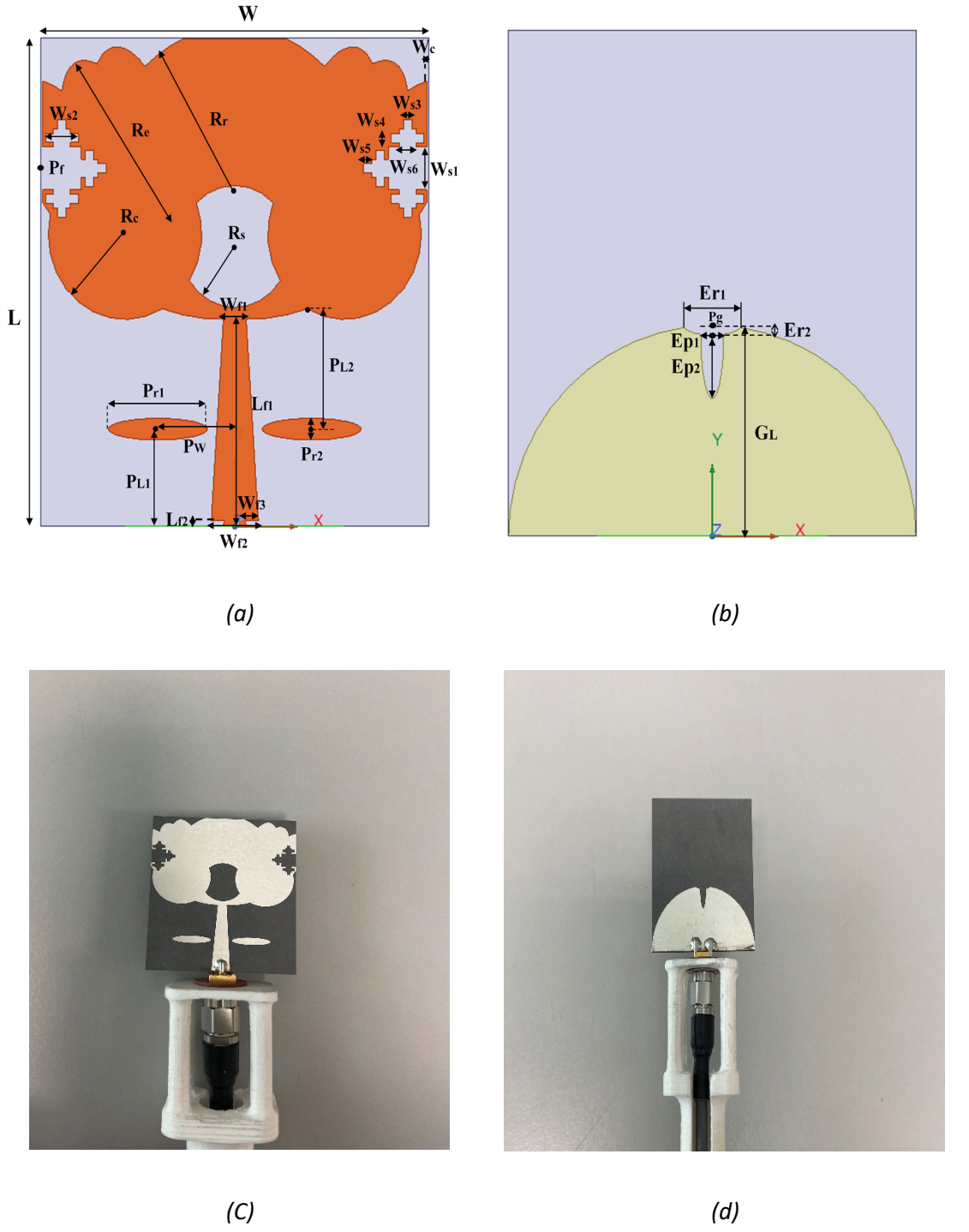

(a) *(b)*

(C) *(d)*

Figure 4- 9 SWB antenna full structure, (a)top view, (b)rear view, (c) prototype top view and (d) prototype rear view.

Table 4- 1 *Dimensions of The Proposed SWB Antenna*

Parameter	Value (mm)	Parameter	Value (mm)	Parameter	Value (mm)
W	35	Wf1	2	Re	4
L	40	Wf2	4.3	Wc	0.15
Ws1	3.5	Wf3	1.16	Pr1	9
Ws2	3	Pr2	1.8	Pw	7
Ws3	0.75	Lf1	17	PL1	8
Ws4	1.5	Lf2	0.5	PL2	9.87
Ws5	0.75	Rr	12	Er1	2.5
Ws6	1.5	Rs	5	Er2	0.75
Pf	29.4	Rc	7	Ep1	2
GL	16.7	Pg	16.7	Ep2	5

4.5 SWB Antenna Parameters Measurements

Different antenna parameters are measured in this section, the reflection coefficient measurement is performed in anechoic chamber using antenna positioner and Anritsu S820E vector network analyser. The results are acquired using VNA advanced mode, and the external cables that operates from DC to 40 GHz need to be calibrated once connected to the VNA ports to calibrate out any frequency response originates from the cables and to obtain high quality measurements. The calibration algorithm used in this research is two ports SOLT (short-open-load-thru). A good agreement between the simulated and measured result of reflection coefficients is displayed in Figure 4-10 below. Fractional bandwidth of more than 173.6% (2.45-35.4) GHz and 171.23% (3.1-40) GHz is achieved during simulation and measurement, respectively. It is depicted that a 14.4:1 and 12.9:1 ratio bandwidth is gained in simulation and measurement, respectively. A very good $|S_{11}|$ level of -20.7 dB is achieved at 3.8 GHz.

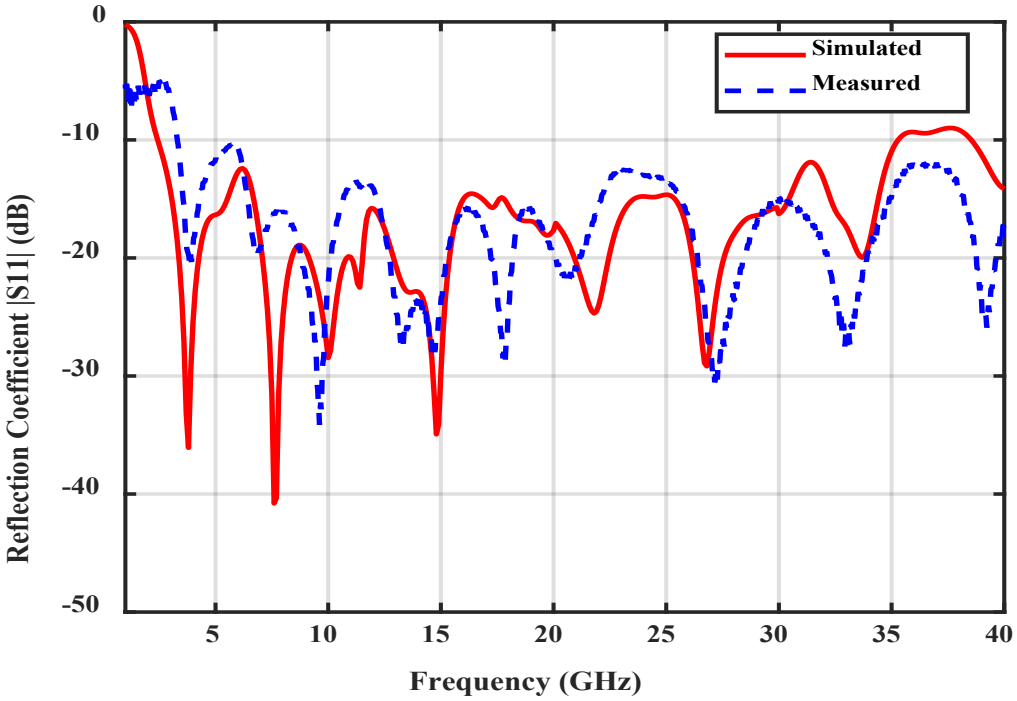

Figure 4- 10 Simulated and measured reflection coefficient results.

4.5.1 Peak Gain Measurement

The peak gain measurement is performed using two identical SWB antennas and the far filed condition is conducted during measurements. The far filed distance is calculated using the largest antenna dimension (D) as shown in Figure 4-11 (a) which is the antenna diagonal length. By substituting 50.3 mm in the below equation the far field distance (S) will be 760 mm. One popular approach in Gain measurement is to employ two identical antennas as the transmitting and receiving antennas and by employing Friis power formula [27], antenna gain can be calculated.

$$S \geq \frac{2D^2}{\lambda} \tag{4.2}$$

$$G = \frac{4\pi r}{\lambda}\sqrt{\frac{P_r}{P_t}} \tag{4.3}$$

$$G_1 = G_2 = ½\,(P_r\,(dB) - P_t\,(dB) + 20log(d) + 20log(f) - 27.56) \tag{4.4}$$

where G_1, G_2 are the gain of antenna 1 and antenna 2, respectively, d is the separation between two antennas in mm and f is the operating frequency in GHz. S_{21}(dB) is used

to replace (P_r (dB)- P_t (dB)) where λ is the wavelength, P_r and P_t are the received power and the transmitted power in Watts, respectively.

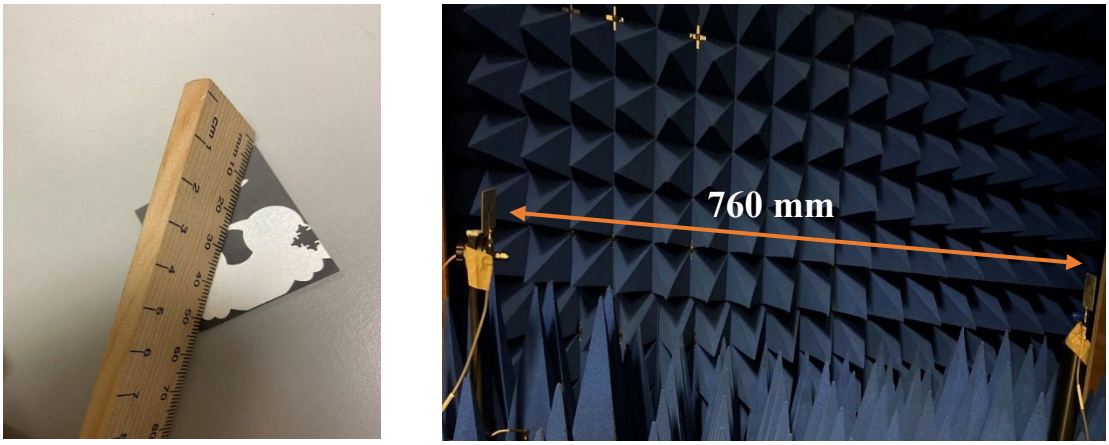

(a) *(b)*

Figure 4- 11 Gain measurement setup: (a)antenna diagonal; (b)measurement setup.

Figure 4-12 illustrates both the simulated and measured broadside gain of the fractal slot-loaded antenna. It demonstrates that the achieved gain tends to rise as the frequency increases and maintains a consistently positive gain across the entire frequency range of operation. This phenomenon is attributed to the effective aperture of the radiating patch being larger than the wavelength corresponding to the higher frequencies. This relationship is explained by the fact that antenna gain is directly linked to the antenna's effective aperture and wavelength.

However, it is important to note that at higher frequencies, there may be some attenuation in antenna gain due to connector losses. The measured peak gain exhibits a minimal value of 3.4 dBi at 2.5 GHz and a maximum value of 9.7 dBi at 39.5 GHz, demonstrating a strong agreement with the simulated results. These gain values align well with those reported for similar antennas in existing literature.

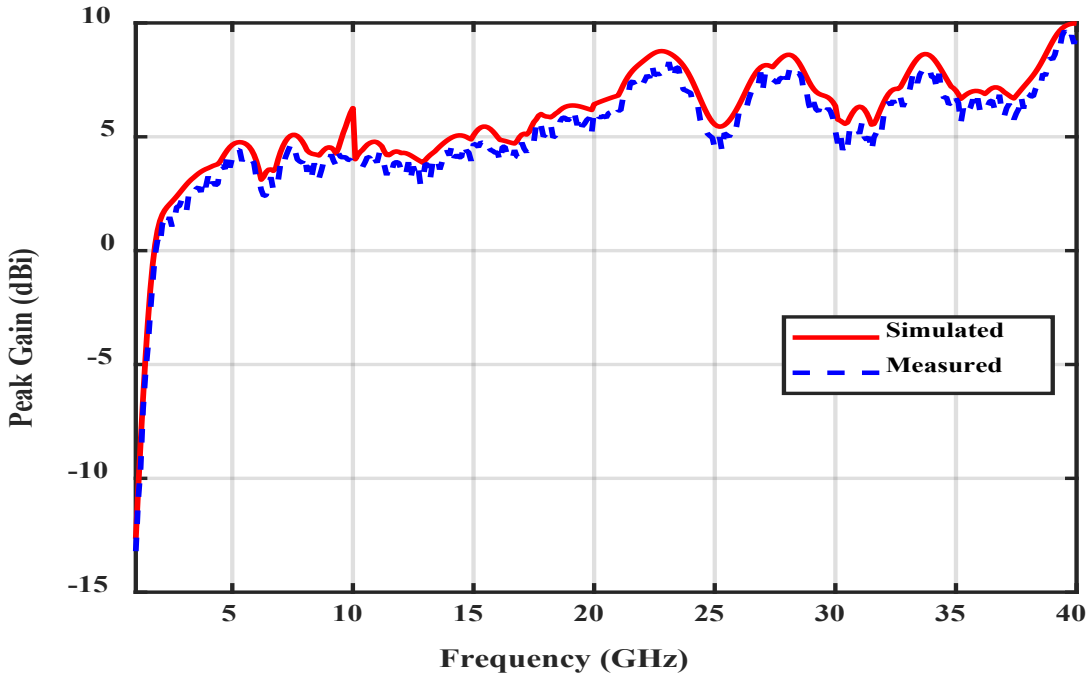

Figure 4- 12 Simulated and measured peak gain results.

4.5.2 Radiation Efficiency Measurement

An ideal antenna should exhibit exceptionally high radiation efficiency, preferably reaching 100%. It is important to note that radiation efficiency depends on the frequency rather than the radiation direction. It is primarily influenced by antenna loss and does not incorporate the impact of antenna impedance mismatch. The disparity between the feedline/connector and the antenna's impedance is factored in when considering the antenna's overall efficiency (η_T). This overall efficiency is defined as the ratio of the total power radiated by the antenna (P_r) to the total power supplied to the antenna (P_s) and can be mathematically expressed as follows:

$$\eta_T = \frac{P_r}{P_s} = \frac{P_a}{P_s}\frac{P_r}{P_a} = (1 - |\Gamma|^2).\eta \tag{4.5}$$

The symbol P_a is the total power accepted by the antenna, and Γ represents the reflection coefficient, equivalent to the S-parameter S_{11} or S_{22}, and it is a complex number that can be easily determined using a vector network analyser. When the reflection coefficient equals zero (indicating a perfect match), the power received by the antenna matches the power delivered to it, resulting in a perfect match with no mismatch. In this scenario, the total efficiency aligns with the radiation efficiency,

making it an ideal situation. However, in practice, the radiation efficiency always surpasses the overall efficiency of the antenna.

In the field of antenna theory, antenna radiation efficiency is defined as the ratio of the antenna's gain (G) to its directivity (D).

$$\eta = G/D \tag{4.6}$$

Directivity and gain differ in their consideration of antenna loss. Gain accounts for antenna loss, whereas directivity does not. Consequently, gain typically registers as a smaller value compared to directivity, and it can be assessed through various well-established measurement techniques. With the significant progress in computational electromagnetics (CEM), obtaining antenna directivity has become relatively straightforward through numerical simulation tools such as HFSS. Since directivity does not factor in antenna losses, the simulated directivity often closely approximates the measured directivity. Therefore, utilizing simulated directivity as an alternative to measurements is also an acceptable practice. As depicted in Figure 4-13, there is a noticeable trend of rising radiation efficiency as the frequency increases. The average efficiency is 94% while the highest one, reaching a peak of 97.9%, is attained at 9.7 GHz. However, beyond 22 GHz, there is a gradual decline in radiation efficiency. This decrease is primarily attributed to impedance mismatching at higher frequencies, stemming from the use of K-type connectors and the influence of high-order modes. It can be noted that radiation efficiency is 97.1% and 95.6% at first resonant frequencies 3.8 and 7.6 GHz, respectively.

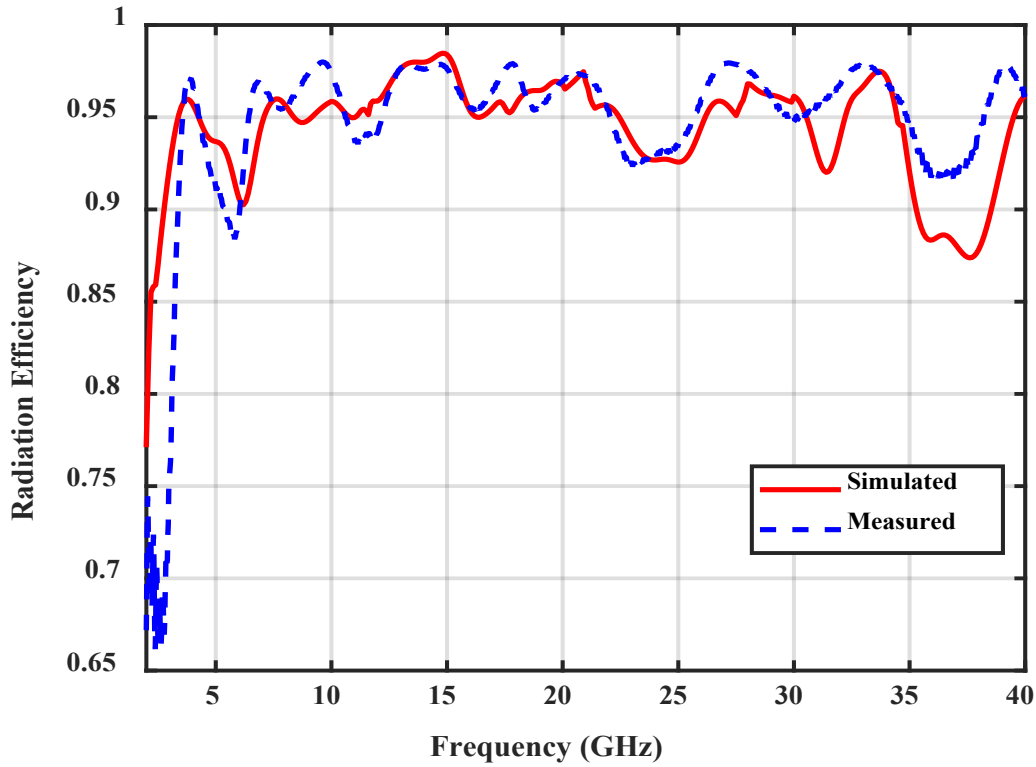

Figure 4- 13 Radiation efficiency results.

4.5.3 Group Delay and Isolation Measurement

The proposed design exhibits a high level of compatibility with medical imaging applications due to its compactness and expansive operational bandwidth. Time domain analysis serves as a fundamental technique for scrutinizing the dispersion characteristics of the antenna. In this context, a proper antenna design is imperative to mitigate distortions in the received pulse, making time domain analysis a crucial for wideband antennas.

To facilitate time domain characterization, two identical antenna configurations are arranged at a fixed separation distance of 760 mm in each case. These two time domain analysis setups, denoted as (a) Face to face and (b) Side by side, are visually represented in Figure 4-14. A critical time domain parameter of interest is the group delay, which is theoretically computed as the negative derivative of phase variation concerning frequency. The negative sign in the group delay formula typically indicates a phase shift that occurs as a function of frequency. Hence, the group delay decreases as the frequency increases. In other words, it shows that higher frequency components tend to arrive earlier than lower frequency components.

$$\tau_g(\omega) = -\frac{d\varphi(\omega)}{d\omega} = -\frac{d\varphi(\omega)}{2\pi df} \tag{4.7}$$

where $\varphi(\omega)$ represents the phase of the system's frequency response, and ω represents the angular frequency. The passage of a signal through a device leads to both amplitude and phase distortions, particularly as the input signal comprises multiple frequency components. Consequently, the group delay quantifies the average time delay experienced by the input signal at each frequency, serving as a gauge of the device's dispersion characteristics. The linearity of the phase response across the entire far-field region is also corroborated by the group delay analysis. In the context of a proficient super-wideband (SWB) system, it is imperative to maintain minimal group delay, ideally exhibiting minimal variation, typically less than 2 ns in practice [84], thereby indicating a linear phase response over the entire frequency spectrum. The formula outlined in Equation (4.7) is employed to calculate the group delay. The results, as illustrated in Figure 4-15, reveals that the group delay remains well within acceptable bounds for both side by side and face to face configurations, thereby rendering the system suitable for wireless communication applications [67].

Furthermore, it is evident from Figure 4-16, that high isolation is achieved in both configurations which ensure a reduction in mutual coupling between adjacent antennas. Additionally, the phase fluctuation across the entire frequency range is linear in both configurations, as depicted in Figure 4-17, indicating that the received pulse is without out-of-phase components [7].

(a)

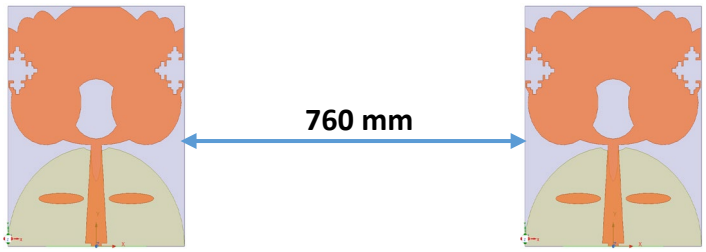

(b)

Figure 4- 14 Group delay and isolation measurement setup for different configurations: (a) face to face; (b) side by side.

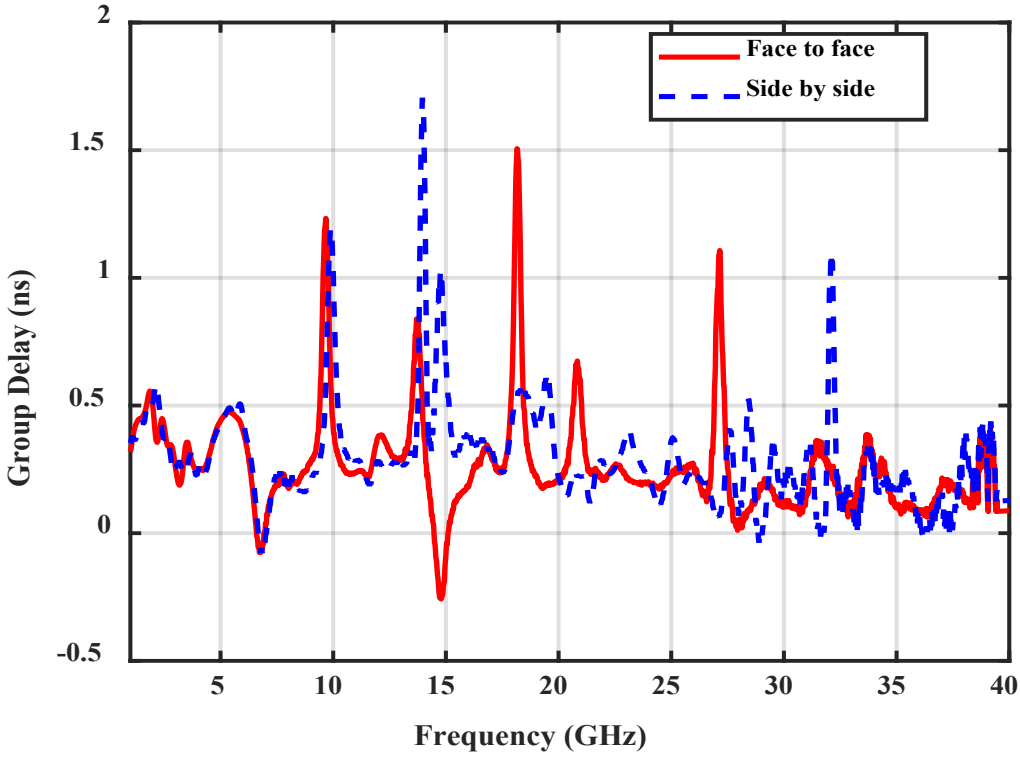

Figure 4- 15 Measured group delay in face to face and side by side configurations.

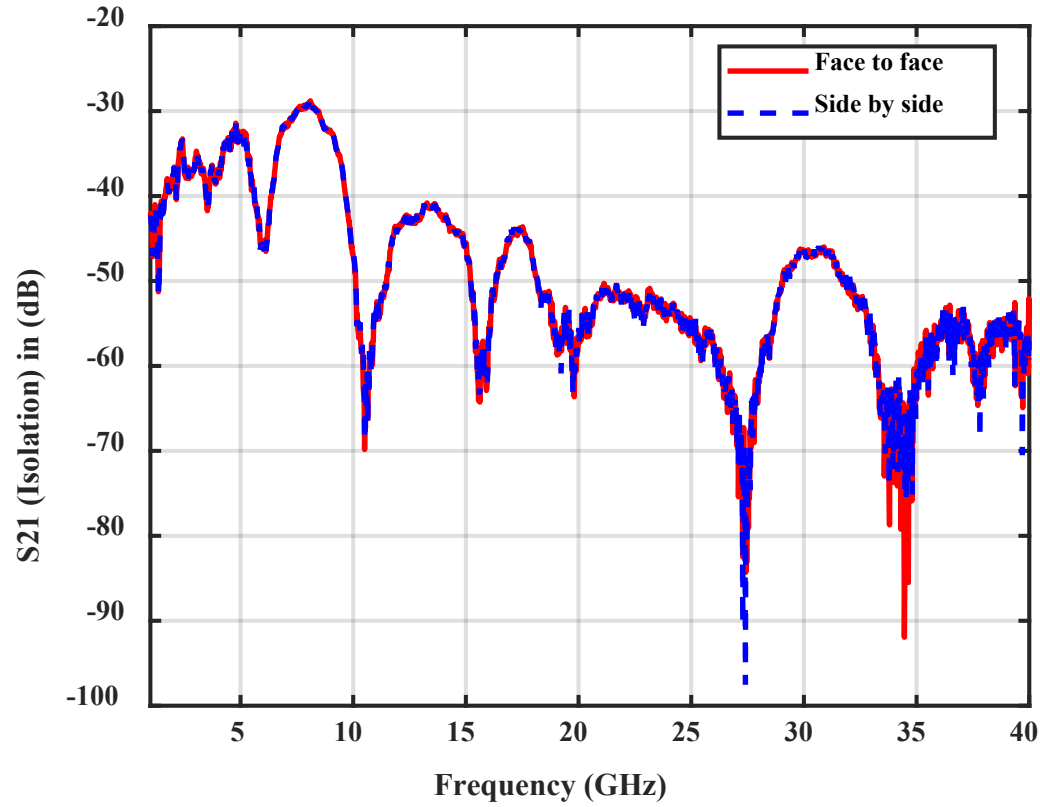

Figure 4- 16 Isolation variation in face to face and side by side configurations.

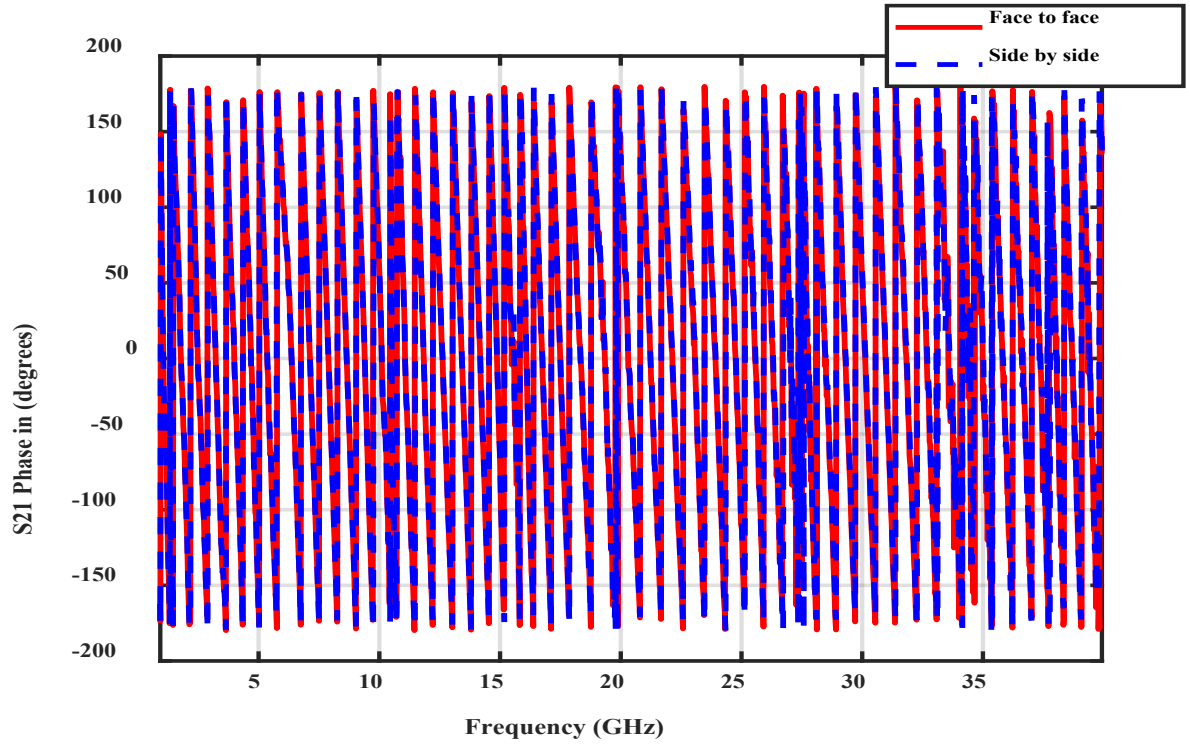

Figure 4- 17 Phase variation in face to face and side by side configurations.

4.5.4 Radiation Pattern Measurement

The radiation pattern, a critical parameter, assesses the antenna's capacity to focus power on a specific direction. The frequencies at which measurements were taken are determined by identifying the points of intersection between measured and simulated $|S_{11}|$ results, as illustrated in Figure 4-18.

In Figure 4-19 (a, b, and c), it can be observed that the configuration employed for radiation pattern measurements, featuring the antenna under test (AUT) and a directional transmitting antenna. Since the AUT is a super-wideband (SWB) antenna covering the frequency range of 3.1 GHz to 40 GHz, three different horn antennas were utilised as transmitting antennas to encompass this entire bandwidth.

All measurements were conducted within an RF anechoic chamber, under far-field conditions, with the assistance of a 3D antenna mechanical positioner controlled by a PC. This positioner allows for a 360-degree rotation in both the vertical and horizontal axes. The radiation pattern measurements were overseen by a MATLAB-based application responsible for altering VNA parameters (such as the type of data being measured, S-parameters, and frequency points) and Arduino parameters, which included specifying the step size for measurements. A step size of 9 degrees was selected for all measurements, striking a balance between measurement accuracy and time efficiency. Increasing the step size would decrease measurement time but compromise accuracy. Notably, the 9-degree step size was found to be optimal for both precision and measurement duration, with each frequency point measurement taking approximately 19 hours and 30 minutes to complete, yielding highly accurate results.

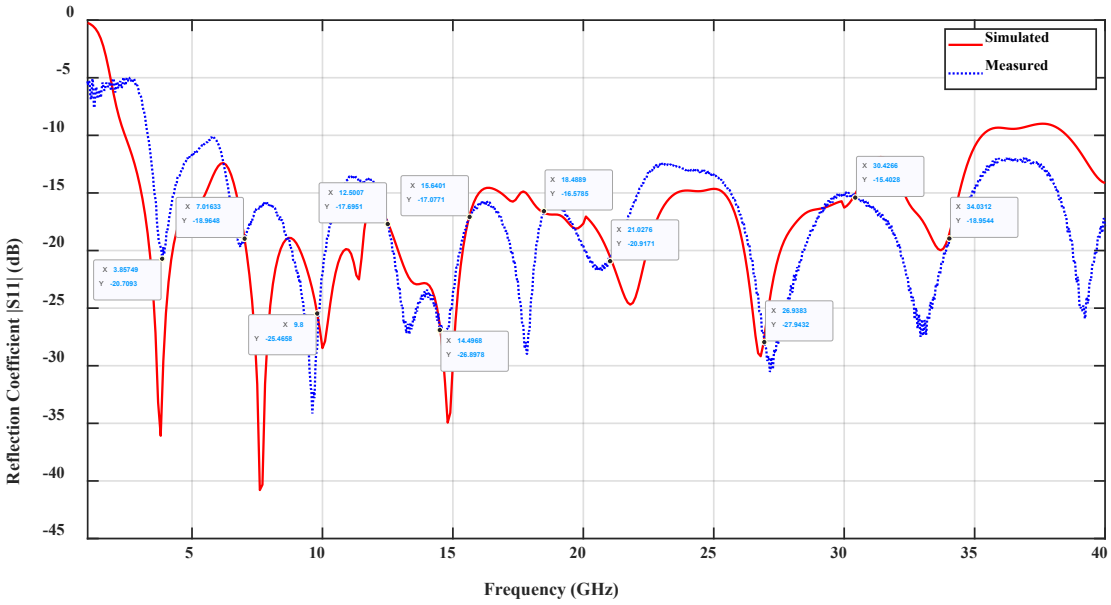

Figure 4- 18 Radiation pattern measurement frequency points.

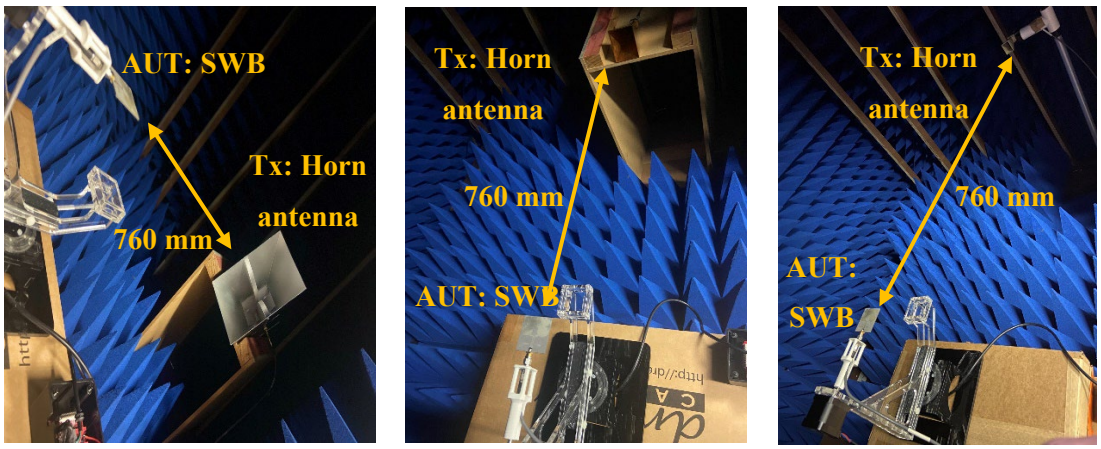

(a) *(b)* *(c)*

Figure 4- 19 Radiation pattern measurement setup: (a) Tx horn antenna: (JH-H-18G-18-SMAJ-AL) operates over (800 MHz- 18 GHz) with (3-18) dBi gain; (b) Tx horn antenna: Mi-Wave's K-Band Horn Antenna 261K-15/595 (WR-42) which operates over (18 – 26.5) GHz with (15) dBi gain; (c) Tx antenna: U233A1 Maury Microwave (WR-28) operates over (26.50 to 40) GHz with (15) dBi.

Following the conclusion of each measurement, the control application displays a 3D power capture of the antenna positioner. This is done to verify the successful completion of all measurement points, and to view the 3D radiation pattern at 3.8 GHz as depicted in Figure 4-20.

The antenna's radiation pattern, as suggested, is assessed in both the E-plane (YZ-plane, φ=90°) and the H-plane (XZ-plane, φ=0°) at various frequency points, as illustrated in Figure 4-21. The pattern demonstrates an omnidirectional configuration in the E-plane and a nearly isotropic configuration in the H-plane at lower frequencies. However, as the frequency increases, the pattern degrades due to the presence of higher-order modes. Measured results showed a good agreement with the simulated one at several resonant frequencies with stable radiation pattern across the encompassed bandwidth. The Co- and Cross-polarization radiations patterns at 3.8 and 33.8 GHz are illustrated in Figure 4-22 (a, b), respectively. The proposed antenna demonstrates low cross-polarisation levels in both E and H plane over the covered bandwidth. Hence, the radiation of the proposed antenna in the undesired direction is minimum and a polarisation purity (Co- to Cross polarisation radiation) of 40 dB and 20 dB in the H-plane are achieved at 3.8 and 33.8 GHz, respectively. So, achieving high polarisation purity is one of the requirements for high performance SWB antenna.

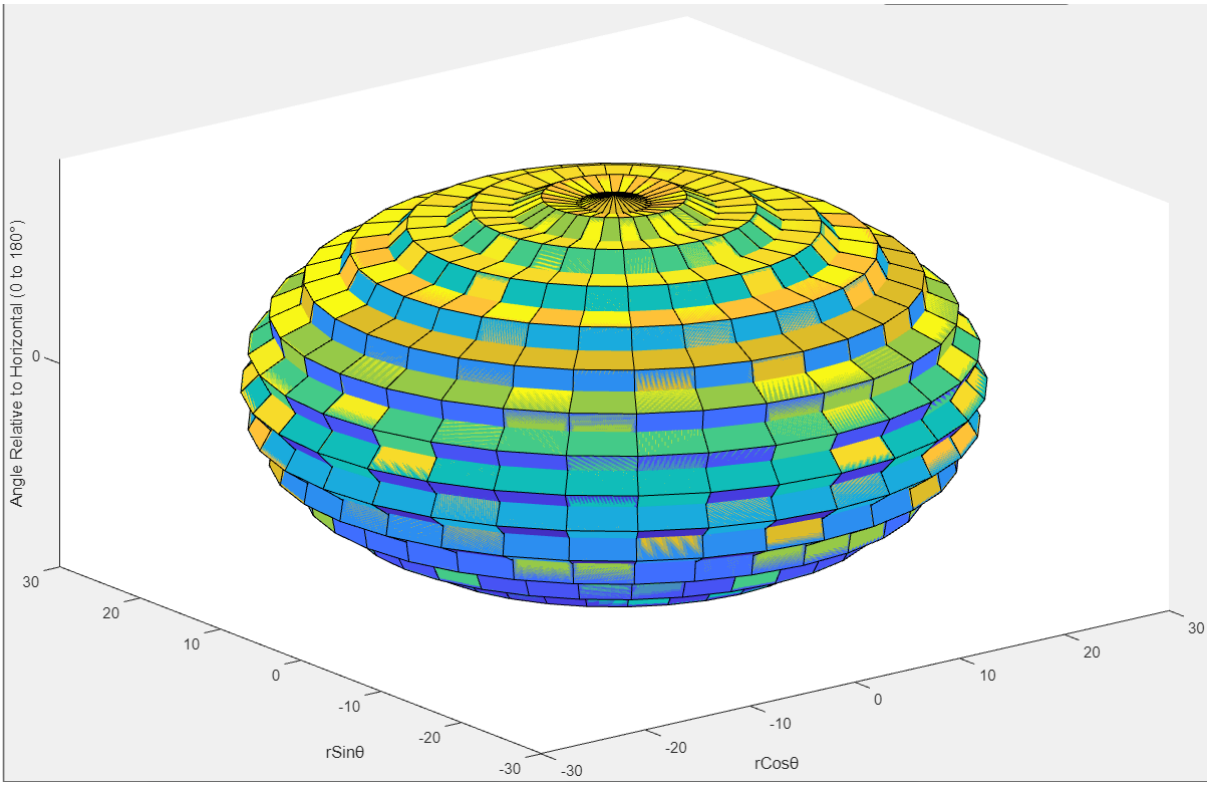

Figure 4- 20 3D power capture by antenna positioner at 3.8 GHz.

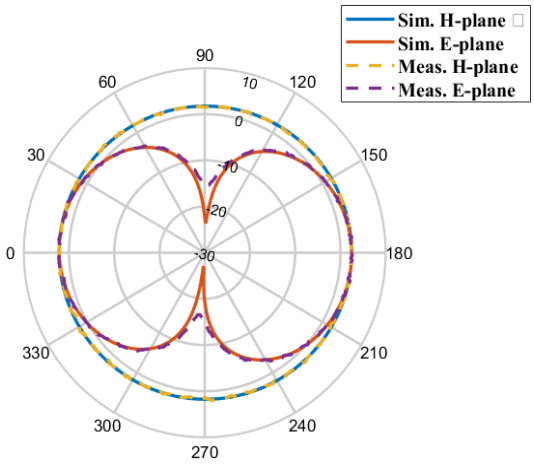

(a) 3.8 GHz

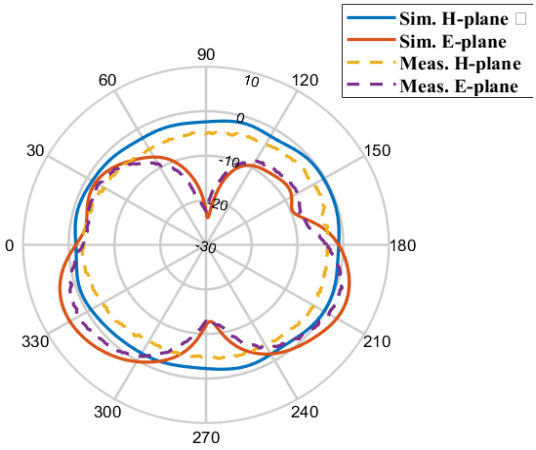

(b) 7 GHz

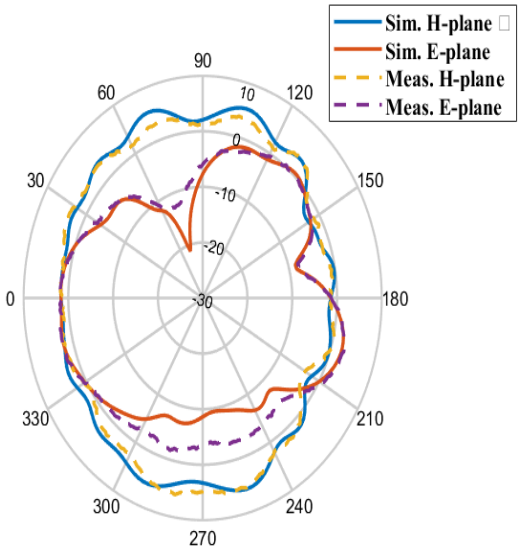

(c) 9.8 GHz

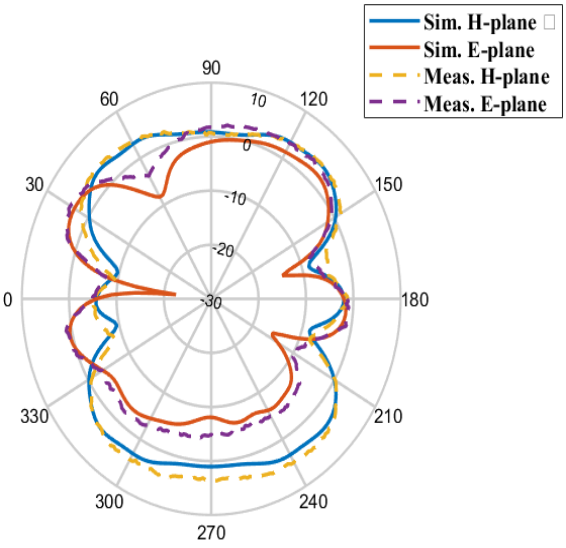

(d) 12.5 GHz

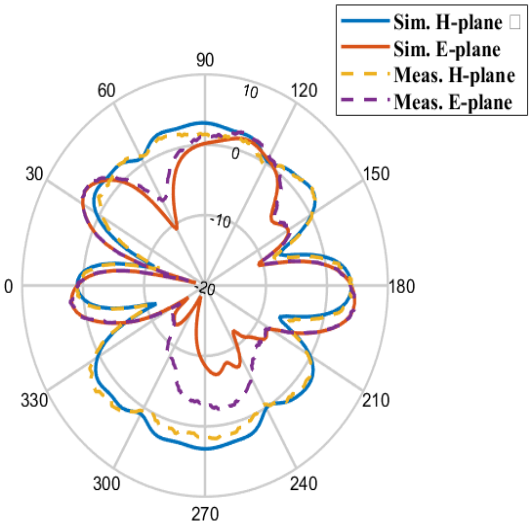

(e) 14.5 GHz

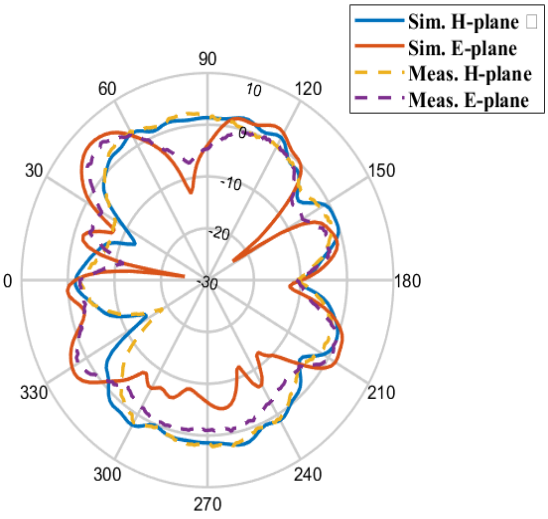

(f) 18.4 GHz

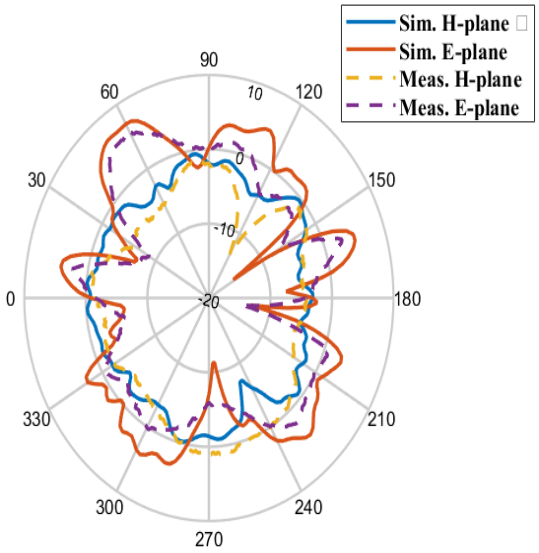

(g) 21 GHz

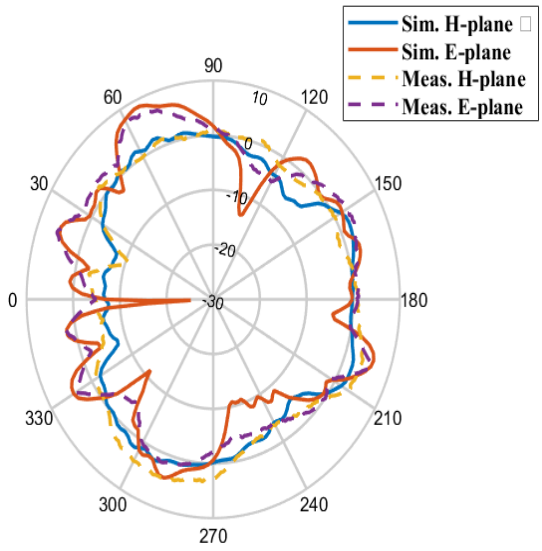

(h) 26.9 GHz

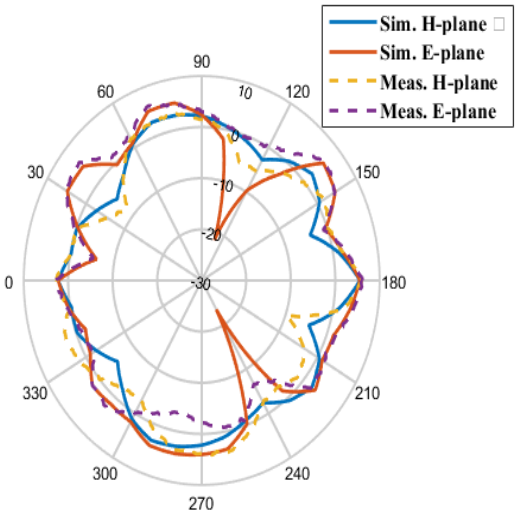

(i) 30.4 GHz

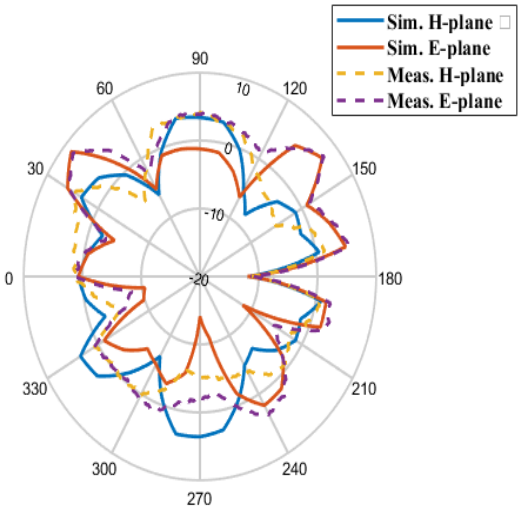

(j) 34 GHz

Figure 4- 21 2D simulated and measured radiation pattern at different frequencies (a-j).

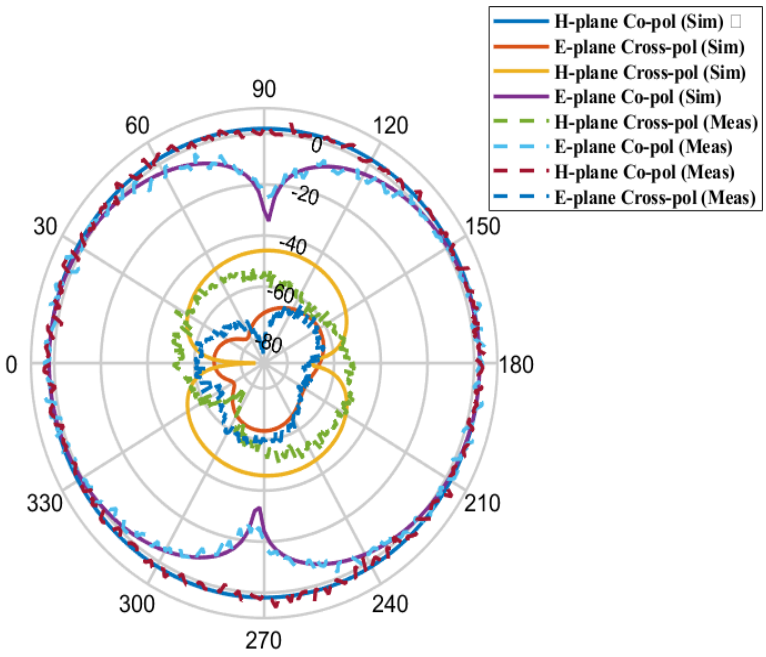

(a)

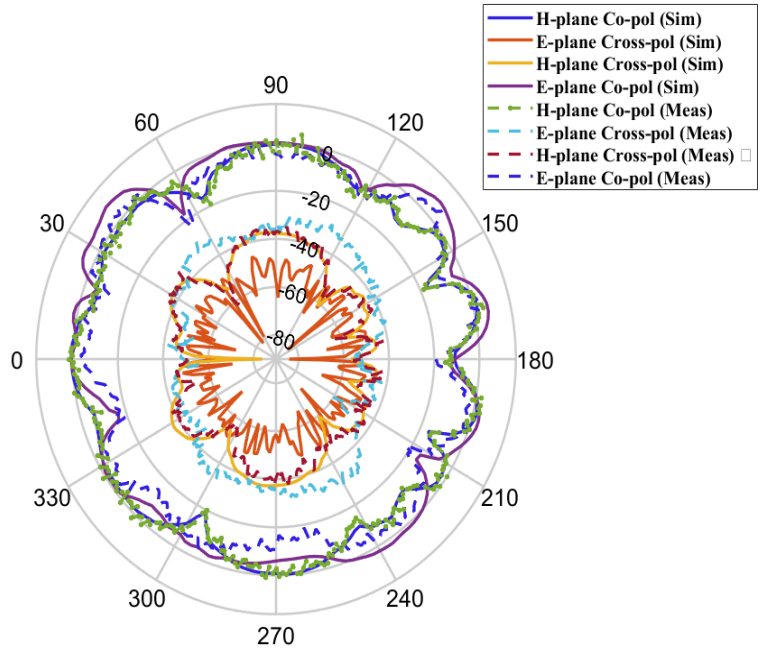

(b)

Figure 4- 22 Simulated and measured (Co- and Cross polarisation) radiation patterns (b) 3.8 GHz; (c) 33.8 GHz.

4.5.5 Surface Current Distribution

The sub-figures (a)-(g) in Figure 4-23 display current distributions at various frequencies. The notable concentration of current in the feedline offers insights into the mode variation. At the lowest operational frequency, which is 3.8 GHz, a first-order harmonic

resonance (fundamental mode) is clearly observed in Figure 4-23 (a). Referring to that, it becomes apparent that the radiated power predominantly confines itself to the antenna's front side. This is attributed to the concentration of current along the lower side of the fractal slot loaded radiator. In Figure 4-23 (b), the second-order harmonics become tangible, with the current distribution primarily focused on the lower portion of the radiating patch. Additionally, current also propagates around the lower segments of the fractal slots, as depicted in Figure 4-23 (b). This propagation gives rise to a standing wave formation around the top section of the radiator, resulting in a radiating null at the antenna's top, relative to what occurs at the first resonant frequency of 3.8 GHz. At the spurious resonant mode 10 GHz that shown in Figure 4-23 (c), the current concentrated more at the lower circular edges of the radiation increasing the size of the radiating null at the top of the antenna. In this scenario, the antenna's far-field pattern continues to exhibit a donut-shaped structure, with the majority of radiated power concentrated around the antenna's front side and the upper section of the radiator. As the frequency increases, higher-order modes begin to be clear, as evidenced by the current distribution at 14.8, 21.8, 26.8 and 33.7 GHz in Figure 4-23 (d-g), leading to a complex distribution along the antenna structure due to the effect of standing waves. Consequently, current predominantly traverses various distributed locations along the edges of the tapered radiator, resulting in significant null points in the current on the radiator's surface. As depicted in Figure 4-21 (j), this sheds light on the degradation in the radiation pattern at 34 GHz.

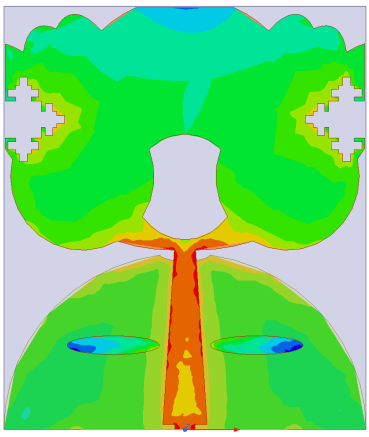

(a)

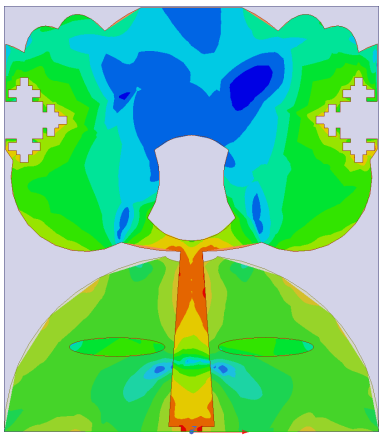

(b)

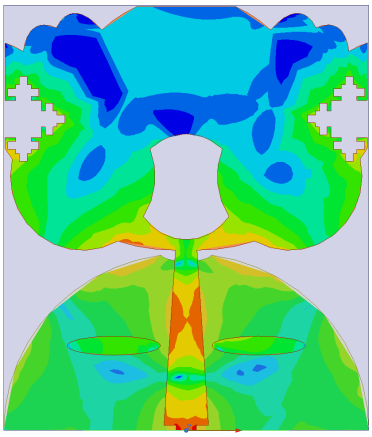

(c)

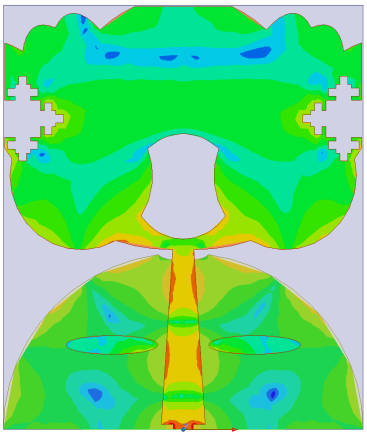

(d)

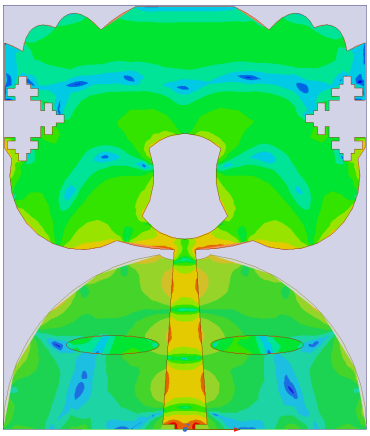

(e)

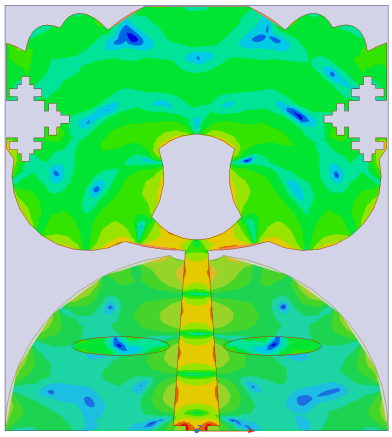

(f)

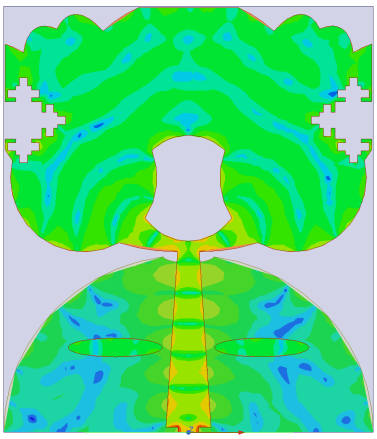

(g)

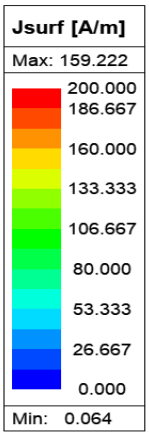

Figure 4- 23 Surface current distribution at different resonant frequencies (a) 3.8 GHz; (b)7.6 GHz; (c) 10 GHz; (d)14.8 GHz; (e)21.8 GHz; (f)26.8 GHz; (g) 33.7 GHz.

4.6 Equivalent Circuit Modelling and Optimization for Fractal Slot Loaded Super Wideband Antenna

The equivalent circuit model (ECM) is constructed based on individual behaviour of each antenna element. Further, a dual sequential optimisation approach is proposed to find the optimal value of each lumped element. The modeled results are compared with both full-wave simulated and measured results, and show that the proposed model can accurately capture the antenna behaviour with a low mean absolute percentage error of 4.9%, 7.5%, and 7.7% for $|S_{11}|$, real, and imaginary impedance, respectively, over the super-wide operating bandwidth.

4.6.1 SWB Antenna Geometry and Circuit Modelling

This section presents the ECM of our SWB antenna, its parameter extraction, and the circuit model's validation. The geometry of the antenna and circuit model for each component part of the antenna are shown in Figure 4-24. The antenna is fabricated on RT5870 substrate (ε_r = 2.33, $tan\delta$ = 0.0012) with physical dimensions of 40 × 35 × 1.57 mm^3. The ECM is developed by analysing the antenna's structure and electromagnetic (EM) properties. It comprises several components, each having a certain influence on the antenna's performance. The primary component is the radiating patch, which plays a vital role in emitting EM waves. It functions as a pass band filter and can be modelled as a parallel RLC branch with a series inductor that corresponds to the inductive nature of the radiating patch at high frequencies [27, 121, 122]. The parallel resistor and inductor represent the loss, and inductive properties in the patch element, respectively; and the parallel capacitor represents the capacitance between the patch and ground plane as shown in Figure 4-24 (a). The feed configuration has a rectangular and tapered feedline that contribute to the inductive nature of the patch [123]. The tapered feedline alters the impedance matching between the top and bottom of the microstrip line. Three series inductors and a parallel capacitor depict this change in the transmission line as displayed in Figure 4-24 (b). The antenna's resonance changes when a notch is incorporated into the patch and ground. A parallel LC circuit is used to model the equivalent circuit of the slots in the middle of the circular patch (Figure 4-24 (c)) and the elliptical slots in the ground (Figure 4-24 (d)) [124]. A parallel RLC branch corresponds to the two elliptically shaped parasitic elements were introduced on either side of the tapered feedline (Figure 4-24 (e)). These elements are not directly connected electrically

to the patch; instead, they resonate in response to the radiator's influence.

Fractal slots, which are duplicating rectangular slots of different dimensions are added to both sides of the rectangular patch. The inclusion of fractal slots enhances the antenna's bandwidth but complicates its ECM. Each added block forming the fractal slots represents a parallel resonant circuit [125], which acts as a bandpass filter that allows specific frequencies to pass while attenuating others. As each fractal slot consists of 10 rectangles, it is modelled as 10 branches of parallel RLC. With 2 fractal slots on each side of the circular patch, 20 parallel RLC circuits will be needed in the ECM.

The evolution process of the proposed ECM is presented in Appendix D Table 5, starting from stage 0 which is corresponding to antenna 0 geometry up to stage 8 (final ECM) which is corresponding to antenna 8 (final design). Each stage of the ECM is optimized up to 20 GHz and compared with the simulated result obtained by the related antenna structure. In stage 0 we present the circular patch by parallel $R_c L_c C_c$ and series inductor L_{f1}. Then after incorporating the tapered feedline in stage 1, the series inductors are combined into L_{f5}. Three intersecting ellipses are added to the circular patch on both sides in stage 2, each ellipse is represented by parallel RLC branch. Since the added ellipses are symmetrical, we can assemble the six RLC branches into three equivalent RLC branches ($R_{e1} L_{e1} C_{e1}$… $R_{e3} L_{e3} C_{e3}$). In stage 3, a polygon is added to the circular patch which is represented as parallel $R_{Po} L_{Po} C_{Po}$ branch. Additionally, in stage 4 a circular slot is included in the radiator which corresponds to parallel $L_P C_P$ branch in the corresponding ECM. Moreover, two circles are added to the patch in stage 5 and a parallel $R_{ci} L_{ci} C_{ci}$ branch is added to the corresponding ECM to represent the additional electrical length of the main radiator. In stage 6, to avoid complexity, we combine all parallel RLC branches into one equivalent parallel branch $R_{Pa} L_{Pa} C_{Pa}$ that represents the patch without affecting the ECM's effectiveness in representing the antenna behaviour. Then, in this stage, two fractal slots are loaded on the upper corners of the patch that can be represented as 10 parallel RLC branches. Then, in stage 7 a feedline and ground slots are included in the antenna structure which can be represented as parallel $L_G C_G$ branch in the corresponding ECM. Finally, in stage 8 two elliptical parasitic elements are added to the ECM as a parallel RLC branch which is also represented inside the equivalent $R_{Pa} L_{Pa} C_{Pa}$ branch.

4.6.2 Lumped Element ECM of SWB Antenna

To simplify the ECM, the 20 parallel RLC circuits can be assembled into 10 equivalent parallel RLC branches ($R_1L_1C_1$… $R_{10}L_{10}C_{10}$), as shown in Figure 4-24 (f). This simplification is possible because the fractal slots are identical and have the same dimensions. Then, the two parallel branches are assembled ($R_{pa}L_{pa}C_{pa}$ and $R_{pr}L_{pr}C_{pr}$) into one parallel $R_{11}L_{14}C_{13}$ branch. The parallel LC branches (L_pC_p and L_gC_g) are further assembled into one parallel $L_{11}C_{11}$ branch. Moreover, the feedline inductors L_{f3} and L_{f4} are combined into L_{f5}. For more simplification L_{f5} and L_{f1} are assembled into L_{13}. In this case the full circuit configuration is presented in Figure 4-25, where C_f corresponds to C_{12} and L_{f2} corresponds to L_{12}.

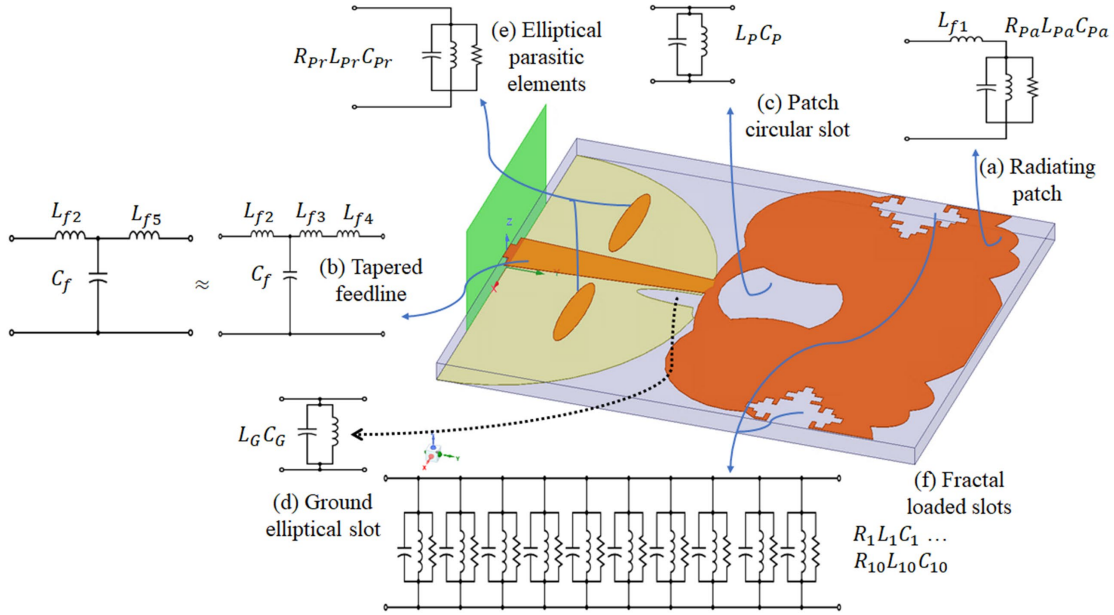

Figure 4- 24 SWB antenna geometry and circuit model of each element.

Figure 4-25 shows the full lumped element ECM of our SWB antenna. Several goals are defined as input to our optimisers as shown in Table 4-2, which are the main resonant frequencies and their respective $|S_{11}|$ values obtained from simulated results to enable finding the best path that matches the real antenna performance.

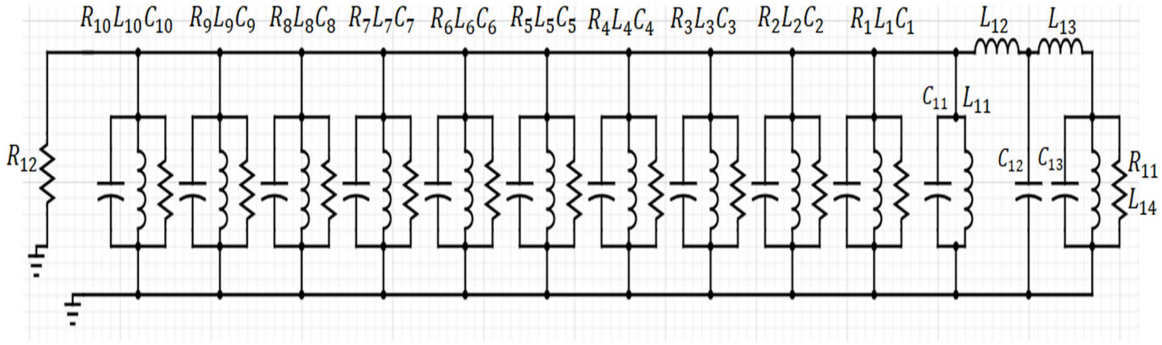

Figure 4- 25 Lumped element ECM of our SWB antenna.

Gradient and Quasi-Newton are the optimization methods used herein to find the optimal lumped element values of our ECM that best fit the measured data using ADS. They mainly differ in how the lumped element values are updated during optimization. The Gradient method computes a cost function for the importance of the lumped elements and updates their values in the direction of the gradient (steepest descent). This method tends to converge quickly to a local minimum, and can be sensitive to the initial values and step size used for updating the importance. We choose the following initial values (*R*=0.001 Ω, *L*=0.001 nH, *C*=0.001 pF) with 0.1 GHz step size. We set the number of iteration (the improvement in the error function) to 1000, in this method we define the seven goals presented in Table 2. A limit line is defined for each goal which contains the acceptable response for each goal based on the $|S_{11}|$ values extracted from the EM simulator. Each limit line will contain the type of relationship between the limit line Min/Max and the response, in addition to the Weight Factor (WF) for the limit line (in this method we assign 1 as a WF for all limit lines). The actual WF used in the error function calculation for the limit line is the product of the goal WF and the limit line WF. So, for example if more efforts need to put on one goal, the weight factor can be increased to value more than 1. Quasi-Newton method, on the other hand, approximates the Hessian matrix to compute the direction of steepest descent. This approximation can allow a more efficient update of the lumped element values, leading to a faster convergence, as it considers the curvature of the cost function. It is used as the second optimizer to tune the ECM after the Gradient method in our dual sequential optimization for better matching performance. In this optimization method the least square error function is used as the Error Calculation Function (ECF), the cost function, to achieve the desired performance as shown in Equation (4.8). The resulting optimal optimized lumped element values for our ECM are listed in Table 4-3.

Table 4- 2 *Defined Goals for Optimizers*

Goal #	$\lvert S_{11} \rvert$ (dB)	Frequency (GHz)
1	-36	3.8
2	-40.8	7.6
3	-28.5	10
4	-34.9	14.8
5	-24.8	21.8
6	-29.2	26.8
7	-20	33.7

$$ECF = \sum_{all\ goals} W_i \times |s_i - g_i|^2 \tag{4.8}$$

where W_i is the ith goal weighing factor, s_i is the ith frequency dependent response that is being optimized, and g_i is the ith goal value that is the optimization criterion corresponding to over the defined frequency range. ECF is calculated by evaluating the error for each goal at each frequency point individually and then the magnitude of the error is squared.

In addition to numeric and simulated results obtained from our ECM, and a full-wave simulator (HFSS), respectively, the fabricated SWB antenna have been measured using an Anritsu S820E vector network analyser in an anechoic chamber (Figure 4-26). Figure 4-27 compares the obtained $|S_{11}|$ performance, which reveals a good agreement between the modelled, simulated, and measured results. Figure 4-28 shows their average root-mean-square error (RMSE) and mean absolute percentage error (MAPE), where a low RMSE of 0.041 and MAPE of 4.9% error are observed, proving the accuracy of the presented model and the chosen optimisers.

Table 4- 3 *Optimal Lumped Element Values for ECM*

Parameter	Value	Parameter	Value	Parameter	Value
R_1	142.428	L_2	6.54311	C_1	0.0028622
R_2	37.3572	L_3	16.3512	C_2	0.49568
R_3	214.458	L_4	1498.73	C_3	0.003439
R_4	2.09613	L_5	2.54945	C_4	0.0074975
R_5	47.9401	L_6	7.40719	C_5	0.420298
R_6	66.8471	L_7	5.95808	C_6	0.0130909
R_7	75.2988	L_8	0.23312	C_7	0.0599383
R_8	70.2402	L_9	2.35217	C_8	0.116726
R_9	57.4437	L_{10}	12.354	C_9	0.0724266
R_{10}	86.2334	L_{11}	4.407	C_{10}	0.0580042
R_{11}	102.605	L_{12}	539.038	C_{11}	0.0816123
R_{12}	50	L_{13}	535.601	C_{12}	103.421
L_1	13.0044	L_{14}	359.686	C_{13}	310.32604

Note: Units of parameters: R (Ω); L (nH); C (pF)

4.7 Simplified ECM Using Transmission Line Theory

In this section, transmission line theory is applied to the ECM of our SWB antenna for simplifying its structure as shown in Figure 4-29. This simplification reduces the complexity of the antenna's behaviour to a few key parameters R, L, G, and C, which often lead to reduce the computational requirements. Moreover, with the simplified model it becomes easier to predict the antenna's performance and make design modifications. The simplification process is achieved by assembling the 10 parallel RLC branches ($R_1L_1C_1$… $R_{10}L_{10}C_{10}$) representing the fractal slot effect into one equivalent branch $R_{eq}L_{eq}C_{eq}$. Distributed transmission line parameters R, L, G, and C, are used to

determine the equivalent circuit elements as follows:

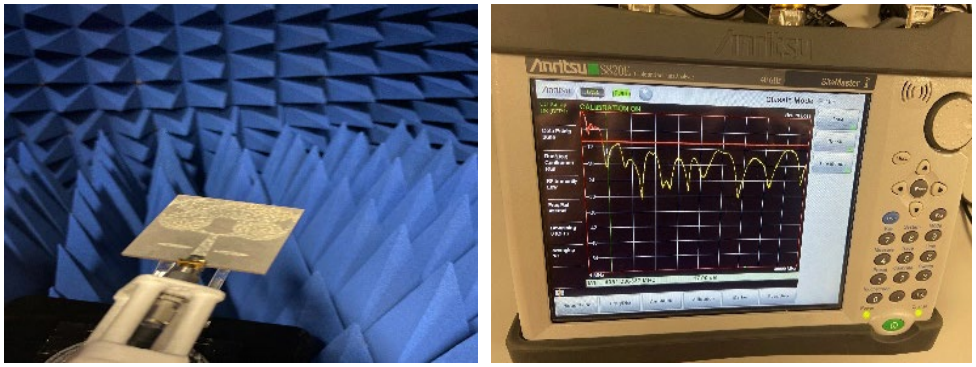

(a) *(b)*

Figure 4- 26 (a) SWB antenna measurement in anechoic chamber; (b) Return loss measured using VNA.

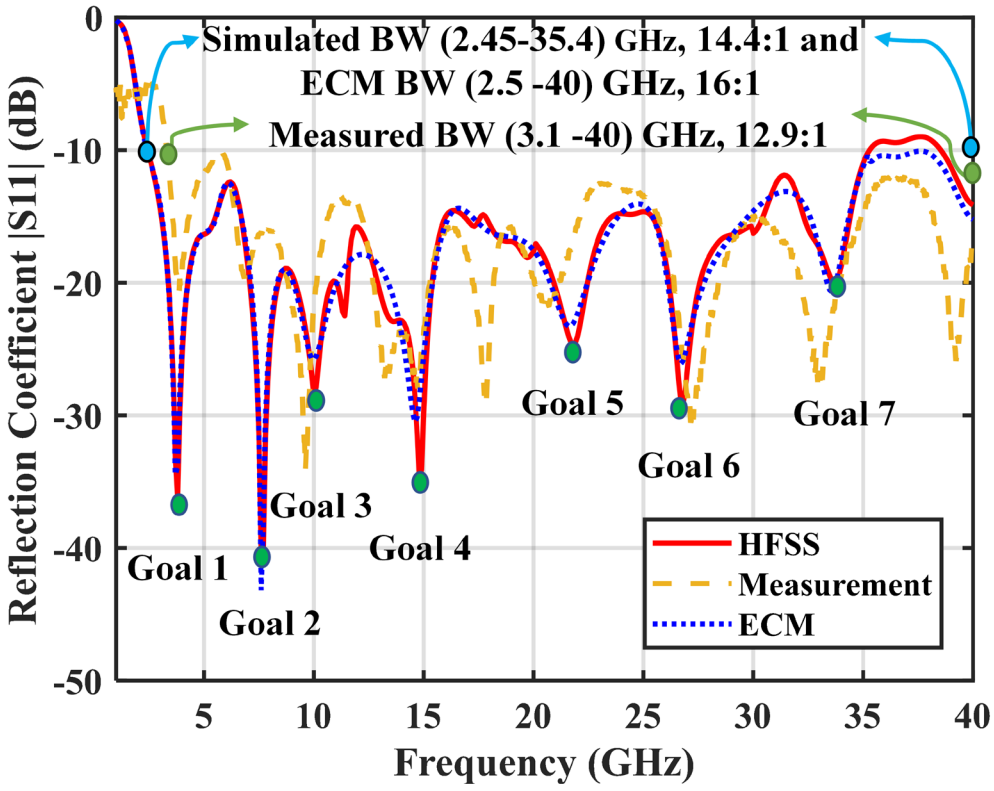

Figure 4- 27 Comparison between modelled, simulated, and measured $|S_{11}|$ over frequency.

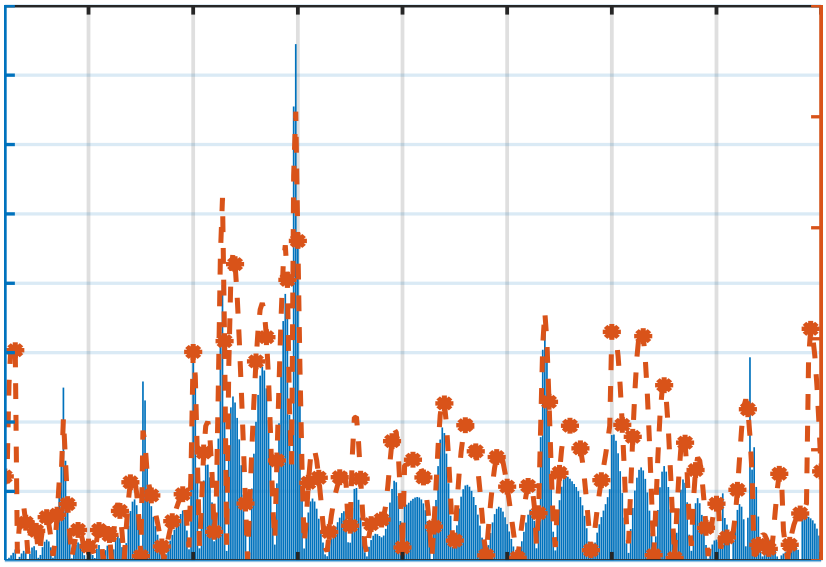

Figure 4- 28 RMSE and MAPE between modelled and simulated $|S_{11}|$ over frequency.

$$R_{eq} = \frac{1}{\sum_{i=1}^{10} 1/R_i} = 1.645107\ \Omega$$

$$L_{eq} = \frac{1}{\sum_{i=1}^{10} 1/L_i} = 0.1729425\ nH$$

$$C_{eq} = \sum_{i=1}^{10} C_i = 1.2499628\ pF$$

$$G_{eq} = \frac{1}{R_{eq}} = 0.6078632\ S$$

Begin by applying Kirchhoff's voltage law into the circuit in Figure 4-29 where z and Δz represents the length, and differential length element of the transmission line, respectively:

$$V(z) - I(z)R_{12}\Delta z - I(z+\Delta z)j\omega L_{12}\,\Delta z - I(z+\Delta z)j\omega L_{13}\Delta z - V(z+\Delta z) = 0 \quad (4.9)$$

Rearranging (4.9) to separate the voltage and current terms and dividing it by Δz:

$$\frac{V(z+\Delta z) - V(z)}{\Delta z} = -\frac{I(z)R_{12}\,\Delta z}{\Delta z} - \frac{I(z+\Delta z)j\omega(L_{12}+L_{13})\,\Delta z}{\Delta z}$$

The limit as $\Delta z \to 0$:

$$\frac{\partial V(z)}{\partial z} = -I(z)\big(R_{12} + j\omega(L_{12} + L_{13})\big) \quad (4.10)$$

Next, applying Kirchhoff's current law to the circuit in Figure 4-29:

$$I(z) - V(z+\Delta z)(G_{eq} + G_{11})\,\Delta z - V(z+\Delta z)\,j\omega\left(C_{eq} + C_{11} + C_{12} + C_{13}\right)\Delta z - \frac{V(z+\Delta z)}{j\omega\left(L_{eq} + L_{11} + L_{14}\right)\Delta z} - I(z+\Delta z) = 0 \quad (4.11)$$

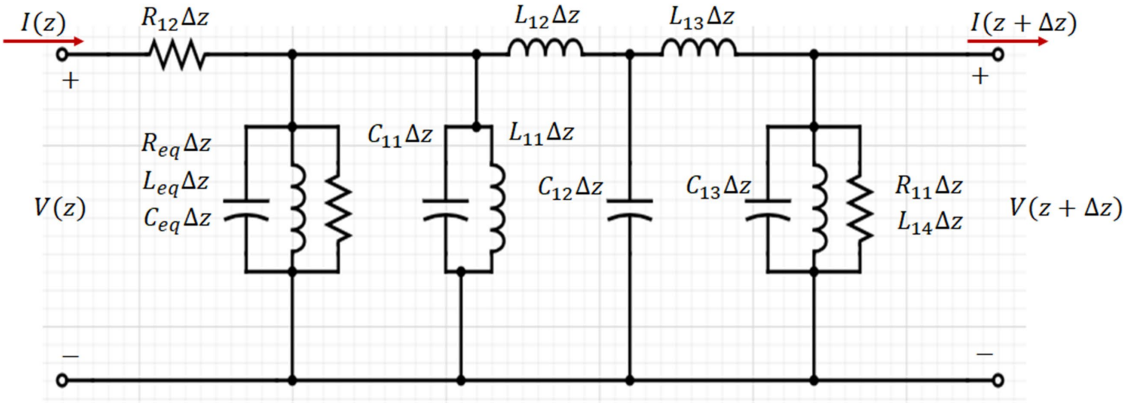

Figure 4- 29 Simplified ECM circuit using transmission line theory.

Likewise, rearranging (4.11) to separate the current and voltage terms and dividing it by Δz:

$$\frac{I(z+\Delta z)-I(z)}{\Delta z} = -V(z+\Delta z)\left[\left(G_{eq} + G_{11}\right) + j\omega\left(C_{eq} + C_{11} + C_{12} + C_{13}\right) + \frac{1}{j\omega\left(L_{eq}+L_{11}+L_{14}\right)}\right]\frac{\Delta z}{\Delta z}$$

Similarly, the limit as $\Delta z \to 0$

$$\frac{\partial I(z)}{\partial z} = -V(z)\left[\left(G_{eq} + G_{11}\right) + j\omega\left(C_{eq} + C_{11} + C_{12} + C_{13}\right) + \frac{1}{j\omega\left(L_{eq}+L_{11}+L_{14}\right)}\right]$$

Considering the term $\frac{1}{j\omega\left(L_{eq}+L_{11}+L_{14}\right)}$ to be negligible (≈ 0) as $\omega\left(L_{eq} + L_{11} + L_{14}\right) \gg 1$:

$$\frac{\partial I(z)}{\partial z} = -V(z)\left[\left(G_{eq} + G_{11}\right) + j\omega\left(C_{eq} + C_{11} + C_{12} + C_{13}\right)\right] \quad (4.12)$$

Since the work is presented in the frequency domain, the general solution of (4.10) and (4.12) are exponential functions. Thus, these can be rewritten as a set of exponential functions related to the wave propagation in the transmission line as follows:

$$V(z) = V_o^+ e^{-\gamma z} + V_o^- e^{\gamma z} \quad (4.13)$$

$$I(z) = I_o^+ e^{-\gamma z} + I_o^- e^{\gamma z} \quad (4.14)$$

where γ is the propagation constant, and their ratio gives the characteristic impedance (Z_o). Rearranging (4.10) to obtain an expression for the current and evaluating the partial derivative:

$$I(z) = -\frac{1}{(R_{12}+j\omega(L_{12}+L_{13}))}\frac{\partial V(z)}{\partial z}$$

$$= -\frac{1}{(R_{12}+j\omega(L_{12}+L_{13}))}(V_o^+(-\gamma)e^{-\gamma z} + V_o^-(\gamma)e^{\gamma z})$$

$$= \frac{\gamma}{(R_{12}+j\omega(L_{12}+L_{13}))}(V_o^+e^{-\gamma z} - V_o^-e^{\gamma z}) \quad (4.15)$$

where $\gamma = \sqrt{[R_{12}+j\omega(L_{12}+L_{13})]\left[\left(G_{eq}+G_{11}\right)+j\omega\left(C_{eq}+C_{11}+C_{12}+C_{13}\right)\right]}$. Then Z_o can be found as:

$$Z_o = \frac{V(z)}{I(z)} = \sqrt{\frac{R_{12}+j\omega(L_{12}+L_{13})}{\left(G_{eq}+G_{11}\right)+j\omega(C_{eq}+C_{11}+C_{12}+C_{13})}} \quad (4.16)$$

To find the impedance at the first resonant frequency (3.8 GHz) of our SWB antenna, this frequency can be substituted into (4.16) and obtain $Z_o = 50.81 + j1.53\ \Omega$, which is very close to the simulated Z_o as shown in Figure 4-30. The corresponding impedance errors depicted in Figure 4-31, show an RMSE of 0.254 and MAPE of 7.7% for the imaginary part, while an RMSE of 0.243 and MAPE of 7.5% are noted for real impedance. Results confirm that our simplified ECM can still effectively model the characteristics of our SWB antenna.

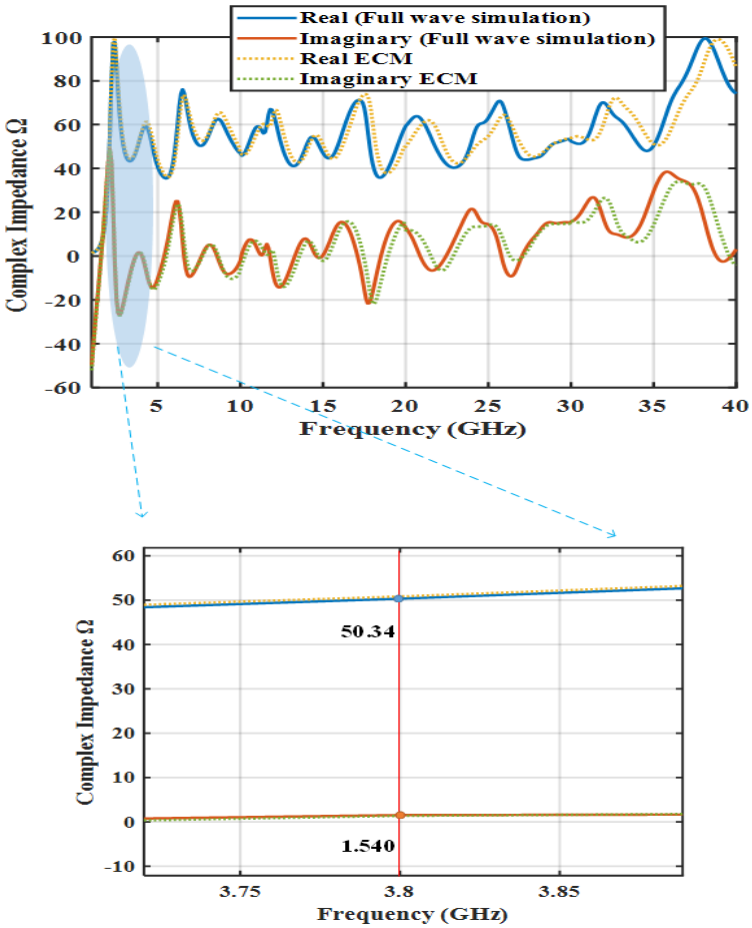

Figure 4- 30 Simulated complex impedance Z_o of our SWB antenna over frequency.

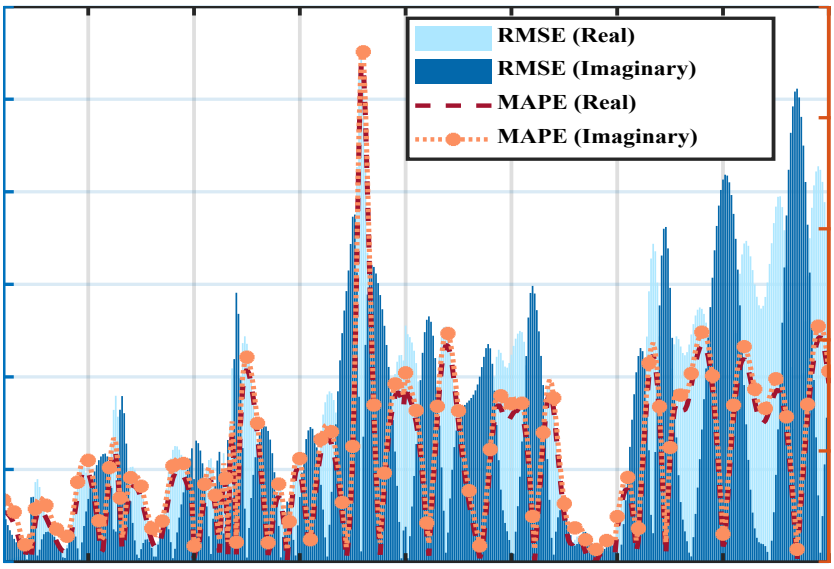

Figure 4- 31 RMSE and MAPE between modelled and simulated complex impedance Z_o of our SWB antenna over frequency.

4.8 Summary

This chapter discusses the evolution stages of the final configuration of the proposed SWB antenna along with the optimised parametric study of different physical parameters. It also investigates the efficacy of the proposed SWB antenna in medical imaging applications in terms of several key performance parameters. Different measurement setups were employed to verify the capability of the fractal slot loaded SWB antenna, results reveal that the proposed antenna fulfils the key characteristics for medical imaging application in terms of 36.9 GHz covered bandwidth, (3.4-9.7) dBi gain, 94% average radiation efficiency and stable radiation pattern over the operating bandwidth (3.1-40) GHz. Moreover, it explores the effectiveness of lumped-element modelling based on transmission line theory in predicting and analysing the characteristics of a custom-designed SWB antenna. It also investigates the effectiveness of dual sequential optimisation based on Gradient and Quasi-Newton methods for extracting the optimal lumped element values. The resulting ECM accurately produces the antenna's characteristics such as reflection coefficients and complex impedances over a super-wide operating bandwidth.

Chapter 5 Early-Stage Lung Tumour Detection based on Super-Wideband Microwave Reflectometry

5.1 Introduction

This chapter aims to detect early-stage lung tumours in deep-seated and superficial locations, and to precisely measure the size of the detected tumour using non-invasive microwave reflectometry over a super-wideband (SWB) frequency range. Human lung phantom and lung tumours are modelled using a multi-layer concentric cylinder structure, and spherical-shaped inclusions, respectively. Firstly, a study on the dielectric properties of human torso tissues is carried out over an SWB frequency range of 1–25 GHz based on the Cole-Cole dispersion model. Intensive full-wave simulations of the modelled phantom under irradiation by a custom-designed SWB antenna array are then performed. Results show that small tumour sizes from 5 mm radius in both deep-seated and superficial locations of the lung tissue can be detected based on the contrast of reflection coefficients and reconstructed images produced from backscattered signals between normal and anomalous tissues. The potential of using SWB microwave reflectometry to successfully detect the lung tumours in their early stages and at different depths of the lung tissue has been demonstrated.

The rest of this chapter is organized as follows. Section 5.2 reviews the related works. Section 5.3 investigates the human torso dielectric properties over the SWB frequency range. Section 5.4 models the human lung phantom and determines the optimal separation distance between antenna elements and the lung phantom. Section 5.5 simulates the lung phantom embedded with tumour at various locations and discusses the reflection coefficient results. The corresponding imaging results for deep-seated lung tumour are presented in Section 5.6. Following that, the experimental results of phantom properties and imaging setup are explored in section 5.7. Finally, Section 5.8 summarises the chapter.

5.2 Related Works

Generally, microwave reflectometry techniques are based on the dielectric contrast between healthy and unhealthy tissues due to the biological difference between normal and anomalous cells. Their performance depends highly on the employed antenna,

which is considered the key element in transmitting and receiving the backscattered signals from the target object. The antenna's parameters such as operating frequency range (bandwidth), peak gain, radiation efficiency, and radiation pattern are the leading factors that determine the capability and efficiency of microwave reflectometry systems. A large covered bandwidth with low S_{11} level (< −20 dB), high peak gain, and stable radiation pattern are the utmost desired characteristics when designing the system's antenna [19]. Several cancer types can be detected using microwave reflectometry with a proper selection of the operating frequency required for signal penetration into human tissues. Previous studies found that the best operating frequency range for detecting deep cancer types such as breast, brain, and lung cancers is between 1−5 GHz to achieve good penetration and accurate detection. In [48], the authors proposed two arrays with rectangular and spiral antennas with operating frequencies between 2−4 GHz for breast cancer detection. In [98], a reconfigurable metamaterial antenna was proposed and tested over the frequency range 2.5–3.2 GHz similarly for breast cancer detection. An ultra-wideband (UWB) antenna was further proposed in [39] to detect breast tumour over 2.3−11 GHz.

On the other hand, several researchers have studied the antenna types and frequency ranges for detecting brain injuries (stroke, haemorrhages, and tumours). In [100], the authors proposed a portable three-dimensional (3D) metamaterial antenna structure operating in the frequency range of 1.12–2.5 GHz to detect brain haemorrhage. A wearable head imaging system based on microwave reflectometry was presented in [36] with 12 antenna elements operating between 1−4 GHz. The resolution of the imaging system is highly related to the employment of large bandwidths and high frequencies. With high frequencies, a reduced penetration will be obtained, which is preferable for shallow cancer types such as skin cancer, where the required penetration inside human tissues is only a few millimetres (mm) [20]. Several enhancements to the antenna design in microwave reflectometry have also been introduced to improve system proficiency. Recent studies have incorporated UWB and SWB technologies in microwave reflectometry systems, leveraging on their high data rate, interference immunity, low profile, and cost-effective properties [7, 75, 80]. Tumour detection based on the contrast of reflection coefficients was introduced in [112, 126] for quick detection of head strokes with promising results.

5.3 Investigation of Human Torso Dielectric Properties

This research study has been accomplished in three work stages (WSs) as depicted in Figure 5-1. The first stage (WS1) conducted a study into the Cole-Cole dispersion model [103] to obtain the dielectric properties of human torso tissues over the SWB frequency range between 1-25 GHz. In WS2, two cylindrical structures were designed using High-Frequency Structural Simulator (HFSS) to model healthy and unhealthy (cancerous) instances of human lung based on the obtained dielectric properties from WS1. Finally, in WS3, we studied the effects of different tumour locations (deep-seated and superficial) on the tumour detection performance by the SWB microwave reflectometry system.

Since radio frequency (RF) signals can penetrate various human body layers with different dielectric characteristics, it is crucial to design a precise human tissue model to assess the backscattered signals from different tissue layers reliably. In this study, a human lung phantom has been modelled using five cylindrical layers: skin, fat, muscle, rib bone (cancellous), and lung (inflated). Each layer has a specific thickness and frequency-dependent dielectric properties that can be found over our frequency range of interest (1–25 GHz) for the proposed SWB microwave reflectometry system using the well-known Cole-Cole model [90] based on the experimental data of human tissues. The Cole-Cole model has four dispersion regions with different relaxation parameters that could depict the superposition of different relaxation processes of biological structure. So far, very few studies have been conducted on the dielectric properties of torso tissues over the SWB frequency range.

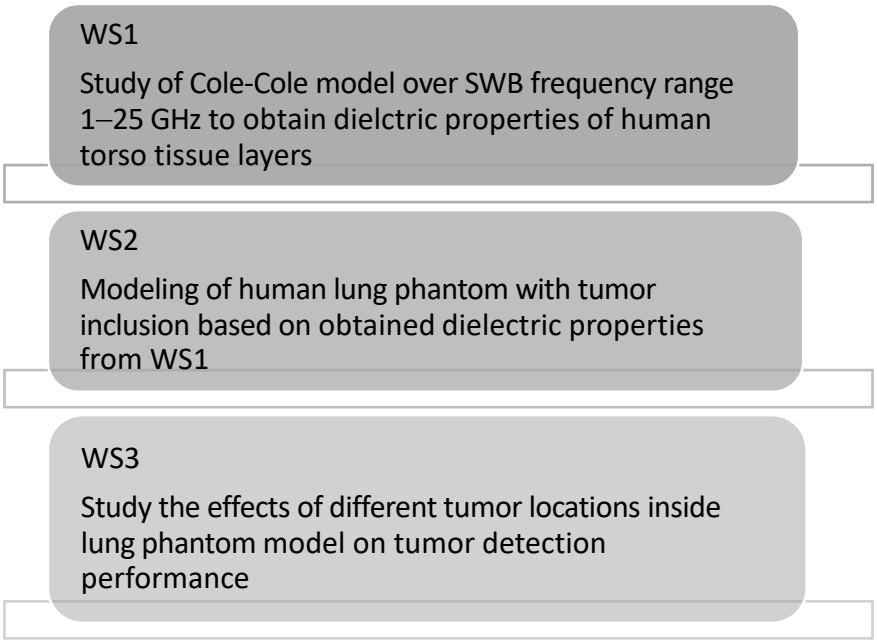

Figure 5- 1 Workflow stages for this study.

The dielectric properties of human tissues vary with signal frequency due to the frequency-dependent polarization of atoms, electrons, and ions caused by the E-fields in tissues. The following Cole-Cole equation can describe the frequency dispersion of the dielectric properties of human tissues:

$$\varepsilon(\omega) = \varepsilon_0 \left(\varepsilon_r - j\frac{\sigma}{\omega\varepsilon_0}\right) = \varepsilon_{s\,(n)} + \sum_n \frac{\Delta\varepsilon_n}{1 + (j\omega\tau_n)^{(1-\alpha_n)}} + \frac{\sigma_i}{j\omega\varepsilon_0} \qquad (5.1)$$

where ε, ε_r, and ε_0 are the relative complex permittivity, relative permittivity, and free space permittivity, respectively; σ_i is the static ionic conductivity; $\varepsilon_{s\,(n)}$, τ_n, and α_n are the static permittivity, relaxation time, and distribution parameter (a measure of dispersion broadening), respectively, where $n = \{1\ to\ 4\}$ is the index representing each of the four dispersion types in human tissues; and $\Delta\varepsilon_n = \varepsilon_{s\,(n+1)} - \varepsilon_{s\,(n)}$ denotes the dispersion magnitude. Using the parameter values in Table 5-1 for each tissue of the human torso [91, 127], their corresponding dielectric properties can be found using the Cole-Cole equation.

Table 5- 1 *Parameter values for each tissue of the human torso.*

Tissue	$\boldsymbol{\varepsilon_\infty}$	$\boldsymbol{\Delta\varepsilon_1}$	$\boldsymbol{\tau_1}$ $(\boldsymbol{ps})$	$\boldsymbol{\alpha_1}$	$\boldsymbol{\Delta\varepsilon_2}$ $(\boldsymbol{10^2})$	$\boldsymbol{\tau_2}$ $(\boldsymbol{ns})$	$\boldsymbol{\alpha_2}$	$\boldsymbol{\Delta\varepsilon_3}$ $(\boldsymbol{10^4})$	$\boldsymbol{\tau_3}$ $(\mu\boldsymbol{s})$	$\boldsymbol{\alpha_3}$	$\boldsymbol{\Delta\varepsilon_4}$ $(\boldsymbol{10^6}$	$\boldsymbol{\tau_4}$ $(\boldsymbol{ms})$	$\boldsymbol{\alpha_4}$	σ $(\boldsymbol{10^{-3}})$
Skin	4	39	7.96	0.1	2.8	79.58	0	3	1.59	0.16	0.03	1.592	0.2	0.4
Fat	2.5	3	7.96	0.2	0.15	15.92	0.1	3.3	159.15	0.05	10	7.958	0.01	10
Muscle	4	50	7.23	0.1	70	353.6	0.1	120	318.31	0.1	25	2.274	0	200
Rib bone	2.5	18	13.3	0.22	3	79.58	0.25	2	159.15	0.2	20	15.91	0	700
Lung	4.44	14.6	16.1	0.0001	6.46	3.22	0.181	2.2	159.15	0.18	10	7.958	0	84.2

The complex relative permittivity $\varepsilon(\omega)$ of each layer can be represented as $\varepsilon_r - j\varepsilon_r'$ where ε_r and ε_r' are the real part, and imaginary part, respectively, and their ratio $(\varepsilon_r'/\varepsilon_r)$ is defined as the loss tangent tanδ of each layer. Based on the above model, increasing the frequency decreases the relative permittivity, but increases the conductivity and loss tangent. From the above relations, the dielectric properties of unhealthy tissue (tumour) will be higher than healthy tissue due to their higher fluid content. The relative permittivity (ε_r), conductivity σ (S/m), loss factor (ε_r'), and loss tangent tanδ in the frequency range of interest (1–25 GHz) can be predicted as shown in Figure 5-2. The numerically obtained results for dielectric properties of human torso tissues are then compared with those measured in [90] at different frequency points, and a very good consistency is observed between them. Consequently, our results have addressed a knowledge gap in the investigation of human torso dielectric properties over SWB frequency range.

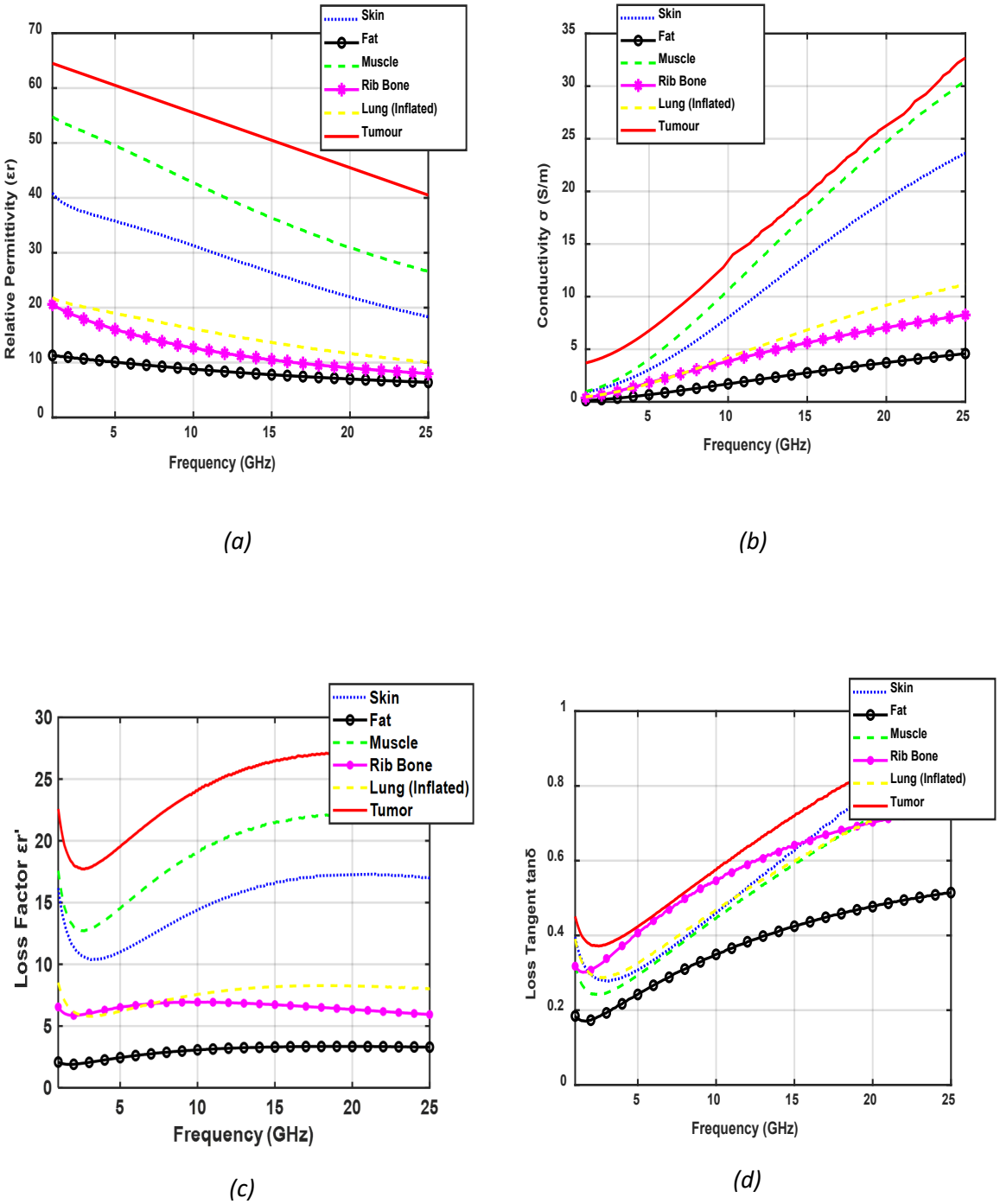

Figure 5- 2 Dielectric properties of human torso and tumour issues: (a) Relative permittivity; (b) Conductivity; (c) Loss factor; (d) Loss tangent.

5.4 Modelling of Human Lung Phantom

In literature, few works on lung cancer detection using microwave reflectometry can be found due to several limitations. One of them is the lack of studies on lung tissue dielectric properties. Another is the complexity of torso tissue layers that makes detection based on RF backscattered signals challenging. In this study, we chose 3.8 GHz

as the signal frequency for lung cancer detection based on contrast of reflection coefficients, as it provides good signal penetration into human tissues. The lung phantom was modelled as a concentric cylinder structure, each layer representing a single human torso tissue with properties given in Table 5-2. The lung phantom has dimensions of 82.31 cm circumference and 9 cm height, which mimic that of an adult human lung. In addition, a spherical inclusion of radius 5−15 mm was inserted into the phantom to represent an early-stage lung tumour as shown in Figure 5-3.

Table 5- 2 *Physical and dielectric properties of lung phantom with tumour inclusion.*

Tissue	Thickness (mm)	Relative dielectric constant ε_r	Conductivity σ (S/m)	tan δ
Skin	3	36.8	2.15	0.283
Fat	2	10.4	0.453	0.211
Muscle	20	51.2	2.74	0.259
Rib Bone	6	17.2	1.28	0.361
Lung	100	19.7	1.21	0.298
Tumour	5−15 (radius)	61.8	5.454	0.428

In this section, the optimal separation distance between array antenna elements and the lung phantom boundary is also investigated. Several simulations have been conducted using different separation distances (5, 10, 15 mm) between array elements and lung phantom along with simulation of array elements placed in free space. The results in Figure 5-4 show that the first resonant frequency of array in free space occurs at 3.8 GHz with return loss −32.31 dB. They also show that varying the distance between array elements and lung phantom will mainly affect the first resonant frequency and return loss level. For example, at 5 mm distance, the resonant frequency is shifted to lower value 3.6 GHz and return loss worsens to −30.5 dB due to the higher reflections from the high-permittivity skin layer. These strong reflections represent a clutter that can easily mask the tumour, particularly when it is deep-seated and still small during the early stage of disease. Increasing the distance to 15 mm resulted in shifting the resonant frequency to 3.5 GHz with return loss of −48 dB. Here, skin reflections are mitigated but the increased frequency shift mainly arises from the impedance mismatch between the

antenna array and lung phantom. On the other hand, at 10 mm distance, good impedance matching occurs at the boundary between lung phantom and array with the first resonant frequency at 3.8 GHz (same as in free space) and return loss level of −36.14 dB. This represents the optimal separation distance that minimizes skin reflection effect while achieving good impedance matching with lung phantom layer. All subsequent results were thus based on 10 mm separation distance in the simulation setup.

5.5 Lung Anomaly Detection Based on SWB Microwave Reflectometry

In this section, we will discuss the capability of SWB microwave reflectometry system in detecting lung anomaly, which can be caused by cancer or other conditions. In this work, we consider the anomaly to be caused by an early-stage tumour of 15mm radius at different locations of the lung. The detection setup consists of a custom-designed eight-element SWB antenna array [25] operating in the frequency range of 1–25 GHz, 12 dBi peak gain at boresight, and stable radiation pattern over the covered bandwidth. The proposed antenna resonates at 3.8 GHz with a −36.2 dB return loss ($|S_{11}|$). Figure 5-5 shows the setup configuration around the lung phantom at a 10 mm distance from the outermost skin layer. In pursuance of achieving low mutual coupling (< −20 dB) with enhanced isolation between adjacent array elements, the array elements are spaced 45˚ apart with 75.7 mm edge-to-edge separation between adjacent elements. Considering the signal wavelength λ at 3.8 GHz is 78.9 mm, the spacing ratio between array elements is 75.7/78.9 = 0.959, which is approximately equal to λ.

Figure 5-6 shows the mutual coupling between the eight array elements in terms of their forward transmission coefficients. For improved readability, we plotted only the forward transmission coefficients from antenna 1 to all other array elements (2-8), as representative of the array's transmission performance, since we found each of the other array elements to exhibit a similar performance trend. The results confirm the low mutual coupling between adjacent array elements, resulting in high isolation. In fact, all transmission coefficients Sij (where i and j = {1 to 8}; i ≠ j) between eight array elements are less than −30 dB over the covered bandwidth. Furthermore, the presence or absence of the tumour inclusion does not seem to impact the isolation performance.

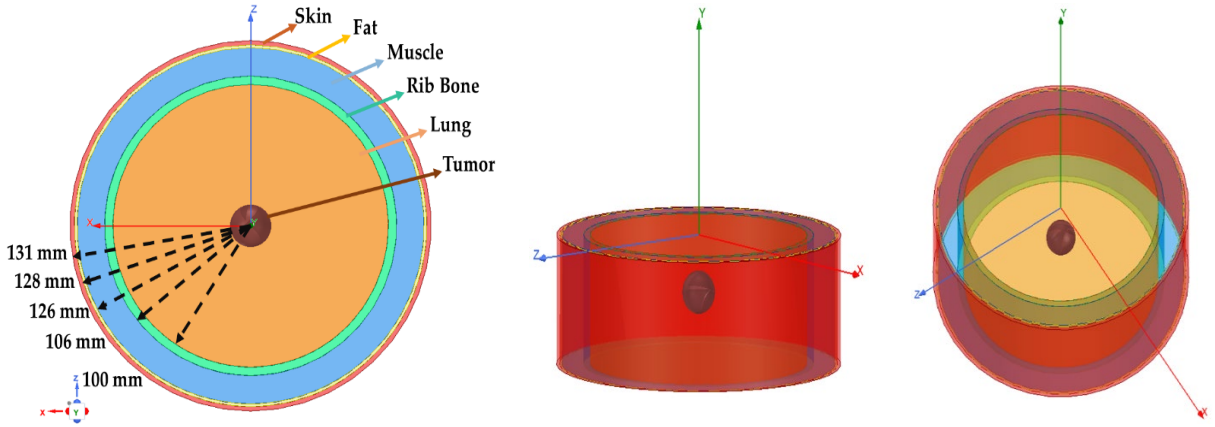

(a) *(b)* *(c)*

Figure 5- 3 Concentric cylinder geometry of lung phantom model with spherical tumour inclusion: (a) Top view; (b) Trimetric view; (c) Dimetric view.

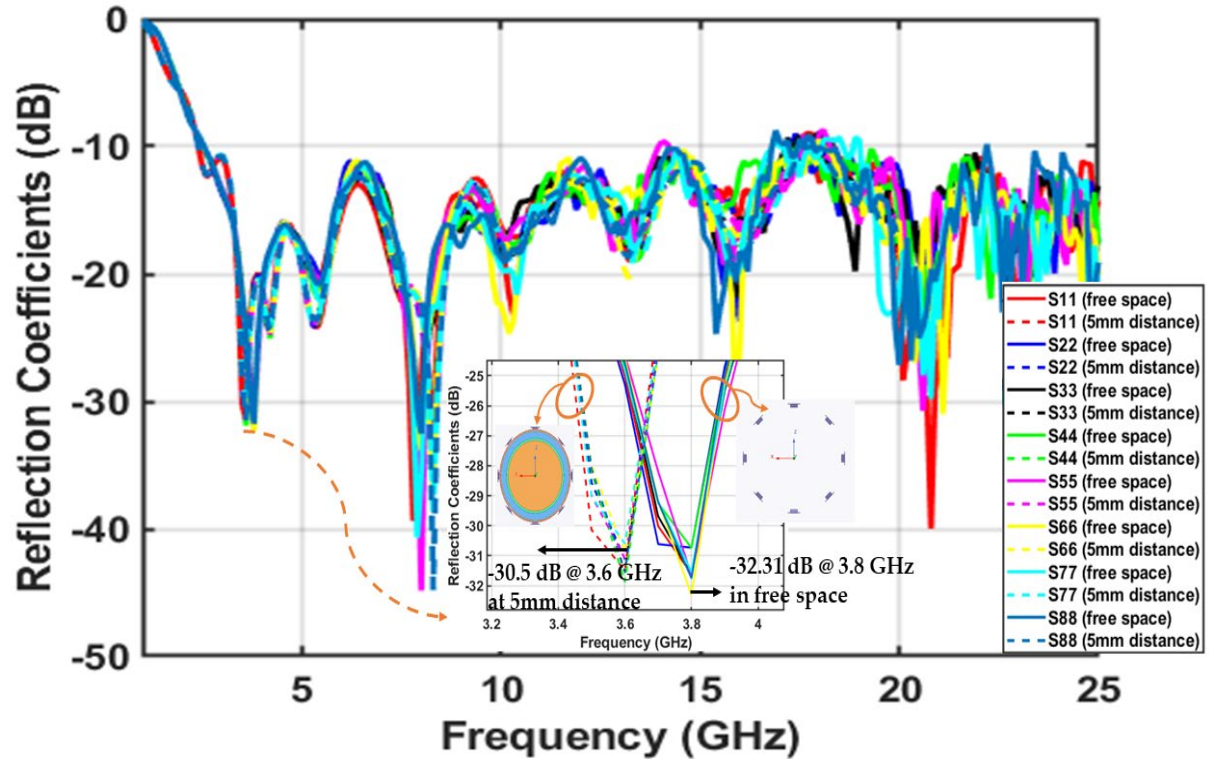

(a)

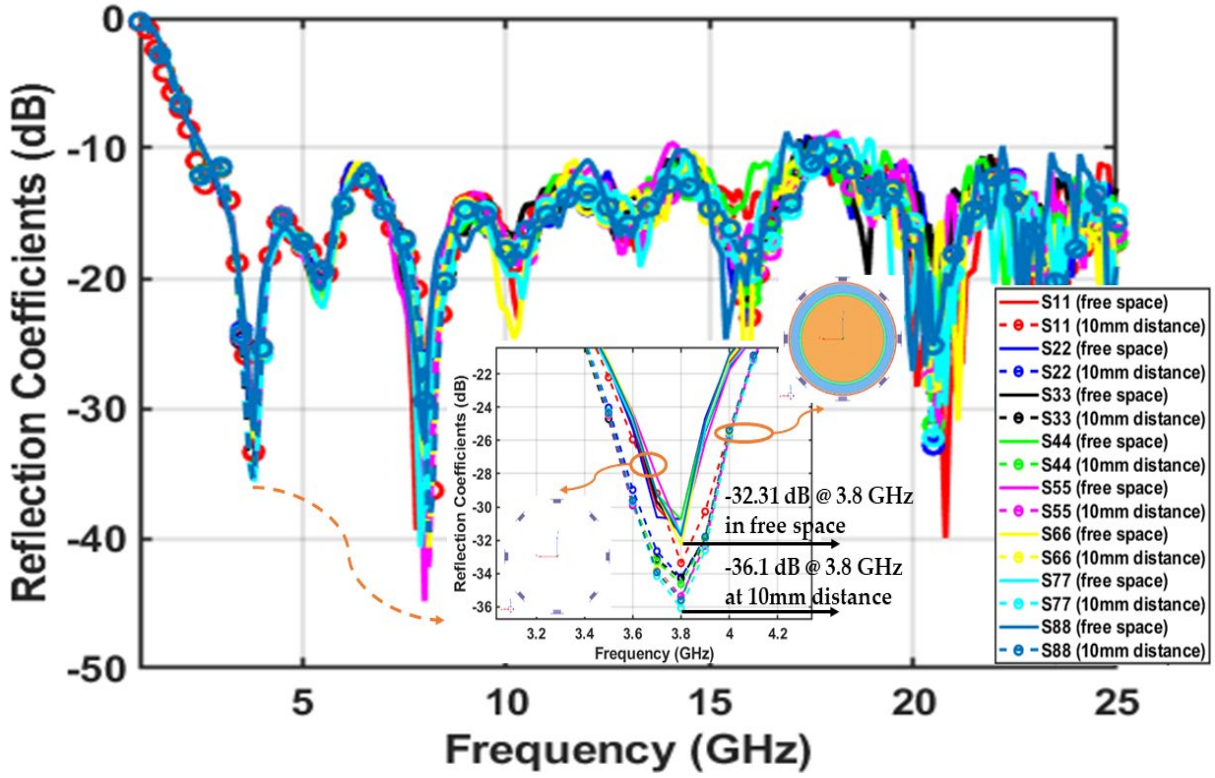

(b)

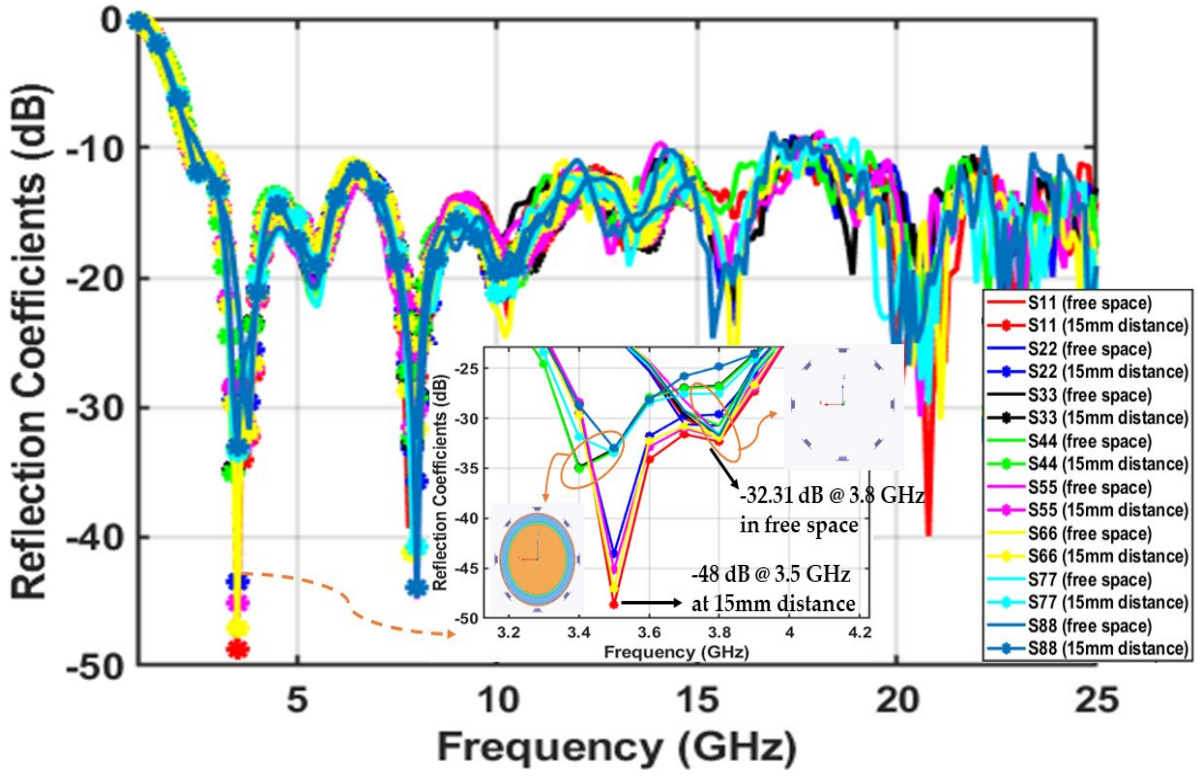

(c)

Figure 5- 4 Comparison between reflection coefficients of array elements placed in free space and in front of a lung phantom at distance of: (a) 5 mm; (b) 10 mm; and (c) 15mm.

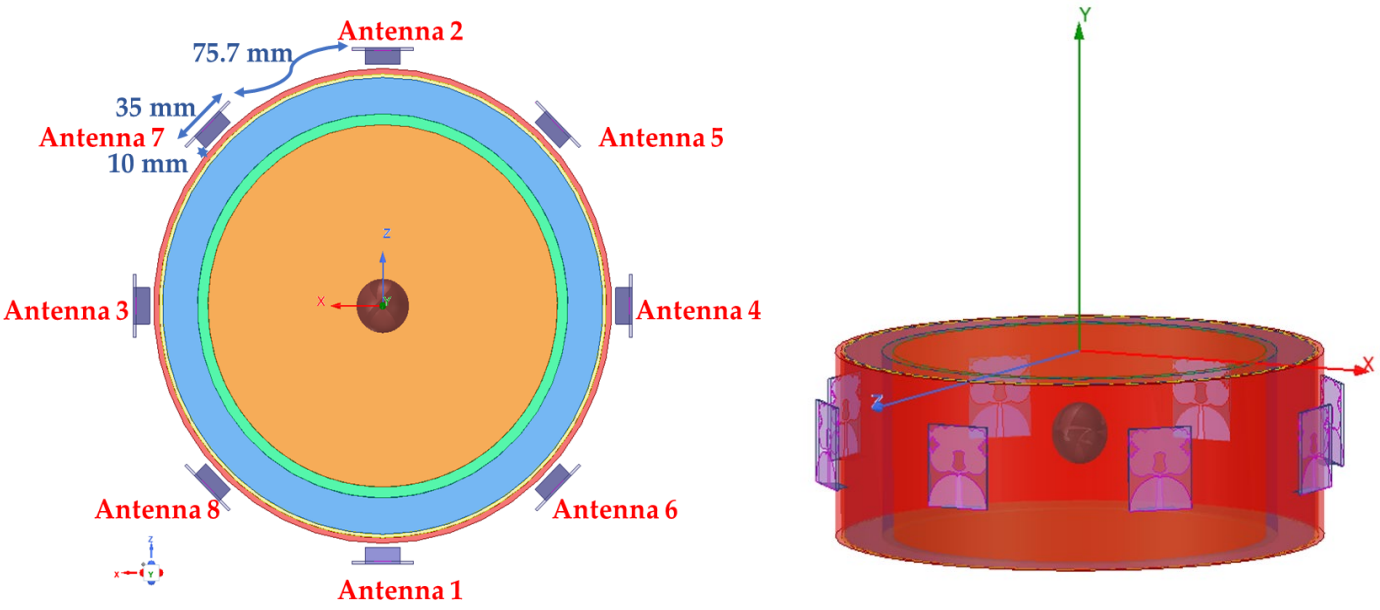

(a) *(b)*

Figure 5- 5 Eight-element array configuration around lung phantom: (a) Top view; (b) Trimetric view.

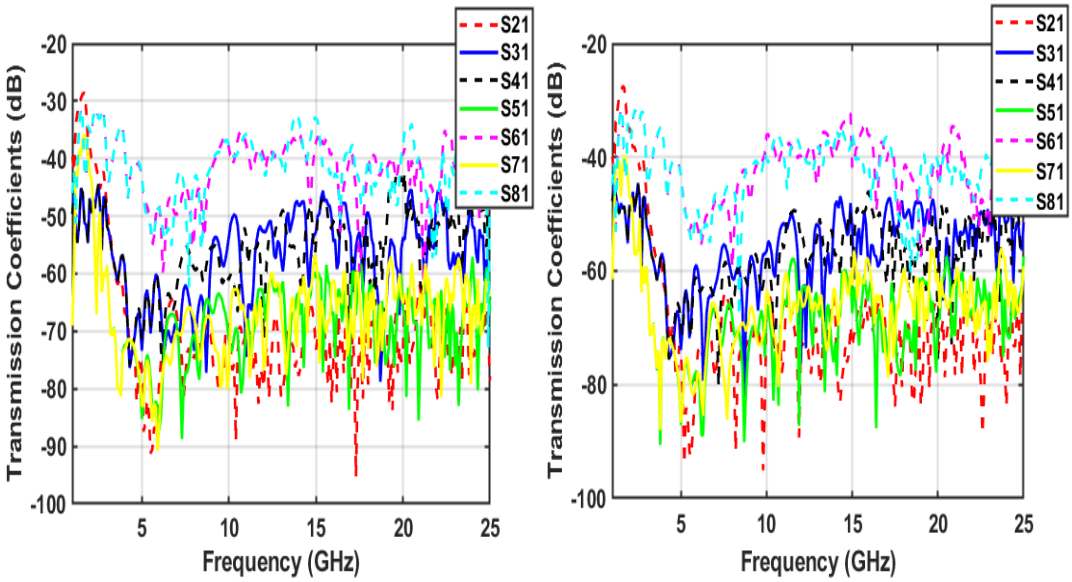

(a) *(b)*

Figure 5- 6 Mutual coupling between eight array elements: (a) With tumour; (b) Without tumour.

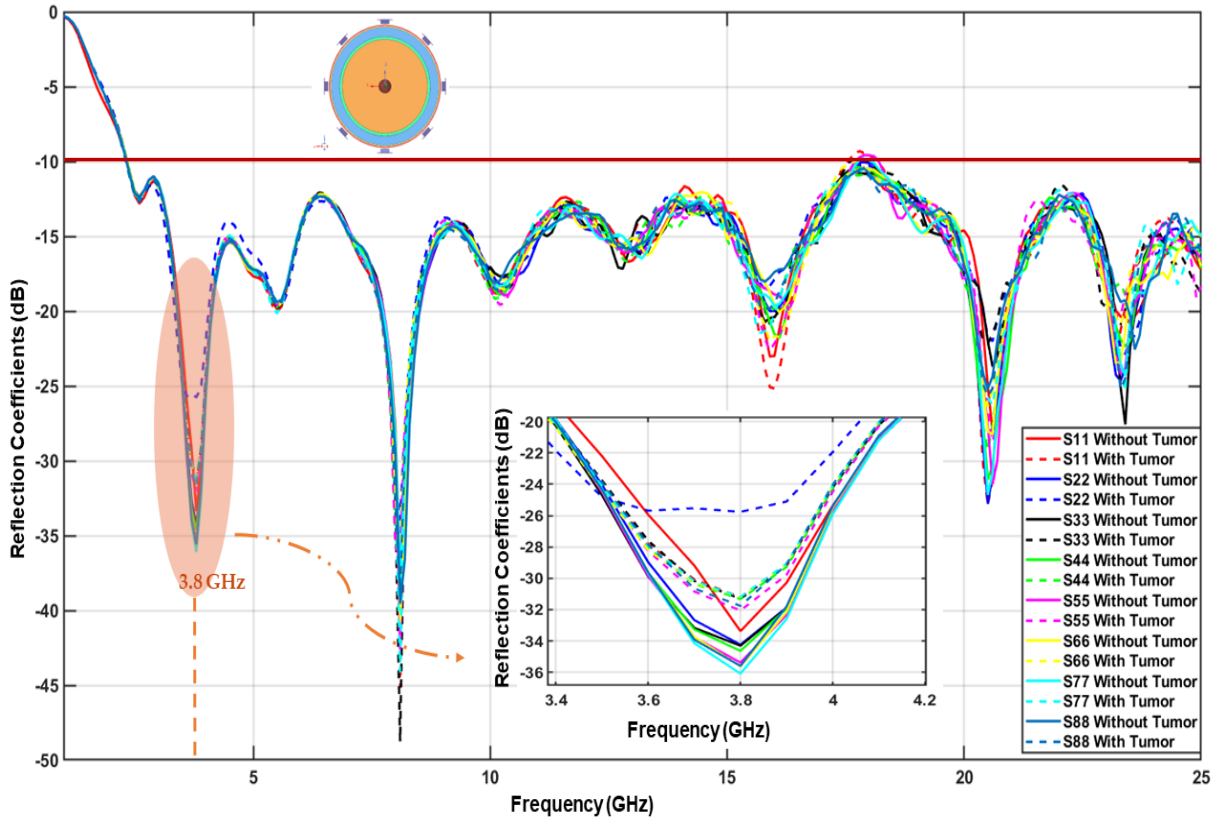

Figure 5- 7 Comparison between reflection coefficients of healthy and unhealthy phantoms when a 15 mm radius tumour is placed in the phantom's centre.

5.5.1 Detection of Deep-Seated Lung Tumour

Intense simulations were conducted to verify the capability of the above system in detecting early-stage lung tumour of different sizes and in different locations of the lung tissue. Firstly, a 15 mm radius tumour is placed in the deep-seated centre location of the phantom, where the tumour centre is 131 mm away in depth from each antenna element. Then, a 5 mm radius tumour is placed in the same centre location to further verify the capability of the system in detecting smaller size tumour. A comparison of the reflection coefficients behaviour of eight array elements has been made between those obtained from healthy and unhealthy phantom for both 15 mm and 5 mm radius tumours as shown in Figures 5-7 and 5-8, respectively.

Table 5- 3 *Difference in reflection coefficient values (in dB) for phantoms with and without tumour in the phantom's centre at 3.8 GHz*

Reflection Coefficient	Healthy phantom	With 15 mm tumour (|Δ|)	With 5 mm tumour (|Δ|)
$\|S_{11}\|$	-33.37	-31.20 (2.17)	-30.26 (3.11)
$\|S_{22}\|$	-34.23	-25.70 (8.53)	-32.37 (1.86)
$\|S_{33}\|$	-34.30	-31.30 (3.00)	-27.27 (7.03)
$\|S_{44}\|$	-34.63	-31.32 (3.31)	-32.49 (2.14)
$\|S_{55}\|$	-35.37	-32.05 (3.32)	-33.05 (2.32)
$\|S_{66}\|$	-35.62	-31.19 (4.43)	-33.48 (2.14)
$\|S_{77}\|$	-36.10	-31.18 (4.92)	-32.68 (3.42)
$\|S_{88}\|$	-35.60	-31.76 (3.84)	-33.68 (1.92)

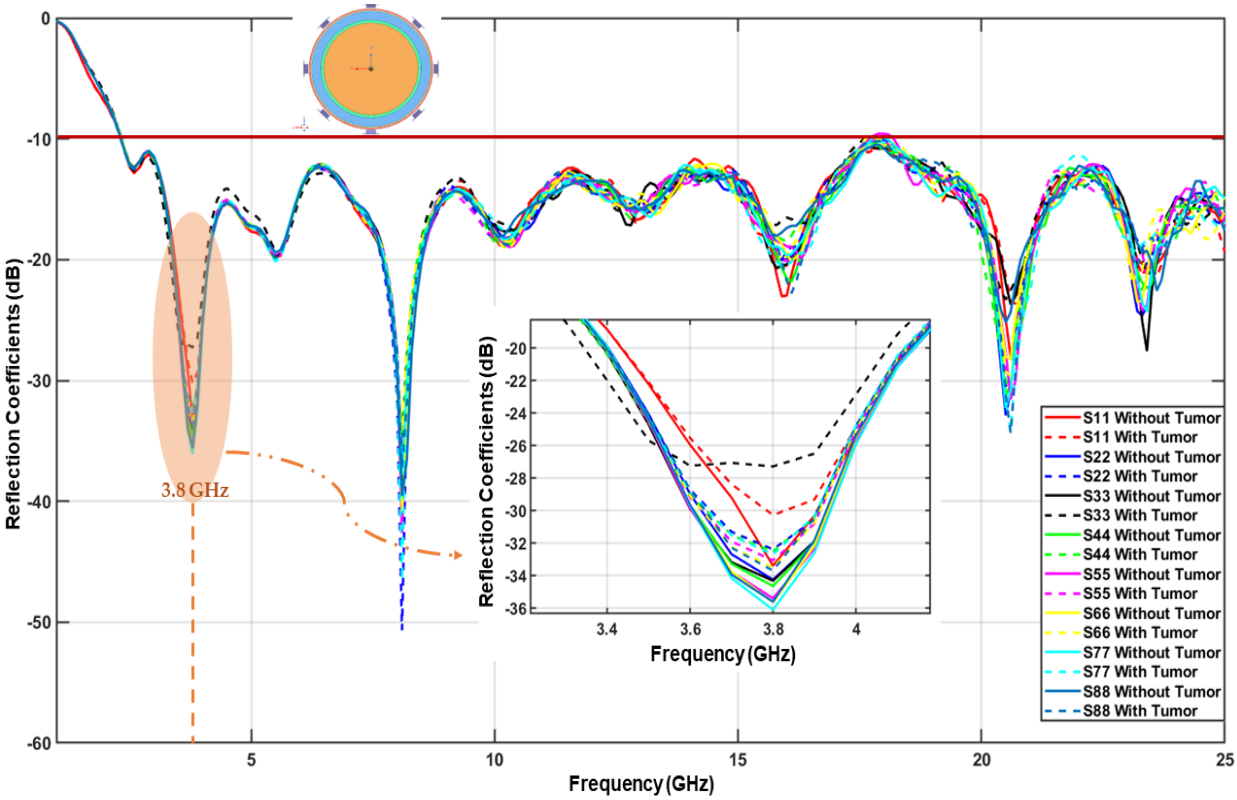

Figure 5- 8 Comparison between reflection coefficients of healthy and unhealthy phantoms when a 5 mm radius tumour is placed in the phantom's centre.

The results revealed that the unhealthy phantom with different sizes of deep-seated tumour placed at 131 mm depth introduced higher reflection than those from the healthy one, which can be attributed to the higher dielectric properties of the tumour mass compared with healthy tissues. This illustrates that the proposed system can detect tumours as small as 5 mm radius simply based on the contrast of reflection coefficients. Table 5-3 shows the obtained reflection coefficient values from both phantoms (healthy and unhealthy) and their absolute difference |Δ| at 3.8 GHz. It can be observed that the minimum and maximum absolute differences in reflection coefficient are 1.86 dB, and 7.03 dB, respectively, which enable good differentiation between healthy and unhealthy tissues.

5.5.2 Detection of Superficially-Located Lung Tumour

Having verified the capability of the proposed system to detect different size tumours in the deepest depth of the lung, i.e. in the phantom's centre, we next verify the capability of the system to detect a 15 mm radius tumour at different superficial locations in the lung. We sweep the frequency from 1–5 GHz, which contains the signal frequency of interest at 3.8 GHz. Figure 5-9 depicts eight superficial locations of the tumour inside the phantom, each corresponding to its proximity to one array element. In each location, the separation between array element and tumour was 61 mm from tumour's centre, i.e., the distance between the tumour edge and the outer surface of the lung layer is 5 mm.

The results show that each array element is capable of lung tumour detection when the tumour is placed close to other array elements. Table 5-4 lists the difference in reflection coefficient values obtained at 3.8 GHz between phantoms with and without tumour for each location. The minimum and maximum absolute differences in reflection coefficients are found to be 1.44 dB, and 9.03 dB, respectively, ensuring good differentiation between healthy and unhealthy tissues. Figure 5-10 shows the same results but in graphical form to illustrate the concluded data pattern.

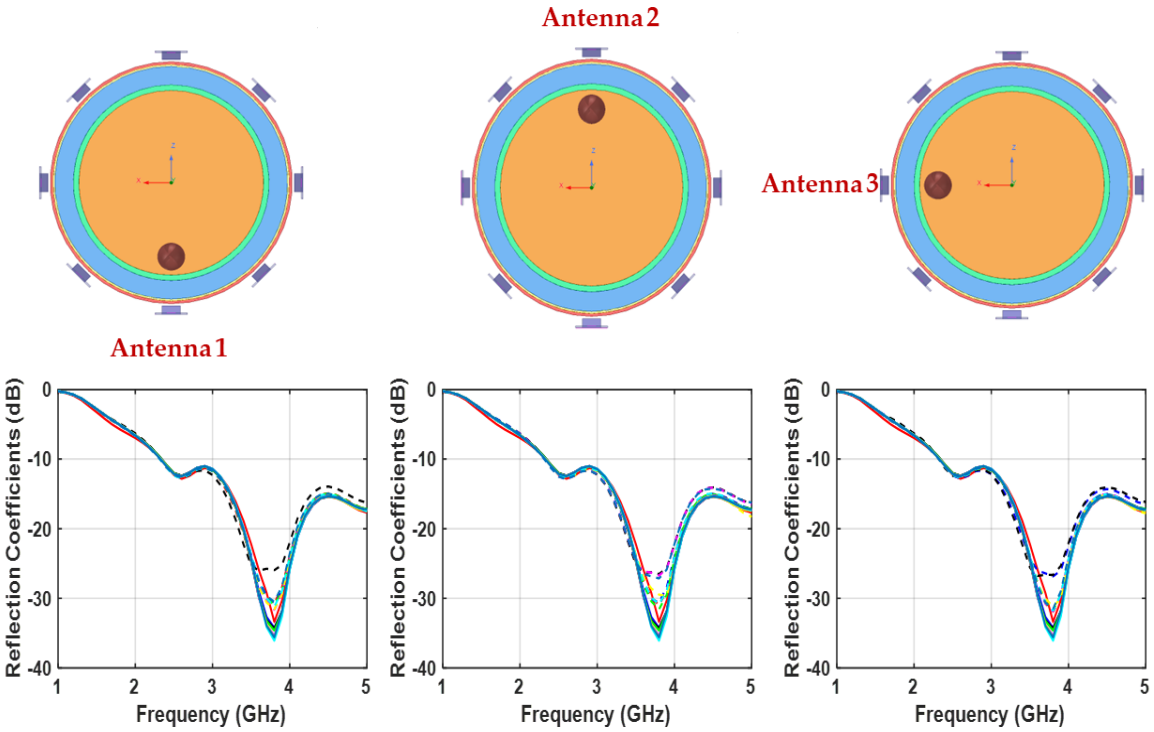
Antenna 1
Antenna 2
Antenna 3
Reflection Coefficients (dB)
Frequency (GHz)

(a) (b) (c)

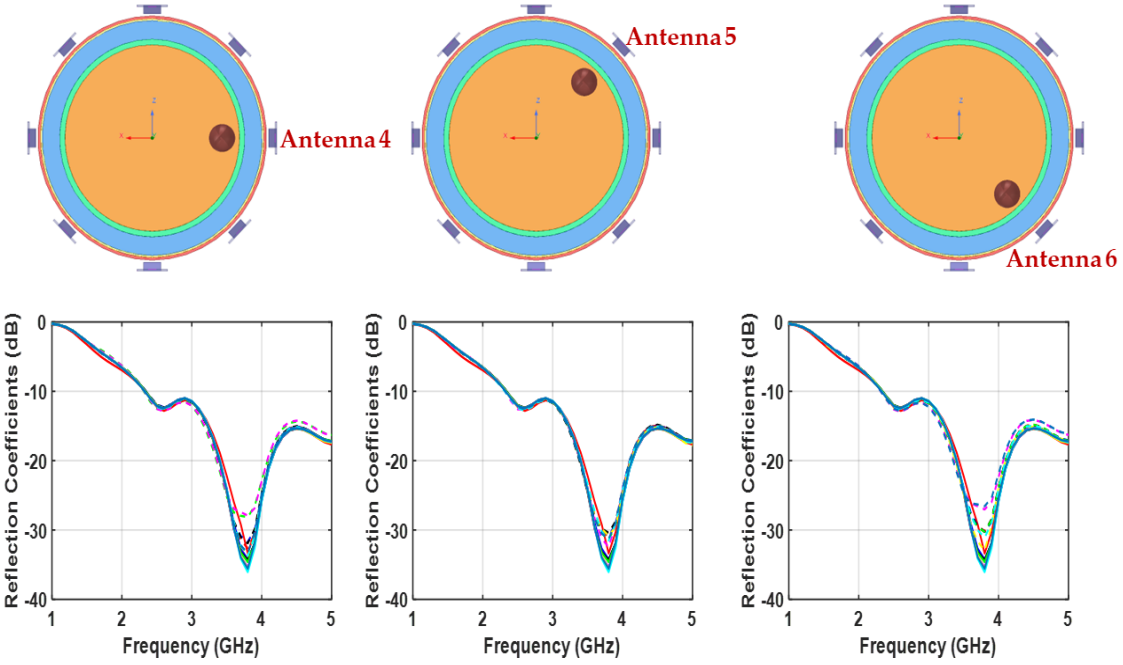
Antenna 4
Antenna 5
Antenna 6
Reflection Coefficients (dB)
Frequency (GHz)

(d) (e) (f)

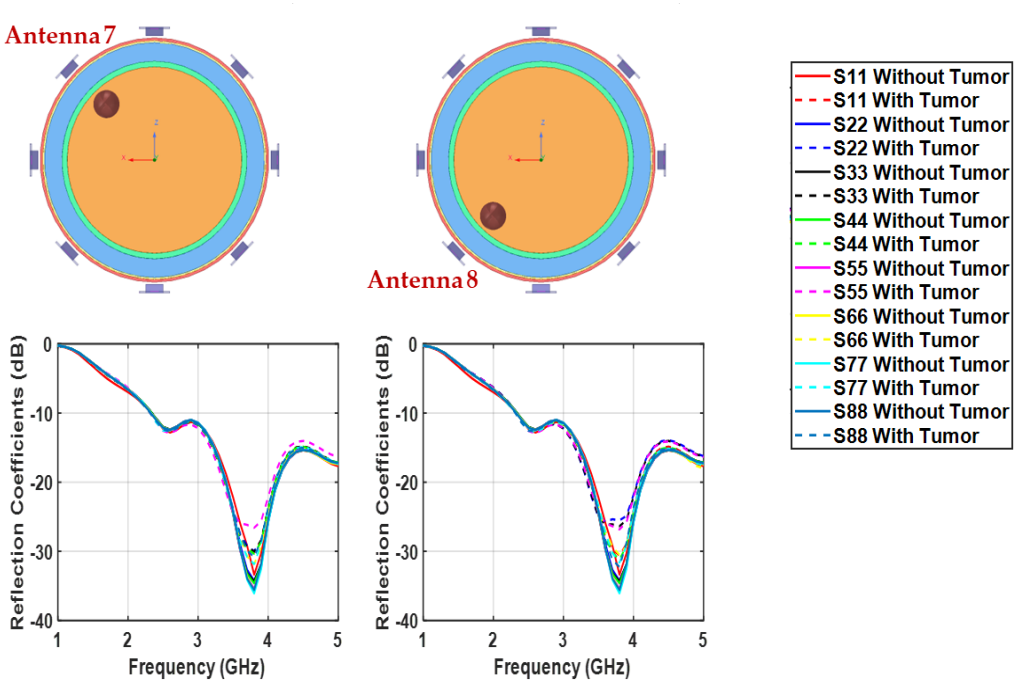

(g) *(h)*

Figure 5- 9 Comparison between reflection coefficients of healthy and unhealthy phantoms when a 15mm radius tumour is placed: (a) near antenna 1 (Case 1); (b) near antenna 2 (Case 2); (c) near antenna 3 (Case 3); (d) near antenna 4 (Case 4); (e) near antenna 5 (Case 5); (f) near antenna 6 (Case 6); (g) near antenna 7 (Case 7); and (h) near antenna 8 (Case 8)

It shows the potential of not only detecting the presence of a tumour, but also predicting its location based solely on the reflection coefficient results. This pattern is only valid for the array configuration shown in Figure 5-5 (a). It predicts the tumour's location in terms of its proximity to certain array element that correlates with a high contrast of reflection coefficients (> 7 dB). For instance, an obtained high $|\Delta S_{22}|$ value predicts the tumour could be located near antennas 3 and 8, while a high $|\Delta S_{88}|$ value predicts the tumour could be in the proximity of antennas 2 and 6, and so on.

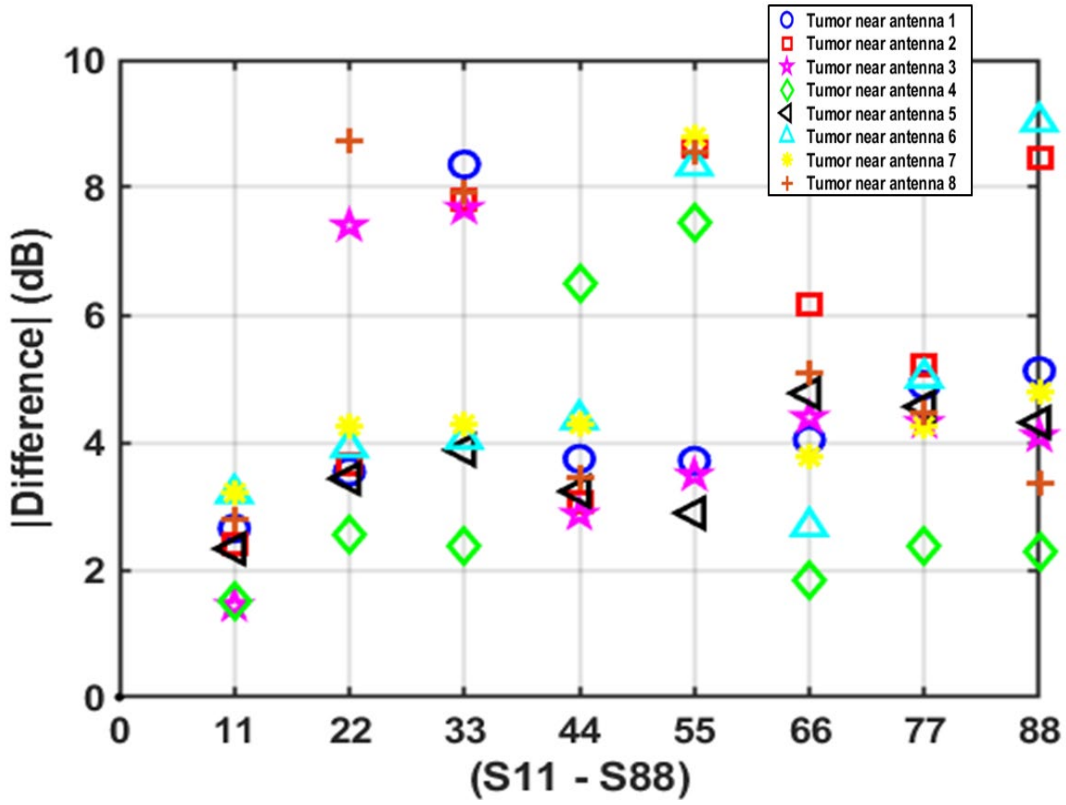

Figure 5- 10 Data pattern showing the difference in reflection coefficient values when tumour is placed at different superficial locations.

Table 5- 4 *Difference in reflection coefficient values between phantoms with and without tumour for each superficial location.*

Δ Reflection Coefficient	Case 1 (dB)	Case 2 (dB)	Case 3 (dB)	Case 4 (dB)	Case 5 (dB)	Case 6 (dB)	Case 7 (dB)	Case 8 (dB)
$\lvert\Delta S_{11}\rvert$	2.65	2.40	1.44	1.5	2.33	3.2	3.22	2.78
$\lvert\Delta S_{22}\rvert$	3.54	3.65	7.4	2.55	3.43	3.92	4.26	8.72
$\lvert\Delta S_{33}\rvert$	8.36	7.81	7.67	2.37	3.88	4.05	4.28	7.94
$\lvert\Delta S_{44}\rvert$	3.74	3.07	2.87	6.49	3.23	4.36	4.29	3.45
$\lvert\Delta S_{55}\rvert$	3.71	8.65	3.49	7.45	2.89	8.34	8.79	8.55
$\lvert\Delta S_{66}\rvert$	4.04	6.15	4.39	1.84	4.77	2.68	3.79	5.10
$\lvert\Delta S_{77}\rvert$	4.9	5.20	4.31	2.38	4.56	5.01	4.25	4.47
$\lvert\Delta S_{88}\rvert$	5.12	8.47	4.1	2.27	4.31	9.03	4.8	3.35

5.6 Reconstructed Imaging Results

In this section, tumour images were produced using a radar-based imaging technique, which relies on reconstructing energy map of backscattered signals within the lung phantom. Tumour tissues often exhibit higher water content that corresponds to higher dielectric properties than healthy tissues. Hence, greater signal reflections will occur at the tumour boundaries and these scatterers will result in high image energy. Image resolution is one of the key factors that potentially controls the efficiency of microwave imaging system, which in turn is highly dependent on the operating bandwidth of the system antenna. Employing a SWB antenna will result in high resolution images of the lung phantom. Consequently, more accurate detection of lung cancer. Two confocal beamforming algorithms: Delay and Sum (DAS); and Delay Multiply and Sum (DMAS) with subtraction clutter removal based on MERIT open-source software [54, 128] were used to reconstruct the images of two deep-seated lung tumours of 5 mm and 15 mm radius located at 131 mm depth of a lung phantom; using backscattering datasets (reflection coefficient data) acquired over a super-wide frequency range, as detailly discussed in Section 5.

The 2D images of the torso phantom are generated using the DMAS algorithm, which is a beamforming confocal imaging algorithm known to be able to localise malignant lesion accurately while reducing background clutter [54, 129]. This technique is based on antenna pair multiplication before the summation of reflected signals measured at different antenna positions. The obtained S-parameters are processed using DMAS and an artefact removal technique described by (5.2):

$$s_m(t) = x_m^U(t) - x_m^H(t) \tag{5.2}$$

where $s_m(t)$ is the resultant reflected signal after the artefact removal, $x_m^U(t)$ and $x_m^H(t)$ are the recorded signals from the unhealthy phantom, and healthy phantom, respectively.

The artefact usually consists of reflections of the incident wave from the interface between the skin and torso, and some residual antenna reverberation. Failure to eliminate this artefact could mask tumours that may be present in the lung, resulting in unsuccessful detection. A commonly employed signal preprocessing method for artefact

removal is to perform a subtraction between two sets of S-parameter data: one acquired under no tumour (healthy phantom); and the other acquired under tumour (unhealthy phantom). This eliminates the common background clutter from the two datasets, resulting in enhanced tumour response.

The reconstructed image can be generated using (5.3):

$$I(r) = \sum_{m=1}^{M-1} \sum_{n=m+1}^{M} s_m[t_m(r)].s_n[t_n(r)] \tag{5.3}$$

where $I(r)$ is the intensity value at point r (position of pixel in the phantom space), M is the number of antenna positions used in the scan, s_m is the delayed reflected signal measured at m^{th} position, s_n is the delayed paired signal of s_m measured at n^{th} position. In this process, the delayed reflected and paired signals are multiplied before being summed. This increases the sample size, which leads to improved clutter reduction, but also longer computation time. The $t_m(r)$ and $t_n(r)$ are the time-of-flight of s_m, and s_n, respectively, as defined in (5.4), $\boldsymbol{r}_m$ and $\boldsymbol{r}_n$ are the m^{th}, and n^{th}antenna position, respectively, and v is the average signal propagation speed of in the phantom space.

$$t_m(r) = 2\frac{|\boldsymbol{r} - \boldsymbol{r}_m|}{v} \tag{5.4a}$$

$$t_n(r) = 2\frac{|\boldsymbol{r} - \boldsymbol{r}_n|}{v} \tag{5.4b}$$

The performance of the above algorithms in locating the tumours and predicting their sizes are shown in Figures 5-11 and 5-12. The tumour size is measured from the reconstructed images based on the areas that represent the higher signal scattering, which are indicated in red in both DAS and DMAS images. In Figure 5-11(a), the location of the 15 mm radius tumour is accurately identified with a slightly higher predicted size of 16 mm radius using the DAS algorithm. A higher resolution of detection can be observed in Figure 5-11(b) and the predicted tumour size is slightly lower at 14 mm radius using the DMAS algorithm. In Figure 5-12(a), the smaller tumour of 5 mm radius is correctly located but with a much larger predicted size of 9 mm radius using DAS. Likewise, for DMAS with a predicted size of 8 mm radius as shown in Figure 5-12(b).

By analysing mean absolute percentage error (MAPE) of the predicted sizes as shown in Table 5-5, it can be seen that the system can predict with good accuracy using DAS or DMAS for the larger tumour of 15 mm radius as MAPE is relatively low. However, prediction is still challenging for the smaller tumour of 5 mm radius, although the MAPE results suggest that DMAS could be the better of the two algorithms.

After analysing the performance of the proposed system for lung tumour detection, a comparison between this work and previous works is given in Table 5-6. It can be concluded that this work is the first to introduce the concept of SWB microwave reflectometry for lung tumour detection. It is also the first to investigate in depth the lung anomaly detection based on contrast of reflection coefficients from different array elements, which provided quick detection without the need for complex processing of backscattered data. Furthermore, the capability to measure different tumour sizes in both deep-seated and superficial locations is demonstrated for the first time, which enables the assessment of the disease stage and the corresponding treatment options for lung cancer patients.

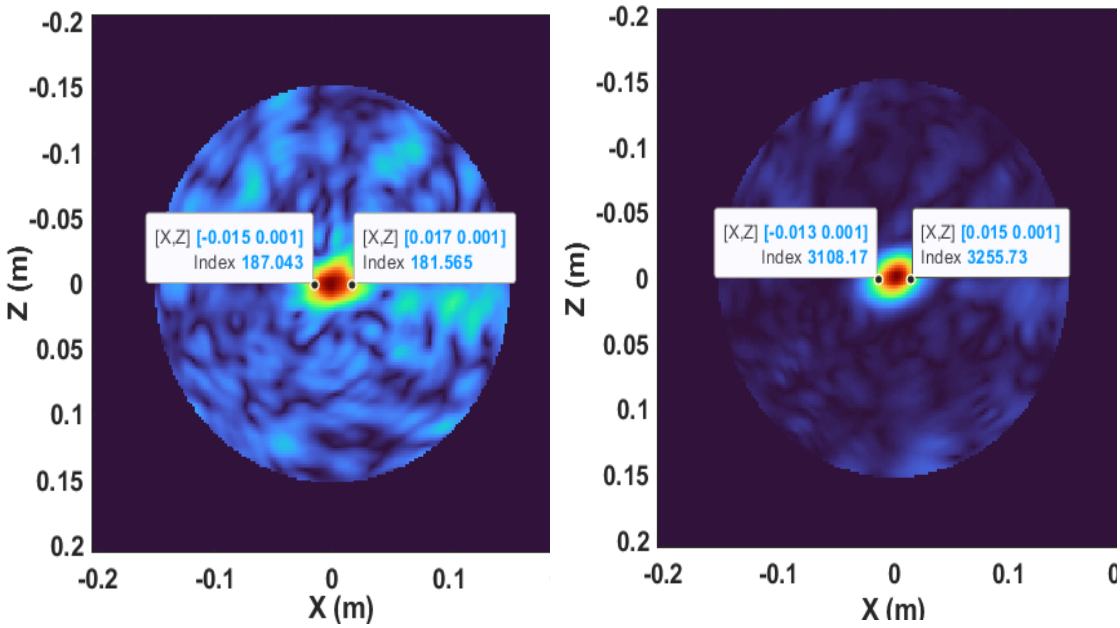

(a) *(b)*

Figure 5- 11 Imaging results of lung phantom with deep-seated 15 mm radius tumour using two beamformers: (a) DAS; and (b) DMAS.

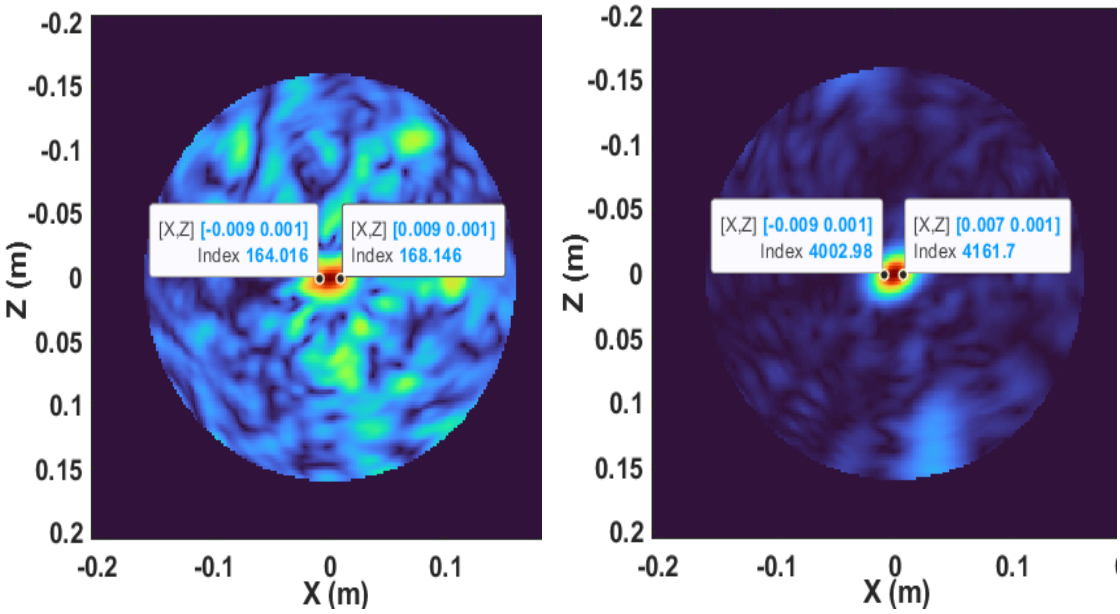

(a) *(b)*

Figure 5- 12 Imaging results of lung phantom with deep-seated 5 mm tumour using two beamformers: (a) DAS; and (b) DMAS.

Table 5- 5 *MAPE of predicted tumour sizes from reconstructed images by DAS and DMAS*

Real tumour radius	Predicted radius (DAS)	Predicted radius (DMAS)	MAPE (DAS)	MAPE (DMAS)
5 mm	9 mm	8 mm	80%	60%
15 mm	16 mm	14 mm	6.66%	6.66%

Table 5- 6 *Comparison between this work and previous works on microwave reflectometry-based lung tumour detection*

Ref.	Freq. (GHz)	Tumour size	Type of antenna(s) deployed	Tumour detection depth	Tumour detection accuracy
[17]	1.5–3	10 mm radius	1× rotated antenna around the phantom	N/A	Accurate
[18]	10	5 mm radius	2× Vivaldi antenna	Superficial (60 mm)	Weak detection
[19]	1–5	15 mL (tube shaped)	2× horn TX antenna, 2× Vivaldi RX antenna	Superficial (50 mm)	Accurate

[20]	3–4	4, 10 mm radius	1× circular shaped antenna	60 mm	Weak detection
[21]	3 –10.7	N/A	2× elliptical shaped antenna	70 mm	Weak detection
[22]	2.9–12	N/A	1× cupcake shaped antenna	N/A	Weak detection
This work	2.45–25	5, 15 mm radius	8× custom-designed SWB array element around the phantom	Deep-seated (141 mm) Superficial (61mm)	Accurate with size measurement capability

5.7 Experimental Investigation of Lung Cancer Detection

This section presents the construction of the human torso phantom, the experimental outcomes, and the imaging setup designed for deep-seated lung tumour detection.

5.7.1 Phantom Preparation and Dielectric Properties Measurement

In order to build a phantom that mimics the composition and the dielectric properties of human torso layers, several experiments were conducted using different mixtures and materials across the operational frequency range of the suggested SWB antenna.

In this phase of the measurement process, the free space method is employed, utilising two identical antennas, T_X and R_X, covering the specified frequency range. These antennas are positioned at a separation distance of 760 mm to facilitate far-field measurements. The measurement procedure entails the utilisation of a large, flat Material Under Test (MUT) featuring two antennas oriented towards it, both linked to a vector network analyser (VNA). Before the measurement, VNA calibration is essential. After successful calibration, moving forward with the measurement involves capturing the S-parameters of an empty sample holder, which is positioned equidistantly between the antennas, specifically at a distance of 380 mm from each antenna. Subsequently, the MUT is positioned on the sample holder between the antennas, and the S-parameter measurement is repeated. Employing a subtraction technique, the impact of the sample holder can be eliminated, enabling to isolate and determine the S-parameters

completely for the MUT. This, in turn, facilitates the determination of both the reflection and transmission coefficients for the MUT.

To process the acquired data and extract the dielectric properties, the Nicolson-Ross-Weir (NRW) method [130] is implemented, which necessitates the measurement of scattering parameters (S-parameters) for the Material Under Test (MUT) both with and without the presence of the material. The measured thickness of various MUT's was recorded, as this measurement is essential for converting S_{11} to gamma (Γ) and S_{21} to the transmission coefficient (T). These conversions enable the extraction of the key properties of the MUT, including its complex relative permittivity, loss tangent, and conductivity [131]:

$$S_{11} = \frac{\Gamma(1 - T^2)}{(1 - \Gamma^2 T^2)} \tag{5.2a}$$

$$S_{21} = \frac{T(1 - \Gamma^2)}{(1 - \Gamma^2 T^2)} \tag{5.2b}$$

where S_{11} and S_{21} can be obtained directly from VNA, the quantities Γ and T can be determined in terms of the measured S_{11} and S_{21} by rearranging (5.2a and b). Then T can be eliminated from the above equations, resulting in quadratic equation for Γ:

$$\Gamma^2 - 2\Gamma X + 1 = 0 \tag{5.3a}$$

where $\Gamma = X \pm \sqrt{X^2 - 1}$ and $|\Gamma| < 1$

The correct root of Γ in terms of S-parameters is:

$$X = \frac{1 - {S_{21}}^2 + {S_{11}}^2}{2S_{11}} \tag{5.3b}$$

Then the transmission coefficient can be found using:

$$T = \frac{S_{11} + S_{21} - \Gamma}{1 - (S_{11} + S_{21})\Gamma} \tag{5.4}$$

Then the complex permittivity ε^* and the loss tangent $tan\delta$ can be calculated as:

$$\varepsilon^* = \frac{\lambda_o^2}{{\mu_r}^*}\left(\frac{1}{\lambda_c^2} - \left[\frac{1}{2\pi L}\, ln\left(\frac{1}{T}\right)\right]^2\right) \tag{5.5a}$$

$${\mu_r}^* = \frac{\lambda_{og}}{\Lambda}\left(\frac{1+\Gamma}{1-\Gamma}\right) \tag{5.5b}$$

$$\lambda_{og} = \frac{1}{\sqrt{\frac{1}{\lambda_0^2} - \frac{1}{\lambda_c^2}}} \tag{5.5c}$$

$$\frac{1}{\Lambda^2} = \left(\frac{\varepsilon^* {\mu_r}^*}{\lambda_o^2} - \frac{1}{\lambda_c^2}\right) = -\left(\left[\frac{1}{2\pi L}\, ln\left(\frac{1}{T}\right)\right]^2\right) \tag{5.5d}$$

where λ_o , λ_c , and λ_{og} are the free space, the cut-off and the sample wavelength, respectively, ${\mu_r}^*$ is the complex permeability and L is the sample thickness. Since the free space method is deployed in the dielectric properties measurement, λ_c is expressed as infinite and the cut-off frequency f_c is evaluated as zero [132, 133].

After the evaluation of the complex permittivity $\varepsilon^* = \varepsilon_r - j\varepsilon_i$, where ε_r and ε_i are the real and imaginary parts of relative permittivity, respectively, $tan\delta = \varepsilon_i/\varepsilon_r$ and the conductivity σ can be deduced using:

$$\sigma = \varepsilon_i\, \varepsilon_o \omega \tag{5.6}$$

where ε_o is the free space permittivity (8.52×10^{-12} F/m) and ω is the angular frequency $(\omega = 2\pi f)$.

Various measurements were conducted using different material mixtures to evaluate the dielectric properties of the human torso phantom as listed in Table 5-7 and presented in Figure 5-13.

Table 5- 7 *Measured properties of different layers for human torso phantom*

Layers	Sample thickness (L)	Tissue equivalent material (Ratio)
Skin	40 mm	Gelatine + Water (1:1.5) [14]
Fat	40 mm	Paraffin wax [134, 135]

Rib Bone (Cancellous)	15 mm	Plaster of Paris [136, 137]
Muscle	55 mm	Gelatine + Water (1:2.5) [14]
Lung (Inflated)	44 mm	Gelatine + Water (1:1) [14]

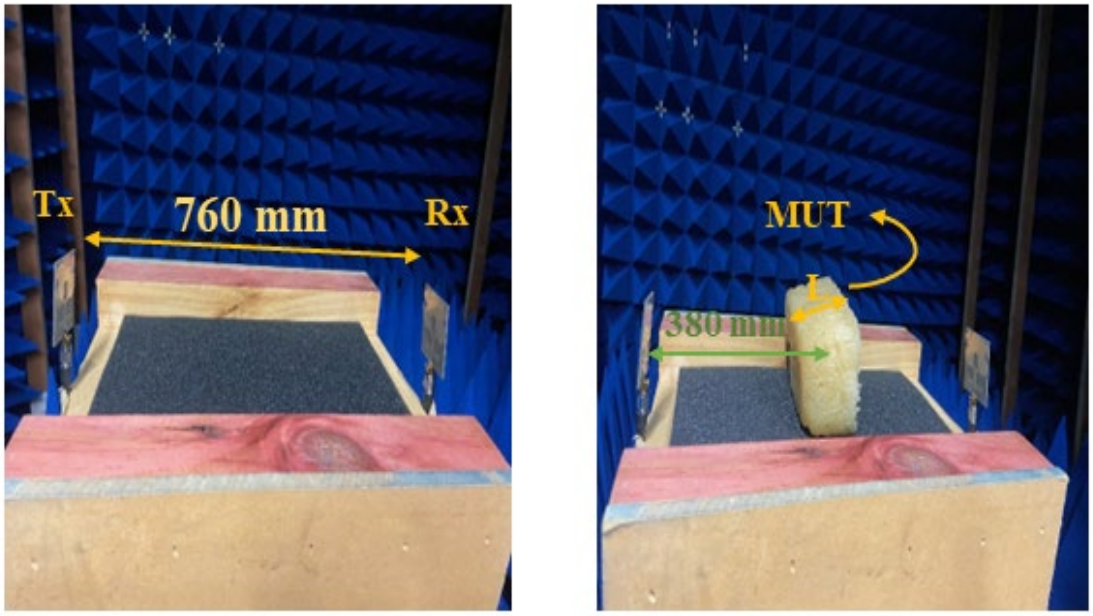

(a) *(b)*

Figure 5- 13 Free space dielectric properties measurement of MUT: (a) without MUT; and (b) with MUT.

Figure 5-14 represents the dielectric properties results of different tissue equivalent materials over the frequency band 1 to 40 GHz, where the relative permittivity tends to decrease with increasing the operating frequency. However, the conductivity shows opposite behaviour where it increases with increasing frequency. The results demonstrate good agreement between the dielectric properties obtained through simulation of Cole-Cole model and the actual measured data of the corresponding mixtures.

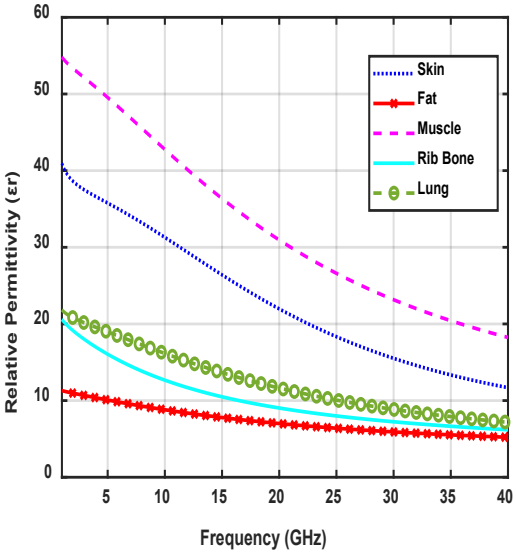
Relative Permittivity (εr)
Frequency (GHz)
Skin
Fat
Muscle
Rib Bone
Lung

(a)

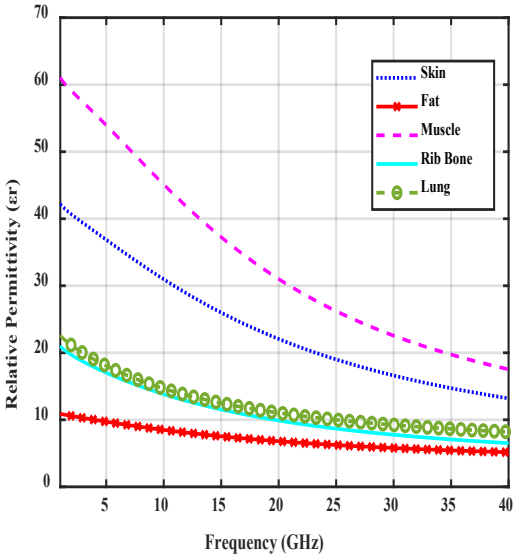
Relative Permittivity (εr)
Frequency (GHz)
Skin
Fat
Muscle
Rib Bone
Lung

(b)

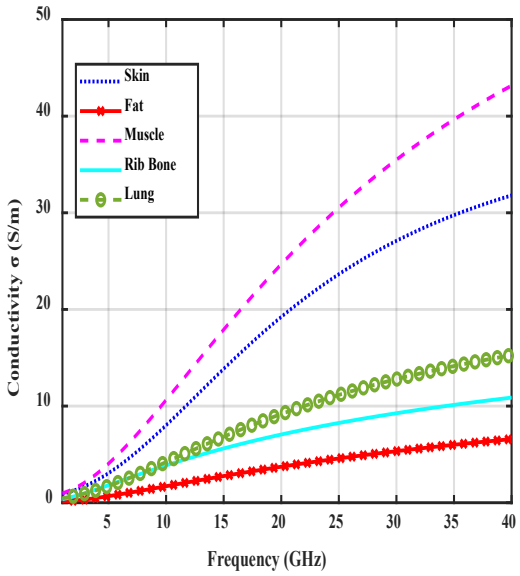
Conductivity σ (S/m)
Frequency (GHz)
Skin
Fat
Muscle
Rib Bone
Lung

(c)

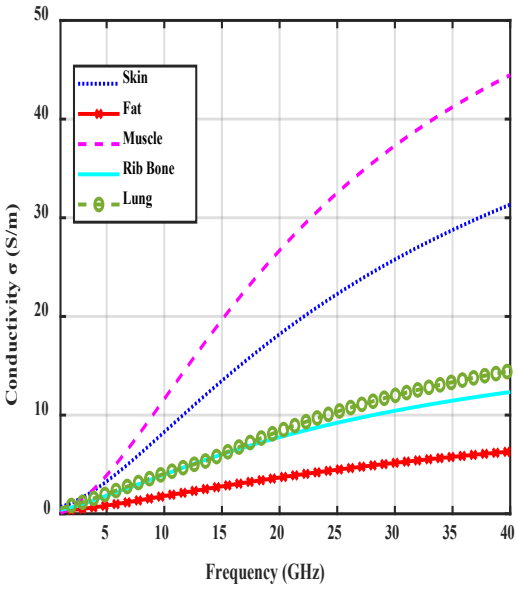
Conductivity σ (S/m)
Frequency (GHz)
Skin
Fat
Muscle
Rib Bone
Lung

(d)

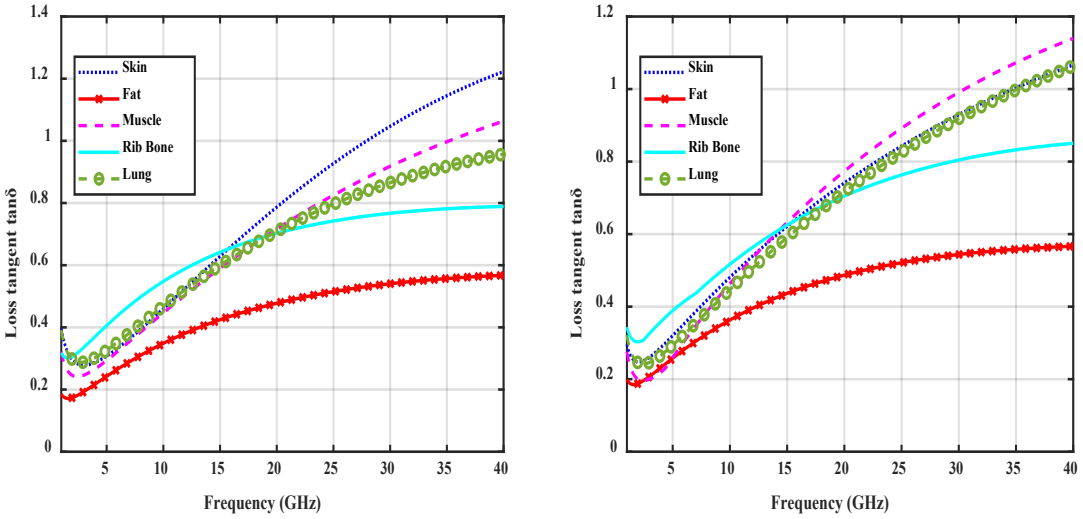

(e) *(f)*

Figure 5- 14 Simulated Cole-Cole dielectric properties (a, c, e); measured dielectric properties (b, d, f).

5.7.2 Imaging Experiment

For the purpose of detecting lung tumour located deep within the lung tissue, precisely at the centre, two human torso phantoms were constructed. One of these phantoms contained a tumour embedded at the centre, while the other represented a healthy scenario with no tumour present. To represent the tumour, a red grape was employed with a 12.5 mm radius (25 mm diameter), which has been recognised in the literature as a suitable equivalent to tumour tissue [138, 139]. In Figure 5-15, the dimensions of the created phantom and the procedure for inserting the tumour can be observed. To set up the imaging configuration, the phantom was positioned on a rotatable platform with a radius of 13.1 cm (diameter of 26.2 cm). Eight SWB elements from the proposed antennas were arranged in a circular configuration around the fabricated phantom, each separated by 45 degrees. A consistent 1 cm separation was maintained between each antenna element and the target object. The imaging setup, as illustrated in Figure 5-16, involves connecting port 1 of the VNA to the transmitting antenna, while port 2 is linked to the common port of the SP6T PE71S6332 Pasternack RF switch, which operates across a frequency range from DC to 40 GHz. In this multistatic approach, signals received from the other 7 antenna elements connected to the RF switch are recorded. Subsequently,

the transmitting antenna is switched to another element to complete the entire measurement process.

This procedure was executed for both fabricated phantoms, the healthy one and the cancerous one. Following this, an artifact removal technique was applied by subtracting the recorded signals obtained from the healthy phantom from those acquired using the cancerous phantom. The backscattered signals collected from all antenna elements were compared over the operational frequency range of the proposed SWB antenna, across 3.1 to 40 GHz. This comparison was conducted using two phantom scenarios: one representing a healthy state and the other simulating a cancerous condition. The outcomes of this comparison are depicted in Figure 5-17.

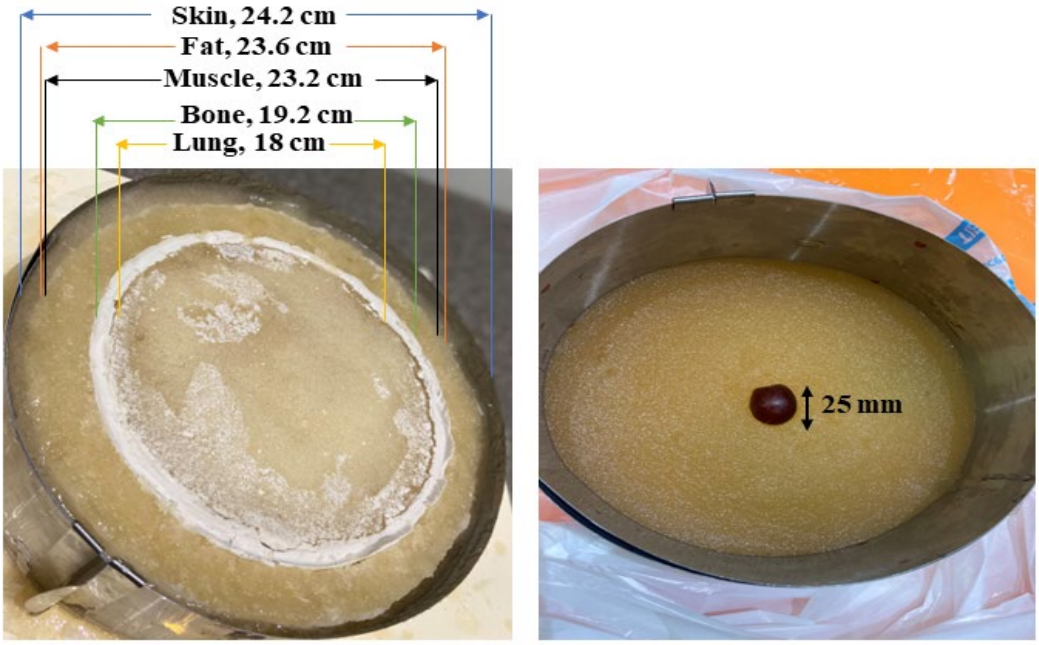

(a) *(b)*

Figure 5- 15 Constructed phantom of human torso: (a) phantom dimensions; and (b) tumour insertion.

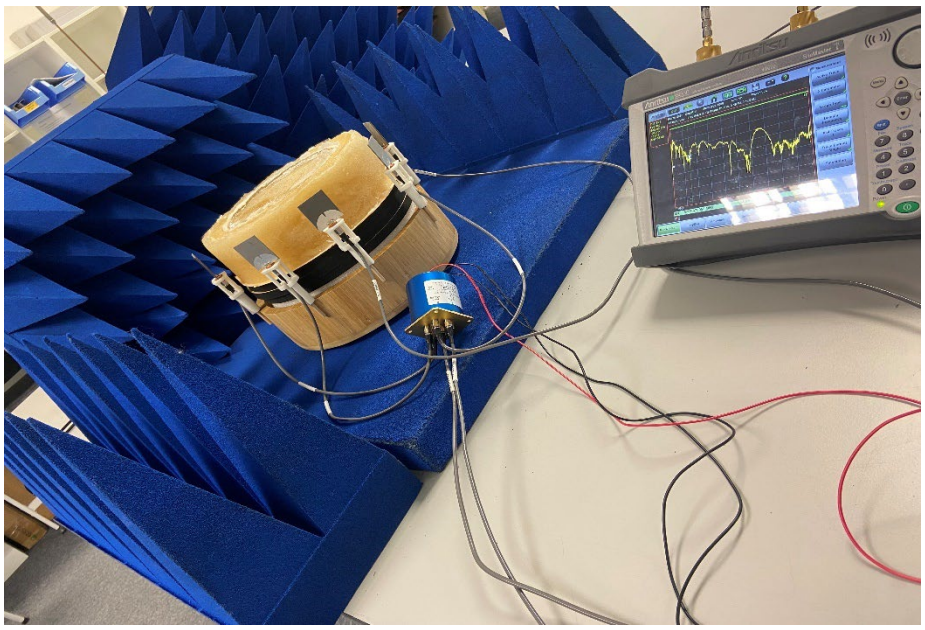

Figure 5- 16 Lung Tumour detection imaging setup.

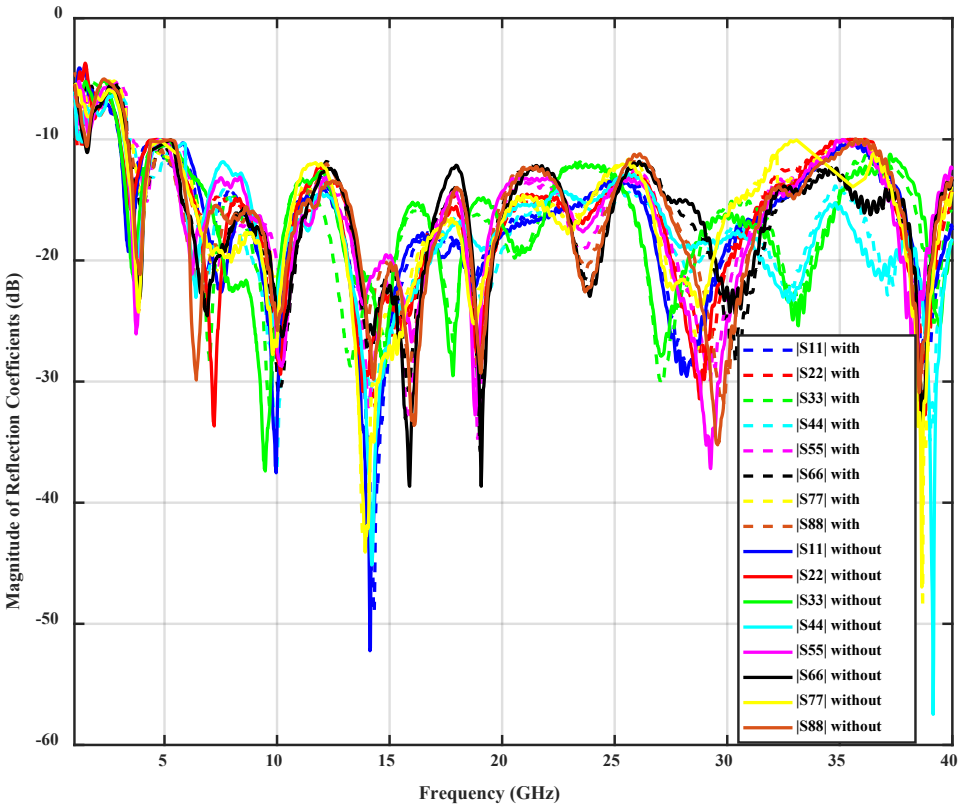

(a)

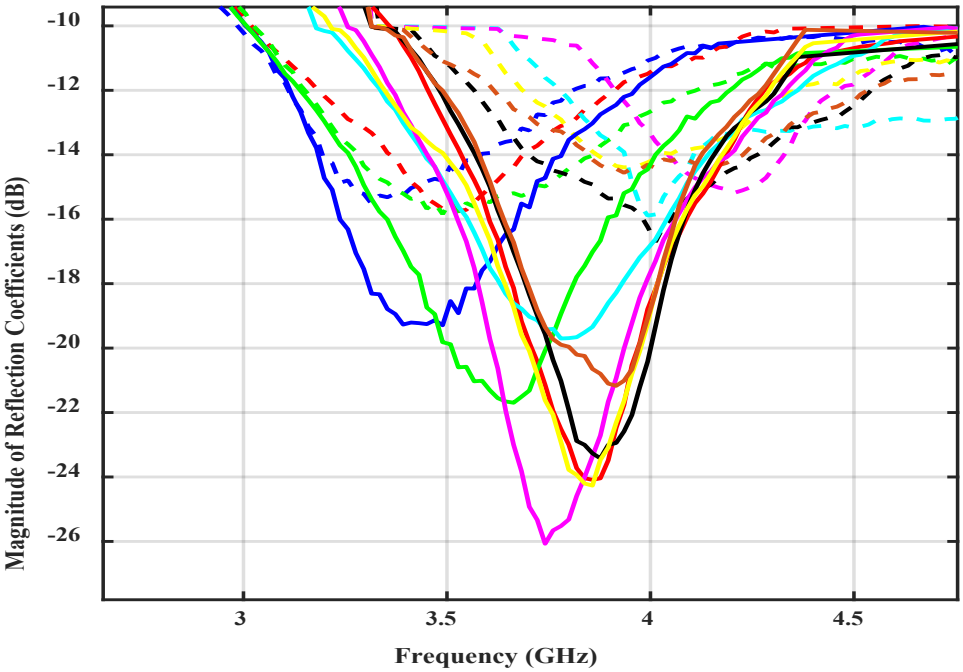

(b)

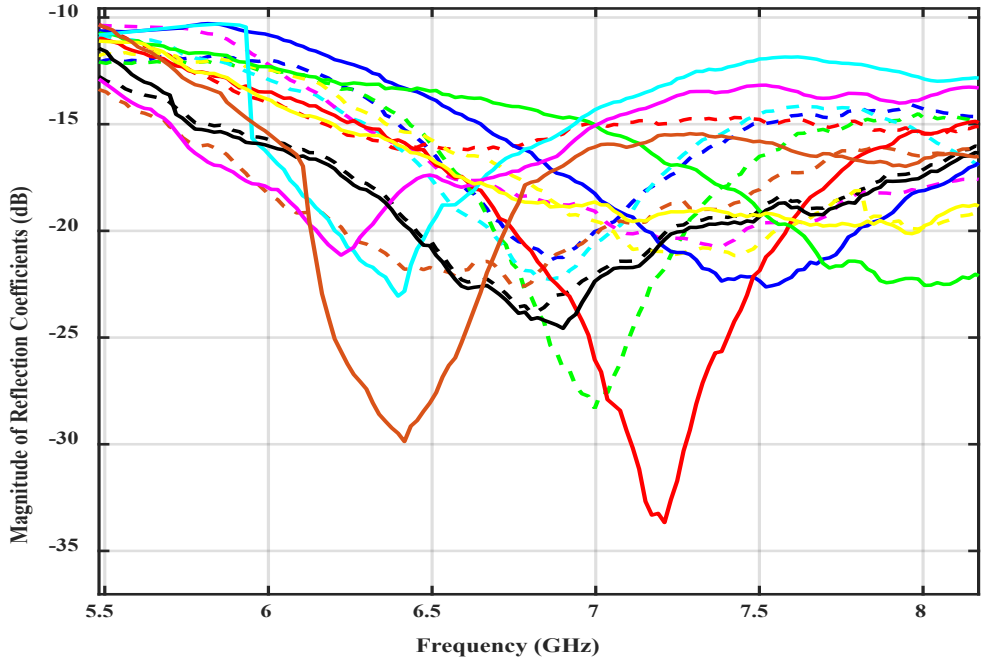

(c)

Figure 5- 17 Measured reflection coefficients data collected from eight antennas around the phantom, (a)zoomed-view at the first resonant frequency; (b) zoomed-view at the second resonant frequency.

The presented results indicate that the reflected signals obtained from the cancerous phantom exhibit higher reflection when compared with those obtained from the healthy phantom. This observation aligns with the expected behaviour due to the higher dielectric properties of cancerous tissues compared to the healthy structures which is related to the higher water content. Notably, this distinction is most prominent at the initial resonant frequencies. In addition, a slight shift in frequency is observed between the collected signals from two phantoms especially at the first resonant frequency. However, as we move to higher frequencies, there is a decrease in signal penetration and an increase in attenuation which affect the behaviour of the signals collected from both phantoms.

Furthermore, the recorded backscattered signals obtained from the circular antenna array undergo additional processing via two beamforming algorithms, DAS and DMAS. Figures 5-18(a, b) and 5-19(a, b) display the resulting 2D reconstructed images of the constructed healthy and unhealthy human torso phantom, respectively. Figures 5-19(a, b) demonstrates the successful detection of the deep-seated tumour using both algorithms. Notably, DMAS exhibits higher image resolution and provides a more precise estimation of the tumour's size when compared to DAS, as detailed in Table 5-8.

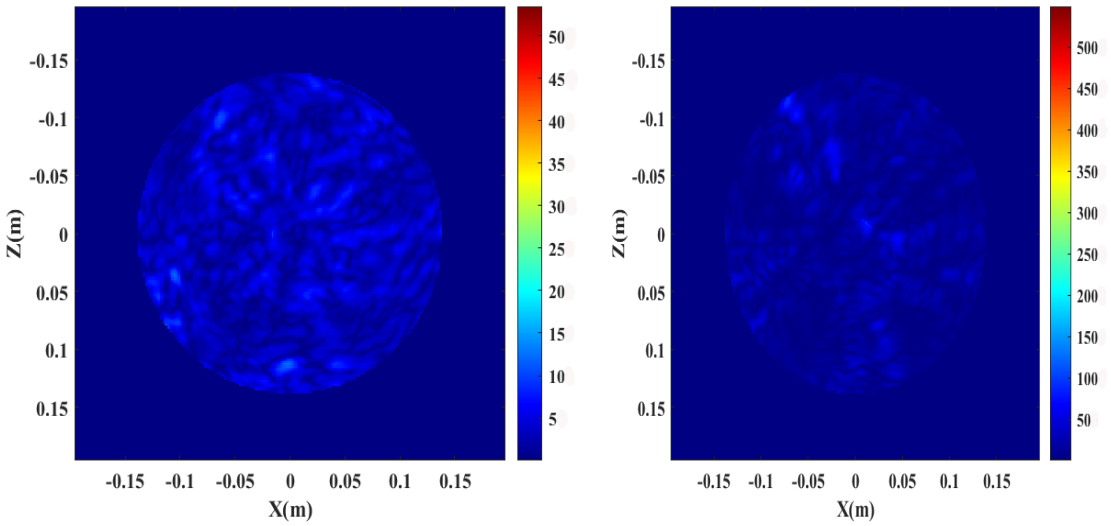

(a) *(b)*

Figure 5- 18 Reconstructed 2D images of the fabricated healthy human torso phantom using: (a)DAS; and (b)DMAS beamforming algorithms.

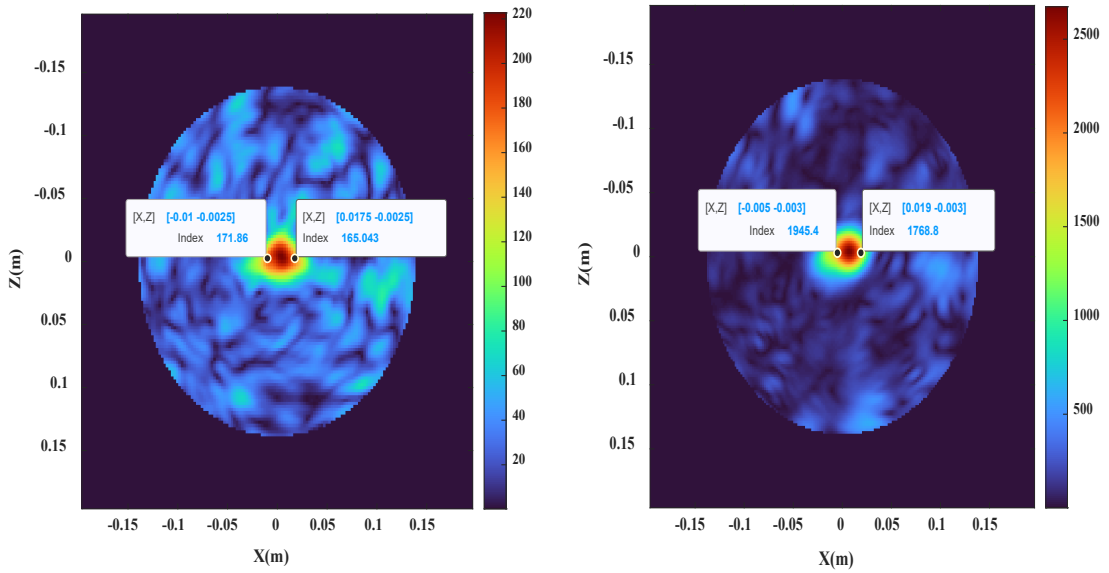

(a) *(b)*

Figure 5- 19 Reconstructed 2D images of the fabricated unhealthy human torso phantom using: (a)DAS; and (b)DMAS beamforming algorithms.

Table 5- 8 *Percentage error of deep-seated lung tumour detection using DAS and DMAS*

Imaging Algorithm	Real tumour radius	Detected tumour radius	% Error
DAS	12.5 mm	13.75 mm	10%
DMAS	12.5 mm	12 mm	4%

5.8 SWB VS UWB Imaging

In this section, we evaluate the impact of an antenna's bandwidth on the imaging performance by comparing the outcomes of utilising super-wide imaging bandwidth to that of utilising ultra-wide imaging bandwidth for lung tumor detection. We chose to compare in the context of detecting lung tumors as this type of cancer presents more detection challenges due to their deep-seated location. To enable a direct comparison between the two cases, instead of using a separate representative UWB antenna to perform UWB imaging that could be affected by the different design and construction of the antenna and not just its bandwidth, the same imaging setup for SWB imaging is

employed for UWB imaging, and the same subtraction technique is utilised where the recorded signals obtained using the healthy phantom are subtracted from those using the unhealthy phantom. However, the range of frequency sweep is changed to reflect an ultra-wide bandwidth. Specifically, we utilise the following frequency ranges: (i) 3.1−40 GHz with 171.23% fractional bandwidth (FBW) for SWB imaging as in our earlier sections; and (ii) 3.1−10 GHz with 105.3% FBW for UWB imaging in this work. This choice of frequency range for UWB imaging is based on recommendations from previous studies on lung and other deep tumour detection [39]. The designed SWB antenna has an impedance bandwidth of 36.9 GHz ($|S_{11}| < -10$ dB), peak realised gain of 3.5 – 6.2 dBi, stable omnidirectional radiation pattern, 97% radiation efficiency, and low cross-polarization level (< −40 dB) within the selected ultra-wide bandwidth.

For a proper comparison between images reconstructed using different imaging bandwidths (SWB and UWB), we employ the SCR metric, which is defined as the ratio of tumour intensity to the clutter intensity in the reconstructed image. Figures 5-20 and Figure 5-21 show the reconstructed images of both cases by DAS, and DMAS algorithm, respectively. The images by SWB imaging have clearer tumour indication and less clutter (light blue and green shades) than those by UWB imaging, affirming that the super-wide bandwidth has enhanced the spatial resolution of the images.

The results in Table 5-9 quantify this enhancement. It shows that SWB imaging can outperform UWB imaging in terms of SCR by up to 84.4%.

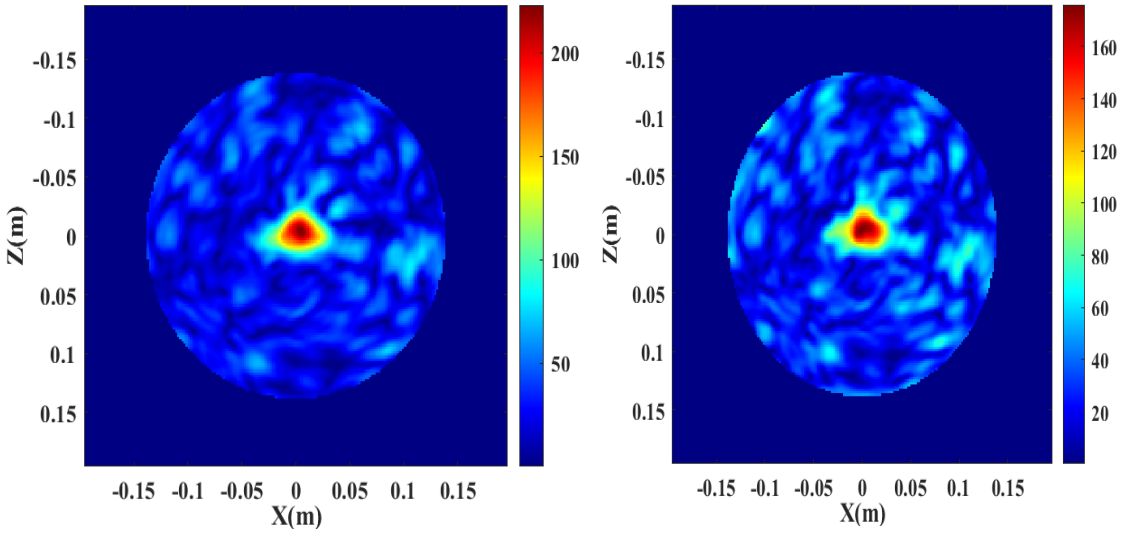

(a) *(b)*

Figure 5- 20 Reconstructed images of lung tumour using DAS by: (a) SWB imaging; and (b) UWB imaging.

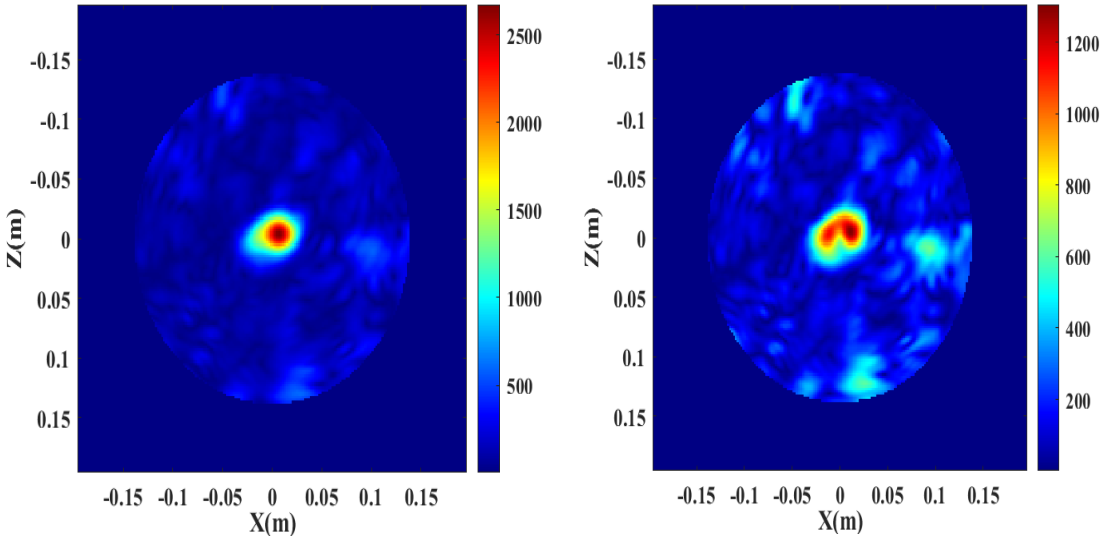

(a) *(b)*

Figure 5- 21 Reconstructed images of lung tumour using DMAS by: (a) SWB imaging; and (b) UWB imaging.

Table 5- 9 *SCR of SWB and UWB imaging of lung tumour*

Beamforming Algorithm	SCR of SWB (dB)	SCR of UWB (dB)	Percentage Improvement
DAS	13.97	9.5	47.1%
DMAS	26	14.1	84.4%

5.9 Summary

This chapter presented a study of dielectric properties of human torso and lung cancer detection based on SWB microwave reflectometry. The obtained dielectric and conducting properties were used to design a phantom model that mimics the biological structure of an adult size human torso. A custom-designed 8-element SWB conformal array set up around the lung phantom was simulated and measured for detecting tumour lesion in both deep and superficial locations. A quick detection was successfully achieved based on the contrast of reflection coefficients between normal and anomalous tissues. A data pattern was further presented to explore the capability of such a detection method for localising the tumour with respect to the array element locations. Furthermore, images of the lung phantom with deep-seated tumour inclusion of different sizes were reconstructed with remarkably enhanced resolution due to using backscattering datasets acquired over a super-wide frequency range. Accurate detection, localisation, and size measurement of deep-seated tumour inclusion was validated using DAS and DMAS beamforming algorithms.

Chapter 6 In-Situ Skin Cancer Detection

6.1 Introduction

This chapter examines the potential of an imaging system based on a SWB antenna for detecting early-stage skin cancer. The structure of this chapter is as follows: In section 6.2, we present the setup for imaging in a simulated environment, including details about the trunk phantom used. Section 6.3 involves the analysis and discussion of S-parameter results. Following that, in section 6.4, we introduce the image reconstruction technique and showcase the reconstructed images. Section 6.5 explores the early-stage skin cancer detection within an actual measurement setting. Finally, section 6.6 summarises the chapter.

6.2 Phantom Modelling for Skin Cancer Detection

In this section, we modelled a human trunk phantom with tumour lesion using a cylindrical structure consisting of six tissue layers (skin, fat, muscle, cancellous bone, lung and skin cancer inclusion). The modelled phantom mimics an adult size torso with a perimeter of 82.3 cm. The skin tumour is further modelled as a cylindrical disc of 7.5 mm radius, 1 mm thickness, and embedded at a depth of 1mm below the external skin tissue. Figure 6-1 shows the structure and dimensions of our phantom. A simulated study is performed using Ansys HFSS where eight SWB antenna elements are positioned uniformly around the phantom and at a distance of 10 mm away from the skin layer as shown in Figure 6-2. The skin tumour is placed near to Antenna 1. The dielectric properties of each phantom layer are calculated using the Cole-Cole model [140] and listed in Table 6-1. The properties are calculated at a frequency of 7.8 GHz, which corresponds to the second resonant frequency of our SWB antenna, and where the signal wavelength provides suitable penetration depth for skin cancer detection while not incurring excessive frequency-related attenuation.

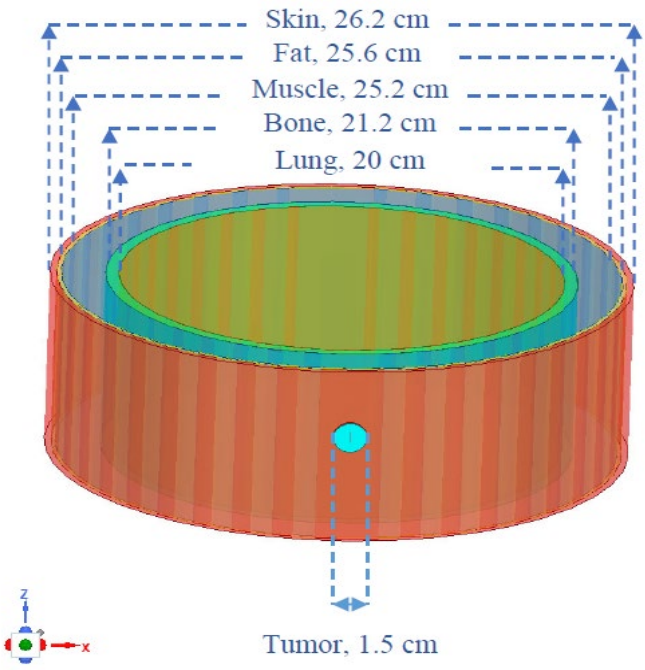

Figure 6- 1 Human trunk phantom with tumour lesion on skin tissue.

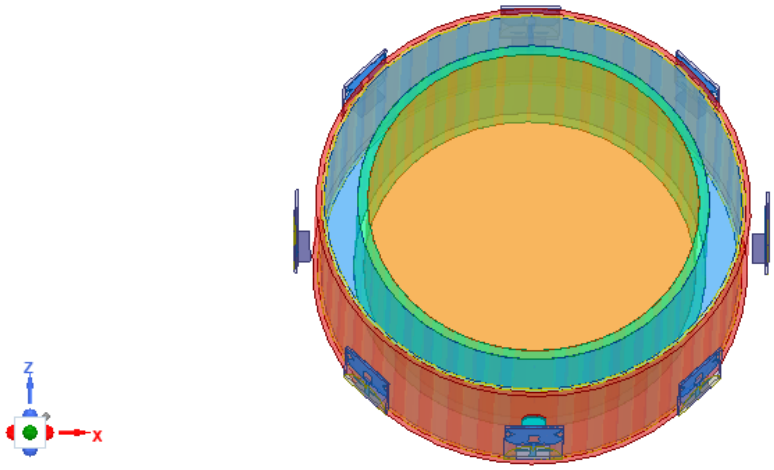

Figure 6- 2 SWB antenna array positioned around phantom with 45˚ separation.

Table 6- 1 *Dielectric properties of trunk phantom with tumour using Cole-Cole model at 7.8 GHz*

Tissue	Relative Permittivity ε_r	Conductivity σ (S/m)	Loss tangent tanδ
Skin	33.36	5.6	0.388
Fat	9.32	1.24	0.306
Muscle	45.74	7.55	0.379
Cancellous bone	13.95	2.98	0.492
Inflated Lung	17.36	3.05	0.405
Tumour	51.01	9.67	0.437

6.3 S-Parameters Results

In this section, we present a comparison between simulated S-parameters of the healthy phantom (without skin tumour) and unhealthy phantom (with skin tumour). It should be noted that the dielectric properties of cancerous tissue would tend to be higher than those of normal tissues, due to the higher water and oil content in the malignant lesions. Figure 6-3 shows the magnitude of reflection coefficients ($|S_{11}|$ to $|S_{88}|$) from all eight antennas, while Figure 6-4 shows their zoomed-in responses at 3.8 GHz, 7.8 GHz, and 14.8 GHz, which represent the first, second, and third resonant frequencies of the antenna, respectively. It can be observed that the unhealthy phantom shows higher reflection compared to the healthy phantom at all three resonant frequencies. The largest observed difference in reflection response between healthy and unhealthy phantoms is ~ 6.8 dB, attributed by Antenna 1, i.e. the antenna nearest to and facing the cancerous lesion; and expectedly occurs at the second resonant frequency (same frequency for calculating the phantom's dielectric properties). This difference in reflection response is due to the significant influence of constituent water content in the malignant lesions.

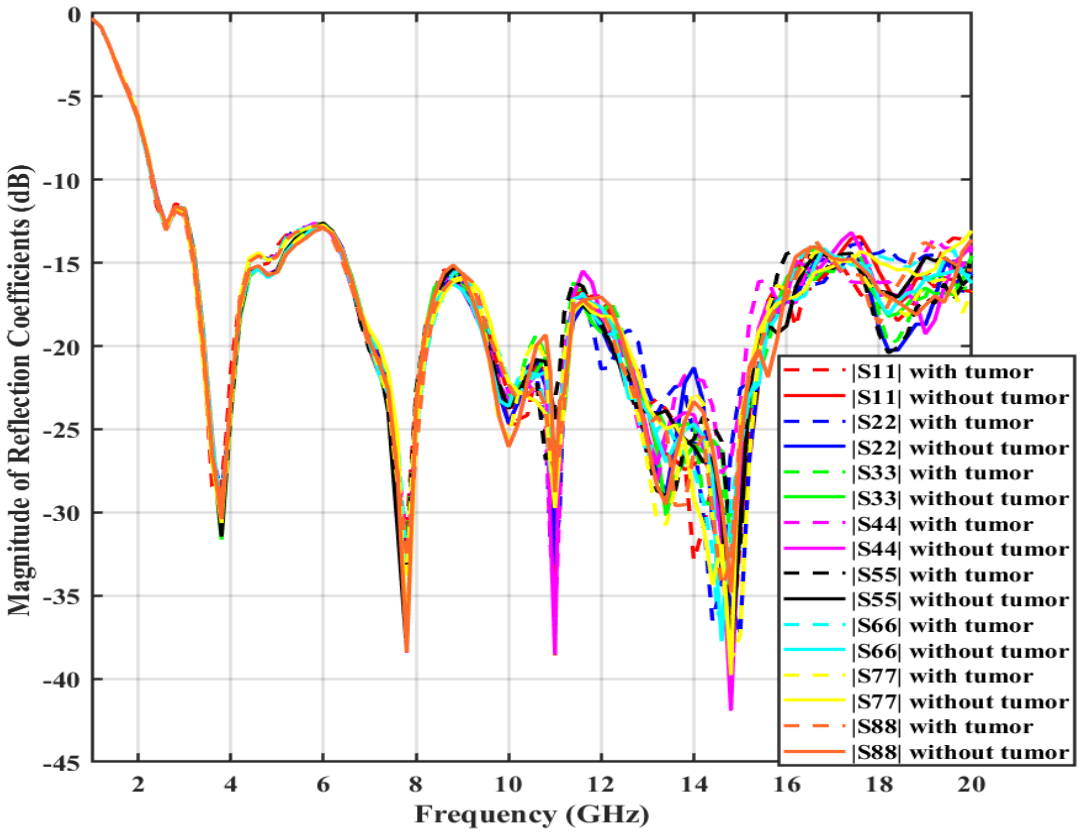

Figure 6- 3 Magnitude of reflection coefficients of all eight antennas from healthy and unhealthy phantoms

Figure 6-5 shows the corresponding magnitude of transmission coefficients, which reflect the degree of undesired mutual coupling between antenna elements in the circular array. For improved presentation, we plotted only forward transmission coefficients from all but one array elements (Antenna 2, 3, .8) to Antenna 1, since the reversed transmission coefficients from Antenna 1 to all other array elements are found to exhibit a similar performance trend. It is observed that a low mutual coupling of below -30 dB, i.e. good isolation between array elements, is preserved over the entire covered bandwidth. Comparing between the healthy and unhealthy phantom, it is also evident that the transmission coefficients in the case of healthy phantom are slightly better (implying lower loss). This observation is consistent with the known effect of tumour lesion, which is the high scattering of signals.

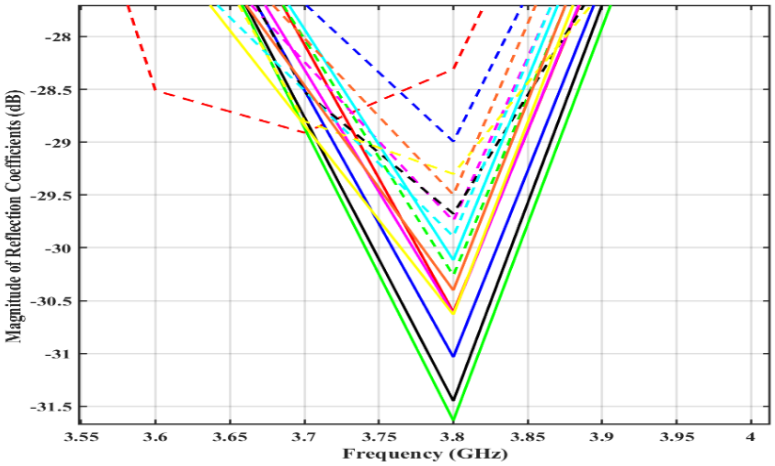

(a)

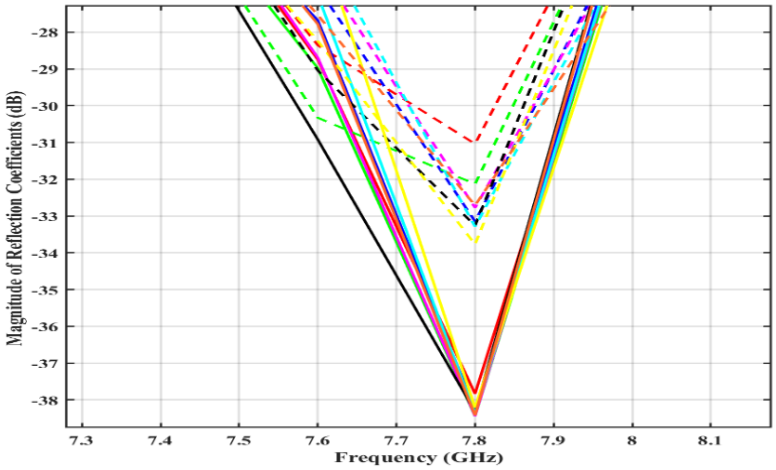

(b)

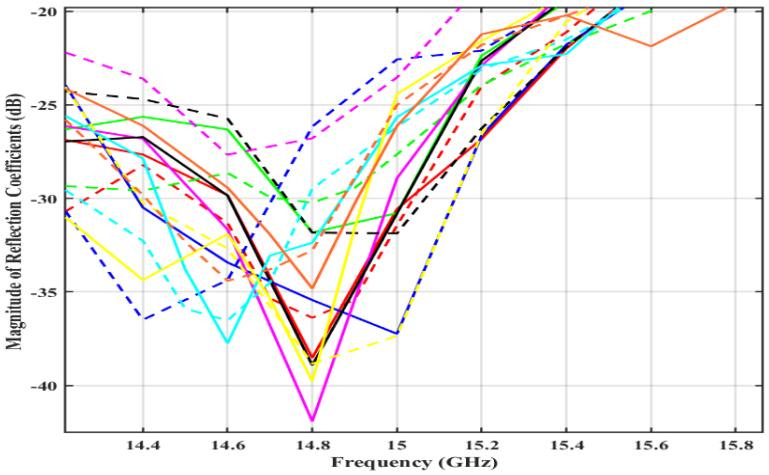

(c)

Figure 6- 4 Zoomed-in reflection response at: (a) 3.5 GHz; (b) 7.8 GHz; and (c) 14.8 GHz.

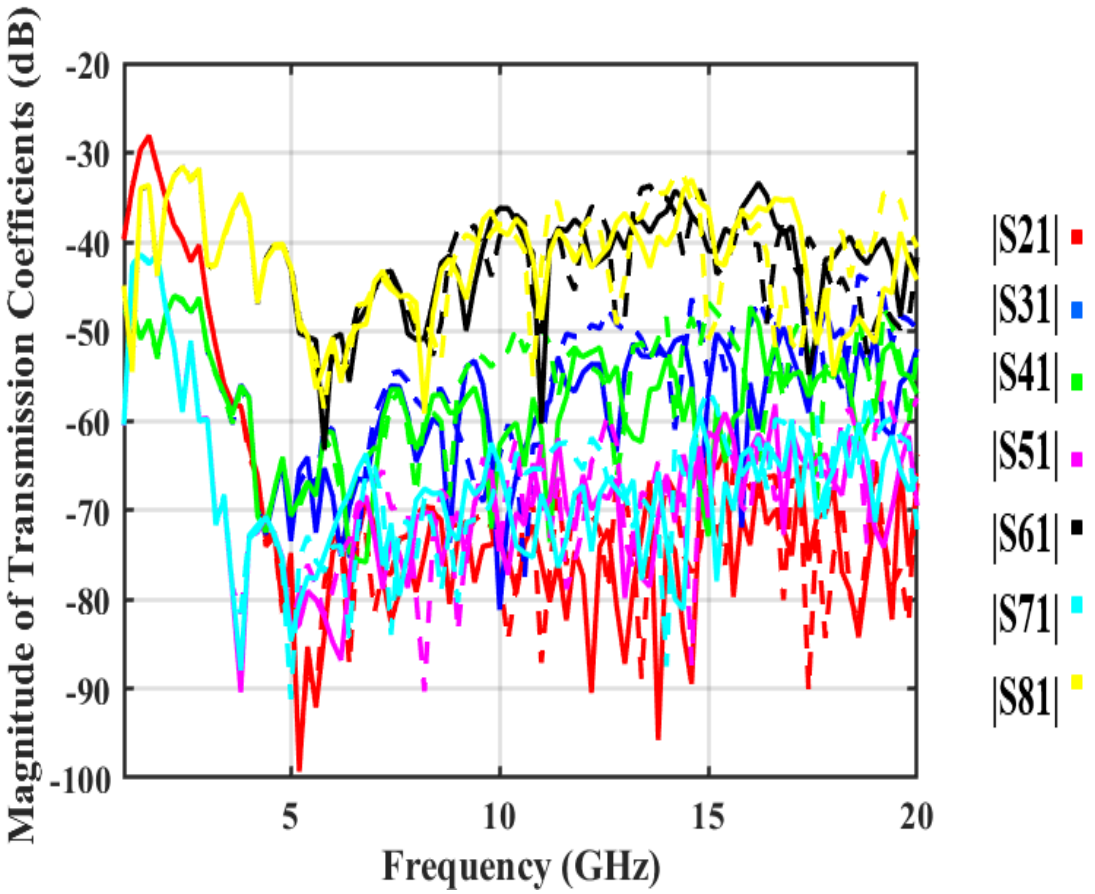

Figure 6- 5 Magnitude of transmission coefficients from all eight antennas in healthy (solid line) and unhealthy (dashed line) phantoms.

6.4 Image Reconstruction

In this section, 2D images of the trunk phantom are generated using the DMAS algorithm, the image reconstruction process is implemented on both healthy and unhealthy phantoms. Figure 6-6 shows the reconstructed image of the healthy phantom where X and Z are the image axes, corresponding to the horizontal plane, and vertical plane in the phantom space, respectively.

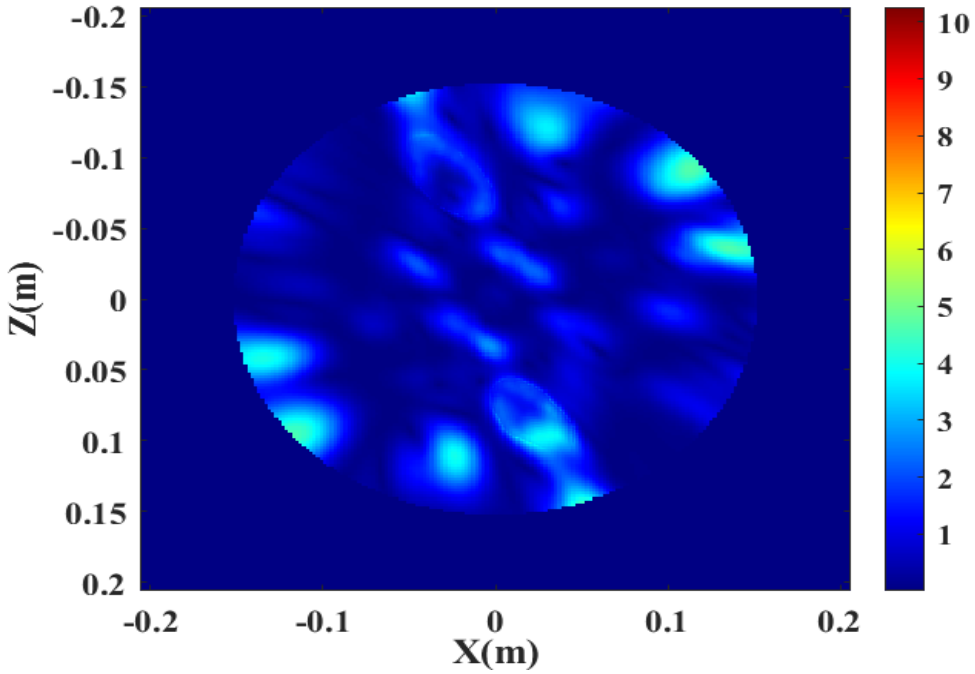

Figure 6- 6 Reconstructed image of healthy phantom using S-parameters obtained in the frequency range of 2.5–20 GHz.

The images of the tumour lesions in unhealthy phantom are obtained using simulated S-parameter data. The image in Figure 6-7 is using S-parameters acquired over a relatively small, covered bandwidth of 7.5 GHz in the frequency range of 2.5–10 GHz. The detected tumour in this scenario is 8.65 mm in radius and 1.4 mm thickness below the skin layer. Another image in Figure 6-8 is using S-parameters acquired over a wider covered bandwidth of 17.5 GHz in the frequency range of 2.5–20 GHz. It is generated with enhanced clutter removal and improved resolution due to the bandwidth enlargement. The detected tumour in this scenario is 8 mm in radius and 1.3 mm thickness below the skin layer. The centre of the detected tumour is estimated to be located at (0, 154.3) mm in both scenarios.

The actual radius, thickness, and location of the tumour are 7.5 mm, 1 mm, and (0, 154.5) mm, respectively. The corresponding percentage errors are calculated as shown in Table 6-2. It can be observed that both scenarios could result in successful tumour detection and localisation. However, utilising a wider covered bandwidth and higher frequency data points expectedly results in better image resolution and consequently more accurate estimation in terms of the tumour's radius and thickness.

Table 6- 2 *Percentage Error*

Parameter	Covered bandwidth	Estimated result	Absolute error	Percentage error
Radius	17.5 GHz	8 mm	1 mm	6.66%
	7.5 GHz	8.65 mm	2.3 mm	15.33%
Thickness	17.5 GHz	1.3 mm	0.3 mm	30%
	7.5 GHz	1.4 mm	0.4 mm	40%
Location	17.5 GHz	(0, 154.3) mm	(0, 0.2) mm	0.13%
	7.5 GHz			

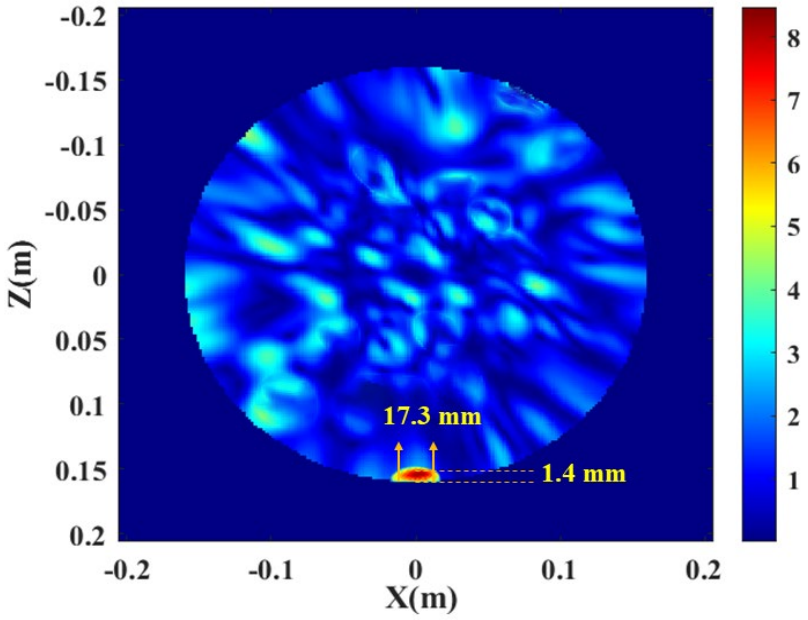

Figure 6- 7 Reconstructed image of unhealthy phantom using S-parameters obtained in the frequency range of 2.5–10 GHz.

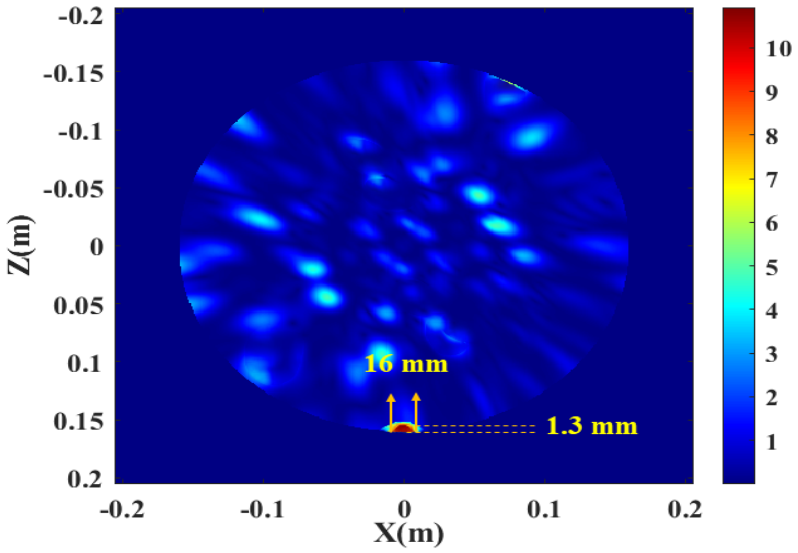

Figure 6- 8 Reconstructed image of unhealthy phantom using S-parameters obtained in the frequency range of 2.5–20 GHz.

6.5 Experimental Investigation of In-Situ Skin Cancer Detection

In this section, real experiments were performed in free space to evaluate the previous finding in the simulated imaging setup and to validate the capability of the proposed SWB antenna array system in detecting several tumour types and locations. A trunk phantom is constructed using five layers (skin, fat, muscle, rib bone and lung) composed of mimicking mixtures. For the purpose of this section, the same phantom composition that was initially designed for lung tumour detection was utilised to assess the capability of the proposed SWB antenna in detecting various types and locations of tumours. The imaging setup, as shown in Figure 6-9, involved the use of two phantoms. One was a healthy phantom, without any tumour inclusion, while the other was a cancerous phantom with a tumour embedded in the external skin layer of the fabricated trunk phantom. In the latter case, a grape slice with dimensions of 1 mm thickness and 10 mm radius was inserted into the healthy phantom after recording the measurements. The imaging setup for in-situ skin cancer detection is illustrated in Figure 6-10.

where the phantom was positioned on a rotatable platform with a radius of 13.1 cm (diameter of 26.2 cm). Eight SWB elements from the proposed antennas were arranged in a circular configuration around the fabricated phantom, each separated by 45 degrees. A consistent 1 cm separation was maintained between each antenna element and the target object. The imaging setup, as shown in Figure 6-10, involves connecting

port 1 of the VNA to the transmitting antenna, while port 2 is linked to the common port of the SP6T PE71S6332 Pasternack RF switch, which operates across a frequency range from DC to 40 GHz. In this multistatic approach, signals received from the other 7 antenna elements connected to the RF switch are recorded. Subsequently, the transmitting antenna is switched to another element to complete the entire measurement process.

This procedure was executed for both fabricated phantoms, the healthy one and the cancerous one. Following this, an artifact removal technique was applied by subtracting the recorded signals obtained from the healthy phantom from those acquired using the cancerous phantom. The backscattered signals collected from all antenna elements were compared over the operational frequency range of the proposed SWB antenna, across 3.1 to 40 GHz.

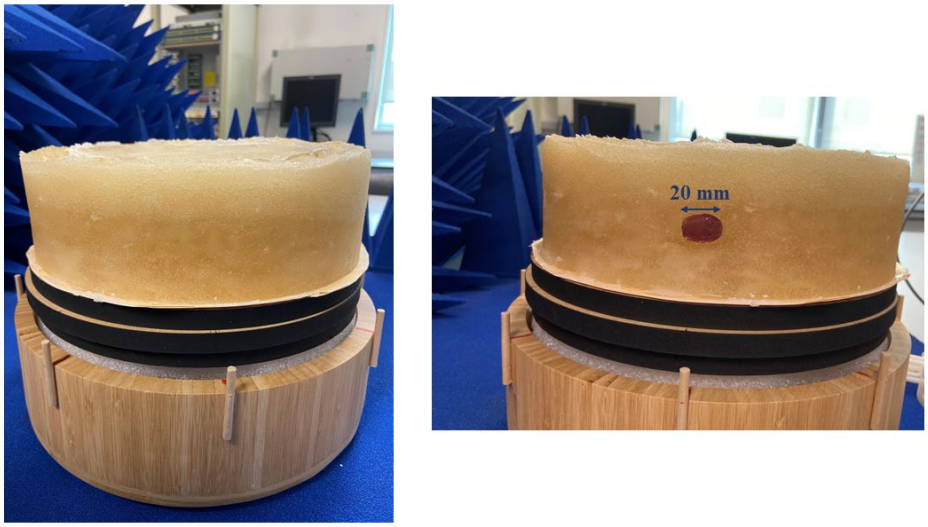

(a) *(b)*

Figure 6- 9 Constructed human trunk phantoms for skin cancer detection: (a)healthy phantom; (b)cancerous phantom with tumour inclusion.

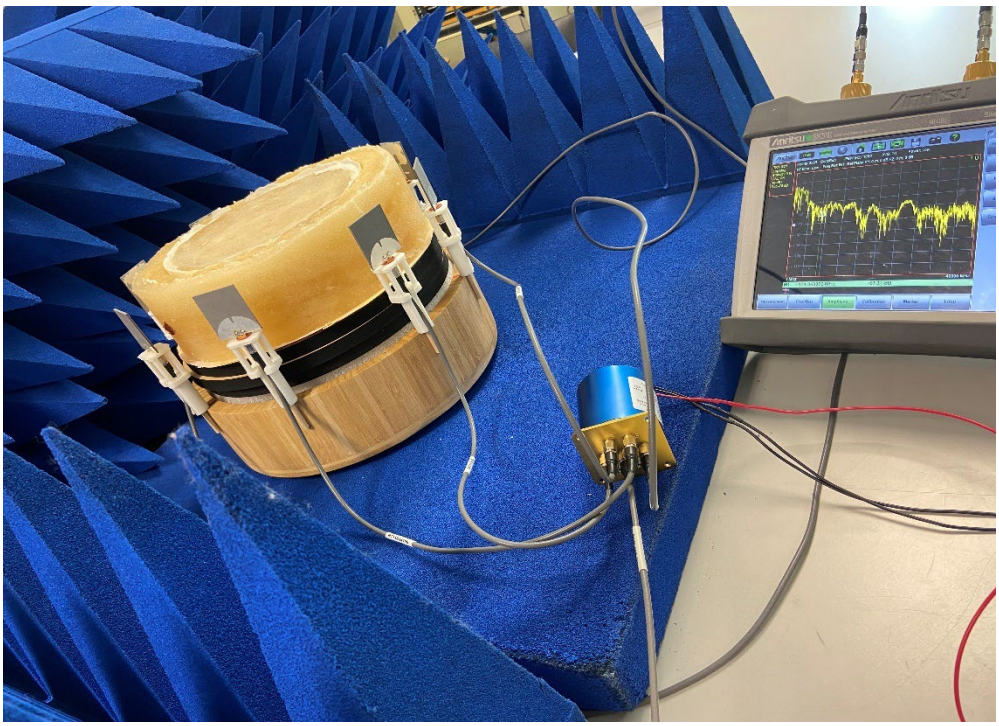

Figure 6- 10 In-situ skin cancer detection experimental setup.

The acquired reflection coefficient from the antenna that is directly mounted toward the inserted tumour is compared with the one obtained from the healthy phantom as illustrated in Figure 6-13. The results show that the reflected signal from the cancerous phantom shows higher reflection compared to the one acquired from the healthy phantom. It is observed that the reflected signal from the cancerous phantom is shifted in frequency to the lower band especially at the first and the second resonant frequencies.

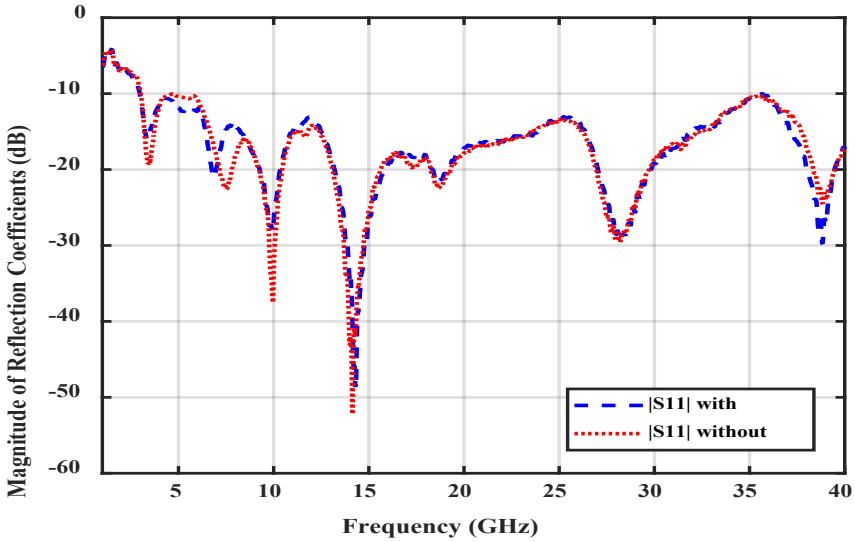

Figure 6- 11 Measured reflection Coefficient at antenna 1 facing the skin tumour.

Observing the data, it's evident that the $|S_{11}|$ level is -21 dB at 6.8 GHz for the cancerous phantom, whereas it indicates -22.6 dB at 7.5 GHz for the healthy phantom. This discrepancy reveals a frequency shift of 0.7 GHz, attributable to the presence of the skin tumour. Then, the recorded signals from all array elements are further processed using two confocal beamforming algorithms, namely DAS and DMAS. The resultant images clearly demonstrate the successful detection of skin cancer using both algorithms. However, it is worth highlighting that DMAS exhibits a superior ability to accurately determine the tumour size, in addition to providing enhanced resolution when compared to DAS. Notably, the utilisation of a super wide bandwidth over the range 3.1 to 40 GHz contributed to the improved resolution of the reconstructed images in both the DAS and DMAS algorithms. For the assessment of in-situ skin cancer detection, the percentage error was calculated for the data acquired using DAS and DMAS, with the results presented in Table 6-3.

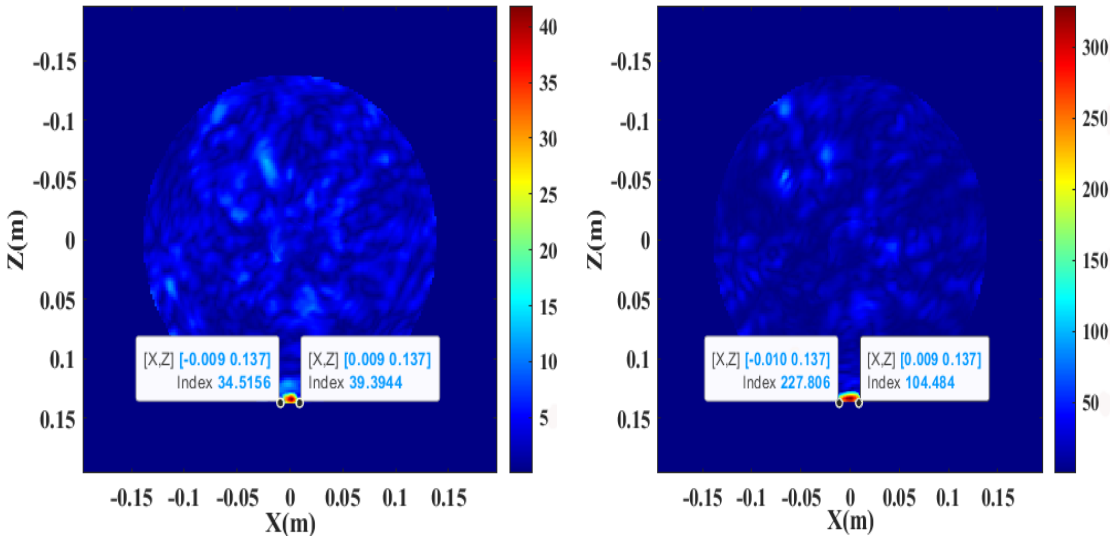

(a) *(b)*

Figure 6- 12 Reconstructed images of skin cancer detection measurement using two beamforming algorithms: (a)DAS; (b)DMAS.

Table 6- 3 *Percentage error of in-situ skin cancer detection using DAS and DMAS*

Imaging Algorithm	Real tumour radius	Detected tumour radius	% Error
DAS	10 mm	9 mm	10%
DMAS	10 mm	9.5 mm	5%

6.6 Summary

In this chapter, we investigated the capability of a SWB antenna array system in detecting in-situ skin cancer through S-parameter analysis and microwave imaging with high resolution. The analysis of the S-parameter results shows notable differences between the backscattered signals from healthy and unhealthy phantoms due to the dielectric contrast. The proposed system shows promising results in detecting and localising early-stage skin tumour with 7.5 mm radius and 1 mm thickness. In future work, a real experimental measurement will be conducted on a fabricated trunk phantom that mimics the dielectric properties of human tissues across a super wide bandwidth in the frequency range from 2.45–35.4 GHz.

Chapter 7 Conclusion and Recommendations for Future Work

7.1 Conclusion

This research and thesis focuses on the development of a super wideband (SWB) antenna designed to operate in the frequency range of 3.1 to 40 GHz for medical imaging applications. The research primarily focuses on three key areas: enhancing the performance of biomedical antennas, refining the accuracy of equivalent circuit modelling, and investigating the potential of SWB antennas in effectively detecting various types of tumours, particularly in their early stages.

The initial three chapters provide an introduction to the research, background context, and an extensive review of related literature. Chapter 4 discussed the exploration of a novel fractal-loaded slot SWB antenna designed for medical imaging applications. This chapter involves various testing of critical performance parameters and an in-depth examination of accurate lumped element circuit modelling across a frequency range of 2.5 to 40 GHz.

Chapter 5 studied the evaluation of the proposed SWB antenna's efficacy in the detection of lung tumours, with a focus on using a circular array system. The research within this chapter entails both simulation and experimental approaches, including the investigation of dielectric properties of the layers comprising a human torso phantom using Nicolson-Ross-Weir (NRW) conversion techniques. Multiple studies involving different tumour sizes and locations are conducted, with a special emphasis on early-stage tumour detection. A human-sized torso phantom, constructed from various tissue-equivalent materials, is utilised for these measurements. Notably, a deep-seated lung tumour, measuring 12.5 mm in radius and positioned at the phantom's centre, is successfully detected and imaged using two beamforming algorithms. The utilisation of super wide bandwidth yields successful detection and high-resolution image generation.

In Chapter 6, the proposed SWB antenna, arranged in a circular array configuration, is subjected to testing for another type of tumour, particularly skin cancer, with a special focus on early-stage detection of this serious disease. Several simulation and measurement experiments are conducted using a small-sized tumour with defined thickness, placed on the external skin layer. Data acquired from the measurement of a grape slice, measuring 10 mm in radius and 1 mm in thickness, demonstrate successful

detection and enhanced image resolution, validating the antenna's adaptability for different medical imaging applications.

7.2 Contributions

- A novel SWB antenna design was introduced and optimised for microwave reflectometry to enhance the detection of early-stage tumours. The antenna, featuring dimensions of 40×35×1.57 mm³, incorporates various bandwidth and gain enhancement techniques, including tapered feedline, a semi-elliptical slotted ground plane, and an elliptical patch embedded with two fractal slots at the upper corners. The compact size of the antenna allow larger array elements which leads to more information and as subsequent, better detection outcome. It achieves an impressive operating bandwidth of 3.1 to 40 GHz (a ratio of 12.9:1) and exhibits low $|S_{11}|$ levels of -20.7 dB, -19.4 dB, and -34.2 dB at the first three resonant frequencies (3.8 GHz, 6.7 GHz, and 9.6 GHz). With a peak gain ranging from 3.4 to 9.7 dBi and 94% radiation efficiency, this antenna design is well-suited for microwave imaging applications.
- A precise and straightforward equivalent circuit model (ECM) that accurately represents the SWB antenna behaviour across the entire bandwidth was proposed. An optimisation approach involving dual sequential optimisation is presented to determine optimal values for each lumped element. This ECM closely matches the antenna's performance when compared to full-wave simulation and measured results, with a low mean absolute percentage error of 4.9% for $|S_{11}|$, 7.5% for real impedance, and 7.7% for imaginary impedance.
- A SWB microwave reflectometry was implemented for enhanced detection of lung tumours, especially in their early stages and in deep-seated and superficial locations. This approach showcases the potential of SWB microwave reflectometry in precisely sizing early-stage tumours, even in deep regions, using a human-sized torso phantom consisting of five layers. The dielectric properties of these phantom layers are thoroughly characterized over the entire bandwidth.
- A SWB antenna-based imaging system was explored for in-situ skin cancer detection. The imaging system employs eight antenna elements in a circular array around a human trunk phantom that mimics five concentric layers of

different tissues. The dielectric properties of these tissues are measured across the bandwidth (3.1 to 40 GHz), and skin tumours are modelled as cylindrical shapes on the outer skin layer. The resulting 2D images of the trunk area exhibit improved resolution, enabling more accurate estimations of tumour radius and thickness.

7.3 Limitations and Future Work

While this research has made significant progress, several limitations remain, opening up promising avenues for future exploration in this field:

Enhancing RFMI Performance:

- Increasing the number of antenna elements used in the imaging scan measurements could be a critical improvement. Exploring suitable configurations for scanning the human torso phantom can further enhance the system's performance. For example, the use of dual-polarized antennas in RFMI may lead to more precise detection and increased information extraction from backscattered signals.
- Investigating alternative clutter removal mechanisms holds potential for reducing interference, thereby improving the accuracy of tumour detection and enhancing image resolution.

Automated Data-Driven Modelling:

- In the area of equivalent circuit modelling, the concept of automated data-driven modelling is a promising direction. Integrating machine learning techniques can help capture complex relationships between physical variables. This approach minimizes the need for extensive human intervention in ECM development, leading to models that offer both high accuracy and time efficiency. Such models can significantly enhance antenna performance while reducing simulation time.

Clinical Testing and Tumour Characterization:

- Expanding the scope of the proposed imaging system involves conducting clinical tests on various cancer types, including lung, breast, skin, and brain tumours. These tests can provide valuable insights into the system's applicability and efficacy in different clinical scenarios.

- Investigating the dielectric properties of freshly excised tumour tissues over the entire covered frequency range offers a valuable avenue for characterizing tumours more accurately. This data can further refine the imaging system's capabilities and contribute to its clinical utility.

In summary, future research endeavours in this field can focus on optimising RFMI performance, automating equivalent circuit modelling, and conducting comprehensive clinical tests to assess the system's effectiveness across various cancer types and tissue characteristics.

References

1. Conceição, R.C., J.J. Mohr, and M. O'Halloran, *An introduction to microwave imaging for breast cancer detection*. 2016: Springer.
2. Chandra, R., et al., *Medical microwave imaging and analysis*, in *Medical Image Analysis and Informatics*. 2017, CRC Press. p. 451-466.
3. Zamani, A., S. Rezaeieh, and A. Abbosh, *Lung cancer detection using frequency-domain microwave imaging.* Electronics Letters, 2015. **51**(10): p. 740-741.
4. Faouri, Y., et al., *Compact super wideband frequency diversity hexagonal shaped monopole antenna with switchable rejection band.* IEEE Access, 2022. **10**: p. 42321-42333.
5. Ez-Zaki, F., et al., *Circuit modelling of broadband antenna using vector fitting and foster form approaches for IoT applications.* Electronics, 2022. **11**(22): p. 3724.
6. Amro, W.H.A.A. and M.K. Abdelazeez, *Analysis and optimisation of super-wideband monopole antenna with tri-band notch using a transmission line model.* IET Microwaves, Antennas & Propagation, 2019. **13**(9): p. 1373-1381.
7. Balani, W., et al., *Design and analysis of super wideband antenna for microwave applications.* Sensors, 2021. **21**(2): p. 477.
8. Lim, J.Z., et al., *Conjunctival Melanoma in Aotearoa—New Zealand: A 21-Year Analysis of Incidence and Survival.* The Asia-Pacific Journal of Ophthalmology, 2023. **12**(3): p. 273-278.
9. Pandeya, N., et al., *The diagnosis and initial management of melanoma in Australia: findings from the prospective, population-based QSkin study.* Medical Journal of Australia, 2023.
10. Alamro, W. and B.-C. Seet, *Review of practical antennas for microwave and millimetre-wave medical imaging.* Electromagnetic Waves and Antennas for Biomedical Applications, 1st ed.; Wang, L., Ed, 2021: p. 185-207.
11. Agrawal, S., Z. Wani, and M.S. Parihar, *Patch loaded slot antenna for super wideband applications with dual-band notch characteristic.* Wireless Personal Communications, 2022: p. 1-14.
12. Kundu, S., *A Compact Super Wideband Planar Monopole Antenna for Microwave Imaging Applications.* National Academy Science Letters, 2023: p. 1-5.
13. Aggarwal, I., S. Pandey, and M.R. Tripathy, *A high gain super wideband metamaterial based antenna.* Journal of Microwaves, Optoelectronics and Electromagnetic Applications, 2021. **20**: p. 248-273.
14. Ahmed, A., V. Kumari, and G. Sheoran, *Experimental investigation of microwave holographic reflectometry for lung tumor detection.* Measurement, 2022. **197**: p. 111336.
15. Khalesi, B., et al., *A Microwave Imaging Procedure for Lung Lesion Detection: Preliminary Results on Multilayer Phantoms.* Electronics, 2022. **11**(13): p. 2105.
16. Babarinde, O., et al. *Microwave imaging technique for lung tumour detection*. in *2016 German Microwave Conference (GeMiC)*. 2016. IEEE.
17. Ameer, W., et al. *Use of directional UWB antenna for lung tumour detection*. in *2019 2nd International Conference on Advancements in Computational Sciences (ICACS)*. 2019. IEEE.

18. Darvazehban, A., et al., *Pattern reconfigurable metasurface antenna for electromagnetic torso imaging.* IEEE Transactions on Antennas and Propagation, 2019. **67**(8): p. 5453-5462.
19. Alani, S., et al., *Microwave imaging of breast skin utilizing elliptical uwb antenna and reverse problems algorithm.* Micromachines, 2021. **12**(6): p. 647.
20. Kaur, K. and A. Kaur, *In vitro detection of skin cancer using an UWB stacked micro strip patch antenna with microwave imaging.* International Journal of RF and Microwave Computer-Aided Engineering, 2022. **32**(12): p. e23407.
21. Khalesi, B., et al. *Skin cancer detection through microwaves: Validation on phantom measurements*. in *2018 IEEE International Conference on Imaging Systems and Techniques (IST)*. 2018. IEEE.
22. Mirbeik-Sabzevari, A., et al., *Synthetic ultra-high-resolution millimeter-wave imaging for skin cancer detection.* IEEE Transactions on Biomedical Engineering, 2018. **66**(1): p. 61-71.
23. Tripathi, A.M., P.K. Rao, and R. Mishra. *An AMC inspired wearable UWB antenna for skin cancer detection*. in *2020 International Conference on Electrical and Electronics Engineering (ICE3)*. 2020. IEEE.
24. Balani, W., et al., *Design techniques of super-wideband antenna–existing and future prospective.* Ieee access, 2019. **7**: p. 141241-141257.
25. Alamro, W.A., et al. *Compact Super-Wideband Antenna for Medical Imaging Applications*. in *2021 IEEE Conference on Antenna Measurements & Applications (CAMA)*. 2021. IEEE.
26. Sheng, X., et al., *Design of miniaturized FSS using equivalent circuit model and multi-objective particle swarm optimization.* Journal of Physics D: Applied Physics, 2021. **54**(40): p. 405001.
27. Balanis, C.A., *Antenna theory: analysis and design*. 2016: John wiley & sons.
28. Pozar, D.M., *Microwave and RF design of wireless systems*. 2000: John Wiley & Sons.
29. Kraus, J.D. and R.J. Marhefka, *Antennas for all applications.* Antennas for all applications, 2002.
30. Pozar, D.M., *Microwave engineering*. 2011: John wiley & sons.
31. Sharma, M.K., et al., *Experimental investigation of the breast phantom for tumor detection using ultra-wide band–MIMO antenna sensor (UMAS) probe.* IEEE Sensors Journal, 2020. **20**(12): p. 6745-6752.
32. Pondicherry, A., et al., *The burden of non-melanoma skin cancers in Auckland, New Zealand.* Australasian Journal of Dermatology, 2018. **59**(3): p. 210-213.
33. Darvazehban, A., S.A. Rezaeieh, and A. Abbosh, *Pattern-reconfigurable loop–dipole antenna for electromagnetic pleural effusion detection.* IEEE Transactions on Antennas and Propagation, 2020. **68**(8): p. 5955-5964.
34. Inum, R., et al., *EBG based microstrip patch antenna for brain tumor detection via scattering parameters in microwave imaging system.* International journal of biomedical imaging, 2018. **2018**.
35. Sohani, B., et al., *Detection of haemorrhagic stroke in simulation and realistic 3-D human head phantom using microwave imaging.* Biomedical Signal Processing and Control, 2020. **61**: p. 102001.
36. Bashri, M.S.R. and T. Arslan, *Low-cost and compact RF switching system for wearable microwave head imaging with performance verification on artificial head phantom.* IET Microwaves, Antennas & Propagation, 2018. **12**(5): p. 706-711.

37. Beckert, L., Laking, G., *All the cancer you cannot see.* The New Zealand Medical Journal, Te ara tika o te hauora hapori, 2022. **135**(1556).
38. Amin, M.B., et al., *The eighth edition AJCC cancer staging manual: continuing to build a bridge from a population-based to a more "personalized" approach to cancer staging.* CA: a cancer journal for clinicians, 2017. **67**(2): p. 93-99.
39. Hossain, A., et al., *A planar ultrawideband patch antenna array for microwave breast tumor detection.* Materials, 2020. **13**(21): p. 4918.
40. Abbosh, A., B. Mohammed, and K. Bialkowski, *Differential microwave imaging of the breast pair.* IEEE Antennas and Wireless Propagation Letters, 2015. **15**: p. 1434-1437.
41. Rezaeieh, S.A., et al., *Feasibility of using wideband microwave system for non-invasive detection and monitoring of pulmonary oedema.* Scientific reports, 2015. **5**(1): p. 14047.
42. Wang, L., *Three-dimensional holographic electromagnetic imaging for accessing brain stroke.* Sensors, 2018. **18**(11): p. 3852.
43. Santos, K.C., Fernandes, C. A., Costa, J. R. , *Feasibility of Bone Fracture Detection Using Microwave Imaging* IEEE Open Journal of Antennas and Propagation, 2022. **3**: p. 836-847.
44. Amin, B., et al., *A feasibility study on microwave imaging of bone for osteoporosis monitoring.* Medical & Biological Engineering & Computing, 2021. **59**: p. 925-936.
45. Wang, M., L. Crocco, and M. Cavagnaro, *On the design of a microwave imaging system to monitor thermal ablation of liver tumors.* IEEE Journal of Electromagnetics, RF and Microwaves in Medicine and Biology, 2021. **5**(3): p. 231-237.
46. Porter, E., et al., *A wearable microwave antenna array for time-domain breast tumor screening.* IEEE transactions on medical imaging, 2016. **35**(6): p. 1501-1509.
47. Subramanian, S., B. Sundarambal, and D. Nirmal, *Investigation on simulation-based specific absorption rate in ultra-wideband antenna for breast cancer detection.* IEEE sensors journal, 2018. **18**(24): p. 10002-10009.
48. Bahramiabarghouei, H., et al., *Flexible 16 antenna array for microwave breast cancer detection.* IEEE Transactions on Biomedical Engineering, 2015. **62**(10): p. 2516-2525.
49. Alhawari, A., *Lung tumour detection using ultra-wideband microwave imaging approach.* Journal of Fundamental and Applied Sciences, 2018. **10**(2).
50. Pastorino, M. and A. Randazzo, *Microwave imaging methods and applications*. 2018: Artech House.
51. Janjic, A., et al., *SAFE: A novel microwave imaging system design for breast cancer screening and early detection—Clinical evaluation.* Diagnostics, 2021. **11**(3): p. 533.
52. Casu, M.R., et al., *A COTS-based microwave imaging system for breast-cancer detection.* IEEE transactions on biomedical circuits and systems, 2017. **11**(4): p. 804-814.
53. Wang, L., *Multi-frequency holographic microwave imaging for breast lesion detection.* IEEE Access, 2019. **7**: p. 83984-83993.
54. Elahi, M.A., et al., *Evaluation of image reconstruction algorithms for confocal microwave imaging: Application to patient data.* Sensors, 2018. **18**(6): p. 1678.

55. Selvaraj, V., et al., *Detection of depth of the tumor in microwave imaging using ground penetrating radar algorithm.* Progress In Electromagnetics Research M, 2020. **96**: p. 191-202.
56. Travis, W.D., *Pathology of lung cancer.* Clinics in chest medicine, 2002. **23**(1): p. 65-81.
57. Ambrosini, V., et al., *PET/CT imaging in different types of lung cancer: an overview.* European journal of radiology, 2012. **81**(5): p. 988-1001.
58. Farina, L., et al., *Histology-Validated Dielectric Characterisation of Lung Carcinoma Tissue for Microwave Thermal Ablation Applications.* Cancers, 2023. **15**(14): p. 3738.
59. Wang, J.-R., et al., *Experimental study of dielectric properties of human lung tissue in vitro.* Journal of Medical and Biological Engineering, 2014. **34**(6): p. 598-604.
60. Linares, M.A., A. Zakaria, and P. Nizran, *Skin cancer.* Primary care: Clinics in office practice, 2015. **42**(4): p. 645-659.
61. Alasadi, A.H.H. and B.M.R. AL-Safy, *Early detection and classification of melanoma skin cancer*. 2016: LAP LAMBERT Academic Publishing.
62. Jin, J.-M., *The finite element method in electromagnetics*. 2015: John Wiley & Sons.
63. Wang, L. and A. Al-Jumaily, *Numerical study of holographic electromagnetic induction technique for imaging arbitrarily shaped biological objects.* Computer Methods in Biomechanics and Biomedical Engineering: Imaging & Visualization, 2018. **6**(3): p. 353-359.
64. Wang, L., Al-Jumaily, A. M., *Imaging of Lung Structure Using Holographic Electromagnetic Induction* IEEE Access, 2017. **5**: p. 20313-20318.
65. Wang, L., Al-Jumaily, A. M., Simpkin, R., *Investigation of Antenna Array Configurations Using Far-Field Holographic Microwave Imaging Technique.* Progress In Electromagnetics Research M, 2015. **42**: p. 1-11.
66. Dey, S., *Design of novel super wide band antenna close to the fundamental dimension limit theory.* Scientific Reports, 2020. **10**(1).
67. Dey, S., M.S. Arefin, and N.C. Karmakar, *Design and experimental analysis of a novel compact and flexible super wide band antenna for 5G.* Ieee access, 2021. **9**: p. 46698-46708.
68. Azim, R., et al., *CPW-fed super-wideband antenna with modified vertical bow-tie-shaped patch for wireless sensor networks.* IEEE Access, 2020. **9**: p. 5343-5353.
69. Alluri, S. and N. Rangaswamy, *Compact high bandwidth dimension ratio steering-shaped super wideband antenna for future wireless communication applications.* Microwave and Optical Technology Letters, 2020. **62**(12): p. 3985-3991.
70. Elhabchi, M., M.N. Srifi, and R. Touahni, *A novel modified U-shaped microstrip antenna for super wide band (SWB) applications.* Analog Integrated Circuits and Signal Processing, 2020. **102**: p. 571-578.
71. Rafique, U., S. ud Din, and H. Khalil, *Compact CPW-fed super wideband planar elliptical antenna.* International Journal of Microwave and Wireless Technologies, 2021. **13**(4): p. 407-414.
72. Garg, R.K., S. Singhal, and R. Tomar, *A CPW fed clown-shaped super wideband antenna.* Progress In Electromagnetics Research Letters, 2021. **99**: p. 159-168.

73. Das, S., D. Mitra, and S.R.B. Chaudhuri, *Staircase fractal loaded microstrip patch antenna for super wide band operation.* Progress In Electromagnetics Research C, 2019. **95**: p. 183-194.
74. Sagne, D. and R.A. Pandhare, *Design and Analysis of Inscribed Fractal Super Wideband Antenna for Microwave Applications.* Progress In Electromagnetics Research C, 2022. **121**.
75. Khan, M.A., et al., *Ultra-wideband pentagonal fractal antenna with stable radiation characteristics for microwave imaging applications.* Electronics, 2022. **11**(13): p. 2061.
76. Mythili, S., et al., *Design and analysis of Koch fractal antenna for WLAN applications.* ICTACT Journal on Microelectronics, 2020. **6**(2): p. 923-927.
77. de Oliveira, A.M., et al., *A high directive K och fractal V ivaldi antenna design for medical near-field microwave imaging applications.* Microwave and optical technology letters, 2017. **59**(2): p. 337-346.
78. Kundu, S. and A. Chatterjee, *A compact super wideband antenna with stable and improved radiation using super wideband frequency selective surface.* AEU-International Journal of Electronics and Communications, 2022. **150**: p. 154200.
79. Tewary, T., et al., *High gain miniaturrized super-wideband microstrip patch antenna.* International Journal of Communication Systems, 2022. **35**(11): p. e5181.
80. Ullah, S., et al., *High efficient and ultra wide band monopole antenna for microwave imaging and communication applications.* Sensors, 2019. **20**(1): p. 115.
81. Ullah, S., et al., *Super wide band, defected ground structure (DGS), and stepped meander line antenna for WLAN/ISM/WiMAX/UWB and other wireless communication applications.* Sensors, 2020. **20**(6): p. 1735.
82. Mohassieb, S.A., et al., *Low-Loss Super-Wide Band Antenna over Customized Substrate.* Advanced Electromagnetics, 2023. **12**(3): p. 33-42.
83. Agarwal, S., et al., *Three-dimensional miniaturized super wideband antenna with filtering capabilities.* International Journal of RF and Microwave Computer-Aided Engineering, 2022. **32**(8): p. e23200.
84. Ayyappan, M. and P. Patel, *On design of a triple elliptical super wideband antenna for 5G applications.* IEEE Access, 2022. **10**: p. 76031-76043.
85. Biswas, B. and A. Karmakar, *Electrical equivalent circuit modelling of various fractal inspired UWB Antennas.* Frequenz, 2021. **75**(3-4): p. 109-116.
86. Sharma, N., S.S. Bhatia, and V.K. Banga, *Design and investigation of pocket shaped fractal antenna using circular ring elements for UWB technology with stub loaded DGS.* International Journal of Electronics, 2023. **110**(8): p. 1516-1533.
87. Khorramizadeh, M. and S. Mohammad-Ali-Nezhad, *Radar cross-section reduction of an UWB MIMO antenna using image theory and its equivalent circuit model.* International Journal of RF and Microwave Computer-Aided Engineering, 2021. **31**(4): p. e22563.
88. Wang, L., *Microwave Imaging and Sensing Techniques for Breast Cancer Detection.* Micromachines, 2023. **14**(7): p. 1462.
89. Anand, G., A. Lowe, and A. Al-Jumaily, *Tissue phantoms to mimic the dielectric properties of human forearm section for multi-frequency bioimpedance analysis at low frequencies.* Materials Science and Engineering: C, 2019. **96**: p. 496-508.

90. Gabriel, C., S. Gabriel, and Y. Corthout, *The dielectric properties of biological tissues: I. Literature survey.* Physics in medicine & biology, 1996. **41**(11): p. 2231.
91. Sasaki, K., K. Wake, and S. Watanabe, *Development of best fit Cole-Cole parameters for measurement data from biological tissues and organs between 1 MHz and 20 GHz.* Radio Science, 2014. **49**(7): p. 459-472.
92. Wang, L. and H. Chen. *Design of a Wideband Antipodal Vivaldi Antenna with High Gain for Detecting Breast Cancer*. in *Computational and Experimental Simulations in Engineering: Proceedings of ICCES2019 24*. 2020. Springer.
93. Zerrad, F.-e., et al., *Microwave Imaging Approach for Breast Cancer Detection Using a Tapered Slot Antenna Loaded with Parasitic Components.* Materials, 2023. **16**(4): p. 1496.
94. Islam, M., et al., *A low cost and portable microwave imaging system for breast tumor detection using UWB directional antenna array.* Scientific reports, 2019. **9**(1): p. 15491.
95. Biswas, B., R. Ghatak, and D. Poddar, *A fern fractal leaf inspired wideband antipodal Vivaldi antenna for microwave imaging system.* IEEE Transactions on Antennas and Propagation, 2017. **65**(11): p. 6126-6129.
96. Alani, S., et al., *Electronic bandgap miniaturized UWB antenna for near-field microwave investigation of skin.* AIP Advances, 2021. **11**(3).
97. Selvaraj, V., et al., *Breast tissue tumor analysis using wideband antenna and microwave scattering.* IETE Journal of Research, 2021. **67**(1): p. 49-59.
98. Hossain, K., et al., *Negative index metamaterial-based frequency-reconfigurable textile CPW antenna for microwave imaging of breast cancer.* Sensors, 2022. **22**(4): p. 1626.
99. Tobon Vasquez, J.A., et al., *A prototype microwave system for 3D brain stroke imaging.* Sensors, 2020. **20**(9): p. 2607.
100. Islam, M.S., et al., *A portable electromagnetic head imaging system using metamaterial loaded compact directional 3D antenna.* IEEE Access, 2021. **9**: p. 50893-50906.
101. Rodriguez-Duarte, D.O., et al., *Experimental assessment of real-time brain stroke monitoring via a microwave imaging scanner.* IEEE Open Journal of Antennas and Propagation, 2022. **3**: p. 824-835.
102. Arayeshnia, A., S. Amiri, and A. Keshtkar, *Miniaturized on-body antenna for small and wearable brain microwave imaging systems.* International Journal of RF and Microwave Computer-Aided Engineering, 2020. **30**(4): p. e22133.
103. Hasgall, P.A., et al., *IT'IS Database for thermal and electromagnetic parameters of biological tissues.* Version 4.0, 2018.
104. Gupta, H.K., R. Sharma, and V.V. Thakare, *Design of Symmetrical Shaped DGS Pattern Rectangular Microstrip Patch Antenna for Brain Tumor Detection by Microwave Imaging.* Materials Today: Proceedings, 2020. **29**: p. 548-555.
105. Alam, M.M., et al., *W-shaped slot-loaded U-shaped low SAR patch antenna for microwave-based malignant tissue detection system.* Chinese Journal of Physics, 2022. **77**: p. 233-249.
106. Widyatama, P.Z., B.S. Nugroho, and L.O. Nur. *Design of circular modified UWB antenna microstrip for brain cancer detection*. in *2019 IEEE Asia Pacific Conference on Wireless and Mobile (APWiMob)*. 2019. IEEE.
107. Jamlos, M., M. Jamlos, and A. Ismail. *High performance novel UWB array antenna for brain tumor detection via scattering parameters in microwave*

imaging simulation system. in *2015 9th European Conference on Antennas and Propagation (EuCAP)*. 2015. IEEE.
108. Bashri, M.S.R., et al. *Wearable device for microwave head imaging*. in *2016 46th European Microwave Conference (EuMC)*. 2016. IEEE.
109. Rodriguez-Duarte, D.O., et al., *Brick-shaped antenna module for microwave brain imaging systems.* IEEE Antennas and Wireless Propagation Letters, 2020. **19**(12): p. 2057-2061.
110. Islam, M.S., M.T. Islam, and A.F. Almutairi, *A portable non-invasive microwave based head imaging system using compact metamaterial loaded 3D unidirectional antenna for stroke detection.* Scientific Reports, 2022. **12**(1): p. 8895.
111. Alqahtani, A., et al., *Slotted monopole patch antenna for microwave-based head imaging applications.* Sensors, 2022. **22**(19): p. 7235.
112. Mohammed, B., A. Abbosh, and D. Ireland. *Stroke detection based on variations in reflection coefficients of wideband antennas*. in *Proceedings of the 2012 IEEE International Symposium on Antennas and Propagation*. 2012. IEEE.
113. Yazid, M.Y.I., et al., *A Sierpinski Arrowhead Curve Slot Vivaldi Antenna for Microwave Head Imaging System.* IEEE Access, 2023. **11**: p. 32335-32347.
114. Salleh, A., et al., *Development of microwave brain stroke imaging system using multiple antipodal vivaldi antennas based on raspberry Pi technology.* J. Kejuruterran, 2020. **32**: p. 1-6.
115. Bao, N., et al., *Multi-objective path planning for lung biopsy surgery.* Multimedia tools and applications, 2022: p. 1-18.
116. Wang, L., *Terahertz imaging for breast cancer detection.* Sensors, 2021. **21**(19): p. 6465.
117. Abdelhamid, M.M., Allam, A. M., *Detection of Lung Cancer Using Ultra Wide Band Antenna*, in *2016 Loughborough Antennas & Propagation Conference (LAPC)*. 2016, IEEE: Loughborough, UK.
118. Nuhel, A.K., et al. *Human Lung Non-Invasive Anomaly Detection through UWB Microwave Imaging and Diagnosis of COVID-19: A Possible Application*. in *2023 3rd International Conference on Robotics, Electrical and Signal Processing Techniques (ICREST)*. 2023. IEEE.
119. Deowan, M.E., et al. *Study of UWB near field microwave imaging system for the diagnosis of lungs damage due to fluid accumulations*. in *2022 International Conference for Advancement in Technology (ICONAT)*. 2022. IEEE.
120. Murugesh, M., et al., *Polarization-insensitive planar patch antenna with large embedded serial capacitance for on-metal tag design.* Scientific Reports, 2023. **13**(1): p. 7702.
121. Al-Amin, M.R., C. Li, and M.S. Sharawi, *Full Lumped Element-Based Equivalent Circuit Model for Connected Slot Antenna Arrays.* IEEE Open Journal of Antennas and Propagation, 2022. **3**: p. 1273-1288.
122. Esmati, Z., et al., *Development of an Equivalent Circuit Model for the Design of Array of Electrically Small Antennas.* IEEE Transactions on Antennas and Propagation, 2022. **71**(1): p. 381-392.
123. Ripin, N., A. Sulaiman, and N. Rashid, *An equivalent circuit model of miniature double e-shaped meander line printed monopole antenna.* Journal of Telecommunication, Electronic and Computer Engineering (JTEC), 2018. **10**(2-5): p. 59-63.

124. Ghosal, S.a.C., S. R. B., *Analysis of a rectangular slot on a microstrip patch antenna with an equivalent circuit model*, in *Proc. IEEE Applied Electromagnetics Conf. (AEMC)*. 2013: Bhubaneswar, India. p. 1-2.
125. Luo, S., et al., *A monopole UWB antenna with sextuple band-notched based on SRRs and U-shaped parasitic strips.* AEU-International Journal of Electronics and Communications, 2020. **120**: p. 153206.
126. Chew, K.M., Sudirman, R., Seman, N. and Yong, C.Y., *Reflection coefficient detection of simulation models for microwave imaging simulation system.* Biomed Mater Eng. , 2014. **24**(1): p. 199-207.
127. Li, X., *Body matched antennas for microwave medical applications*. Vol. 72. 2014: KIT Scientific Publishing.
128. O'Loughlin, D., et al., *Open-source software for microwave radar-based image reconstruction.* 2018.
129. Reimer, T., M. Solis-Nepote, and S. Pistorius, *The application of an iterative structure to the delay-and-sum and the delay-multiply-and-sum beamformers in breast microwave imaging.* Diagnostics, 2020. **10**(6): p. 411.
130. de Paula, A.L., M.C. Rezende, and J.J. Barroso. *Modified Nicolson-Ross-Weir (NRW) method to retrieve the constitutive parameters of low-loss materials*. in *2011 SBMO/IEEE MTT-S international microwave and optoelectronics conference (IMOC 2011)*. 2011. IEEE.
131. Rothwell, E.J., et al., *Analysis of the Nicolson-Ross-Weir method for characterizing the electromagnetic properties of engineered materials.* Progress In Electromagnetics Research, 2016. **157**: p. 31-47.
132. Tereshchenko, O., F.J.K. Buesink, and F.B.J. Leferink. *An overview of the techniques for measuring the dielectric properties of materials*. in *2011 XXXth URSI General Assembly and Scientific Symposium*. 2011. Ieee.
133. Khan, M.T. and S.M. Ali, *A brief review of measuring techniques for characterization of dielectric materials.* International Journal of Information Technology and Electrical Engineering, 2012. **1**(1): p. 1-5.
134. Vieira, S.L., et al., *Paraffin-gel tissue-mimicking material for ultrasound-guided needle biopsy phantom.* Ultrasound in medicine & biology, 2013. **39**(12): p. 2477-2484.
135. Shrotriya, D., et al., *Design and development of an indigenous in-house tissue-equivalent female pelvic phantom for radiological dosimetric applications.* Iranian Journal of Medical Physics, 2018. **15**(3): p. 200-205.
136. Holmes, R.B., et al., *Creation of an anthropomorphic CT head phantom for verification of image segmentation.* Medical Physics, 2020. **47**(6): p. 2380-2391.
137. Ali, A.M., et al., *Construction and validation of a low cost paediatric pelvis phantom.* European Journal of Radiology, 2018. **108**: p. 84-91.
138. Wang, L., R. Simpkin, and A. Al-Jumaily, *Holographic microwave imaging for medical applications.* Journal of Biomedical Science and Engineering, 2013. **2013**.
139. Wang, L., R. Simpkin, and A. Al-Jumaily. *Three-Dimensional Holographic Microwave Imaging Array: Experimental Investigation of Tumour Detection in Breast Phantom*. in *ASME International Mechanical Engineering Congress and Exposition*. 2013. American Society of Mechanical Engineers.
140. Mirbeik-Sabzevari, A. and N. Tavassolian, *Ultrawideband, stable normal and cancer skin tissue phantoms for millimeter-wave skin cancer imaging.* IEEE Transactions on Biomedical Engineering, 2018. **66**(1): p. 176-186.

Appendices

Appendix A *Ethics Approval (may be more than one letter)*

Not required.

Appendix B *Tools*

Not required.

Appendix C *MATLAB code for calculating the dielectric properties based on NRW method.*

```
clear all;
% Define the frequency range (1-40 GHz)
frequency_range = 1e9:1e9:40e9; % 1 GHz to 40 GHz in Hz

% Initialize arrays to store results
epsilon_star = zeros(size(frequency_range));
mu_r_star = zeros(size(frequency_range));
loss_tangent = zeros(size(frequency_range));
conductivity = zeros(size(frequency_range));

% Constants
epsilon_0 = 8.854187817e-12; % Free space permittivity (F/m)
c = 2.99792458e8; % Speed of light (m/s)

% Sample thickness (you should provide this value)
sample_thickness = 0.01; % Assuming a 1 cm thick sample (0.01 m)

% Load S21 and S11 data from CSV files
S21_data = csvread('S21_data.csv'); % Replace with your S21 CSV file name
S11_data = csvread('S11_data.csv'); % Replace with your S11 CSV file name

% Loop through each frequency point in the range
for i = 1:length(frequency_range)
    % Extract S21 data at the current frequency (assuming CSV columns for real and
imaginary parts)
    S21_real = S21_data(i, 1);
    S21_imag = S21_data(i, 2);
    S21 = S21_real + 1i * S21_imag;

    % Extract S11 data at the current frequency (assuming CSV columns for real and
imaginary parts)
    S11_real = S11_data(i, 1);
    S11_imag = S11_data(i, 2);
    S11 = S11_real + 1i * S11_imag;

      % Calculate X (5.3b)
    X = (1 - abs(S21).^2 + abs(S11).^2) ./ (2 * real(S11));

    % Calculate Γ using the correct root (5.3a)
    root = sqrt(X^2 - 1);
    if real(S21) >= 0
        gamma = X - root;
    else
        gamma = X + root;
    end

    % Calculate T (5.4)
    T = (real(S11) + real(S21) - gamma) / (1 - (real(S11) + real(S21)) * gamma);

    % Calculate λ_0 and λ_og (5.5c)
    lambda_0 = c / frequency_range(i);
    lambda_og = 1 / sqrt(1 / lambda_0^2 - 1);
```

```
    % Calculate ε* and μr* (5.5a, 5.5b)
    L = sample_thickness; % Sample thickness in meters
    mur_star = lambda_og / sample_thickness * ((1 + gamma) / (1 - gamma));
    inv_lambda_sq = -((1 / (2 * pi * L)) * log(1 / T))^2;
    epsilon_star = (lambda_0^2) / mur_star * (1 / lambda_og^2 - inv_lambda_sq);

    % Calculate ε_r and ε_i
    epsilon_r = real(epsilon_star);
    epsilon_i = imag(epsilon_star);

    % Calculate tanδ and conductivity (5.6)
    tan_delta = epsilon_i / epsilon_r;
    sigma = epsilon_i * epsilon_0 * (2 * pi * frequency_range(i));

    % Store the results
    epsilon_star(i) = epsilon_star;
    mu_r_star(i) = mur_star;
    loss_tangent(i) = tan_delta;
    conductivity(i) = sigma;
end

% (Plotting and displaying results)
% ...
figure;
subplot(2, 2, 1);
plot(frequency_range / 1e9, real(epsilon_star));
xlabel('Frequency (GHz)');
ylabel('\epsilon'''');
title('Real Part of Complex Permittivity');

subplot(2, 2, 2);
plot(frequency_range / 1e9, imag(epsilon_star));
xlabel('Frequency (GHz)');
ylabel('\epsilon"');
title('Imaginary Part of Complex Permittivity');

subplot(2, 2, 3);
plot(frequency_range / 1e9, real(loss_tangent));
xlabel('Frequency (GHz)');
ylabel('tan \delta');
title('Loss Tangent');

subplot(2, 2, 4);
plot(frequency_range / 1e9, conductivity);
xlabel('Frequency (GHz)');
ylabel('\sigma (S/m)');
title('Conductivity');

% Display the calculated dielectric properties at a specific frequency (e.g., 10
GHz)
desired_frequency = 10e9; % 10 GHz
index = find(frequency_range == desired_frequency);
fprintf('At %d GHz:\n', desired_frequency / 1e9);
```

```
fprintf('Real Part of \epsilon*: %.4f\n', real(epsilon_star(index)));
fprintf('Imaginary Part of \epsilon*: %.4f\n', imag(epsilon_star(index)));
fprintf('Loss Tangent (tan \delta): %.4f\n', real(loss_tangent(index)));
fprintf('Conductivity (\sigma): %.4f S/m\n', conductivity(index));
```

Appendix D ECM Evolution Stages.

ECM Stage	Corresponding Antenna Stage	Response
Stage 0 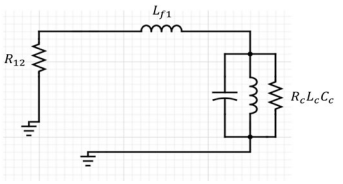	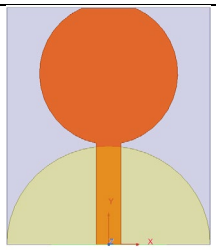	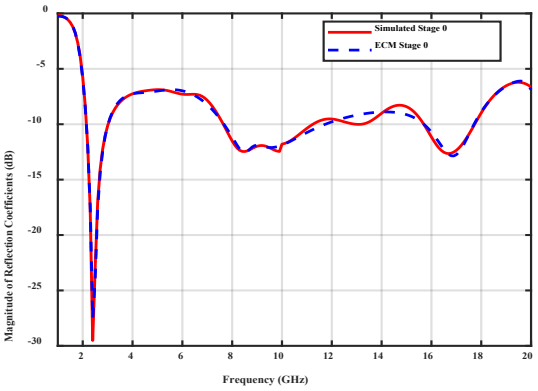
Stage 1 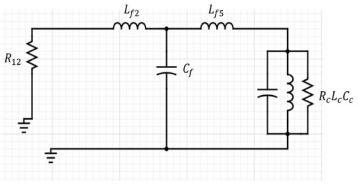	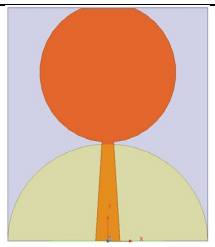	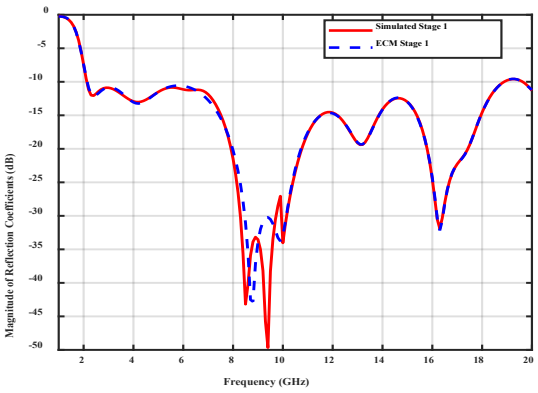
Stage 2 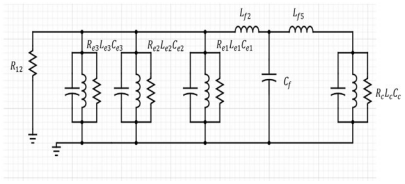	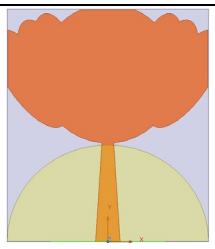	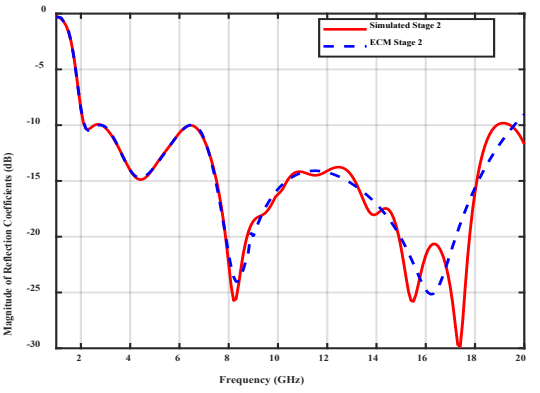

Stage 3	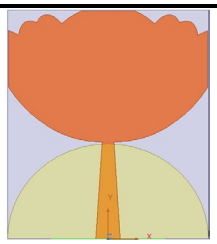	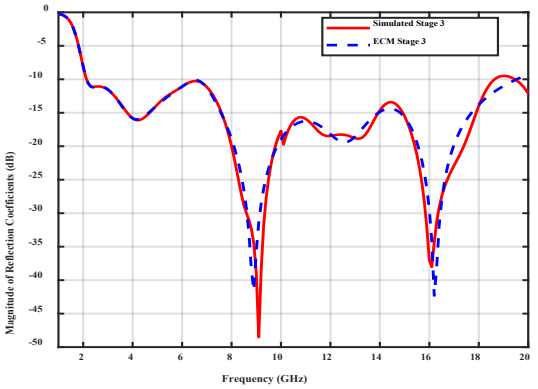
Stage 4	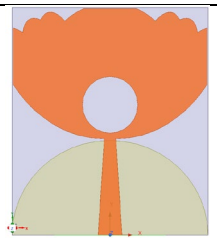	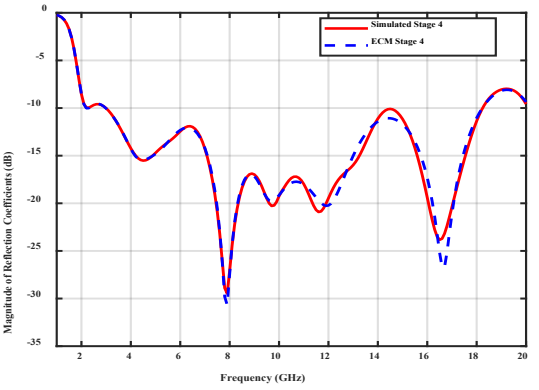
Stage 5	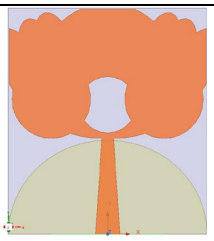	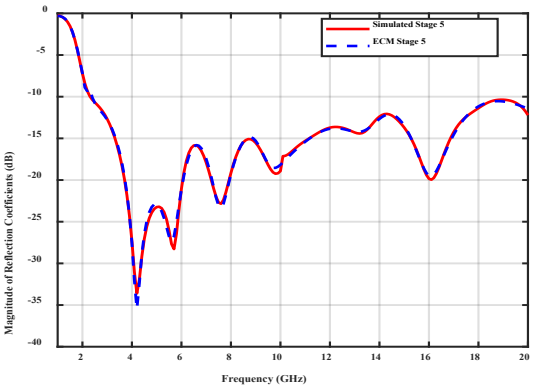

Stage 6

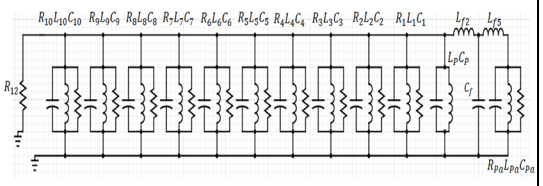

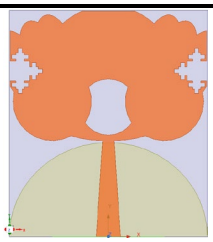

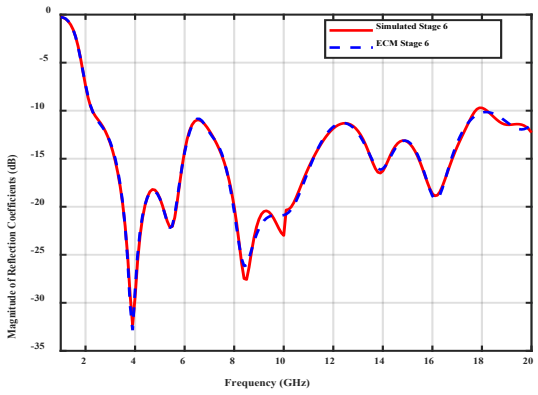

Stage 7

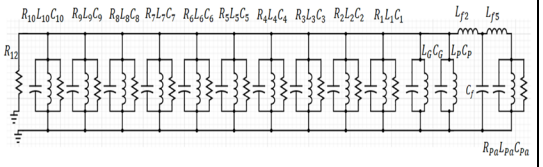

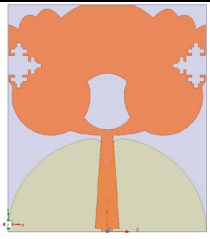

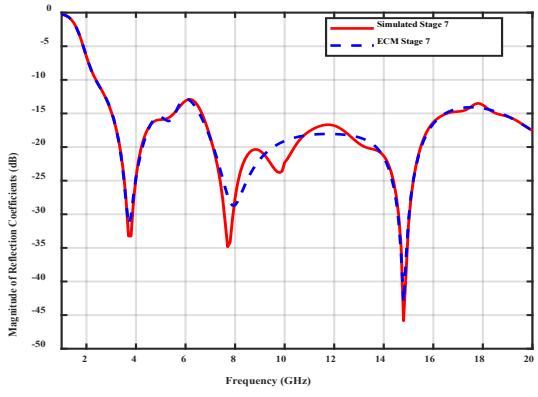

Stage 8

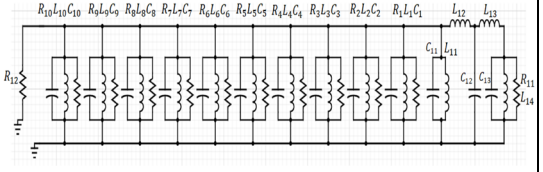

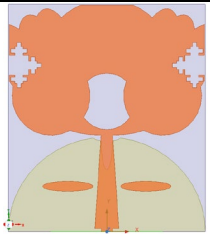

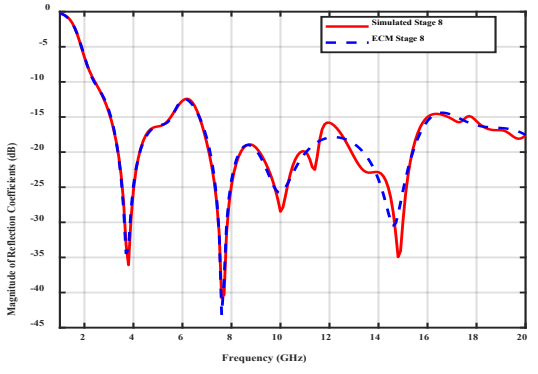

Appendix E *Research outputs from thesis or publication from thesis (if applicable)*

- W. Alamro, B. -C. Seet, L. Wang and P. Parthiban, “Experimental Detection of Early-Stage Lung and Skin Tumors Based on Super Wideband Imaging,” in *IEEE Journal of Electromagnetics, RF and Microwaves in Medicine and Biology*, vol. 8, no. 2, pp. 182-189, June 2024, doi: 10.1109/JERM.2024.3395923.
- W. Alamro, B.C. Seet, L. Wang, P. Parthiban, “Equivalent Circuit Modeling and Optimization for Fractal Slot Loaded Super Wideband Antenna for Medical Imaging Applications”, (under submission to a journal)
- W. Alamro, B.C. Seet, L. Wang, P. Parthiban, “Early-Stage Lung Tumor Detection Based on Super-Wideband Microwave Reflectometry”, *Electronics*, vol. *12*, no. 36, 2023. https://doi.org/10.3390/electronics12010036
- W. A. Alamro and B. C. Seet, ‘’Review of practical antennas for microwave and millimetre-wave medical imaging’’ (Healthcare Technologies, 2021), Chapter 6 in *Electromagnetic Waves and Antennas for Biomedical Applications,* IET, UK, 2021, pp. 185-207, DOI: 10.1049/PBHE033E_ch6
- W. A. Alamro, B. C. Seet, L. Wang and P. Parthiban, “Compact Super-Wideband Antenna for Medical Imaging Applications*”, 2021 IEEE Conference on Antenna Measurements & Applications (CAMA),* 2021, pp. 505-508. DOI: 10.1109/CAMA49227.2021.9703550.
- W. Alamro, B. C. Seet, L. Wang and P. Parthiban, “High Resolution In-Situ Skin Cancer Microwave Imaging Using Super Wideband Antenna, ” *2023 16th International Congress on Image and Signal Processing, BioMedical Engineering and Informatics (CISP-BMEI)*, Taizhou, China, 2023, pp. 1-5, doi: 10.1109/CISP-BMEI60920.2023.10373355.
- W. Alamro, B.C. Seet, L. Wang, P. Parthiban, “Early-Stage Lung and Skin Tumour Detection with Super Wideband Antenna Array Imaging”, oral abstract presentation*, Workshop on Sensing, Measurement and Instrumentation for Healthcare, Food, Agriculture, Environment and Security,* IEEE Instrumentation and Measurement Society New Zealand Chapter, 2023 (accepted).